

# Characterization of bonding differences by advanced synchrotron based X-ray spectroscopy

Zur Erlangung des akademischen Grades eines  
DOKTORS DER NATURWISSENSCHAFTEN  
(Dr. rer. nat.)

von der Fakultät für Chemie und Biowissenschaften  
des Karlsruher Instituts für Technologie (KIT)  
genehmigte

DISSERTATION

von

Dipl. Min. Tim Prüßmann

aus

Hamburg

KIT-Dekan:	Prof. Dr. Willem Klopper
Referent:	KIT Associated Fellow Dr. Tonya Vitova
Korreferenten:	Prof. Dr. Horst Geckeis Prof. Dr. Petra Panak
Tag der mündlichen Prüfung:	12. 02. 2016



This document is licensed under the Creative Commons Attribution – Share Alike 3.0 DE License (CC BY-SA 3.0 DE): <http://creativecommons.org/licenses/by-sa/3.0/de/>

I hereby declare that this thesis is my own unaided work. All direct or indirect sources used are acknowledged as references.

Karlsruhe, 12. 02. 2016



# Contents

<b>1. Introduction and motivation</b>	<b>1</b>
<b>2. Fundamental principles of X-ray Absorption and X-ray Emission Spectroscopy</b>	<b>7</b>
2.1. X-ray absorption spectroscopy (XAS)	7
2.2. Resonant inelastic x-ray scattering (RIXS)	12
2.3. General experimental setup	16
2.4. XES spectrometer	21
<b>3. Experiment</b>	<b>31</b>
3.1. Samples	31
3.1.1. Ligands and complexes	31
3.2. N K edge	34
3.2.1. BESSY	34
3.2.2. ANKA	35
3.2.3. N K edge general considerations	35
3.2.4. APS	39
3.2.5. ESRF	41
3.2.6. ALS	41
3.3. $An/Ln$ $L_3$ edge	43
3.3.1. HASYLAB	43
3.3.2. ANKA	43
3.3.3. ESRF	43
3.3.4. $An/Ln$ $L_3$ edge general considerations	45
3.4. Modeling and Calculation	53
3.4.1. Modeling	53
3.4.2. Structure optimization	53
3.4.3. N K edge	55
3.4.4. $An/Ln$ $L_3$ edge	55
3.4.4.1. Comparison of methods	55

---

3.4.4.2.	Comparison of structures . . . . .	56
3.4.4.3.	FEFF – XANES pre-edge . . . . .	56
3.4.4.4.	FEFF – EXAFS trends . . . . .	56
3.4.4.5.	FDMNES – XANES trends . . . . .	57
<b>4.</b>	<b>Results</b>	<b>59</b>
4.1.	N K edge . . . . .	59
4.1.1.	General description of the spectrum . . . . .	59
4.1.2.	Comparison of $[An/Ln(n\text{-Pr-BTP})_3](\text{OTf})_3$ spectra . .	65
4.1.3.	Quantum chemical investigations of H-BTP and $An/Ln(\text{H-BTP})_3$ . . . . .	70
4.1.4.	Comparison of N K edge spectra of ligands similar to $n\text{-Pr-BTP}$ . . . . .	75
4.1.5.	NRIXS feasibility studies . . . . .	79
4.1.6.	Conclusions . . . . .	82
4.2.	$Ln/An$ $L_3$ edge HR-XANES and RIXS . . . . .	85
4.2.1.	General description of the spectrum . . . . .	85
4.2.2.	Calculations of $Ln$ $L_3$ edge HR-XANES spectra of $[Ln(n\text{-Pr-BTP})_3](\text{OTf})_3$ . . . . .	90
4.2.3.	Comparison between Gd $L_3$ edge HR-XANES of $[\text{Gd}(n\text{-Pr-BTP})_3](\text{NO}_3/\text{OTf})_3$ and $\text{Gd}(\text{NO}_3/\text{OTf})_3$ . . .	97
4.2.4.	Comparison between $Ln$ $L_3$ edge HR-XANES spectra of $[Ln(n\text{-Pr-BTP})_3](\text{OTf})_3$ and $Ln(\text{OTf})_3$ . . . . .	99
4.2.4.1.	EXAFS calculations with the <i>FEFF</i> code . .	102
4.2.4.2.	XANES calculations with the <i>FDMNES</i> code	108
4.2.5.	Comparison between $An$ $L_3$ edge HR-XANES of $[An(n\text{-Pr-BTP})_3](\text{NO}_3)_3$ and $An(\text{NO}_3)_3$ . . . . .	110
4.2.6.	Conclusions . . . . .	113
<b>5.</b>	<b>Summary and Outlook</b>	<b>117</b>
	<b>Bibliography</b>	<b>121</b>
	<b>List of Figures</b>	<b>147</b>
	<b>List of Tables</b>	<b>153</b>
	<b>List of Abbreviations</b>	<b>157</b>

---

<b>Acknowledgments</b>	<b>159</b>
<b>A. Calculations</b>	<b>A-1</b>
A.1. Comparison of methods . . . . .	A-1
A.1.1. FEFF . . . . .	A-1
A.1.2. FDMNES – FMS . . . . .	A-6
A.1.3. FDMNES – FP . . . . .	A-7
A.2. FEFF – XANES pre-edge . . . . .	A-8
A.3. FEFF – EXAFS . . . . .	A-9
A.4. FDMNES . . . . .	A-10
<b>B. EXAFS paths</b>	<b>B-1</b>
<b>C. List of Publications</b>	<b>C-1</b>



# 1 | Introduction and motivation

Worldwide  $\sim 10\,500\text{ t}_{\text{HM}}$  of spent fuel is discharged annually from nuclear power plants [1], leading to  $\sim 370\,500\text{ t}_{\text{HM}}$  total amount of spent fuel that has been discharged globally up to December 2013 [2]. Approximately  $112\,800\text{ t}$  of this has been reprocessed [2] to be used as fuel for a new generation of nuclear reactors [3–6]. Separated Pu and U can also be used as mixed oxide (MOX) fuel in current nuclear power plants. The remaining spent fuel and the high-level waste (HLW) generated as a by-product in the reprocessing are currently stored in at-reactor or away-from-reactor storage facilities [2]. The long-term hazard of spent fuel and HLW is associated with actinides (*Ans*), especially the transuranium elements, and with long-lived fission and activation products. A way to significantly reduce the volume, the heat load of a repository after some decades and the long-term radiotoxicity of the spent fuel is the so-called Partitioning and Transmutation (P&T) strategy [3, 5–7]. Here the different components are separated (partitioning) and the transuranium elements are converted to short-lived or stable nuclides (transmutation) using neutron-induced fission or capture reactions; fission product transmutation is not considered as reasonably achievable. In the first step of the partitioning U and Pu are extracted from spent nuclear fuel using the PUREX (Plutonium-Uranium Recovery by EXtraction) process, which is already used commercially in reprocessing plants [8]. Additional processes necessary to separate fission products, minor *An* and lanthanide (*Ln*) from the PUREX raffinate are still under development [9], e.g. the *i*-SANEX (innovative Selective ActiNide EXtraction) concept where *An* and *Ln* are co-extracted from the PUREX raffinate, followed by a back-extraction of *An*.

Figure 1.1 shows the radiotoxicity evolution (based on ICRP72 effective dose coefficients [10]) of light water reactor (LWR) fuel at a burnup of  $50\text{ GW} \cdot \text{d} \cdot \text{t}_{\text{HM}}^{-1}$  [3]. As a reference value the radiotoxicity of  $7.83\text{ t}$  natural

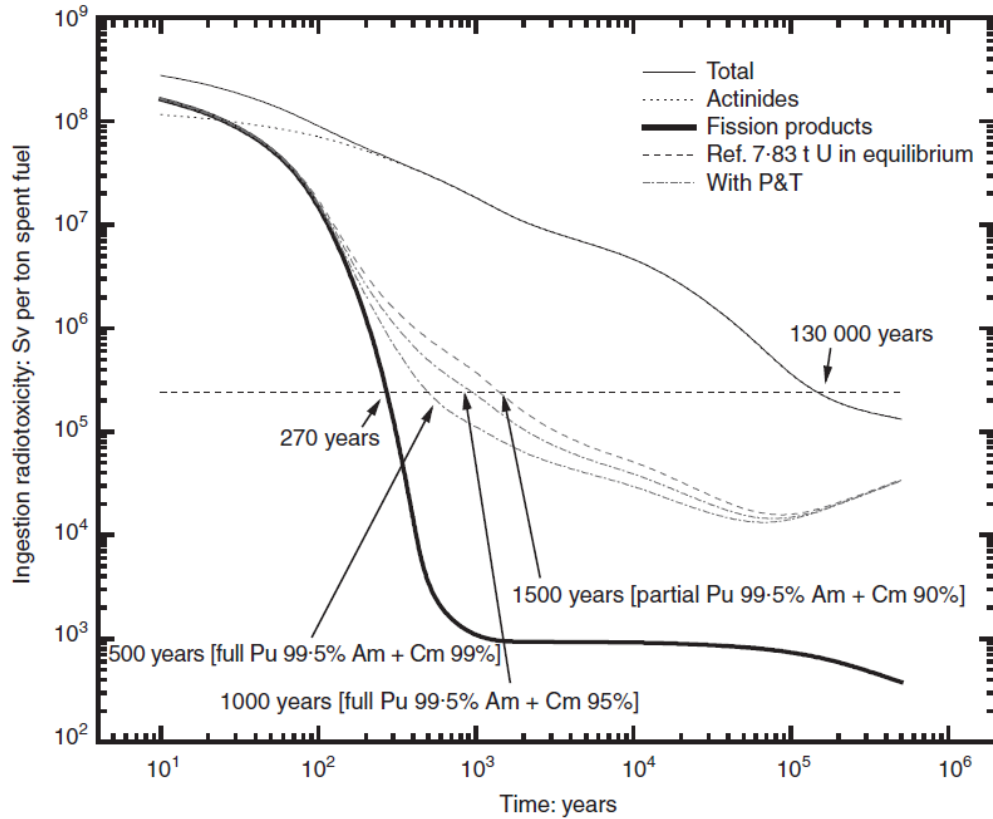


**Figure 1.1.:** Ingestion radiotoxicity of one ton used nuclear fuel based on ICRP72 effective dose coefficients [10]. From [3].

U in equilibrium with its decay series is used, which is the amount needed to produce 1 t of fuel. Without any P&T of the fuel the reference level will be reached after 130 000 years. Exemplary calculations for P&T processes with different efficiencies reach the reference level after 500 to 1500 years, reducing the long-term radiotoxicity inventory after several hundred years by two orders of magnitude or more. A major step in P&T is the separation of  $5f$  elements, especially the minor actinides, from their chemically similar  $4f$  counterparts. This separation is necessary, as the  $Ln$  fission products have large neutron absorption cross sections and thereby compromise transmutation efficiency in the nuclear fission process. Selective liquid-liquid extraction of  $An^{3+}$  from  $Ln^{3+}$  has been demonstrated using soft nitrogen-

or sulfur-donor ligands [11–17], especially heterocyclic N-donor ligands, e.g., bistriazinylpyridines (BTP) [18–20] and bistriazinylbipyridines (BTBP) [21] with separation factors (SF) for  $\text{Am}^{3+}$  over  $\text{Eu}^{3+}$  greater than 100 (SF = distribution ratio  $D_{\text{Am}}/D_{\text{Eu}}$ ;  $D_M = [M]_{\text{org}}/[M]_{\text{aq}}$ ). Additionally, the  $L_n$  elements exhibit a trend in selectivity as a function of their ionic radii [22]. However, 2,6-bis(5,6-dipropyl-1,2,4-triazin-3-yl)-pyridine ( $n$ -Pr-BTP) has slow extraction kinetics [23] and low chemical and radiation stability [24, 25]. Modifications like different alkyl groups [17, 20, 26, 27], substitution in the 4-position of the pyridine ring [27–29] or annulation (e.g. 6,6'-bis(5,5,8,8-tetramethyl-5,6,7,8-tetrahydrobenzo-1,2,4-triazin-3-yl)-pyridine (CyMe<sub>4</sub>-BTP) [30, 31], bis-2,6-(5,6,7,8-tetrahydro-5,9,9-trimethyl-5,8-methano-1,2,4-benzotriazin-3-yl)-pyridine (CA-BTP) [29]) lead to improvements only of some properties at the cost of others. Structural changes in the lateral rings [22, 32–37] can lead to drastic changes in extraction properties, e.g. the separation factors (SF) for  $\text{Am}^{3+}$  over  $\text{Eu}^{3+}$  change from  $SF_{\text{Am}/\text{Eu}} = 130$  for  $n$ -Pr-BTP [19] to  $SF_{\text{Am}/\text{Eu}} = 5$  for 6-bis(4-ethyl-pyridazin-1-yl)-pyridine (Et-BDP) [38].

The physical and chemical properties leading to strong differences in the selectivity, kinetics and stability of these related organic molecules are not yet well understood. There are numerous experimental and theoretical structural studies in the literature looking for small electronic and geometric structural variations, which might be associated with differences in bonding affinities for  $An$  compared to  $L_n$ . This work is focused on the  $n$ -Pr-BTP molecule and the respective  $An^{3+}$  and  $L_n^{3+}$  complexes with this ligand ( $[\text{M}(n\text{-Pr-BTP})_3]^{3+}$ ).

$n$ -Pr-BTP forms 1:3 complexes with  $An^{3+}$  and  $L_n^{3+}$  ( $[\text{M}(n\text{-Pr-BTP})_3]^{3+}$ ) both in the solid state and in organic solution [17, 39–46]. Time-resolved laser fluorescence spectroscopy (TRLFS) confirms the predominant formation of 1:3 complexes for different ligand and solvent combinations [43–45, 47, 48]. It was observed that the relative fluorescence intensity of  $[\text{Eu}(n\text{-Pr-BTP})_3]^{3+}$  is higher than of  $[\text{Cm}(n\text{-Pr-BTP})_3]^{3+}$  indicating a stronger ligand to metal energy transfer [17, 45, 47]. The metal ion is coordinated by the pyridine nitrogen and by the two triazinyl nitrogens in the 2-position of each  $n$ -Pr-BTP molecule. The  $L_n^{3+}$ -N bond length shortens following the contraction of the  $L_n^{3+}$  cation radius [44, 45, 49], while the  $An^{3+}$ -N bond length remains constant from U to Cm [44, 45, 50]. This leads to a decrease in the difference between bond length and  $An^{3+}$  ionic radii indicating a higher covalency in the actinide complexes [49] as previously reported for similar systems [51–54].

Nuclear magnetic resonance (NMR) studies of  $[\text{Am}(n\text{-Pr-BTP})_3](\text{NO}_3)_3$  show a chemical shift that is significantly larger than in  $[\text{Ln}(n\text{-Pr-BTP})_3](\text{NO}_3)_3$  indicating covalent bonding for the  $[\text{Am}(n\text{-Pr-BTP})_3](\text{NO}_3)_3$  complex [55]. Similar effects were observed in NMR studies of  $[\text{Am}(\text{C5-BPP})_3](\text{OTf})_3$  [56]. However, for model systems no contributions from  $f$  electrons to the bonding could be found with NMR (e.g.  $\text{Ln}$  in aqueous solution [57]), Mössbauer spectroscopy (e.g.  $(\text{Ln}/\text{An})\text{I}_3$  [58]), thermodynamic studies [59] and density functional theory (DFT) calculations [52]. Instead it is suggested that metal  $s$  orbitals play a major role in the covalent bonding [51]. Even though  $5f$  electrons in  $\text{An}$  are less localized than  $4f$  electrons in  $\text{Ln}$  [60],  $5f$  contributions to  $\pi$  type ligand based molecular orbitals were shown to arise from a coincidental energy match with the bonding orbitals, e.g. in  $\text{An}(\eta^5\text{-C}_5\text{H}_5)_4$  [61]. On the other hand,  $5f$  and  $6d$  contributions have been found for the covalent uranyl bond [62–65] and the U – C bond in uranocene [66–74] and have been used to explain the selectivity of soft donor S- and N-based ligands separating trivalent  $\text{Ans}$  from  $\text{Lns}$  [52, 75–81]. Systematic comparative X-ray absorption near edge structure (XANES) spectroscopy investigations at the  $\text{Ln}/\text{An}$   $\text{L}_3$  edge and N K edge can have substantial contribution in the ongoing discussion and differentiate bonding mechanisms between  $\text{Ln}$  and  $\text{An}$  bound to different ligands and counter ions, e.g. molecular orbital energy differences, relative electronic populations and orbital mixing [81–85].

The goal of this dissertation is the characterization of small electronic and geometric structural differences between complexes of  $\text{An}^{3+}$  and  $\text{Ln}^{3+}$  bound to N-donor ligands (e.g.  $n\text{-Pr-BTP}$ , C5-BPP) using conventional and high-energy resolution XANES (HR-XANES) and inelastic X-ray scattering (IXS) techniques. This doctoral project pioneers the applications of HR-XANES and IXS for structural studies of actinide containing materials in general and specifically of partitioning complexes. The proposed methods are element and bulk sensitive probes and can be applied to all  $\text{Ln}$  and  $\text{An}$  elements and N in materials in solid and liquid phase, which is not always possible with other methods. Investigations from the “point of view” of the metal and the ligand can facilitate understanding the fundamental principles of the N-donor ligands’ selectivity. Complementary quantum chemical ab initio calculations of the N K and  $\text{An}/\text{Ln}$   $\text{L}_3$  edge spectra applied here help to elucidate the origin of spectral features and possible bonding mechanisms. A major part of this work is the design specification, building and commissioning

---

of a multi analyzer crystal (MAC) spectrometer for high-energy resolution X-ray emission spectroscopy (HRXES) (including HR-XANES and IXS) investigations currently installed at the INE-Beamline for actinide research at the ANKA synchrotron radiation facility in Karlsruhe. Worldwide this is the only state-of-the-art instrument operational in a dedicated controlled laboratory at a synchrotron.



## 2 | Fundamental principles of X-ray Absorption and X-ray Emission Spectroscopy

### 2.1. X-ray absorption spectroscopy (XAS)

When light passes through matter, it loses intensity due to its interaction with the matter. This loss can be described with the Lambert-Beer law,

$$I(E) = I_0 e^{-\mu(E)t}, \quad (2.1)$$

where  $I_0$  is the intensity of the primary beam,  $I$  is the intensity of the transmitted beam,  $t$  is the thickness of the sample and  $\mu$  is the absorption coefficient. In the case of X-rays,  $\mu$  is strongly dependent on the X-ray energy  $E$  and atomic number  $Z$ , and on the density  $\rho$ , and atomic mass  $A$ :

$$\mu \approx \frac{\rho Z^4}{AE^3}. \quad (2.2)$$

From Fermi's golden rule and the one-electron [86] and dipole approximations, the quantum-mechanical description of the X-ray absorption coefficient is given by

$$\mu(E) \propto \sum_f^{E_f > E_F} |\langle f | \hat{\epsilon} \cdot \mathbf{r} | i \rangle|^2 \delta(E - E_f) \quad (2.3)$$

where  $\hat{\epsilon} \cdot \mathbf{r}$  is the dipole operator for the incident electromagnetic wave interacting with the material.  $|i\rangle$  is an initial core state and  $\langle f|$  is a final state with energy  $E$  and  $E_f$ , respectively. The sum is over all energies above the Fermi level ( $E_F$ ) [87, 88].  $\mu(E)$  decreases with increasing energy

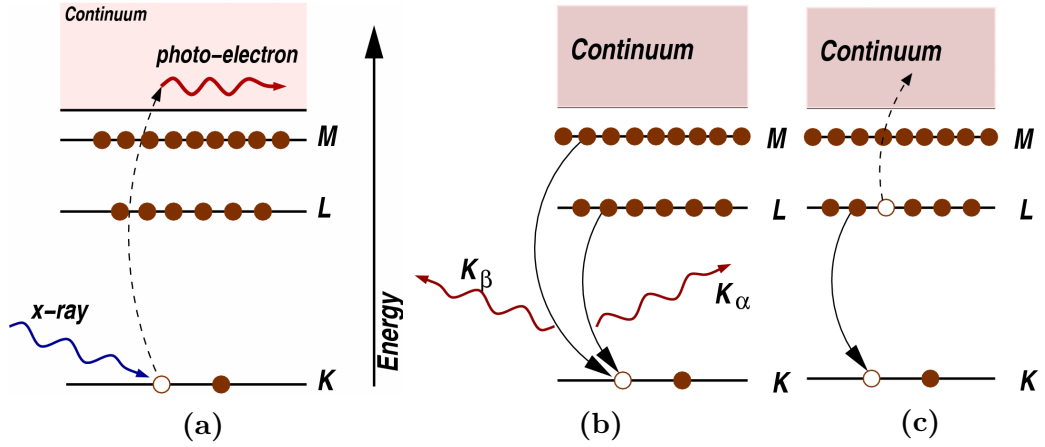


**Figure 2.1.:** The photoelectric effect where an X-ray photon is absorbed by a core-shell electron that is ejected, i.e. excited into the continuum (a). This is followed by the relaxation of the atom via X-ray fluorescence ( $K_\alpha$  or  $K_\beta$ ) (b) or the Auger effect (c) (picture taken from [89]).

approximately as  $1/E^3$ . However, at energies  $E_0$  specific to the elements of the irradiated material, there are sudden increases called X-ray absorption edges. Here the energy of the X-ray photon is high enough to excite an electron out of its shell and into the continuum (photoelectric effect, figure 2.1a). Following this, the atom relaxes by filling the core-hole with higher-shell electrons. The energy difference between the electron levels is released as radiation (fluorescence, figure 2.1b) or the ejection of another electron (Auger effect, figure 2.1c). For elements with low atomic number  $Z$  Auger processes dominate while X-ray fluorescence becomes more probable with increasing  $Z$ . The energy dependence of the absorption coefficient can be measured in transmission as

$$\mu(E) = \log(I_0/I) \quad (2.4)$$

or in X-ray fluorescence (or Auger emission) as

$$\mu(E) \propto I_f/I \quad (2.5)$$

In an X-ray absorption spectroscopy (XAS) experiment the X-ray energy is tuned by using a double crystal monochromator (DCM) [90, 91] across an absorption edge of the element of interest. These edges are labeled K, L, M,

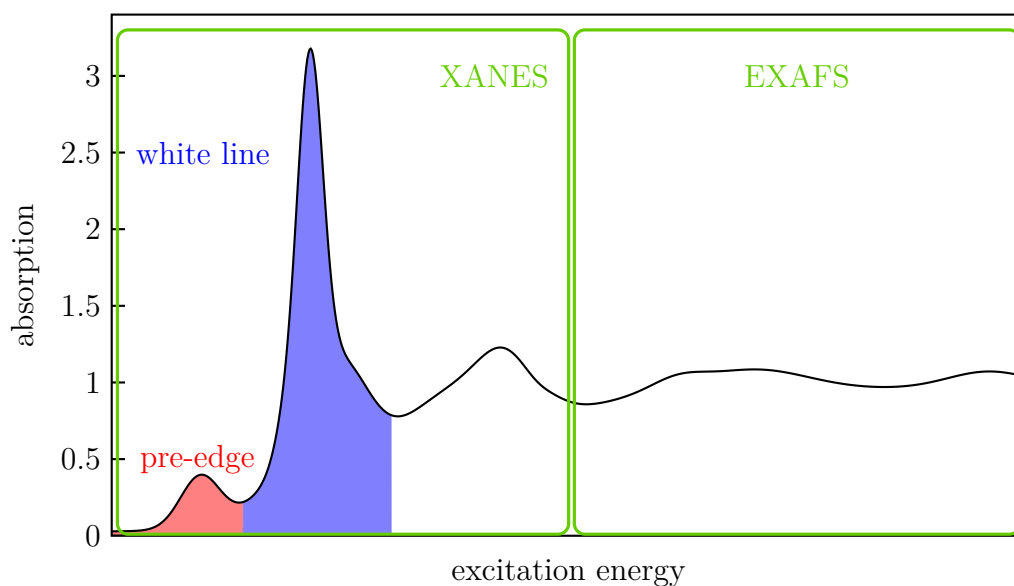


**Figure 2.2.:** Schematic example spectrum showing pre-edge, WL, XANES and EXAFS region.

etc., which corresponds to the principal quantum number  $n = 1, 2, 3, \dots$  of the main electron shell. The excited electrons are labeled with the principal quantum number  $n$  and azimuthal quantum number  $l$  which describes the orbital angular momentum  $0 \leq l \leq n - 1$  ( $1s, 2(s,p), 3(s,p,d)$ , etc.). Figure 2.2 shows a schematic X-ray absorption spectrum. The most intense feature, also called white line (WL), is due to transitions following dipole selection rules  $\Delta l = \pm 1$  ( $2p \rightarrow nd$  for lanthanide ( $Ln$ )/actinide ( $An$ )  $L_{2,3}$  absorption edges). The low intensity pre-edge feature can arise from dipole forbidden transitions ( $\Delta l = \pm 2, 2p \rightarrow nf$  for  $Ln/An$ ) [83, 92–94]. Both the pre-edge and edge region are summarized as near edge X-ray absorption fine structure (NEXAFS) or X-ray absorption near edge structure (XANES). After the WL follows the extended X-ray absorption fine structure (EXAFS) region due to excitations to the continuum. It typically extends to several hundred eV above the edge and gives information about the local environment of the absorbing atom by interaction of the photoelectron with the neighboring

atoms. This interaction is best described in wave form, so the energy is converted to photoelectron wavenumber  $k$  by

$$k = \sqrt{\frac{2m(E - E_0)}{\hbar^2}} \quad (2.6)$$

where  $E_0$  is the absorption edge energy. The ejected photoelectron can be viewed as an outgoing spherical wave, which is scattered at the neighboring atoms, resulting in additional scattering electron waves that interact with the outgoing wave leading to an interference pattern. A common point for the beginning of the EXAFS range is the point where the de Broglie wavelength is comparable to the interatomic distances. The Hamiltonian of the propagating electron is  $H = H_0 + V$  with  $V$  the so-called muffin tin potential [95] consisting of a spherical potential near the atom and a flat interstitial. With the one particle Green's function

$$G(E) = \frac{1}{E - H + i\zeta} \quad (2.7)$$

Fermi's golden rule (equation (2.3)) can be rewritten as

$$\mu(E) \propto -\frac{1}{\pi} \text{Im} \langle i | \hat{\epsilon}^* \cdot \mathbf{r} G(E) \hat{\epsilon} \cdot \mathbf{r} | i \rangle \Theta(E - E_f) \quad (2.8)$$

with the Heaviside step function  $\Theta$  ensuring that  $\mu(E) \neq 0$  only for  $E > E_f$ . The Green's function can be expanded as

$$G = G_0 + G_0 t G_0 + G_0 t G_0 t G_0 + \dots \quad (2.9)$$

$$\iff G = (1 - G_0 t)^{-1} G_0 \quad (2.10)$$

with  $G_0$  the Green's function of the central atom and  $t$  describing the scattering from the surrounding atoms. The first term  $G_0$  describes the propagation of a free electron in space, while the following terms represent contributions with increasing numbers of scattering atoms. For the XANES region,  $G$  has to be calculated explicitly because the large photoelectron wavelength relative to the nearest neighbor distance amplifies the importance of multiple scattering events. For EXAFS on the other hand, many low intensity multiple scattering contributions can be neglected because also longer distance

single scattering and collinear multiple scattering paths, which have high intensities [96], are taken into account. The photoelectron decays as it moves through the material due to interaction with atoms and the finite lifetime of the core-hole. Therefore, XAS can only measure the local atomic structure in a range in the order of tens of angstroms limited by the effective mean free path of the electron [86, 97].

For a quantitative analysis the high energy range of a spectrum can be described by the EXAFS equation [96, 98–102]

$$\chi(k) = S_0^2 \sum_j \frac{N_j f_j(k)}{k R_j^2} e^{-2k^2 \sigma_j^2} e^{-2R_j/\lambda(k)} \sin[2kR_j + \phi_j(k)] \quad (2.11)$$

where  $f(k)$  and  $\phi(k)$  are scattering amplitude and phase-shift of the atoms neighboring the excited atom,  $N$  is the number of neighboring atoms and  $R$  is the distance to the neighboring atom.  $\sigma^2$  is the mean-square disorder in the distribution of interatomic distances, commonly called the Debye-Waller factor, even though it would be more accurate to use the whole term  $e^{-2k^2 \sigma^2}$  as it describes the attenuation of the signal due to disorder analogous to the Debye-Waller factor used in diffraction. Knowing  $f(k)$  and  $\phi(k)$  of the atoms neighboring the excited atom (e.g. from a *FEFF* calculation)  $N$ ,  $R$ , and  $\sigma^2$  can be determined.

A fluorescence-detected absorption spectrum is often recorded with a small energy bandwidth for the incident beam ( $\Delta E_{in} \sim 1$  eV) and a large energy window (no energy resolution or  $\Delta E_{out} \sim 200$  eV) for the emission detection [103]. Additional chemical information can be detected by reducing the bandwidth of the emission detection to the order of the core-hole lifetime using an X-ray emission spectrometer.

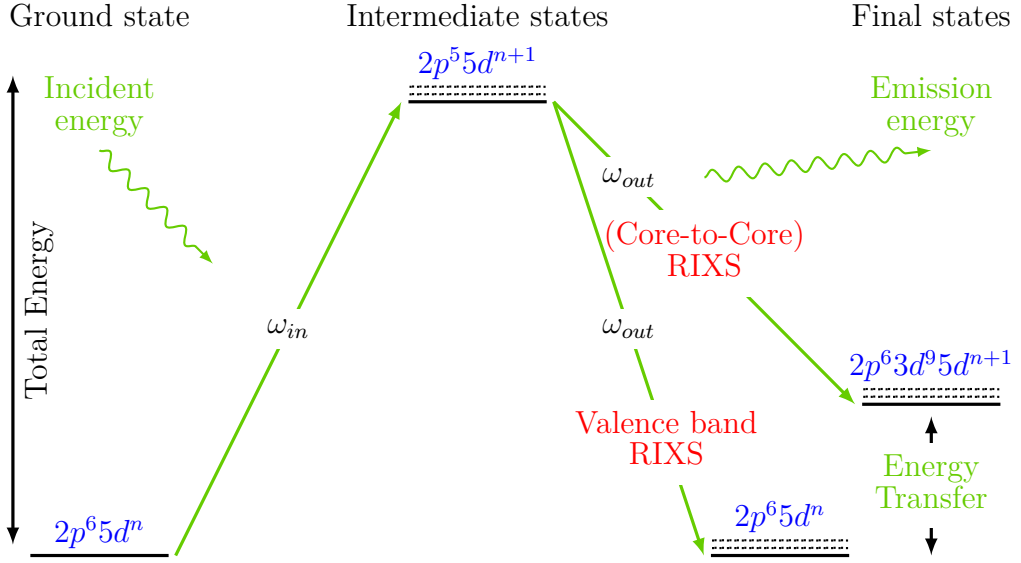


**Figure 2.3.:** Schematic diagram of different RIXS processes.

## 2.2. Resonant inelastic x-ray scattering (RIXS)

Resonant inelastic x-ray scattering (RIXS) is a two-step process involving the excitation of an electron (XAS) and the subsequent relaxation of the system by emission of an X-ray photon (X-ray emission spectroscopy (XES)) [103–110]. Figure 2.3 shows a schematic view of different RIXS processes on the example of  $Ln$  at the  $L_3$  edge. From the  $2p^6 5d^n$  ground state an electron is excited to the valence band leaving behind a  $2p$  core-hole and resulting in a  $2p^5 5d^{n+1}$  intermediate state. In Core-to-Core RIXS (called RIXS throughout this work) the  $2p$  core-hole is filled with another core electron, in this example from  $3d$  states, leading to a  $2p^6 3d^9 5d^{n+1}$  final state. The energy difference between final state and ground state is called energy transfer. The orbitals, in which the intermediate and final state core-holes are located, are often used to label the RIXS process, in this example it is named  $2p3d$  RIXS. In valence band RIXS (VB-RIXS) the  $2p$  core-hole is filled from the filled part of the valence band (VB) emulating a direct excitation from the VB and describing the unoccupied  $5d$  states [111, 112].

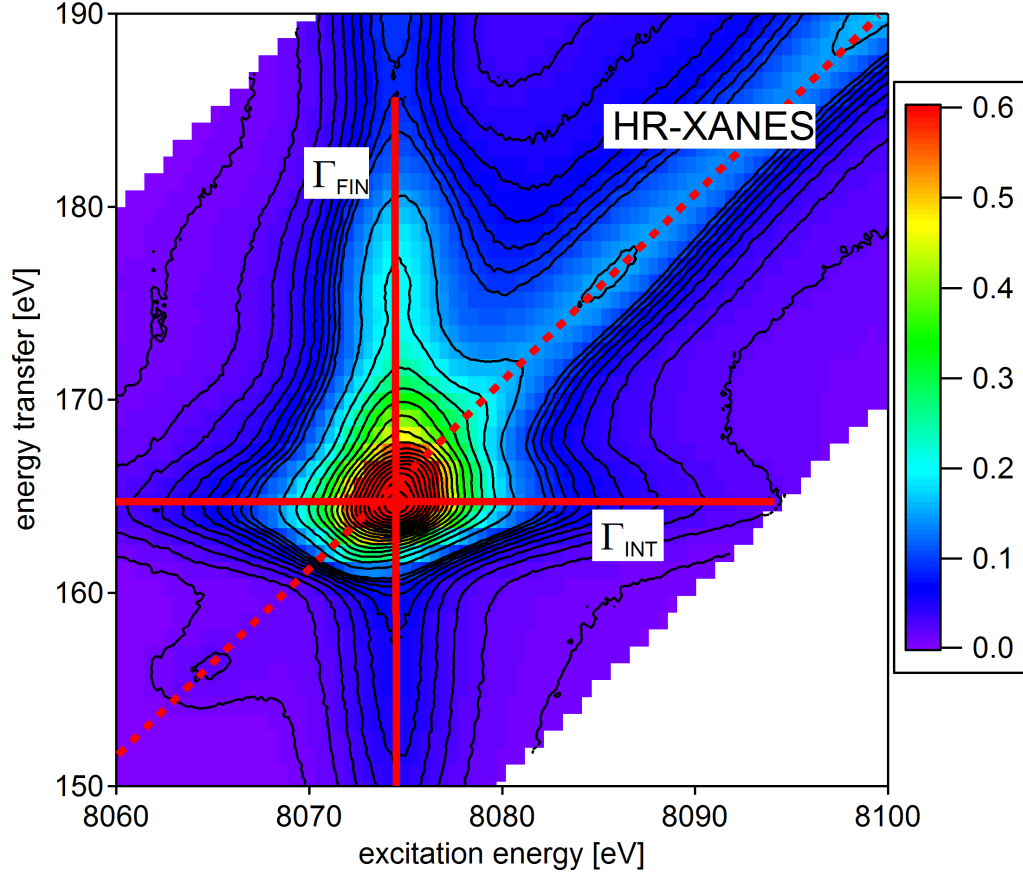


**Figure 2.4.:** RIXS map of Ho(OTf)<sub>3</sub> with intermediate ( $\Gamma_{INT}$ ) and final state ( $\Gamma_{FIN}$ ) broadenings (solid lines) and HR-XANES (dashed line).

Figure 2.4 shows the RIXS of Ho(OTf)<sub>3</sub> with the incident energy plotted versus the energy transfer. The core-hole lifetime broadenings of the intermediate ( $\Gamma_{INT}$ ) and final state ( $\Gamma_{FIN}$ ) are marked with solid lines. The diagonal line corresponds to the HR-XANES spectrum measured as a scan of the incident energy at a fixed emission energy. Spectral features off the diagonal along the energy transfer scale are due to final state effects, e.g. spin-orbit and electron-electron interactions [108, 113, 114]. The core-hole lifetime broadening arises from the finite lifetime  $\tau$  of the core-hole, which according to the Heisenberg uncertainty relation induces an uncertainty (broadening)

of the energy  $\Delta E \approx \hbar/\tau$  [115, 116]. The lifetime  $\tau$  decreases with the atomic number  $Z$  and increasing electron binding energy, so the core-hole broadening  $\Delta E$  increases [115]. The overall process is theoretically described by a reduced form of the Kramers-Heisenberg equation [104, 117]

$$I(\omega_{in}, \omega_{out}) = \sum_f \left| \sum_n \frac{\langle f | T_2 | n \rangle \langle n | T_1 | g \rangle}{E_g + \omega_{in} - E_n - i\Gamma/2} \right|^2 \times \delta(E_g + \omega_{in} - E_f - \omega_{out}). \quad (2.12)$$

Here  $\omega_{in}$  is the energy of the incoming X-ray that excites the atom, by means of the transition operator  $T_1$ , from the ground state  $g$  with energy  $E_g$  to the intermediate state  $n$  with energy  $E_n$ .  $\Gamma_n$  is the lifetime broadening due to the core-hole in the intermediate state. The subsequent radiative decay of the atom, where an X-ray of energy  $\omega_{out}$  is emitted, is described by  $T_2$  and leads to the final atomic state  $f$  with energy  $E_f$ . The summation is with respect to all intermediate and final states  $n$  and  $f$ , respectively, that are accessible via the specific in- and outgoing X-ray. The core-hole lifetime broadenings of the intermediate ( $\Gamma_{INT}$ ) and final ( $\Gamma_{FIN}$ ) states determine the apparent overall spectral broadening ( $\Gamma_{APP}$ ) [118] and can be estimated as the full width at half maximum (FWHM) of a Lorentzian-type profile.

$$\Gamma_{APP} = \frac{1}{\sqrt{\frac{1}{\Gamma_{INT}^2} + \frac{1}{\Gamma_{FIN}^2}}} \quad (2.13)$$

In addition to the inherent core-hole lifetime broadening, it is necessary to include the instrumental broadening (energy bandwidth). The total experimental energy bandwidth  $E_{TOT}$  is a combination of the incident ( $E_{INC}$ ) and emission ( $E_{EM}$ ) energy bandwidths,

$$E_{TOT} = \sqrt{E_{INC}^2 + E_{EM}^2} \quad (2.14)$$

and can be estimated as the FWHM of a Gauss-type profile.  $E_{INC}$  describes the resolving power of the DCM

$$E_{INC}/E = K, \quad (2.15)$$

with  $K$  a constant depending on the used monochromator crystals and other beamline properties. At the INE-Beamline Ge(422) crystals are used for  $An L_3$

XAS and  $K$  is estimated to be  $\sim 2 \times 10^{-4}$ .  $E_{EM}$  depends on the geometry of the spectrometer and the intrinsic resolution of the crystal (Bragg angle  $\theta$ , the bending radius, crystallographic orientation) and can be calculated for an ideal crystal with ray-tracing software (e.g., RT4XES [119], XCRYSTAL\_BENT module [120] of the XOP package [121]). Additionally  $E_{EM}$  is influenced by the quality of the crystal surface, the X-ray spot size on the sample, aberrations, and misalignment of the spectrometer [122–125]. These effects are further discussed in section 2.4. The overall energy broadening of a high-energy resolution XANES (HR-XANES) spectrum can be calculated by convoluting the Gaussian-type broadenings  $f_G$  and the Lorentzian-type broadenings  $f_L$  using the approximate broadening of a Voigt profile  $f_V$  [126]:

$$f_V = 0.5346f_L + \sqrt{0.2169f_L^2 + f_G^2} \quad (2.16)$$

The overall energy broadening of the spectrum is obtained using the following steps [127, 128]:

1. The Lorentzian-type final state lifetime broadening  $\Gamma_{FIN}$  is convoluted with the Gaussian-type emission energy broadening  $E_{EM}$  using equation (2.16):

$$f_V = 0.5346\Gamma_{FIN} + \sqrt{0.2169\Gamma_{FIN}^2 + E_{EM}^2} \quad (2.17)$$

2. The spectral broadening  $\Gamma_{APP}$  is calculated by inserting  $f_V$  instead of  $\Gamma_{FIN}$  into equation (2.13):

$$\Gamma_{APP} = \frac{1}{\sqrt{\frac{1}{\Gamma_{INT}^2} + \frac{1}{f_V^2}}} \quad (2.18)$$

3. The effect of the Gaussian-type incident energy broadening  $E_{INC}$  is taken into account by using equation (2.16) again with  $f_L = \Gamma_{APP}$  and  $f_G = E_{INC}$  resulting in the total broadening  $\Gamma_{TOT}$ :

$$\Gamma_{TOT} = f_V = 0.5346\Gamma_{APP} + \sqrt{0.2169\Gamma_{APP}^2 + E_{INC}^2} \quad (2.19)$$

The broadenings relevant for the samples investigated in this work are summarized in table 3.10.

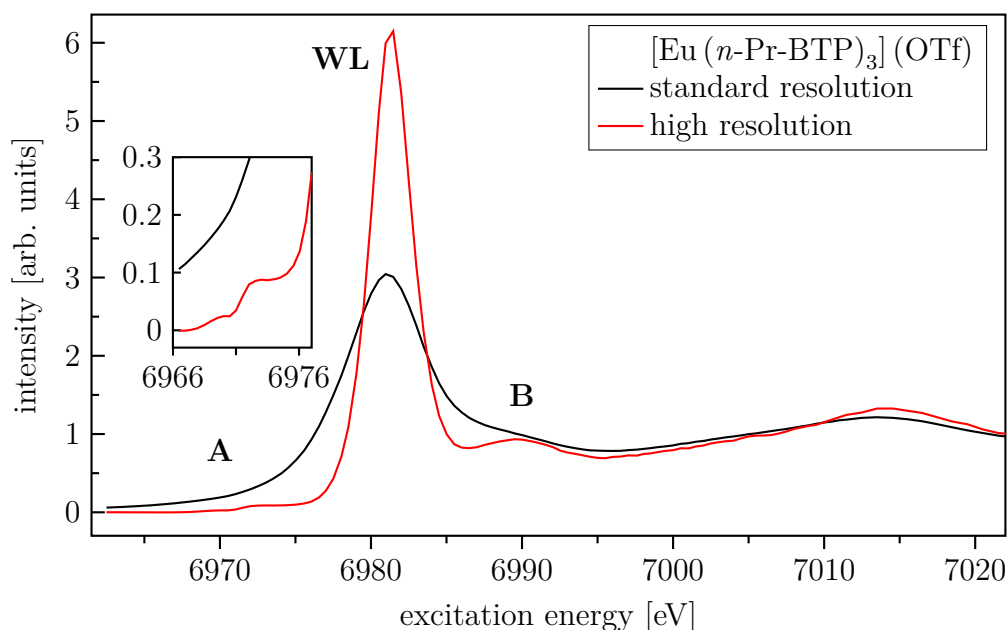


**Figure 2.5.:** Standard and HR-XANES of  $[\text{Eu}(n\text{-Pr-BTP})_3](\text{OTf})_3$ .

In a standard measurement, the final state effects and lifetime broadenings are included in a XANES spectrum leading to a significant spectral broadening compared to HR-XANES (see figure 2.5). Most notably a pre-edge (feature **A**) can be resolved in HR-XANES, the WL is sharper and has higher intensity and post-edge features (**B**) are well separated from the WL. The pre-edge and WL provide electronic structure information not available with the conventional method. Post-edge features close to the WL are often sensitive to multiple scattering of the photoelectron and therefore not only to bond lengths but also the local atomic geometry around the absorbing atom, e.g. bonding angles, which is generally not possible with EXAFS.

### 2.3. General experimental setup

X-ray spectroscopy requires a tunable X-ray source with high intensity such as a synchrotron radiation facility. A synchrotron radiation facility, or a synchrotron light source, is a specific type of particle accelerator built

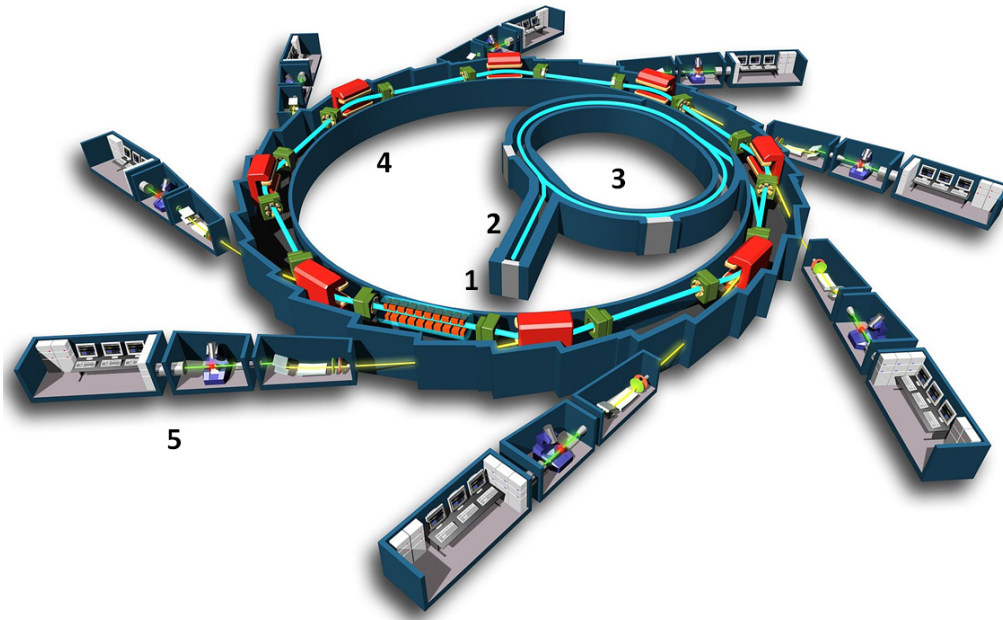


**Figure 2.6.:** Scheme of a typical synchrotron radiation facility (taken from [129]) with (1) an electron gun, (2) a linear accelerator, (3) a booster ring, (4) a storage ring and (5) several beamlines.

to accumulate a high electron current and maintain it for a long lifetime. Figure 2.6 shows a scheme of a typical synchrotron radiation facility consisting of:

1. An electron gun that produces electrons via thermionic emission.
2. A linear accelerator (linac) accelerating the electrons to about 100 MeV using radio frequency (RF) cavities.
3. A booster ring accelerating the electron further, in most cases to their final energy of several GeV.
4. The storage ring maintaining the electrons on a closed path. Dipole- or bending magnets keep the electron on the path, quadrupole magnets focus the electron beam and sextupole magnets correct for chromatic aberrations. The ring consists of arced sections, where the bending magnets are placed, and straight sections used for insertion devices

(wigglers or undulators) that produce the most intense synchrotron radiation.

5. The beamlines running off along the axes of the insertion devices and tangentially at the bending magnets.

If a relativistic electron is accelerated, in this case forced on a non-linear path by a magnetic field, it emits a broad spectrum of radiation along the path of movement. The properties of this spectrum depend on the electron energy (typically between 2–8 GeV) and the magnetic field strength. Bending magnets show a broad spectrum with relatively low intensity. A wiggler can be thought of as a series of bending magnets moving the electron beam in sinusoidal over a certain range. The emitted radiation cones do not overlap, leading to an increase in intensity depending linearly on the number  $N$  of dipoles in the wiggler. In an undulator, the amplitude of the lateral electron movement is smaller than in a wiggler, so the radiation cones overlap and interfere with each other. As only certain wavelength interfere constructively the spectrum consists of a fundamental energy and a series of higher harmonics, but the intensity increases with  $N^2$ . To shift the maxima to different energies the gap between the magnets is changed, thereby changing the overall magnetic field and the path of the electrons. The geometry and resulting spectra for wiggler and undulator are schematically shown in figure 2.7.

Figure 2.8 shows a schematic view of a typical XAS beamline. The source (bending magnet or insertion device) emits a broad spectrum of radiation including many energies that are not required and only lead to heat load on optical components. These energy regions can be cut out of the white beam using cooled apertures and/or slits in the front end. In the optical hutch, the preconditioned beam is further modified. The first mirror collimates the divergent beam coming from the source causing all X-rays to hit the DCM at the same angle. At the DCM (or in case of a soft X-ray beamline the grating) a specific energy is selected by changing the angle according to the Bragg condition  $n\lambda = 2d \sin(\theta)$ , where  $n$  is a positive integer and describes the order of diffraction,  $\lambda$  is the wavelength of the incident beam,  $d$  is the lattice plane distance in the crystal and  $\theta$  is the scattering angle. The second mirror then focuses the beam on the sample. The actual measurements take place in the experimental hutch. The first element in the experimental hutch is usually an ionization chamber recording the intensity of the incident beam

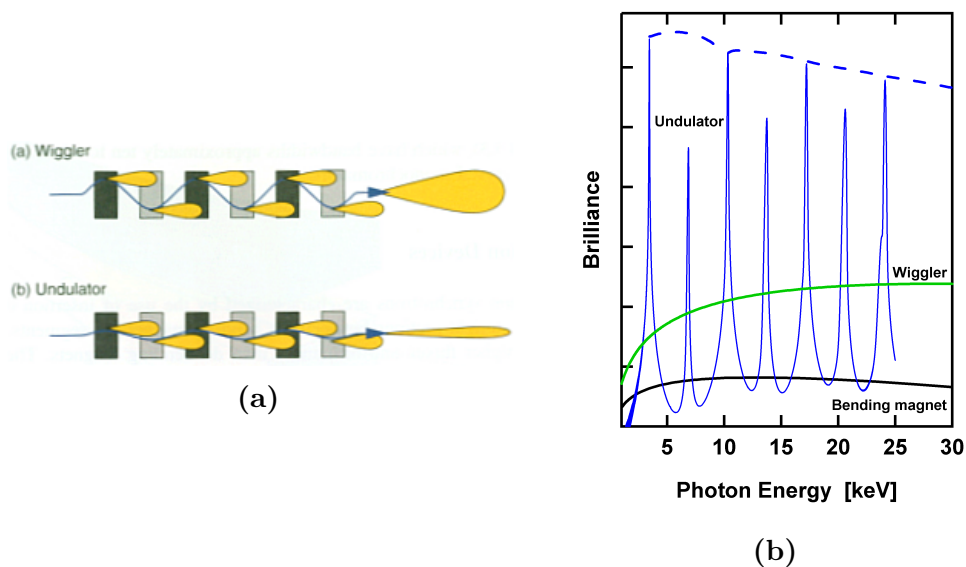


**Figure 2.7.:** Scheme of the (exaggerated) electron paths and emitted radiation in wiggler and undulator (taken from [130]) (a) and the spectral brilliance of wiggler and undulator compared to a standard bending magnet (taken from [131]) (b).

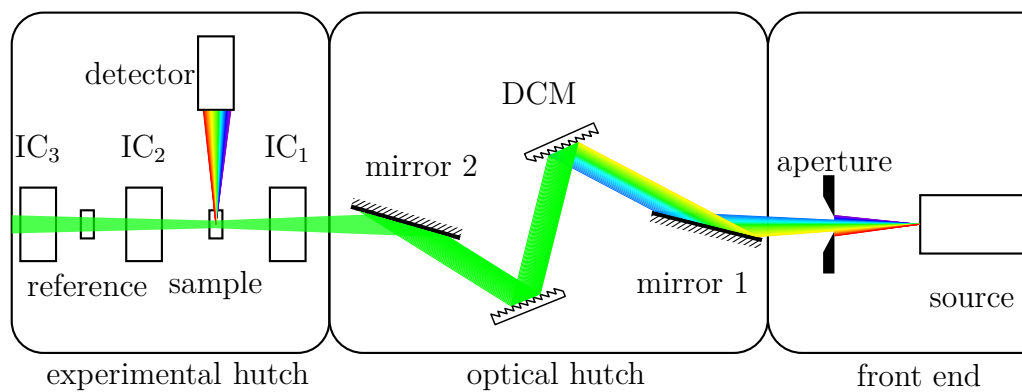


**Figure 2.8.:** Schematic view of a typical XAS beamline (angles and distances are not to scale).

for normalization purposes. After interaction with the sample, there are different possibilities to collect a spectrum. In transmission, the intensity is measured again after the sample. After that, the absorption of a reference (usually a thin metal foil with an absorption edge close to the edge measured for the sample) is measured to be able to calibrate the energy of the incident beam. Alternative to transmission the fluorescence emitted from the sample can be collected using a fluorescence detector. This type of detector records the whole emission spectrum of the sample including inelastic and elastic scattering signals. To extract an absorption spectrum a window can be set in the detector electronics restricting the signal output to an energy range around the emission line corresponding to the element and absorption edge of interest. Instead of a fluorescence detector other devices can be placed, e.g. a spectrometer for high-energy resolution measurements as it was used for most  $An/Ln$   $L_3$  edge XANES spectra shown in this work. For details of such type of spectrometer, see section 2.4.

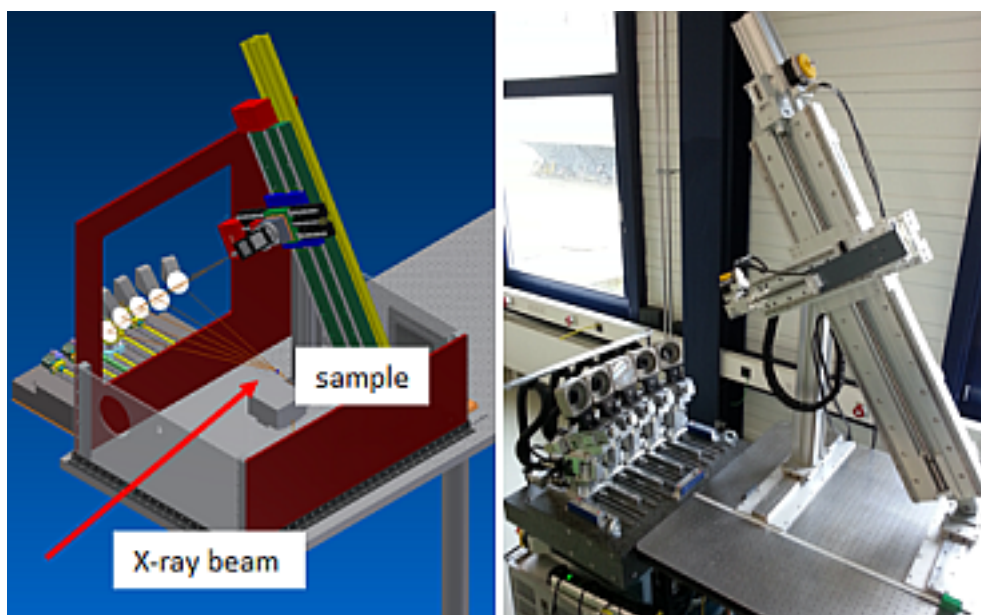


**Figure 2.9.:** 3D CAD model with part of the He environment (left) and photo of the MAC-Spectrometer during initial mechanical performance tests (right).

## 2.4. XES spectrometer

A high-energy resolution multi analyzer crystal (MAC)-Spectrometer (figure 2.9) has been designed, built and commissioned at the INE-Beamline [132] as part of this doctoral project. The spectrometer is an adapted design of the spectrometer at the ID26 Beamline (European Synchrotron Radiation Facility (ESRF)) and is built in Johann geometry [122] for up to five spherically bent Si/Ge analyzer crystals of 1 m bending radius. In this geometry sample, crystal and detector are positioned on the Rowland circle, whose diameter equals the bending radius of the crystal, while the distance sample – crystal equals the distance crystal – detector (figure 2.10).

This setup allows selecting emitted fluorescence with certain energy according to the Bragg condition ( $n\lambda = 2d\sin(\theta)$ ) and focusing it on a detector. The MAC-Spectrometer assembly comprises a mobile and a stationary positioning unit, both supplied by HUBER Diffraktionstechnik GmbH (Rimsting,

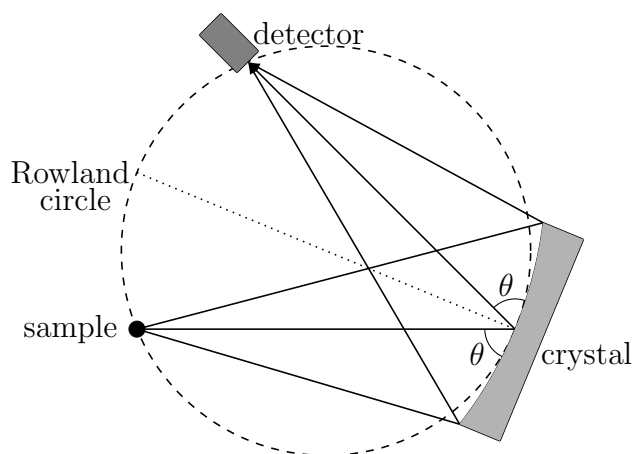


**Figure 2.10.:** Scheme of the Johann geometry [122] (adapted from [125]).

Germany). The five analyzer crystal positioning stages possess four degrees of freedom each (figure 2.11). The crystal stages are mounted on a diabase block. This block is fixed on a mobile rack hosting power supplies and motion controllers for all 23 spectrometer motors. The stationary detector positioning unit comprises three degrees of freedom (a long and a short linear stage and a rotation stage), which allow the detector to be moved along the Rowland circle. The motion controllers are connected to the existing control and data acquisition system via Ethernet. Macros for the synchronous movement of all 23 motors and the necessary alignment procedures have been adapted as part of this work.

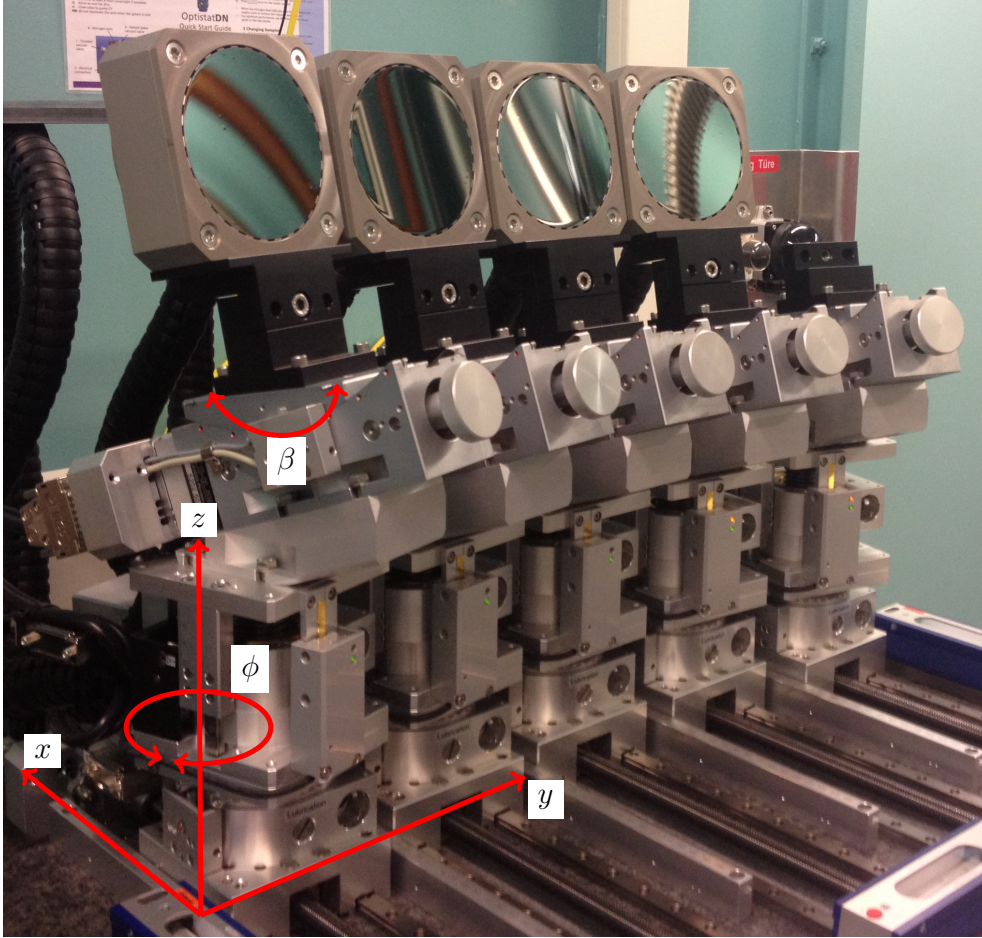


**Figure 2.11.:** Crystal positioning stages with four degrees of freedom.

The position of a crystal  $C_i$  is calculated depending on the Bragg angle  $\theta$  necessary for the chosen type of crystal and energy according to [125] as:

$$x_i = R \sin(\theta) \cos^2(\theta) + x p_i \sin(\theta) \quad (2.20)$$

$$z_i = R \cos(\theta) \sin^2(\theta) + x p_i \cos(\theta) \quad (2.21)$$

$$y_i = (i - 3) dz \quad (2.22)$$

$$\phi_i = \pi - \arctan\left(\frac{z_i}{xp_i \sin(\theta)}\right) \quad (2.23)$$

$$\beta_i = \arctan\left(\frac{\sqrt{y_i^2 + xp_i^2 \sin^2(\theta)}}{xp_i \cos(\theta)}\right) \quad (2.24)$$

$$xp_i = \sqrt{R^2 \sin^4(\theta) - y_i^2} \quad (2.25)$$

where  $R$  is the bending radius of the crystal and  $xp_i$  is a factor describing the influence of an off-center crystal, i.e. a crystal that has an offset in  $y$  direction. The detector has three degrees of freedom:

$$x_d = 2R \sin(\theta) \cos^2(\theta) \quad (2.26)$$

$$z_d = 2R \cos(\theta) \sin^2(\theta) \quad (2.27)$$

$$\beta_d = (3/2)\pi - 2\theta \quad (2.28)$$

The distance  $L$  between sample and crystal, which is equal to the distance between crystal and detector, is:

$$L = R \sin(\theta) \quad (2.29)$$

The energy resolution of the spectrometer is influenced by the intrinsic resolution of the crystal, the quality of the crystal surface, the X-ray spot size on the sample, aberrations, and misalignment of the spectrometer [122–125]. The resolution of the crystal depends on the properties of the crystal, in particular stress in the lattice caused by the bending of the crystal, and lies typically in the range of 0.1 eV–0.3 eV [123–125, 133]. The best resolution can be achieved with a large radius  $R$ , with a small crystal diameter  $d$ , and close to back-scattering ( $\theta = 90^\circ$ ) [122–125]. In the alignment of the spectrometer the distance crystal – sample has the largest influence on the resolution [125].

The spectrometer has been tested with a Medipix2 area detector [134] with 256x256 pixels (pixel size 55  $\mu\text{m}$ ) and a Vortex silicon drift detector [135]. The Medipix detector has been used for first alignments at the Cu  $K\alpha_1$  emission line (8046.3 eV) as it allows the direct observation of changes in position and shape of the focused fluorescence (figures 2.12 and 2.13). The Vortex detector was used for alignment and subsequent HR-XANES measurements at the U  $L_3$  edge.

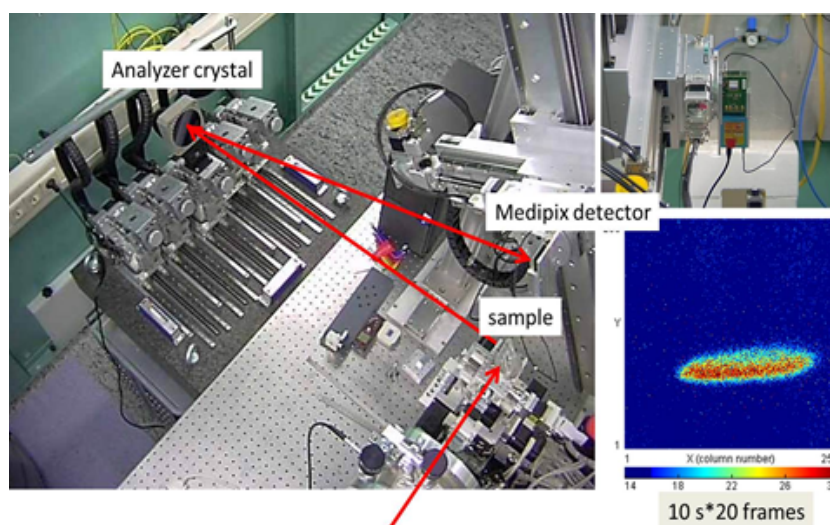


**Figure 2.12.:** Example of the  $\text{Cu K}\alpha_1$  fluorescence focused on the Medipix detector with one crystal.

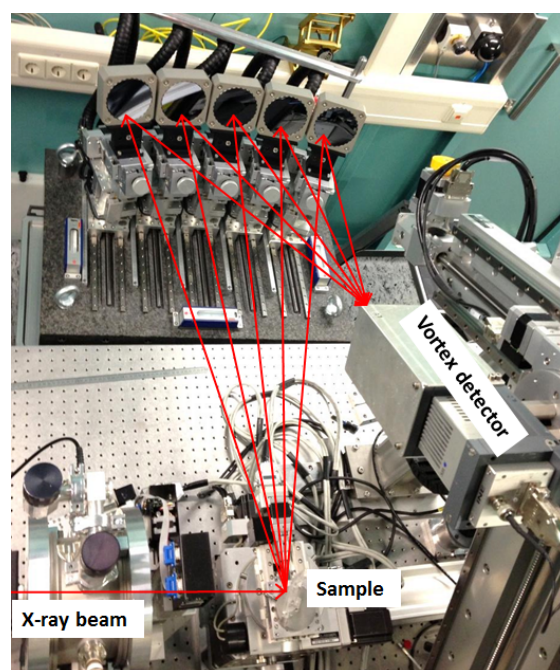


**Figure 2.13.:** Experimental setup for U  $L_3$  edge HR-XANES measurements with the Vortex detector.

Figure 2.14 shows U  $L_3$  XANES spectra of the mineral Metastudtite ( $\text{UO}_4 \cdot 2\text{H}_2\text{O}$ ) in high-energy resolution (30 min, 3 h measurement time) and standard transmission mode. As previously observed [83], the most intense  $2p_{5/2} \rightarrow 6d$  transition (**B**, WL) has higher intensity and is separated from post-edge feature **C** in the high-energy resolution spectra. There are also indications for a pre-edge (**A**) arising from  $2p_{5/2} \rightarrow 5f$  transitions. A HR-XANES spectrum was measured for 30 min with 17 wt% U concentration in the sample. The intensity measured at the maximum of the WL is 260 counts/s at 120 mA ring current, which is about 100 times reduction compared to a standard fluorescence measurement of the same sample. U concentration of 1 wt% requires four to five hours measuring time with the current setup at the INE-Beamline. All relevant  $An L_3$  edges (Th – Cm) are accessible over the  $L\alpha_1$  emission lines with the available (5 Si(111), 5 Ge(111), 5 Si(220)) analyzer crystals (figure 2.15a).

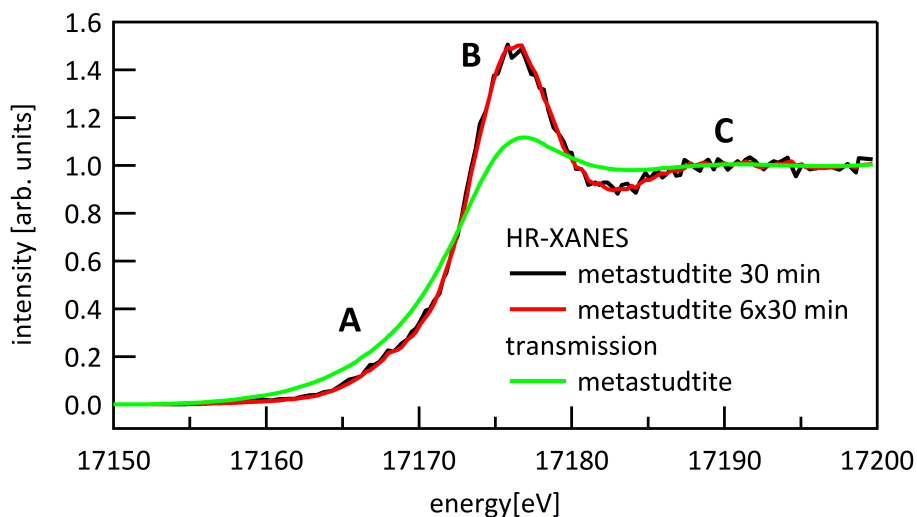


**Figure 2.14.:** U  $L_3$  edge HR-XANES 30 min (black) and 3 h measurement time (red) and standard transmission mode (green) spectra of Metastudtite.

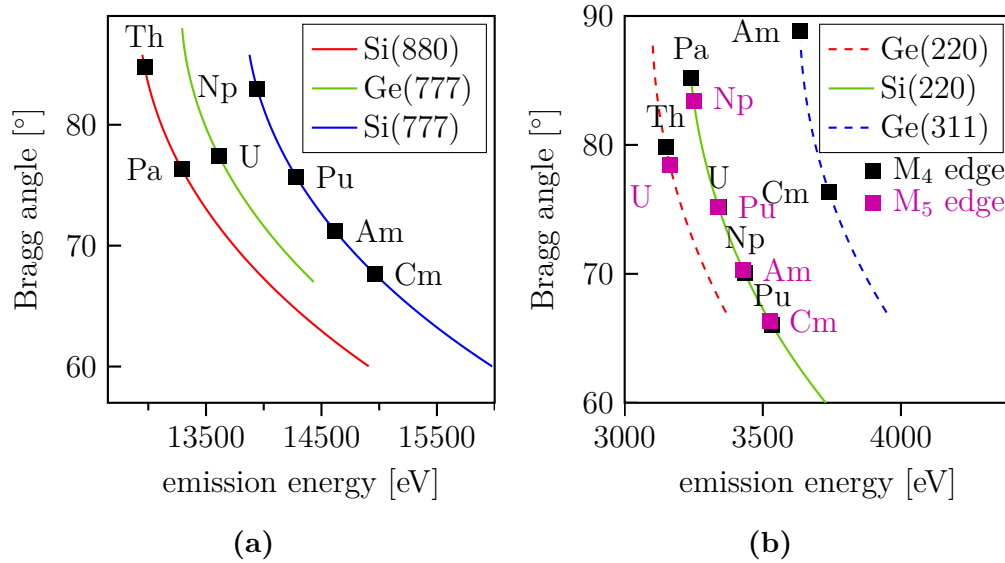


**Figure 2.15.:** Emission energies and the corresponding analyzer crystals and Bragg angles for An  $L\alpha_1$  (a) and An  $M\alpha/M\beta$  (b) emission lines. Ge(311) and Ge(220) are marked with dash lines, as they are currently not available.

Investigations of An  $M_4/M_5$  edges (figure 2.15b) are possible using a He environment (figure 2.16) that allows using up to 99% He atmosphere. The He environment enclosing the MAC-Spectrometer has been designed, assembled and successfully tested at the INE-Beamline. The He containment comprises a solid, modular bottom, which is mounted gas tight on the optical table inside the experimental hutch and a flexible top part consisting of a polyethylene bag attached to the solid base enclosing the detector stage and a smaller front bag enclosing the analyzer crystals (figure 2.16a). During data acquisition the containment is constantly flushed by He gas, thereby minimizing the absorption of photons with 3–4 keV energy, which is necessary for An M edge investigations. A polyethylene window in front of the detector with 10  $\mu\text{m}$  thickness and continuous N flow on the backside prevents He penetration through the detector Be window, which would damage the thermoelectrically cooled device. The lower part of the He containment includes a transfer lock and three glove box sleeves to facilitate insertion and positioning of samples (figure 2.16b).



**Figure 2.16.:** He environment for the HR-XANES spectrometer at the INE-Beamline (a). Transfer lock for the He environment (b).

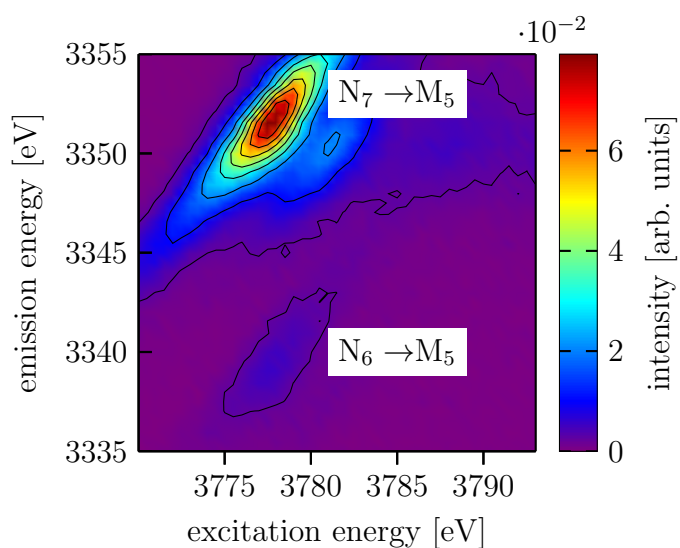


**Figure 2.17.:**  $3d4f$  RIXS map of  $Pu^{6+}$  in aqueous solution.

Figure 2.17 shows an example of  $Pu$   $3d4f$  RIXS. This also demonstrates the higher energy resolution of a XES spectrometer since in addition to the  $M_{\alpha_1}$  emission line at 3352 eV emission energy the  $M_{\alpha_2}$  emission line is resolved.

---

The spectrometer described here will be moved to the CAT-ACT Beamline currently being commissioned at Angströmquelle Karlsruhe (ANKA). The higher incident photon flux there will increase the signal-to-noise ratio, which will reduce the time necessary to measure a spectrum and make it possible to investigate  $An$   $L_3$  edge using  $L_{\beta 5}$  emission lines, which will increase the resolution due to the decreased core-hole lifetime broadening.



# 3 | Experiment

## 3.1. Samples

### 3.1.1. Ligands and complexes

The ligands investigated in this work are 2,6-bis(5,6-dipropyl-1,2,4-triazin-3-yl)-pyridine (*n*-Pr-BTP) (figure 3.1, [18–20]), bis-2,6-(5,6,7,8-tetrahydro-5,9,9-tri-methyl-5,8-methano-1,2,4-benzo-triazin-3-yl)-pyridine (CA-BTP) (figure 3.2, [27]), 6,6'-bis(5,5,8,8-tetramethyl-5,6,7,8-tetrahydrobenzo-1,2,4-triazin-3-yl)-2,2'-bipyridine (CyMe<sub>4</sub>-BTBP) (figure 3.3, [21]), 6-bis(4-ethylpyridazin-1-yl)-pyridine (Et-BDP) (figure 3.4, [36, 136]) and 2,6-Bis(5-(2,2-dimethylpropyl)-1H-pyrazol-3-yl)-pyridine (C5-BPP) (figure 3.5, [35]). For density functional theory (DFT) calculations 2,6-bis-(1,2,4-triazin-3-yl)-pyridine (H-BTP) [18, 137] has been used as an approximation for *n*-Pr-BTP. An example of a *An/Ln*(H-BTP)<sub>3</sub> complex is shown in figure 3.6.

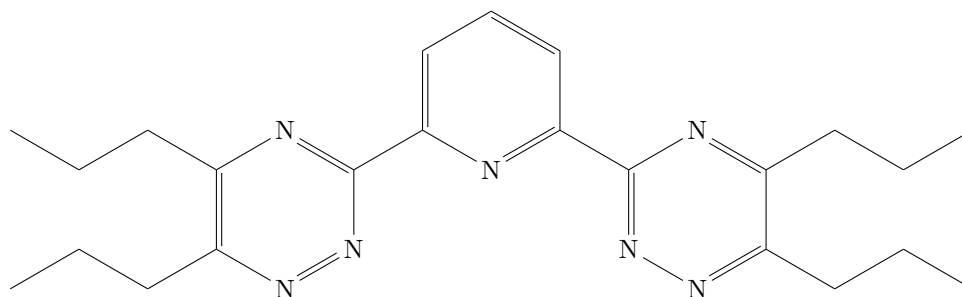
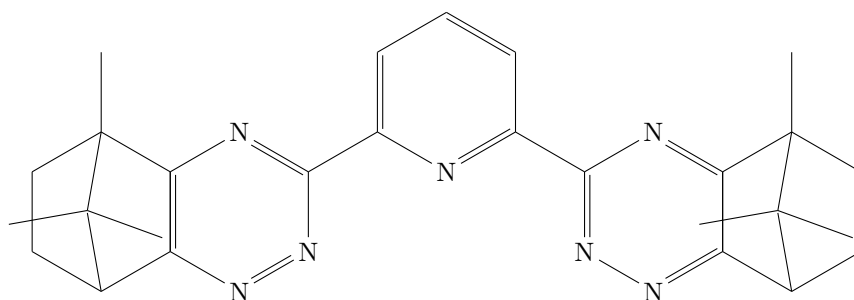
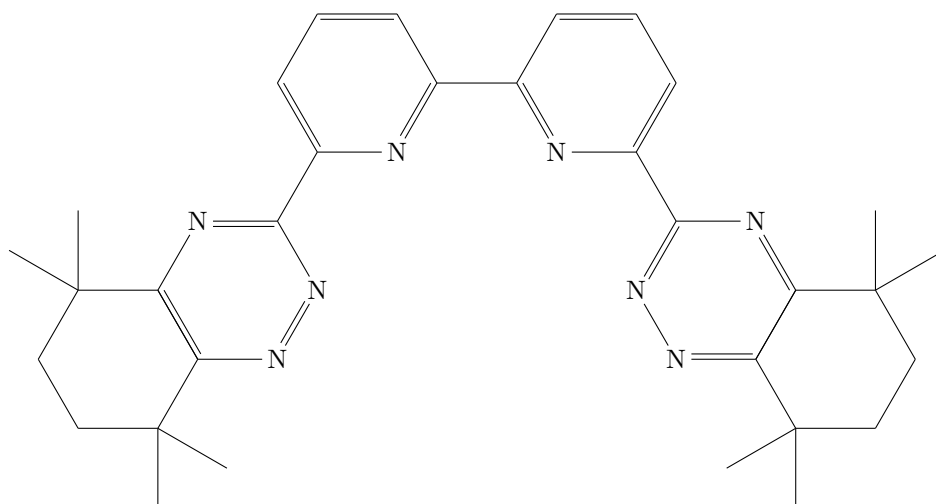


Figure 3.1.: *n*-Pr-BTP



**Figure 3.2.:** CA-BTP



**Figure 3.3.:** CyMe<sub>4</sub>-BTBP

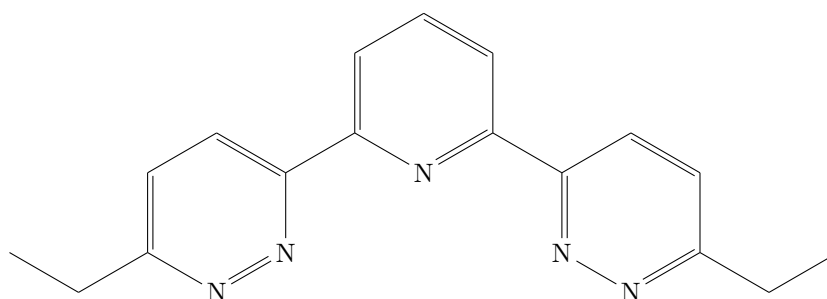


**Figure 3.4.:** Et-BDP

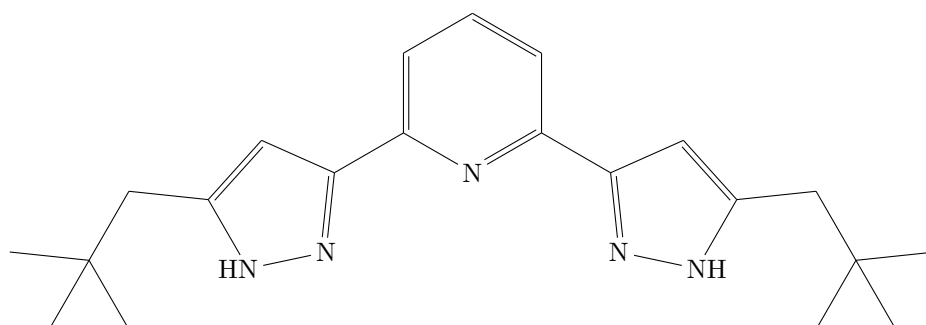


Figure 3.5.: C5-BPP

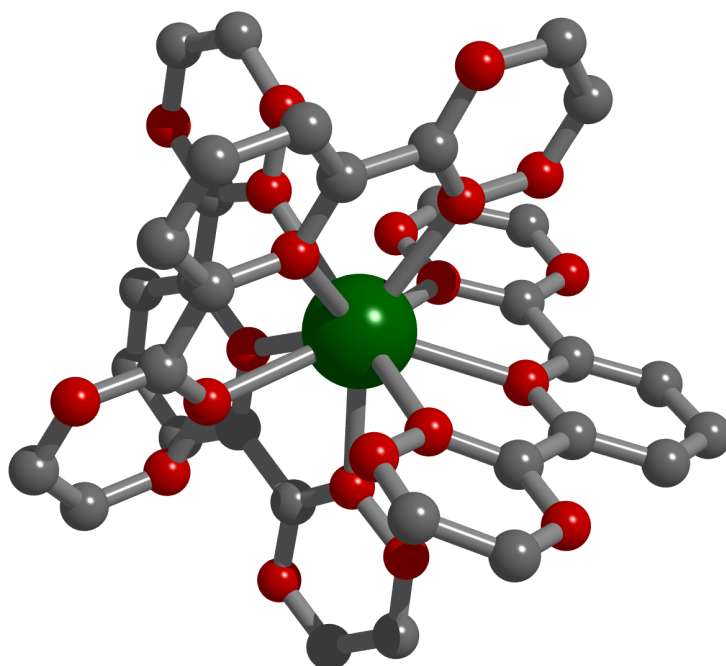


Figure 3.6.:  $An/Ln(H-BTP)_3$

*An/Ln* complexes with different ligands and *An/Ln* salts have been investigated.  $\text{NO}_3^-$  is the preferred counter ion as the extraction process of *An* and the separation from *Ln* (chapter 1) takes place in nitric acid solution. However, the  $\text{NO}_3^-$  N K edge spectrum has a small contribution in the *n*-Pr-BTP N K edge spectrum (see figure 3.10). In  $\text{ClO}_4^-$  containing solution precipitation occurs after adding *n*-Pr-BTP therefore it is discarded as an alternative to  $\text{NO}_3^-$ . Complexes with  $\text{CF}_3\text{SO}_3^-$  (OTf) as counter ion exhibit good solubility and OTf has a lower bonding affinity to the metal than  $\text{NO}_3^-$  thereby enhancing the formation of 1:3 complexes. In some of the early experiments over stoichiometric amounts of *n*-Pr-BTP were added to the solution in order to assure formation of 1:3 complexes. However, the excess amount of *n*-Pr-BTP minimizes N K edge spectral characteristics initiated by the metal-ligand bonding. Additionally, from time-resolved laser fluorescence spectroscopy (TRLFS) experiments [17, 47] on Cm and Eu can be seen that already above  $\sim 0.6 \text{ mmol L}^{-1}$  *n*-Pr-BTP concentration 1:3 complexes are formed exclusively. The concentrations used in this work are approximately one order of magnitude higher. As an alternative, the  $[\text{An/Ln}(\textit{n}\text{-Pr-BTP})_3](\text{OTf})_3$  complexes were first crystallized before solving and drying on substrates. Solutions of  $[\text{An/Ln}(\textit{n}\text{-Pr-BTP})_3](\text{OTf}/\text{ClO}_4/\text{NO}_3)_3$  complexes have been also dried on substrates in some of the experiments. The *Ln* salts that have been used in the preparation of the complexes and as reference materials for the  $\text{L}_3$  edge measurement are hydrophilic and can contain up to nine  $\text{H}_2\text{O}$  in the first coordination shell. Especially for experiments in solution, a high  $\text{H}_2\text{O}$  coordination has to be assumed but could not be quantified during the measurements. Calculations have been performed with  $[\text{Ln}(\text{H}_2\text{O})_9](\text{OTf})_3$ . For the sake of simplicity, coordinating  $\text{H}_2\text{O}$  molecules are not explicitly named throughout this work.

## 3.2. N K edge

### 3.2.1. BESSY

N K edge XANES spectra were measured at the UE52-PGM beamline at the BESSY II synchrotron source of the Helmholtz-Zentrum Berlin using partial electron yield (PEY) detection. A plane grating monochromator (PGM) with

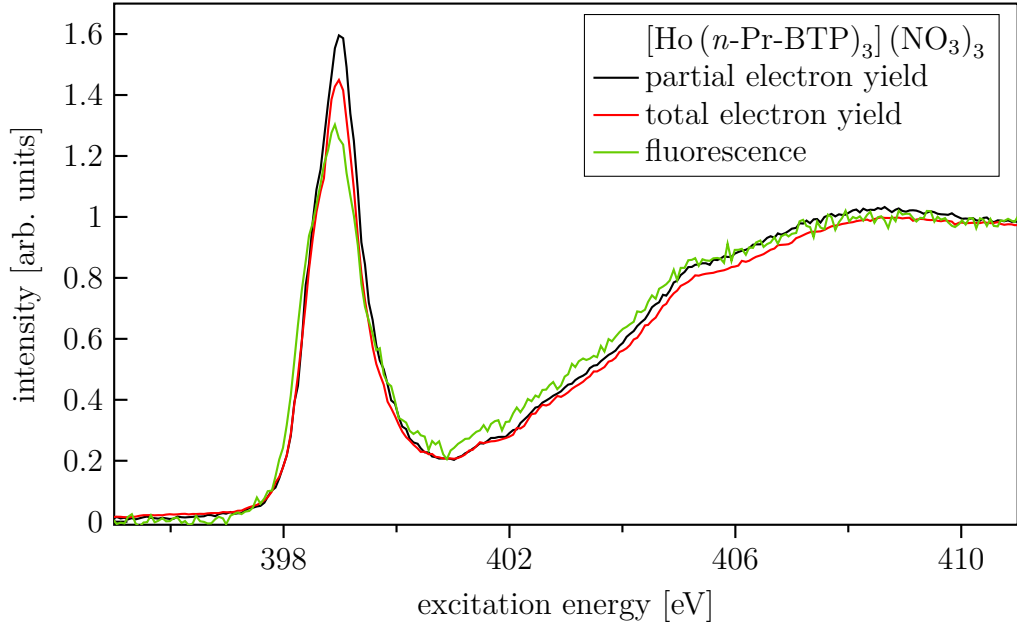
a 1200 lines/mm grating was used to tune the incident X-Rays from 380 to 420 eV. The energy of the incident X-ray beam was scanned with 0.05 eV step size. *n*-Pr-BTP,  $[Ln(n\text{-Pr-BTP})_3](\text{ClO}_4)_3$  and  $[Ln(n\text{-Pr-BTP})_3](\text{NO}_3)_3$  ( $Ln=\text{La, Pr, Eu, Gd, Ho, Yb}$ ) were solved in isopropanol ( $10 \text{ mmol L}^{-1}$ ) and  $\sim 2 \mu\text{L}$  were dried on aluminum sample holders. About 40% excess *n*-Pr-BTP was used in the complex solutions to ensure the formation of 1:3 complexes.

### 3.2.2. ANKA

The N K edge XANES experiments were performed in fluorescence mode at the WERA-Beamline at the ANKA. The incident beam was monochromatised by a PGM. The energy of the incident beam was scanned with 0.05 eV step size across the pre-edge and edge region and up to 0.5 eV in the post edge region. The scanned energy range is from 370 to 485 eV. The spectra have been calibrated using the Ni  $L_3$  edge of a NiO reference.  $[\text{Pu}(n\text{-Pr-BTP})_3](\text{OTf})_3$  solid complexes were synthesized at the Institute for Transuranium Elements (ITU).  $[Ln(n\text{-Pr-BTP})_3](\text{OTf})_3$  ( $Ln=\text{La, Pr, Gd, Ho, Yb}$ ) and  $[Ln(\text{C5-BPP})_3](\text{OTf})_3$  ( $Ln=\text{Pr, Yb}$ ) solid complexes were synthesized at the Institute for Nuclear Waste Disposal (INE). The samples were prepared by solving the ligands and complexes in ethanol and drying  $\sim 2 \mu\text{L}$  of the solutions on Al foil.

### 3.2.3. N K edge general considerations

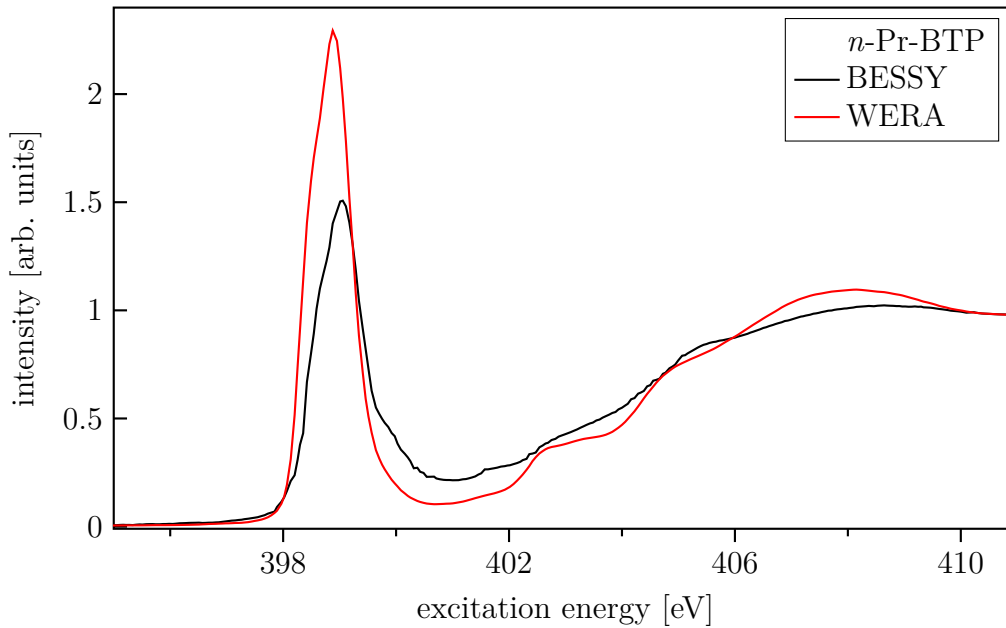
Figure 3.7 shows N K edge spectra of  $[\text{Ho}(n\text{-Pr-BTP})_3](\text{NO}_3)_3$  measured in PEY, total electron yield (TEY) and fluorescence mode. PEY detection measures electrons emitted from the sample and discriminates between photo and Auger electrons. This method is surface sensitive up to a depth of tens of nm. TEY detection measures all emitted electrons by counting the current necessary to neutralize the sample. Both electron detection methods are susceptible to charge build-up in non-conducting samples like *n*-Pr-BTP and its complexes. They also are not element selective, which is especially problematic for N K edge spectra in the presence of C due to a large non-linear background from the C K edge. Thus, fluorescence detection is generally preferred for materials for N K edge investigations in the presence of C, even though it has worse signal-to-noise ratio compared to the electron detection



**Figure 3.7.:** N K edge spectra of  $[\text{Ho}(n\text{-Pr-BTP})_3](\text{NO}_3)_3$  measured in different detection modes.

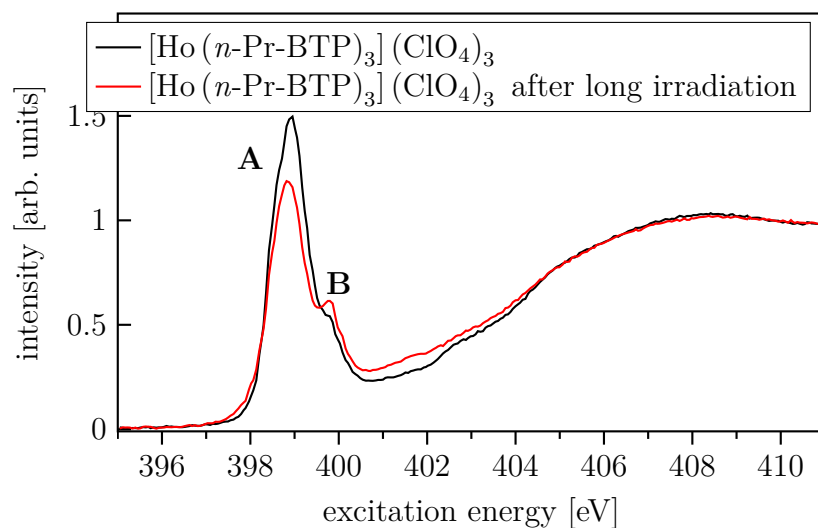
methods due to the lower fluorescence probability in the soft X-ray range. At the UE52-PGM beamline however, the fluorescence detector was not working reliably during the beamtime, so PEY has been used.

Figure 3.8 shows N K edge spectra of  $n\text{-Pr-BTP}$  measured at the UE52-PGM beamline at BESSY and at the WERA-Beamline at ANKA. Both spectra have a similar signal-to-noise ratio. The spectrum collected at the UE52-PGM beamline is shifted to higher energies compared to the spectrum collected at the WERA-Beamline, because at the UE52-PGM beamline no reference spectra could be collected to calibrate the energy scale. In both spectra the FWHM is  $\sim 1$  eV indicating a similar resolution of both beamlines.



**Figure 3.8.:** N K edge spectra of *n*-Pr-BTP measured at the UE52-PGM beamline at BESSY and at the WERA-Beamline at ANKA.

During the measurements at BESSY II, changes of pre-edge features are observed after irradiation of the samples (figure 3.9). Feature **A** loses intensity while the intensity of feature **B** is increased. These effects are attributed to radiation damage, i.e. ionization and breaking of bonds by the incident X-ray beam, and were not observed at the WERA-Beamline (ANKA) due to the lower photon flux impinging on the sample. Figure 3.10a shows an N K edge spectrum of  $\text{Ho}(\text{NO}_3)_3$  compared to  $[\text{Ho}(n\text{-Pr-BTP})_3](\text{NO}_3)_3$ . The main intensity of the  $\text{Ho}(\text{NO}_3)_3$  spectrum lies at higher energies than the  $[\text{Ho}(n\text{-Pr-BTP})_3](\text{NO}_3)_3$  pre-edge, which is barely influenced. This is confirmed by direct comparison between  $\text{NO}_3^-$  containing and  $\text{NO}_3^-$  free ( $[\text{Ho}(n\text{-Pr-BTP})_3](\text{NO}_3)_3$  and  $[\text{Ho}(n\text{-Pr-BTP})_3](\text{ClO}_4)_3$ ) complexes, see figure 3.10b.



**Figure 3.9.:** The effects of radiation damage in  $[\text{Ho}(n\text{-Pr-BTP})_3](\text{ClO}_4)_3$  N K edge spectra after irradiation of the samples.

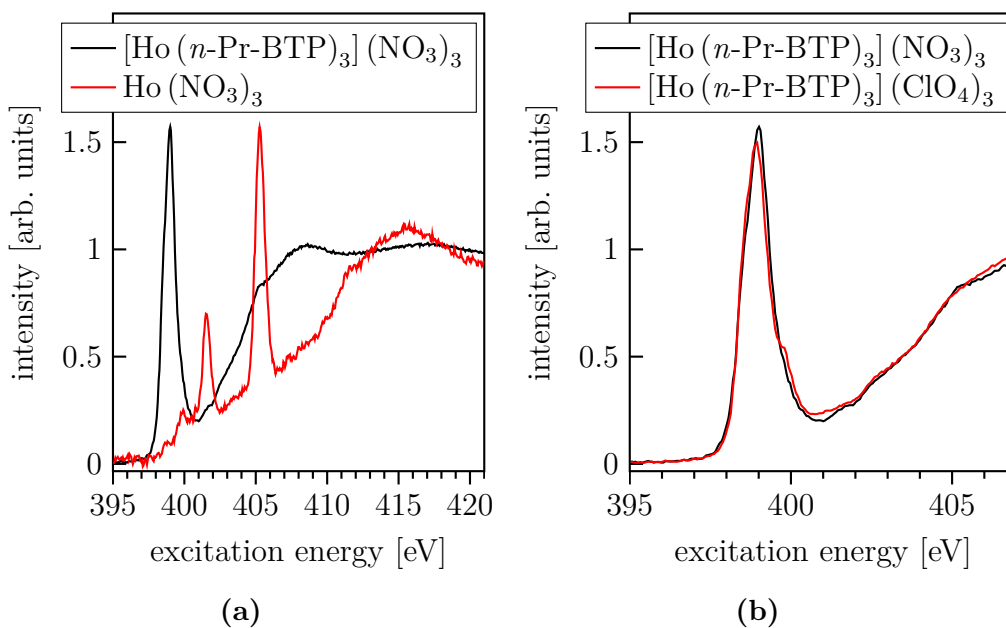


**Figure 3.10.:** The contribution of  $\text{NO}_3^-$  to  $[\text{Ln}(n\text{-Pr-BTP})_3](\text{NO}_3)_3$  N K edge spectra.

### 3.2.4. APS

Non-resonant inelastic x-ray scattering (NRIXS) experiments were performed at the 20-ID beamline at the Advanced Photon Source (APS) using the Lower Energy Resolution Inelastic X-ray scattering (LERIX) spectrometer ([138], figure 3.11). O K edge NRIXS spectra of water and isopropanol and N K edge NRIXS spectra of crystalline *n*-Pr-BTP pressed into a pellet and *n*-Pr-BTP solved in isopropanol ( $30 \text{ mmol L}^{-1}$ ) were measured with the analyzer energy set at 9890 eV (Si(555),  $\theta = 88.27^\circ$ )/7912 eV (used for *n*-Pr-BTP in solution, Si(444),  $\theta = 88.27^\circ$ ). The incident photon flux was  $2 \times 10^{12}$  photons/s for the 9890 eV setup and  $5 \times 10^{12}$  photons/s for the 7912 eV setup using a DCM with Si(311) and Si(111) crystals, respectively. The overall experimental energy resolution was 1.3 eV estimated by measuring the FWHM of the elastically scattered radiation. The liquid samples were measured using a flow-through cell developed in cooperation with Diamond Materials GmbH (Freiburg, Germany). (figure 3.12). The cell has a diamond window with thickness of 50  $\mu\text{m}$  and was set at  $45^\circ$  or  $30^\circ$  with respect to the incident

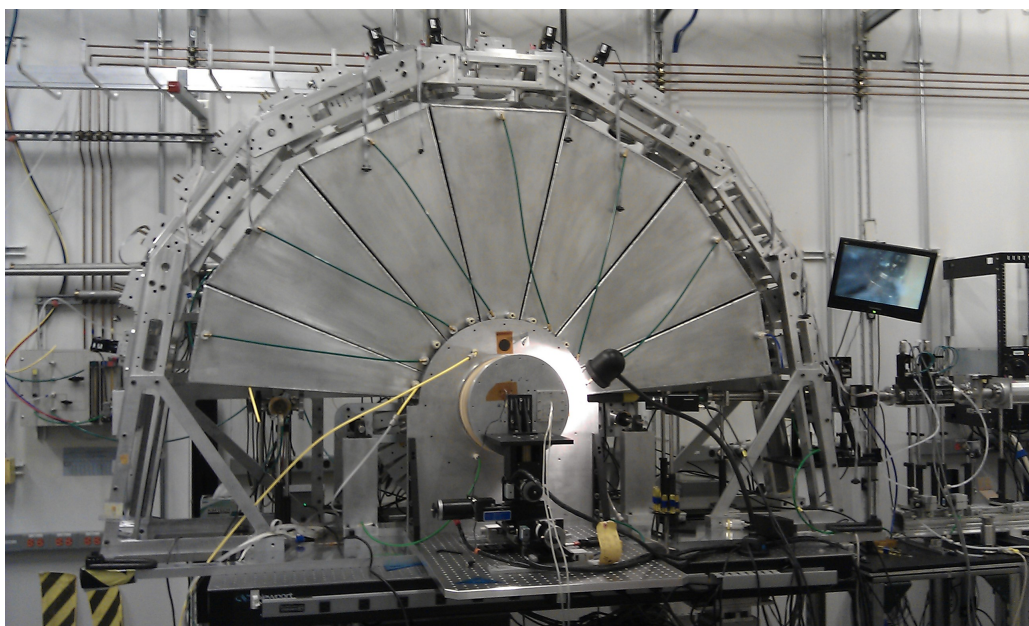


**Figure 3.11.:** LERIX spectrometer at the 20-ID beamline at the APS.

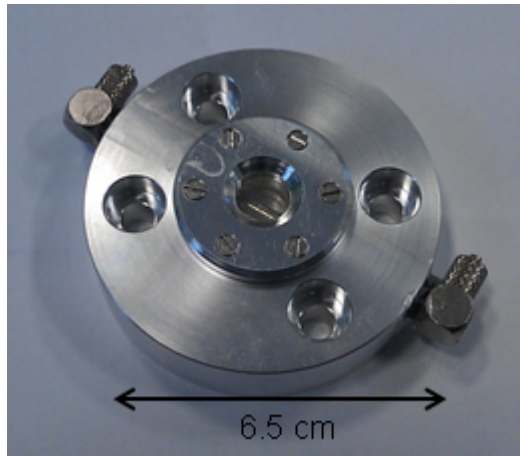


**Figure 3.12.:** Constant-liquid-flow cell for NRIXS measurements.

beam inside a He filled chamber. A peristaltic pump set to a flow rate of  $5 \text{ mL min}^{-1}$  was used to pump the liquids. For the crystalline sample, 18 detectors were employed. Due to the cell blocking part of the scattered energy only 15 detectors (cell at  $30^\circ$ ) or 12 detectors (cell at  $45^\circ$ ) out of 18 detectors could be used for liquid measurements.

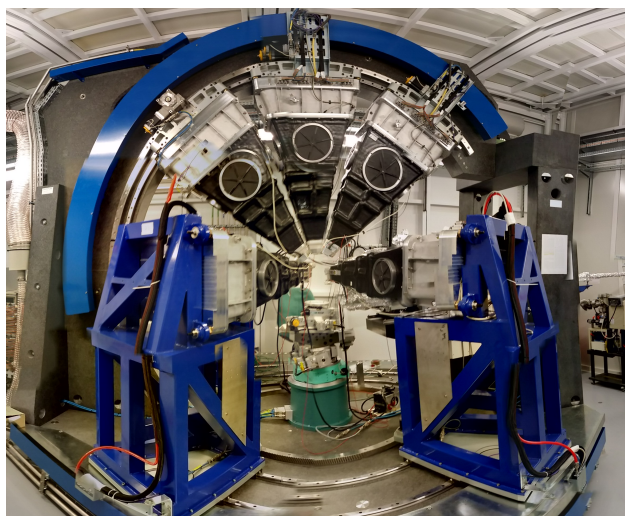


**Figure 3.13.:** NRIXS spectrometer at the ID20 beamline at the ESRF.

### 3.2.5. ESRF

NRIXS experiments were performed at the ID20 beamline at the ESRF using a spectrometer with 72 analyzer crystals (figure 3.13). N K edge NRIXS spectra of crystalline *n*-Pr-BTP and *n*-Pr-BTP solvated in isopropanol ( $30 \text{ mmol L}^{-1}$ ) were measured with the analyzer energy set at 9690 eV (Si(660),  $\theta = 88.5^\circ$ ). The incident photon flux was  $\sim 10^{14}$  photons/s. The cell and pump setup was the same as described in section 3.2.4 with the cell set at  $45^\circ$  to the incident beam. Due to the cell blocking part of the scattered X-rays only 24 detectors could be used for liquid measurements. The crystalline *n*-Pr-BTP powder was pressed into a depression in an Al plate set at  $30^\circ$  to the incident beam. This allowed the use of 48 crystals.

### 3.2.6. ALS

N K edge spectra of  $[\text{Am}(n\text{-Pr-BTP})_3](\text{OTf})_3$  have been measured using scanning transmission X-ray microscopy (STXM) at beamline 11.0.2 at the Advanced Light Source (ALS), Berkeley.

1  $\mu\text{L}$  of  $30 \text{ mmol L}^{-1}$   $\text{Am}(n\text{-Pr-BTP})_3(\text{OTf})_3$  solution was dried on a 100 nm

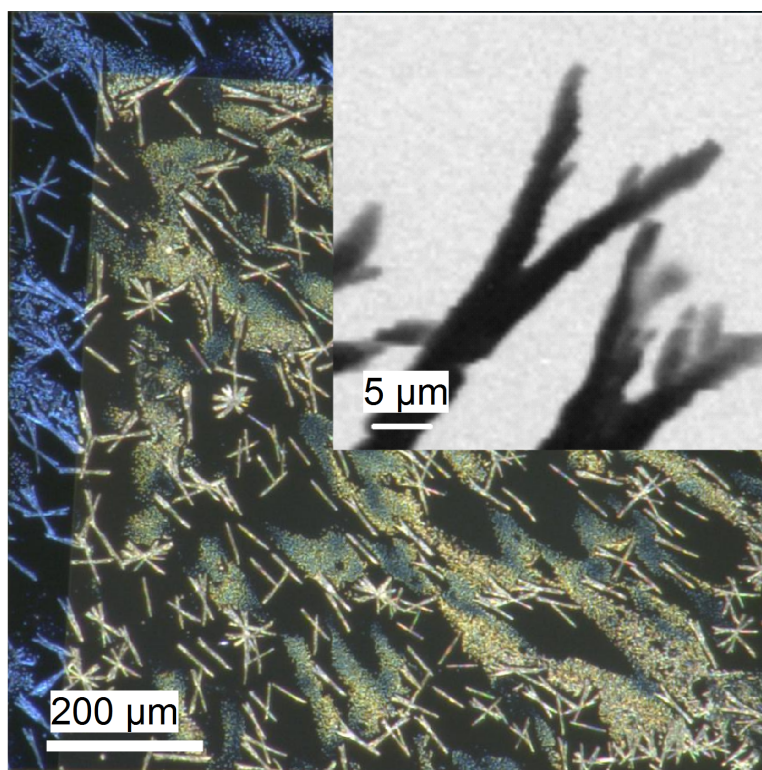


**Figure 3.14.:** Optical microscopy image and STXM image (inset) of  $[\text{Am}(n\text{-Pr-BTP})_3](\text{OTf})_3$ .

thick  $\text{Si}_3\text{N}_4$  window. A second window was glued on top to provide containment. Optical microscopy (figure 3.14) showed that columnar crystals with a length up to  $\sim 100\ \mu\text{m}$  have grown on the  $\text{Si}_3\text{N}_4$  window. XANES spectra were extracted from stacks of STXM images using the *aXis2000* software [139, 140]. Even though the sample was prepared under Ar and the measurement took place in a He atmosphere, an additional peak was visible in the edge attributed to  $\text{N}_2$  gas. The removal of this artifact resulted in a different intensity ratio between pre-edge and WL, but no changes in peak position were observed.

### 3.3. *An/Ln* L<sub>3</sub> edge

#### 3.3.1. HASYLAB

HR-XANES spectra at the Gd L<sub>3</sub> edge (7243 eV) were collected at the W1 beamline at the Hamburger Synchrotronlabor (HASYLAB). Incident X-rays were tuned to energies from 40 eV below to 70 eV above the Gd L<sub>3</sub> edge (7243 eV). The X-rays emitted from the sample were energy analyzed by a Johann spectrometer in dispersive geometry [141] and were detected by a CCD camera. The Lα<sub>1</sub> emission line (6053.4 eV) was diffracted and focused by one spherically bent Si(333) crystal with a 1 m radius of curvature at a Bragg angle  $\theta = 78.4^\circ$ . Samples were prepared by drying 10  $\mu$ L isopropanol solutions of Gd(NO<sub>3</sub>)<sub>3</sub> (2 mmol L<sup>-1</sup>) and [Gd(*n*-Pr-BTP)<sub>3</sub>](NO<sub>3</sub>)<sub>3</sub> (2 mmol L<sup>-1</sup> Gd(NO<sub>3</sub>)<sub>3</sub>, 10 mmol L<sup>-1</sup> *n*-Pr-BTP) on plastic holders.

#### 3.3.2. ANKA

Pu and Am L<sub>3</sub> edge HR-XANES spectra have been collected at the INE-Beamline [132] at ANKA. The X-rays emitted from the sample were energy analyzed by the MAC-Spectrometer described in section 2.4 and detected by a Vortex silicon drift detector [135]. The Lα<sub>1</sub> emission lines of Pu (14 282 eV) and Am (14 620 eV) were diffracted and focused by five spherically bent Si(777) crystal with a 1 m radius of curvature at Bragg angle 75.7° and 71.2°, respectively. The samples were measured in solution. Details of the sample composition are shown in table 3.1.

#### 3.3.3. ESRF

Powder samples of *Ln*(OTf)<sub>3</sub> and [*Ln*(*n*-Pr-BTP)<sub>3</sub>](OTf)<sub>3</sub> (*Ln* = La, Ce, Pr, Sm, Eu, Gd or Lu) were measured as pellets by mixing and pressing 2 mg compound with 20 mg cellulose. Solutions of *Ln*(OTf)<sub>3</sub> and [*Ln*(*n*-Pr-BTP)<sub>3</sub>](OTf)<sub>3</sub> (*Ln* = Pr, Gd, Ho or Yb) in isopropanol (~5 mM/L) were measured using the flow cell that was also used for the NRIXS experiments (see section 3.2.4) to prove the feasibility of constant flow experiments with partitioning ligands

**Table 3.1.:** Sample composition for  $An$  HR-XANES measurements.

Sample	Composition	Solvent	Volume
$\text{Pu}(\text{NO}_3)_3$	2 mM Pu, 0.01 M Rongalite	0.4 M $\text{HNO}_3$	200 $\mu\text{L}$
$[\text{Pu}(n\text{-Pr-BTP})_3(\text{NO}_3)_3]$	1.5 mM Pu, 0.01 M Rongalite, 40 mM $n\text{-Pr-BTP}$	kerosene: octanol (7:3)	200 $\mu\text{L}$
$\text{Am}(\text{NO}_3)_3$	8 mM Am	isopropanol	200 $\mu\text{L}$
$[\text{Am}(n\text{-Pr-BTP})_3(\text{NO}_3)_3]$	8 mM Am, 24 mM $n\text{-Pr-BTP}$	isopropanol	200 $\mu\text{L}$

**Table 3.2.:** The crystals and Bragg angles  $\theta$  used for  $Ln$   $L_3$  edge HR-XANES.

$Ln$	Emission line	Em. energy [eV]	Crystal	Num. of crystals	$\theta$ [°]
La	$L\alpha_1$	4647	Si(400)	1	79.28
Ce	$L\alpha_1$	4839.2	Ge(331)	1	80.76
Pr	$L\alpha_1$	5035.2	Ge(331)	1	71.55
Sm	$L\alpha_1$	5632.6	Si(422)	1	83.12
Eu	$L\alpha_1$	5849.5	Ge(333)	1	76.75
Gd	$L\alpha_1$	6053.4	Ge(333)	1	70.15
Lu	$L\alpha_1$	7655	Ge(444)	1	82.63

and to investigate possible differences between solid and solvated complexes. With a flow rate of  $\sim 5 \text{ ml L}^{-1}$  no radiation damage was observed.

HR-XANES spectra and RIXS maps at  $Ln$   $L_3$  edges were collected at the ID26-Beamline at the ESRF, Grenoble. The X-rays emitted from the sample were energy analyzed by a Johann spectrometer in scanning geometry [142] and detected by an avalanche photodiode (APD). The  $L\alpha_1$  or  $L\beta_2$  emission lines of different  $Lns$  were diffracted and focused by spherically bent crystals with a 1 m radius of curvature at the corresponding Bragg angle  $\theta$  (tables 3.2 and 3.3).

**Table 3.3.:** The crystals and Bragg angles  $\theta$  used for  $Ln$   $L_3$  edge HR-XANES in solution.

$Ln$	Emission line	Em. energy [eV]	Crystal	Num. of crystals	$\theta$ [°]
Pr	$L\alpha_1$	5033	Ge(331)	5	71.62
Gd	$L\alpha_1$	6057.5	Si(333)	5	78.28
Gd	$L\beta_2$	7101.6	Ge(620)	5	77.39
Ho	$L\alpha_1$	6719	Si(440)	5	73.95
Yb	$L\alpha_1$	7414.8	Ge(620)	5	69.17

### 3.3.4. $An/Ln$ $L_3$ edge general considerations

In this section possible systematic effects on  $An/Ln$   $L_3$  edge spectra are discussed, in particular radiation damage, experimental and core-hole lifetime broadenings and the differences between the crystalline samples and the samples in solution.

At the ID26-Beamline, radiation damage in static solution samples could be observed by discoloration of the sample. When using the flow cell described in section 3.2.4 no discoloration was visible.

$[\text{Pr}(n\text{-Pr-BTP})_3](\text{OTf})_3$  spectra of samples in solution and crystallized (figure 3.15) show intensity differences in the WL and post-edge region that can be attributed to self-absorption effects in the crystalline sample, i.e. the dampening of features due the absorption of emitted fluorescence in concentrated samples. The post-edge features of the spectrum of the solved sample are slightly broader indicating the higher disorder in a non-crystalline sample. There are however no shifts between the spectra allowing the direct comparison between crystalline samples and samples in solution. This was confirmed by EXAFS analysis of  $[\text{Eu}(n\text{-Pr-BTP})_3](\text{OTf})_3$ ,  $[\text{Ho}(n\text{-Pr-BTP})_3](\text{OTf})_3$  and  $[\text{Pu}(n\text{-Pr-BTP})_3](\text{OTf})_3$  samples both crystalline and in solution. The EXAFS spectra have been collected at the INE-Beamline [132] at ANKA. The  $k^2$  weighted EXAFS and Fourier transformed data of  $[\text{Eu}(n\text{-Pr-BTP})_3](\text{OTf})_3$  are shown in figure 3.16, of  $[\text{Ho}(n\text{-Pr-BTP})_3](\text{OTf})_3$  in figure 3.17 and of  $[\text{Pu}(n\text{-Pr-BTP})_3](\text{OTf})_3$  in figure 3.18. The results are summarized in tables 3.4 and 3.5, tables 3.6 and 3.7 and tables 3.8 and 3.9, respectively. The  $An/Ln$ -N distance in the first shell is in all cases shorter than reported in

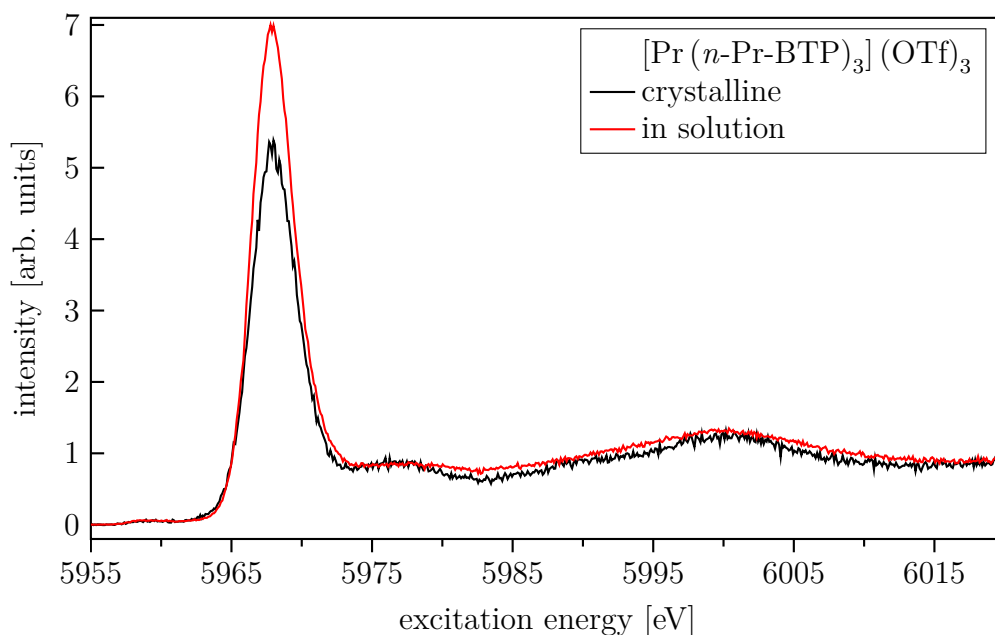


**Figure 3.15.:** Comparison of  $L_3$  edge HR-XANES spectra of  $[\text{Pr}(n\text{-Pr-BTP})_3](\text{OTf})_3$  in crystalline form and in solution.

literature [17, 49]. For  $[\text{Eu}(n\text{-Pr-BTP})_3](\text{OTf})_3$  and  $[\text{Ho}(n\text{-Pr-BTP})_3](\text{OTf})_3$  the coordination numbers fit well to the expected 1:3 complex. For  $[\text{Pu}(n\text{-Pr-BTP})_3](\text{OTf})_3$  the coordination numbers of the first two shells are smaller and of the last two shells larger than expected. Additionally the Debye-Waller factor  $\sigma^2$  is larger, which indicates larger disorder in the system. There was, however, not enough material for further investigations, e.g. with X-ray diffraction (XRD). For all compounds, the EXAFS parameters are similar or identical for crystalline samples or samples in solution.

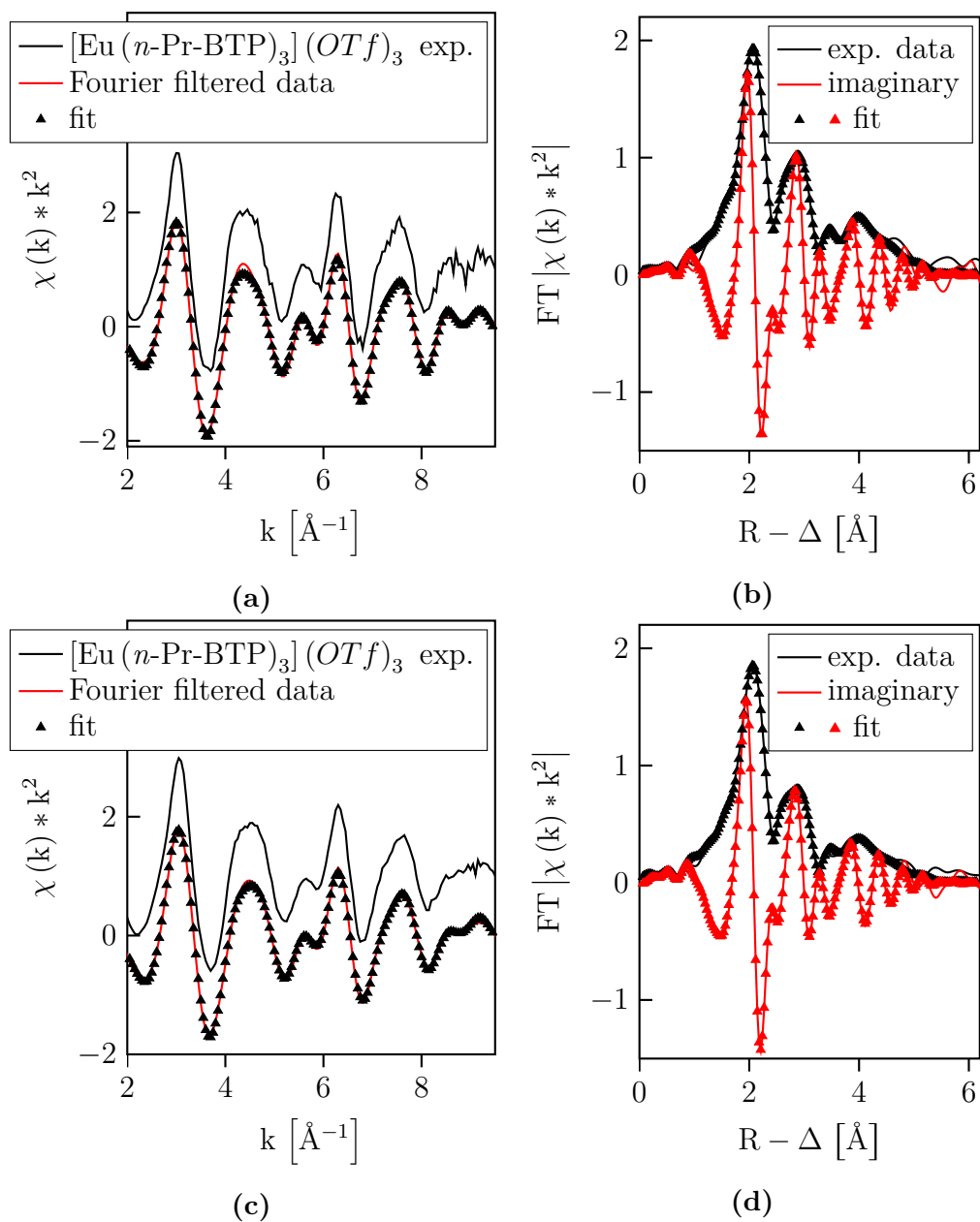


**Figure 3.16.:**  $k^2$  weighted  $L_3$  edge EXAFS (left) of  $[\text{Eu}(n\text{-Pr-BTP})_3](\text{OTf})_3$  in solution (top) and crystalline (bottom) and their corresponding Fourier transform data (right).

**Table 3.4.:** Parameters of EXAFS fit of  $[\text{Eu}(n\text{-Pr-BTP})_3](\text{OTf})_3$  in solution.

shell	N	R[Å]	$\sigma^2[\text{Å}^2]$	$\Delta\text{E}[\text{eV}]$	$S_0^2$	r factor
N	9.2(4)	2.51(1)	0.006(2)	4.5(4)	1.0(1)	0.0034
C/N	18(2)	3.37(1)	0.008(2)	4.5(4)	1.0(1)	0.0034
C/N	19(5)	4.84(4)	0.012(6)	4.5(4)	1.0(1)	0.0034
C	9(2)	5.18(3)	0.002(4)	4.5(4)	1.0(1)	0.0034

**Table 3.5.:** Parameters of EXAFS fit of crystalline  $[\text{Eu}(n\text{-Pr-BTP})_3](\text{OTf})_3$ .

shell	N	R[Å]	$\sigma^2[\text{Å}^2]$	$\Delta\text{E}[\text{eV}]$	$S_0^2$	r factor
N	9.1(3)	2.497(8)	0.006(1)	5.4(7)	0.98(8)	0.002
C/N	18(1)	3.37(1)	0.011(2)	5.4(7)	0.98(8)	0.002
C/N	19(6)	4.84(4)	0.016(6)	5.4(7)	0.98(8)	0.002
C	9(3)	5.19(3)	0.004(4)	5.4(7)	0.98(8)	0.002

**Table 3.6.:** Parameters of EXAFS fit of  $[\text{Ho}(n\text{-Pr-BTP})_3](\text{OTf})_3$  in solution.

shell	N	R[Å]	$\sigma^2[\text{Å}^2]$	$\Delta\text{E}[\text{eV}]$	$S_0^2$	r factor
N	8.9(3)	2.49(1)	0.007(2)	4.4(8)	1.09(11)	0.0017
C/N	18(1)	3.35(1)	0.009(2)	4.4(8)	1.09(11)	0.0017
C/N	18(3)	4.82(4)	0.010(6)	4.4(8)	1.09(11)	0.0017
C	9(2)	5.15(3)	0.007(7)	4.4(8)	1.09(11)	0.0017

**Table 3.7.:** Parameters of EXAFS fit of crystalline  $[\text{Ho}(n\text{-Pr-BTP})_3](\text{OTf})_3$ .

shell	N	R[Å]	$\sigma^2[\text{Å}^2]$	$\Delta\text{E}[\text{eV}]$	$S_0^2$	r factor
N	9.0(3)	2.48(1)	0.007(2)	4.05(87)	1.06(12)	0.0021
C/N	18(1)	3.34(1)	0.009(2)	4.05(87)	1.06(12)	0.0021
C/N	18(3)	4.81(4)	0.010(7)	4.05(87)	1.06(12)	0.0021
C	9(2)	5.14(4)	0.003(5)	4.05(87)	1.06(12)	0.0021

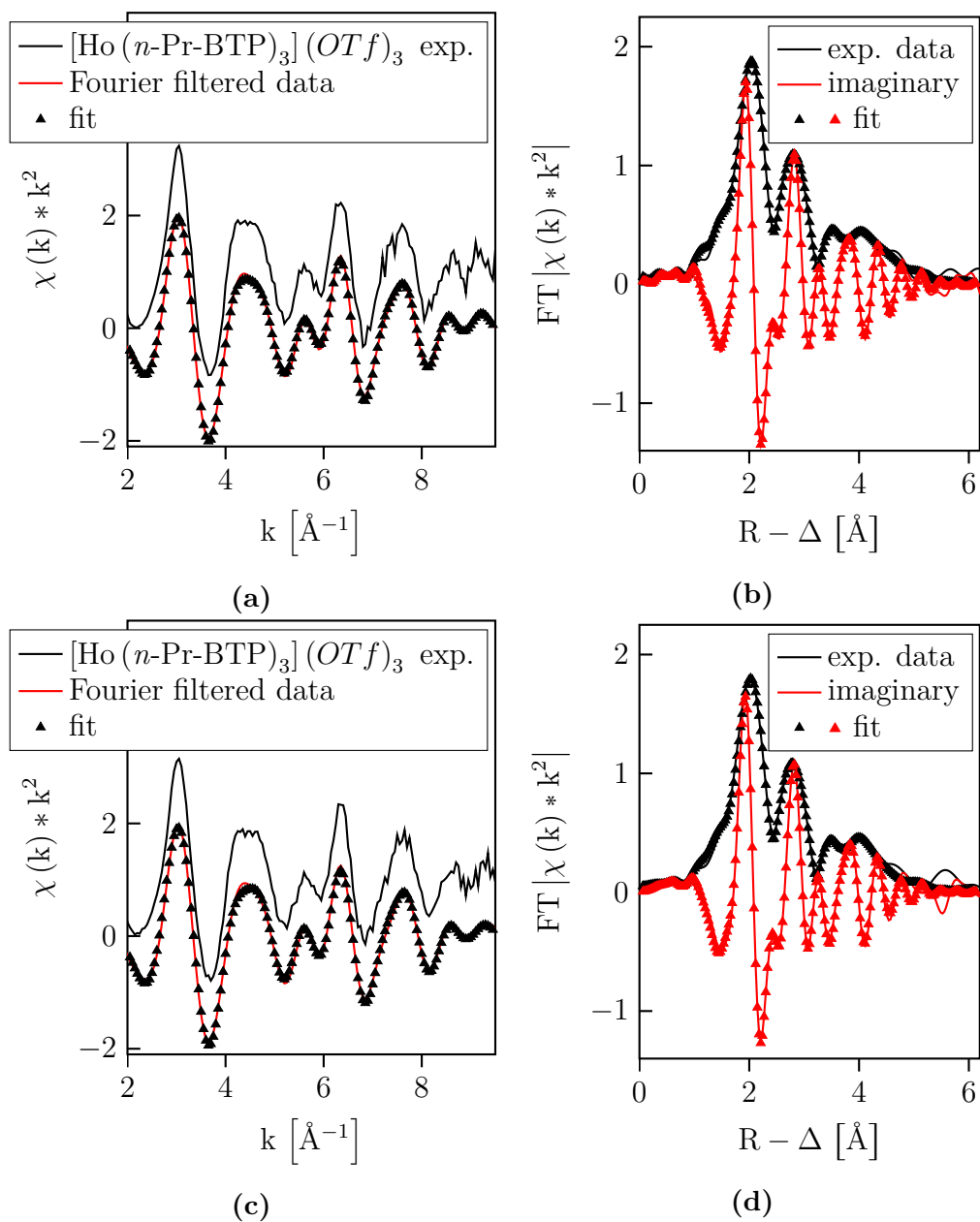


**Figure 3.17.:**  $k^2$  weighted  $L_3$  edge EXAFS (left) of  $[\text{Ho}(n\text{-Pr-BTP})_3](\text{OTf})_3$  in solution (top) and crystalline (bottom) and their corresponding Fourier transform data (right).

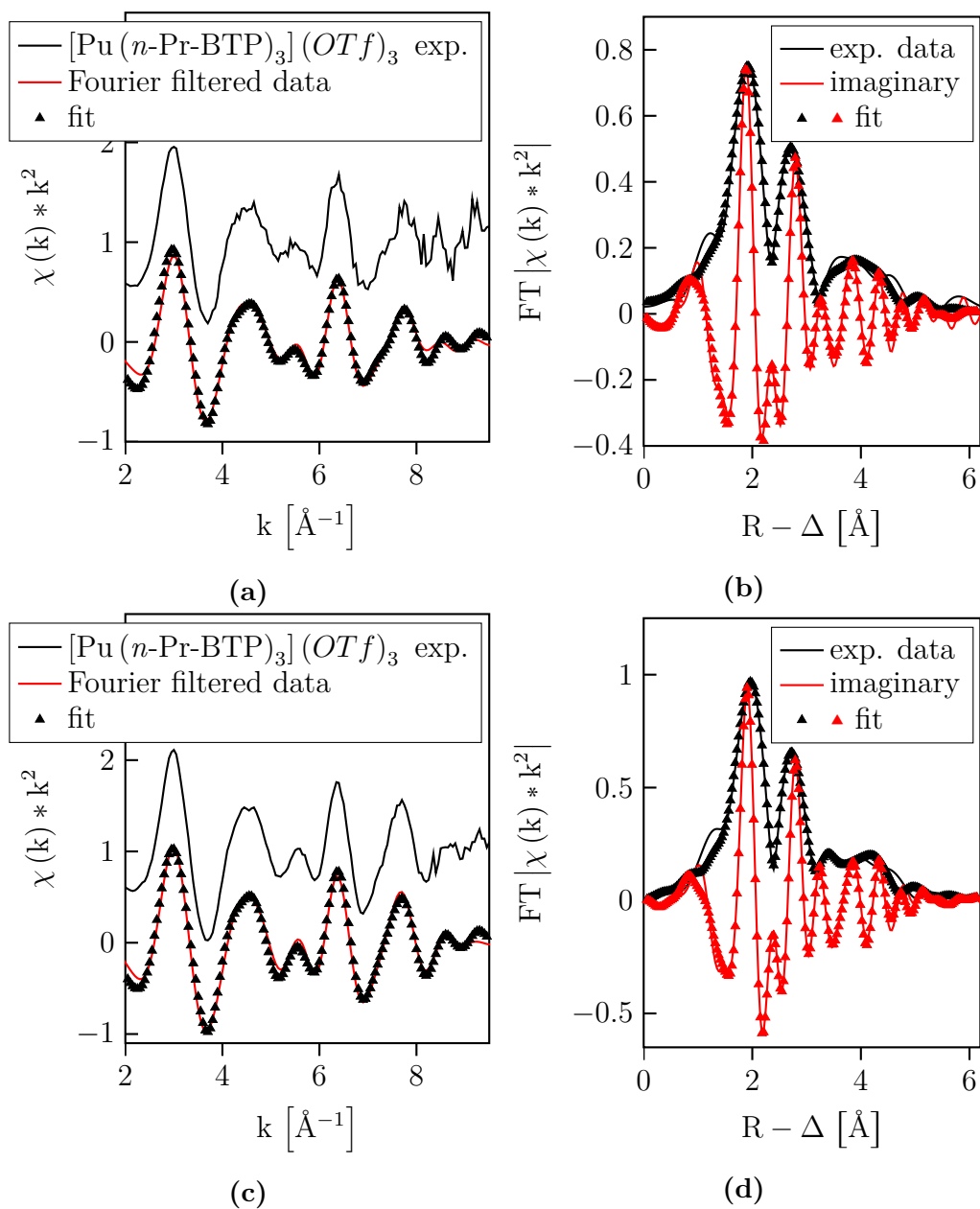


**Figure 3.18.:**  $k^2$  weighted  $L_3$  edge EXAFS (left) of  $[\text{Pu}(n\text{-Pr-BTP})_3](\text{OTf})_3$  in solution (top) and crystalline (bottom) and their corresponding Fourier transform data (right).

**Table 3.8.:** Parameters of EXAFS fit of [Pu(*n*-Pr-BTP)<sub>3</sub>](OTf)<sub>3</sub> in solution.

shell	N	R[Å]	$\sigma^2[\text{Å}^2]$	$\Delta E[\text{eV}]$	$S_0^2$	r factor
N	7(0.9)	2.53(1)	0.01(0.2)	5.2 (7)	1	0.0099
C/N	14(1.8)	3.41(1)	0.01(0.2)	5.2(7)	1	0.0099
C/N	23(6)	4.83(2)	0.01(0.2)	5.2(7)	1	0.0099
C	19(8)	5.17(4)	0.01(0.2)	5.2(7)	1	0.0099

**Table 3.9.:** Parameters of EXAFS fit of crystalline [Pu(*n*-Pr-BTP)<sub>3</sub>](OTf)<sub>3</sub>.

shell	N	R[Å]	$\sigma^2[\text{Å}^2]$	$\Delta E[\text{eV}]$	$S_0^2$	r factor
N	7(0.7)	2.53(0.8)	0.0086(14)	5.8(6)	1	0.0093
C/N	13(1.4)	3.4(0.8)	0.0086(14)	5.8(6)	1	0.0093
C/N	20 (4.3)	4.84 (2)	0.0086(14)	5.8(6)	1	0.0093
C	16(6)	5.17(3)	0.0086(14)	5.8(6)	1	0.0093

Table 3.10 shows an overview of the total broadening  $\Gamma_{TOT}$  of the L<sub>3</sub> edge HR-XANES spectra used in this work and the core-hole lifetime and experimental broadenings contributing to  $\Gamma_{TOT}$ . The intermediate ( $\Gamma_{INT}$ ) and final ( $\Gamma_{FIN}$ ) state core-hole lifetime broadenings are taken from *FEFF9.6* [143, 144].  $E_{INC}$  is the broadening of the incident energy and is calculated with  $\Delta E/E = 3 \cdot 10^{-5}$  for *Lns* measured at the ID26-Beamline and with  $\Delta E/E = 2 \cdot 10^{-4}$  for *Ans* measured at the INE-Beamline. The spectrometer broadening  $E_{EM}$  was calculated using the RT4XES (Ray Tracing for X-ray Emission Spectrometers) software [119]. The calculations are described in detail in section 2.2. The experimental broadening is determined by measuring the FWHM of the elastic peak and is larger than  $E_{TOT}$ , due to crystal imperfections, misalignment of the spectrometer etc. (see also section 2.4).

**Table 3.10.:** The emission line, emission energy, crystal and angle  $\theta$  at which the HR-XANES spectra were measured.  $\Gamma_{INT}$  and  $\Gamma_{FIN}$  are the intermediate and final state core-hole lifetime broadening (taken from *FEFF9.6*) and  $\Gamma_{APP}$  is the resulting spectral broadening.  $E_{INC}$  and  $E_{EM}$  are the beamline and spectrometer broadening and  $E_{TOT}$  is the total theoretical experimental broadening.  $\Gamma_{TOT}$  is the combined spectral and experimental broadening. For details of the calculation see section 2.2.  $E_{INC}$  for  $Ln$  is calculated with  $\Delta E/E = 3 * 10^{-5}$  and for  $An$  with  $\Delta E/E = 2 * 10^{-4}$ .

$Ln/An$	Emission line	Emission energy [eV]	Crystal	$\theta$ [°]	$\Gamma_{INT}$	$\Gamma_{FIN}$	$\Gamma_{APP}$	$E_{INC}$	$E_{EM}$	$E_{TOT}$	$\Gamma_{TOT}$	experimental broadening
La	$L_{\alpha 1}$	4647	Si(400)	79.28	3.160	0.820	0.794	0.164	0.102	0.194	0.841	
Ce	$L_{\alpha 1}$	4839.2	Ge(331)	80.76	3.270	0.870	0.841	0.172	0.079	0.189	0.884	
Pr	$L_{\alpha 1}$	5035.2	Ge(331)	71.55	3.381	0.916	0.884	0.179	0.347	0.390	1.027	
Pr	$L_{\alpha 1}$	5033	Ge(331)	71.62	3.381	0.916	0.884	0.179	0.344	0.388	1.026	1.1
Sm	$L_{\alpha 1}$	5632.6	Si(422)	83.12	3.655	1.069	1.026	0.201	0.050	0.208	1.070	
Eu	$L_{\alpha 1}$	5849.5	Ge(333)	76.75	3.735	1.126	1.078	0.209	0.200	0.289	1.151	
Gd	$L_{\alpha 1}$	6053.4	Ge(333)	70.15	3.817	1.185	1.132	0.217	0.481	0.528	1.324	
Gd	$L_{\alpha 1}$	6057.5	Si(333)	78.28	3.817	1.185	1.132	0.217	0.160	0.270	1.195	0.8
Gd	$L_{\beta 2}$	7101.6	Ge(620)	77.39	3.817	2.010	1.778	0.217	0.219	0.308	1.824	1.2
Ho	$L_{\alpha 1}$	6719	Si(440)	73.95	4.074	1.383	1.310	0.242	0.343	0.420	1.427	1.2
Yb	$L_{\alpha 1}$	7414.8	Ge(620)	69.17	4.347	1.615	1.514	0.268	0.655	0.707	1.755	2.1
Lu	$L_{\alpha 1}$	7655	Ge(444)	82.63	4.443	1.700	1.588	0.277	0.078	0.288	1.642	
Pu	$L_{\alpha 1}$	14282	Si(777)	75.7	8.671	4.143	3.739	3.61	0.572	3.656	6.53	
Am	$L_{\alpha 1}$	14620	Si(777)	71.2	8.970	4.286	3.867	3.7	1.049	3.847	6.323	

The experimental resolution for  $An L_3$  edges could not be measured at the INE-Beamline due to the large difference between absorption edge and emission line energies ( $\sim 4$  keV). For the Pu  $M_5$  edge an experimental broadening of 1.34 eV and a theoretical experimental broadening  $E_{TOT} = 0.769$  eV have been found showing a similar difference between theoretical and real broadening compared the  $Ln L_3$  edge broadenings measured at the ID26-Beamline. Therefore, it can be assumed that the two spectrometers have a similar resolution.

## 3.4. Modeling and Calculation

### 3.4.1. Modeling

The N K edge spectra were modeled with an arctangent function for the edge step and pseudo-Voigt (PV) [ $f(x) = \alpha Gaussian + (1 - \alpha)Lorentzian$ ] functions for all other features using the Fityk software [145]. The shape parameter  $\alpha$  of the PV functions, i.e. the mixing of Lorentzian and Gaussian functions, was set to 0.5 to account for both experimental and core-hole lifetime broadening effects.

### 3.4.2. Structure optimization

$Ln(H-BTP)_3$  and  $An(H-BTP)_3$  structures were optimized imposing the  $D_3$  point group at the DFT-level with the BP86 functional [146, 147] employing the resolution-of-the-identity (RI) routines as implemented in TURBOMOLE [148]. Def2-TZVP basis sets [149] were used for the light elements whereas the def-TZVP basis sets [150] and small-core Stuttgart-PP were taken for the  $f$ -elements. Structures optimized in this way are denoted structure **1** throughout this work. H-BTP is used as an approximation for  $n$ -Pr-BTP as it has been proved that the substituents on the triazine rings hardly affect the complex structure [42, 44, 151]. The average metal-ligand bond lengths for the calculated structures are shown in table 3.11 and compared to EXAFS bond lengths from literature. The calculated values are overestimated, but follow a similar trend like the experimental values.

**Table 3.11.:**  $Ln/An$ -ligand bond length  $R$ . Calculated values are for  $Ln/An(\text{H-BTP})_3$ , EXAFS bond length as found in literature for  $Ln/An(n\text{-Pr-BTP})_3$  with estimated uncertainties.

$Ln/An$	av. calc. R[pm]	EXAFS R[pm]
La	271	—
Ce	270	261(8) [44]
Pr	268	—
Nd	266	—
Pm	265	—
Sm	263	260(2) [49]
Eu	262	256(0.8) [44]
Gd	261	255(0.7) [45]
Tb	260	—
Dy	258	256(2) [49]
Ho	257	256(2) [49]
Er	256	—
Tm	255	254(2) [45]
Yb	254	—
Lu	253	—
Pu	261	256(1) [50]
Am	260	256(0.5) [45]

$Ln(\text{OTf})_3$  structures were optimized in the  $C_{3h}$  point group at the DFT level with the BP86 functional [146, 147] employing the RI routines as implemented in TURBOMOLE [148]. Def2-TZVP basis sets [149] were used for the light elements whereas ECPnMWB-II [152, 153] basis sets were used for the  $Lns$ . Bond lengths for this compounds are also overestimated, but reproduce experimental results well [154].

Additionally  $\text{Gd}(\text{H-BTP})_3$  structures in gas and aqueous phase (called structure **2** and structure **3**, respectively) have been calculated. The structures were optimized on the DFT level in  $C_1$  symmetry using a SVP basis set and the BH-LYP functional [155]. For the aqueous phase the structure has been solvated with COSMO-RS [156].

### 3.4.3. N K edge

Time dependent density functional theory (TD-DFT) calculations of the N K edge of H-BTP were performed using: the ORCA package [157] with cc-pVDZ basis sets [158], BP86 functional [146, 147] and TightSCF approximation; the TURBOMOLE package [148] with second order Algebraic Diagrammatic Construction (ADC(2)) [159, 160]; the Amsterdam Density Functional (ADF) package [161–163] with DZP basis sets, BP86 functional [146, 147] and scalar-relativistic ZORA [164–167]. The theoretically calculated electronic transitions are broadened by 0.5 eV to account for experimental and core-hole lifetime broadening effects and thereby achieve closer agreement with the experiment. The energy scale of the calculated spectra are shifted to resemble the experimental spectra.

La(H-BTP)<sub>3</sub> and Ac(H-BTP)<sub>3</sub> were calculated using the ADF package [161–163] with the same parameters as the ligand. Ground state molecular orbitals (MOs) from the same calculations were plotted with the relative contributions from atomic orbitals.

### 3.4.4. An/Ln L<sub>3</sub> edge

#### 3.4.4.1. Comparison of methods

To compare different codes and methods the spectrum of [Eu(*n*-Pr-BTP)<sub>3</sub>](OTf)<sub>3</sub> was calculated with *FEFF9.6* [143, 144] and *FDMNES* [168]. The structural data of [Eu(*n*-Pr-BTP)<sub>3</sub>](OTf)<sub>3</sub> was taken from unpublished XRD data. With *FEFF*, the self-consistent field (SCF) was calculated for a cluster of 28 atoms and the full multiple scattering (FMS) for a cluster of 46 atoms. A Hedin-Lundqvist type exchange correlation potential was used. *FDMNES* FMS and full potential (FP) calculation were performed on a cluster of 28 atoms. In all calculations quadrupole transitions were taken into account. The input files are shown in appendix A.1.

#### 3.4.4.2. Comparison of structures

To compare different structure optimizations the experimental spectrum of  $[\text{Gd}(n\text{-Pr-BTP})_3](\text{OTf})_3$  was compared to *FDMNES* FMS spectra calculated from  $\text{Gd}(\text{H-BTP})_3$  optimized in the different ways described in section 3.4.2, i.e. optimization with  $D_3$  symmetry, with  $C_1$  symmetry and with  $C_1$  symmetry and solvation shell.

#### 3.4.4.3. FEFF – XANES pre-edge

The  $[\text{Gd}(n\text{-Pr-BTP})_3](\text{OTf})_3$  spectrum and the  $f$  and  $d$  angular momentum projected density of states ( $f$ -,  $d$ -DOS) were calculated using the ab initio multiple-scattering theory based *FEFF9.5* code [143, 144]. The SCF and FMS calculations were performed on a cluster of 152 atoms corresponding to one  $[\text{Gd}(n\text{-Pr-BTP})_3](\text{OTf})_3$  molecule. A Hedin-Lundqvist type exchange correlation potential was used. The  $f$ -DOS was calculated self-consistently by using the UNFREEZE card. The Fermi level was set to 3 eV below the calculated value of  $-9.6$  eV in order to reproduce the pre-edge structure in the spectrum. To reach convergence, the core-hole type was set to random phase approximation (RPA card) and the core-hole potential was calculated for a cluster of 47 atoms (SCREEN card). The input file can be found in appendix A.2

#### 3.4.4.4. FEFF – EXAFS trends

Spectra of  $\text{La}(\text{H-BTP})$  and  $\text{Ln}(\text{H-BTP})$  with different optimized  $\text{Ln}(\text{H-BTP})$  structures (see section 3.4.2) and  $\text{Ln}(\text{H-BTP})$  with  $\text{La}(\text{H-BTP})$  structure were calculated using the *FEFF9.6* code [143, 144] for all  $\text{Ln}$ . A Hedin-Lundqvist type exchange correlation potential was used. The SCF calculations were performed on a cluster of 19 atoms corresponding to one  $\text{Ln}(\text{H-BTP})$  molecule. The EXAFS was calculated up to  $k = 20 \text{ \AA}^{-1}$  and MS paths with an effective length up to  $5 \text{ \AA}$  were included. An example of an input file is shown in appendix A.3.

#### 3.4.4.5. *FDMNES* – *XANES* trends

Spectra of  $\text{La}(\text{H-BTP})_3$  and  $\text{Ln}(\text{H-BTP})_3$  with different optimized  $\text{Ln}(\text{H-BTP})_3$  structures (see section 3.4.2) and  $\text{Ln}(\text{H-BTP})_3$  with  $\text{La}(\text{H-BTP})_3$  structure were calculated using the *FDMNES* code [168] for all  $\text{Ln}$ . The SCF and multiple scattering calculations were performed on a cluster of 76 atoms corresponding to one  $\text{Ln}(\text{H-BTP})_3$  molecule. Spin-orbit interactions and quadrupole transitions were allowed. The step-size in the calculations was set to 0.1 eV to be able to correctly calculate the localized  $4f$  states. For convolution of the spectra core-hole and final state broadening were set to 1 eV to make sure all experimentally observed features are resolved in the calculation. Like the experimental spectra, the calculated spectra are aligned on the maximum of the WL. An example of an input file is shown in appendix A.4.



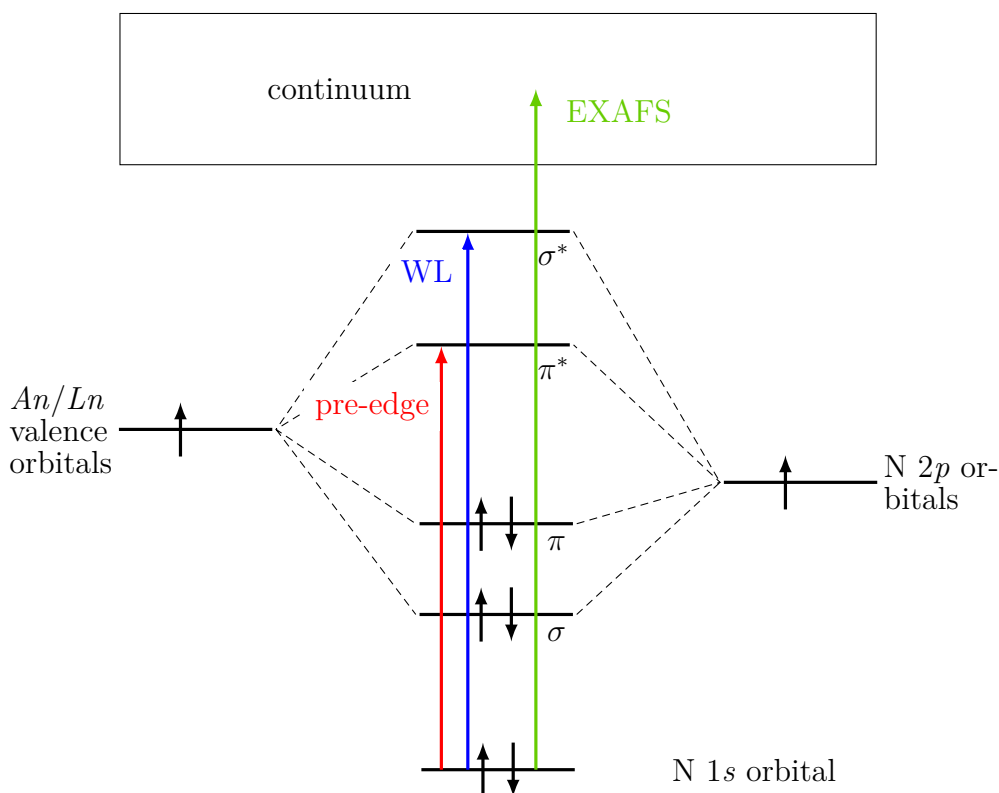
## 4 | Results

### 4.1. N K edge

In this chapter the electronic structure of the  $An/Ln$  partitioning complexes is discussed from the ligand 'point-of-view' using the N K edge XANES technique. The main focus is on the pre-edge region of the  $[Ln/An(n\text{-Pr-BTP})_3](\text{OTf})_3$  N K edge XANES spectra. Experimental trends are compared to extraction behavior of the  $n\text{-Pr-BTP}$  molecule. Insights on the electronic structure are gained by correlating experimental observations with results from TD-DFT calculations. The spectra of the  $n\text{-Pr-BTP}$  and other ligands with variable extracting properties are compared. The results from a NRIXS feasibility study are discussed. This method is an advanced tool for XANES investigations of low  $Z$  elements like for example N and C in materials in a liquid phase.

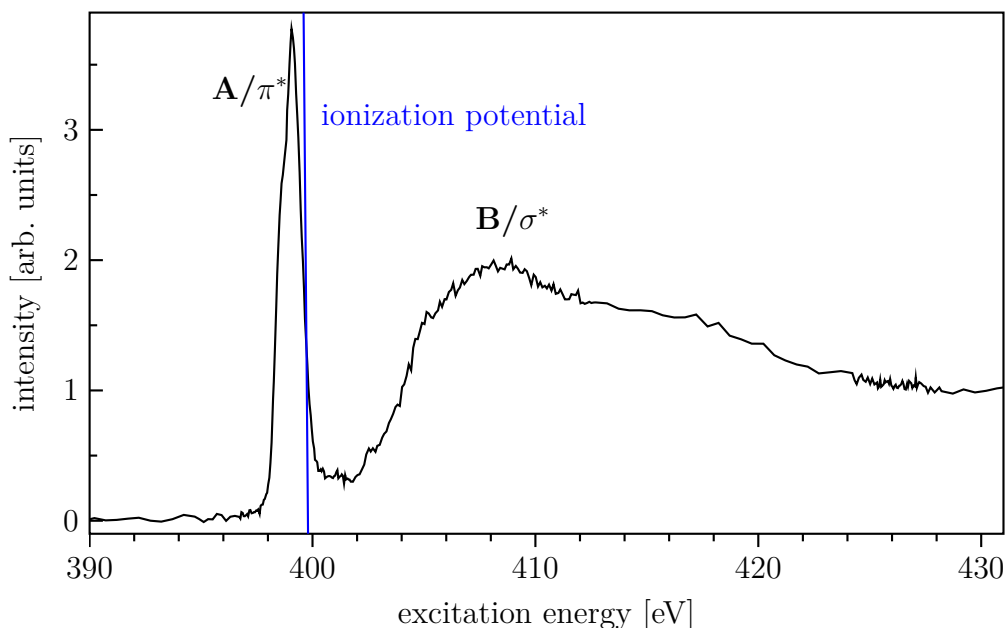
#### 4.1.1. General description of the spectrum

Figure 4.1 depicts a simplified MO scheme of  $Ln/An$  bound to one N atom and the excitations relevant for XAS at the N K edge. When the energy of the incident photons is close to the binding energy of the N  $1s$  electrons the N  $1s$  electrons are excited to the lowest unoccupied molecular orbital (LUMO). In this case, it is an antibonding, unoccupied  $\pi^*$  MO with predominant N  $2p$  content mixed with  $Ln/An$   $5d/6d$  and/or  $4f/5f$  based atomic orbitals [65]. These transitions are described by a pre-edge in the N K edge XAS spectrum (see figure 4.2, **A**). The  $\pi^*$  MO is localized below the ionization potential due to the relaxation shift of the  $1s$  orbital in the excited state to smaller binding energies and the downward shift of outer orbitals due to the increased attractive Coulomb potential created by the core-hole [169]. The lifetime



**Figure 4.1.:** Simplified MO scheme of  $An/Ln$  bound to N and the excitations generating the pre-edge (red), WL (blue) and EXAFS (green) features observed in N K edge spectra.

broadening for the N  $1s$  core-hole is very small ( $\sim 0.1$  eV) leading to a sharp, energy resolved  $\pi^*$  absorption resonance. Due to the four nonequivalent N atoms in the molecule having slight differences ( $\sim 0.3$  eV) in the  $1s$  binding energies and electronic densities in their vicinity the pre-edge describes a superposition of at least four different spectra with characteristic energy positions and shapes. Hence, in figure 4.2 the  $\pi^*$  resonance has an asymmetric shape (see also section 4.1.2). Due to dipole selection rules ( $\Delta l = \pm 1$ ), the oscillatory strength for  $1s \rightarrow \pi^*$  transitions depends on the N  $2p$  contribution in the MOs and can be relatively measured by determining the area of the peaks. Mixing of metal  $4f/5f$  and/or  $5d/6d$  with N  $2p$  valence electronic states can also lead to new MOs and energy shifts. A change of the pre-edge



**Figure 4.2.:** Pre-edge **A** and WL **B** of the N K edge XANES of *n*-Pr-BTP. The energy position of the ionization potential is marked by a line.

area indicates changed orbital mixing and thereby can be related to variations in the covalency of the chemical bond [82, 84, 85, 170–172]. For example, reduction of the pre-edge area means less N  $2p$  content in the probed MOs.

The  $1s$  ionization potential for N in the *n*-Pr-BTP ligand is at 399.80 eV as measured by X-ray photoelectron spectroscopy (XPS). However, an error of 0.15 eV has to be assumed due to charge-up effects in the material that is especially noticeable in N  $1s$  spectra [173].

The pre-edge of the spectra of the  $[An/Ln(n\text{-Pr-BTP})_3](\text{OTf})_3$  compounds as well as the *n*-Pr-BTP ligand consists of a main peak (see figure 4.6, **2**) and a shoulder (**1**) on the low energy side. As discussed above these features arise from excitations of N  $1s$  electrons to  $\pi^*$  MOs. An additional peak (**3**) between pre-edge and edge appears in some of the spectra. Multi-electron effects (i.e. the excited electron excites other electrons) and Rydberg resonances can also lead to additional features in the region above the sharp pre-edge peak (e.g. [174–177]). The main absorption (WL; see figure 4.2, **B**) arises from

excitations of N  $1s$  electrons to  $\sigma^*$  MOs. The energy position of  $\sigma^*$  is sensitive to the internuclear distances [178–182] and the molecular potential [177]. However, evaluation of the energy position, width, intensity and area of the  $\sigma^*$  resonance can provide unreliable results as it overlaps with multiple scattering resonances originating from elastic scattering of the photon electron from the atoms surrounding the N atoms (EXAFS part of the spectrum). Additionally,  $\sigma^*$  resonances are asymmetrically broadened by the vibrational motion of atoms in the molecule [183].

This work concentrates on the pre-edge regions of the N K edge XAS spectra, which are well separated from the main transitions and therefore can be carefully evaluated. Figures 4.3 and 4.4 depict the contributions of the N  $p$ , C  $p$  and La (figure 4.3)/Ac (figure 4.4)  $s$ ,  $d$  and  $f$  atomic unoccupied orbital constituents of the lowest group of unoccupied MOs of the La(H-BTP)<sub>3</sub> and Ac(H-BTP)<sub>3</sub> complexes. These MO Mulliken population analyses are performed with the ADF code (see section 3.4.3 for details). The calculations reveal that the pre-edges of the experimental spectra probe the group of MOs around and below  $-11$  eV, which consist mainly of N  $2p$  and C  $2p$  atomic orbitals with small admixtures of metal  $5d/6d$  and  $6s/7s$  orbitals. For La(H-BTP)<sub>3</sub> La  $4f$  orbitals also have minor contributions. It is apparent that the N K-edge XANES pre-edge region is more sensitive to the level of mixing of  $4f Ln$  than  $5f An$  with ligand valence orbitals. The MOs containing mainly  $f$  type atomic orbitals are in the range from  $-10$  eV to  $-9.5$  eV for La(H-BTP)<sub>3</sub> and between  $-7$  eV and  $-6$  eV for Ac(H-BTP)<sub>3</sub> due to the more localized character of the  $Ln 4f$  orbitals compared to the  $An 5f$  orbitals. The  $Ln 4f$  based orbitals likely do not match in energy with N/C valence orbitals therefore they do not mix with them [74, 85]. Due to large broadening effects dominating the spectrum in the post edge region the N K edge XANES method does not allow to study in details the energy region at about  $-6$  eV where the  $An 5f$  and  $6d$  strongly mix with ligand orbitals as demonstrated by the calculations. The population analyses strongly suggest that the  $An$ -ligand bond has stronger covalent character compared to the  $Ln$ -ligand bond due to larger mixing of  $An 5f$  with ligand valence orbitals. These quantum chemical results can be compared only in a qualitative manner to the experimental data since they do not account for the relaxation effects caused by the core-hole in the N atom. Such calculations have been carried on and are discussed in section 4.1.3 below. The population analyses for

---

La/Ac(H-BTP)<sub>3</sub> can only be used as an approximation for the  $Ln/An$  series, since partially filled  $4f/5f$  orbitals lead to variations in the energies of the MOs.

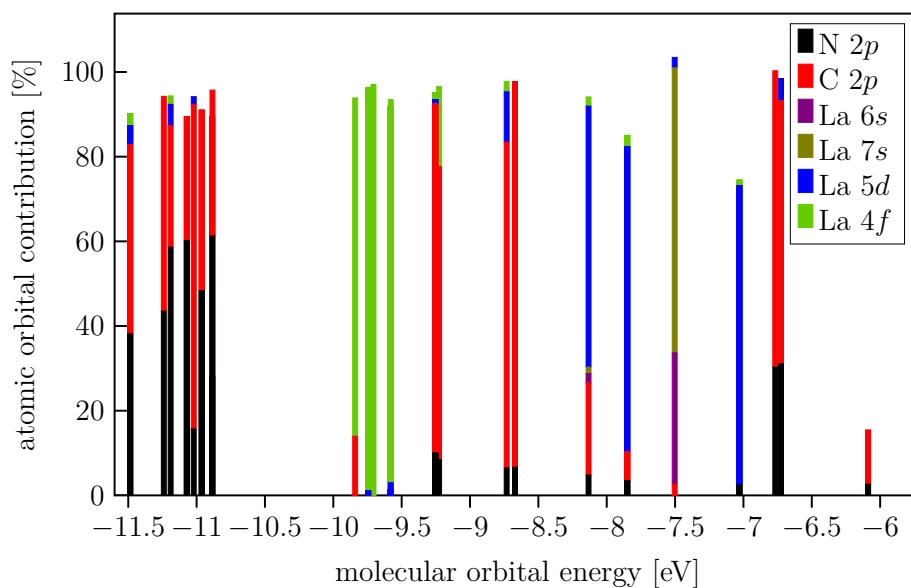


**Figure 4.3.:** Unoccupied MOs of La(H-BTP)<sub>3</sub> with N 2p, C 2p, La 6s, La 7s, La 5d and La 4f contributions.

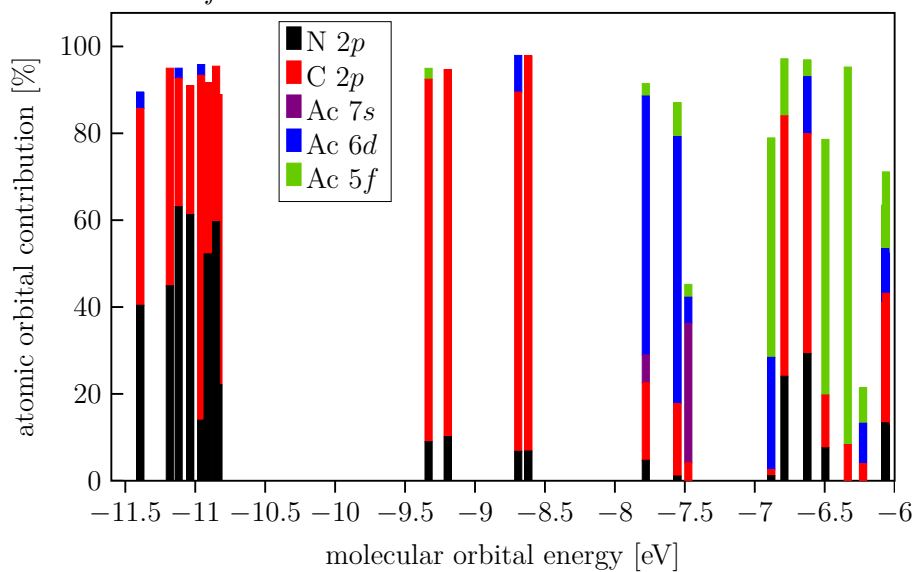


**Figure 4.4.:** Unoccupied MOs of Ac(H-BTP)<sub>3</sub> with N 2p, C 2p, Ac 7s, Ac 6d and Ac 5f contributions.

### 4.1.2. Comparison of $[An/Ln(n\text{-Pr-BTP})_3](\text{OTf})_3$ spectra

In extraction experiments (e.g. [17, 22, 49]) it was shown that *n*-Pr-BTP has a higher bonding affinity to *An* compared to *Ln*, but also a trend of the *n*-Pr-BTP bonding affinity to *Ln* as a function of the *Ln* Z number was demonstrated (see figure 4.5). Since increased ionicity of the metal–ligand bond has been suggested for *Ln* compared to *An* [49, 53] it is expected that the trends in selectivity are reflected in differences in the electronic structures of the *Ln* and *An* compounds. This work attempts to probe these variations by comparing N K-edge XANES spectra of the *n*-Pr-BTP ligand and *Ln* and *An* complexes. In addition, spectra within the *Ln* series are evaluated.

Comparison between experimental spectra of the *n*-Pr-BTP ligand and different  $[An/Ln(n\text{-Pr-BTP})_3](\text{OTf})_3$  reveals a shift of about 0.15 eV of the main pre-edge peak of the *n*-Pr-BTP spectrum to lower energies (figure 4.6). This energy shift indicates lower electron density on some of the N atoms in the complexes. The position of the rising edge of the pre-edge peak, defined as the maximum of the first derivative, is partially dependent on the intensity of the

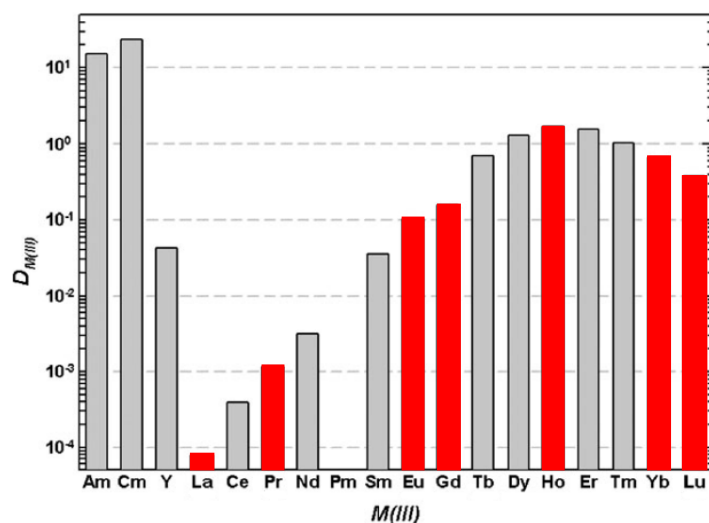


**Figure 4.5.:** Distribution ratios for lanthanide extraction to the organic phase with a BTP ligand. *Ln* used in this work are marked in red. Taken from [22].

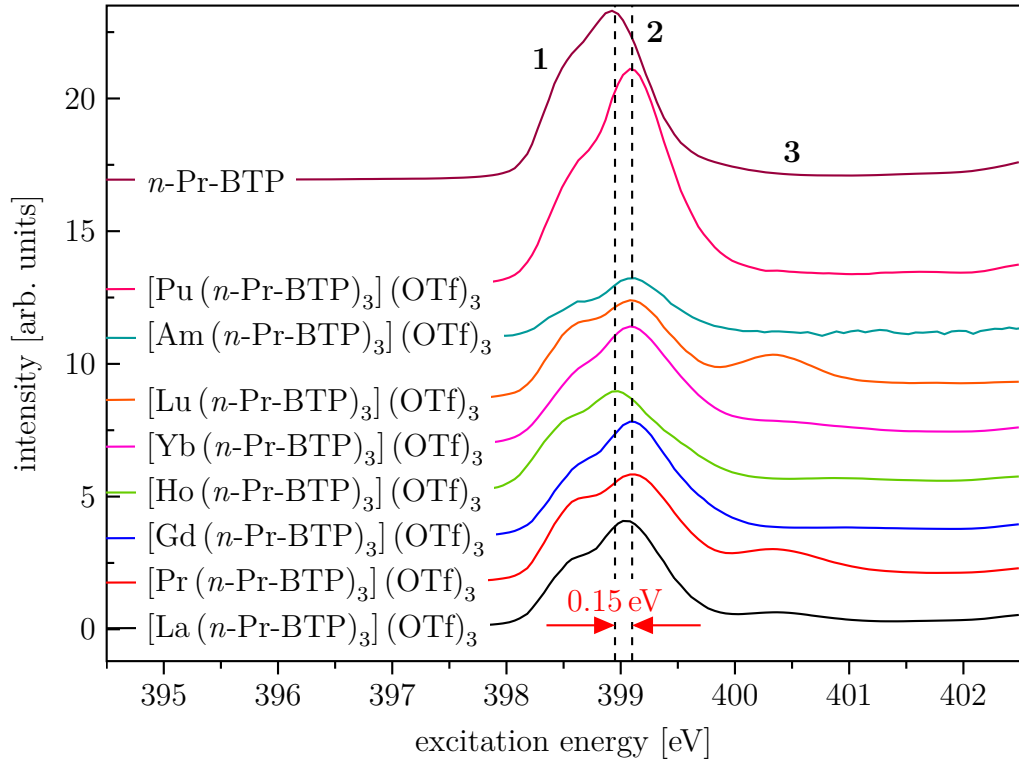


**Figure 4.6.:** Comparison of the pre-edge features of different  $[\text{An}/\text{Ln}(n\text{-Pr-BTP})_3](\text{OTf})_3$  compounds. Spectra are vertically shifted for clarity.

shoulder (**1**) of the pre-edge peak and peak **3** (discussed further below) and therefore does not give reliable results. Differences in energy positions and areas in the pre-edge range are quantified by modeling the spectra with three PV functions (figure 4.7). Two PV functions (**1**, **2**) are used in the pre-edge region. The third PV function models the transition to the  $\sigma^*$  resonance.

The peak positions (figure 4.8) and the distance between peaks **1** and **2** (figure 4.9a) of  $n$ -Pr-BTP complexed with  $\text{OTf}^-$ ,  $\text{ClO}_4^-$  and  $\text{NO}_3^-$  counter-ions show similar behavior over a series of  $\text{Ln}$  and  $\text{An}$ . The peak positions for the  $[\text{Ln}(n\text{-Pr-BTP})_3](\text{NO}_3)_3$  and  $[\text{Ln}(n\text{-Pr-BTP})_3](\text{ClO}_4)_3$  compounds tend to be shifted to higher energies compared to the  $[\text{Ln}(n\text{-Pr-BTP})_3](\text{OTf})_3$  compounds (figure 4.8). This effect is also observed for  $n$ -Pr-BTP and is an

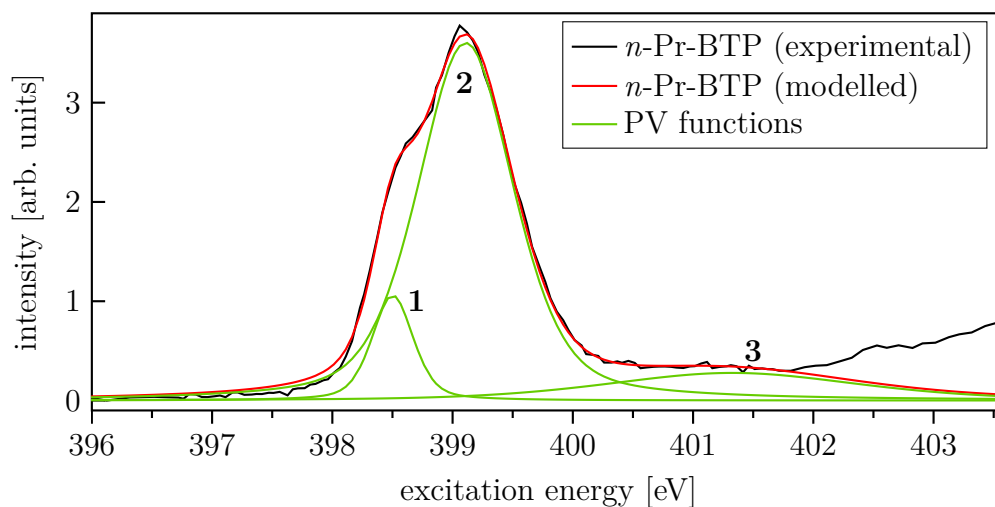


**Figure 4.7.:** An example of the pre-edge of N K edge XANES pre-peak modelled with PV functions.

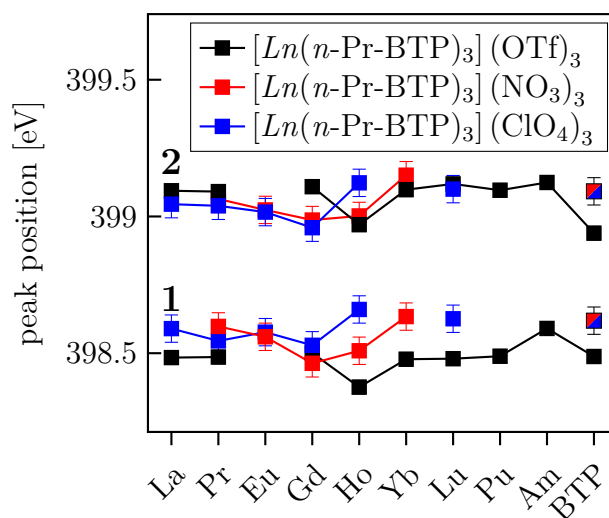


**Figure 4.8.:** Peak positions of  $n$ -Pr-BTP and  $An/Ln(n$ -Pr-BTP) $_3$  complexes with different counter-ions. The colors of the  $n$ -Pr-BTP peak positions mark the beamline at which they were measured.

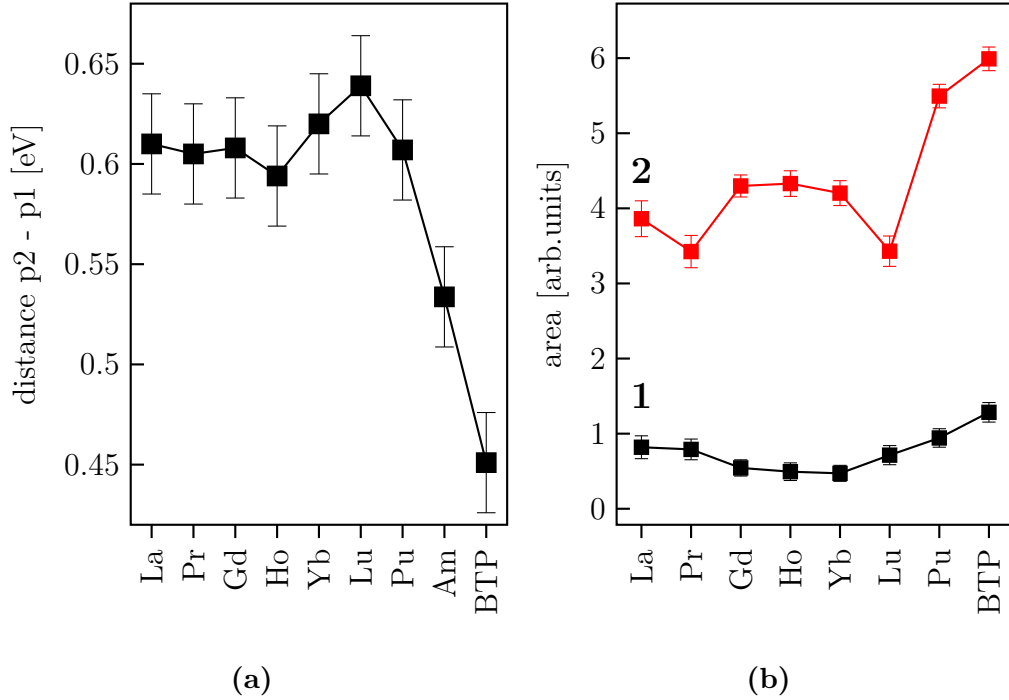


**Figure 4.9.:** Energy difference between peaks **1** and **2** as shown in figure 4.7 for different  $[Ln/An(n\text{-Pr-BTP})_3](\text{OTf})_3$  complexes and  $n\text{-Pr-BTP}$  (a) and areas of peaks **1** and **2** for  $n\text{-Pr-BTP}$  and  $[Ln/Pu(n\text{-Pr-BTP})_3](\text{OTf})_3$  (b).

experimental artifact since  $[Ln(n\text{-Pr-BTP})_3](\text{NO}_3)_3$ ,  $[Ln(n\text{-Pr-BTP})_3](\text{ClO}_4)_3$  and the corresponding  $n\text{-Pr-BTP}$  sample were measured at a beamline without an internal reference (for details of the beamlines, see sections 3.2.1 and 3.2.2). The results for the peak positions as well as the distance between the peaks suggest a weak trend anti-correlated to the distribution coefficient for extraction of  $Ln$  from the aqueous to the organic phase reported in the literature and shown in figure 4.5 [22]. The  $[Pu(n\text{-Pr-BTP})_3](\text{OTf})_3$  spectrum depicts no differences in peak positions compared to the spectra of the  $[Ln(n\text{-Pr-BTP})_3](\text{OTf})_3$  complexes. In the  $[Am(n\text{-Pr-BTP})_3](\text{OTf})_3$  spectrum the main peak shows no difference in peak position compared to the spectra of the  $[Ln(n\text{-Pr-BTP})_3](\text{OTf})_3$  complexes too, while the shoulder is shifted to a higher energy position. For the  $n\text{-Pr-BTP}$  spectrum compared to the spectra of the complexes, the main pre-edge peak **2** is

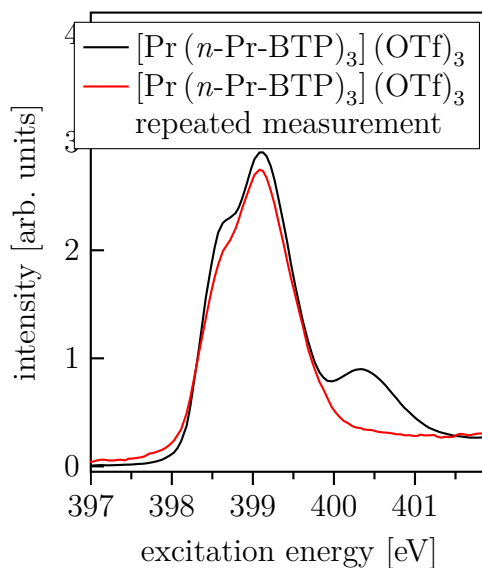


**Figure 4.10.:**  $[\text{Pr}(n\text{-Pr-BTP})_3](\text{OTf})_3$  N K edge spectra from different measurement campaigns.

shifted to lower energies, whereas the shoulder **1** has a similar energy position. The increased area of the peaks for  $[\text{Pu}(n\text{-Pr-BTP})_3](\text{OTf})_3$  (figure 4.9b) indicates decreased mixing in the  $-11$  eV molecular orbital energy range between N  $p$  and Pu valence orbitals compared to the  $Ln(n\text{-Pr-BTP})$  complexes. This result agrees with the orbital population analyses discussed in section 4.1.1. Areas for  $[\text{Am}(n\text{-Pr-BTP})_3](\text{OTf})_3$  are not shown because the different background subtraction that was necessary for the STXM data (see section 3.2.6) influenced the area of the pre-edge peak. For  $[\text{La}(n\text{-Pr-BTP})_3](\text{OTf})_3$ ,  $[\text{Pr}(n\text{-Pr-BTP})_3](\text{OTf})_3$  and  $[\text{Lu}(n\text{-Pr-BTP})_3](\text{OTf})_3$  the areas of peak **2** are lower than for the other compounds while the areas of peak **1** are slightly higher. This effect correlates with the appearance of peak **3** as seen in figure 4.6. However, repeated measurements at the same beamline do not show peak **3** for these compounds. As an example the spectra of  $[\text{Pr}(n\text{-Pr-BTP})_3](\text{OTf})_3$  from two different measurement campaigns are shown in figure 4.10. The peak does not change with time and appears at  $\sim 400.5$  eV while the radiation damage peak appears at  $\sim 399.5$  eV; therefore it is unlikely to be caused by radiation damage (see section 3.2.3). The origin of this peak has to be further investigated.

### 4.1.3. Quantum chemical investigations of H-BTP and $An/Ln(\text{H-BTP})_3$

To further analyze the experimental trends TD-DFT calculations of N K edge XANES were performed. They allow distinguishing between the spectra of the different N atoms. The theoretical N 1s spectra of H-BTP calculated with different methods (TD-DFT, ADC(2)) and programs (ORCA, TURBOMOLE, ADF) reproduce the number of peaks observed in the experimental spectra (figure 4.11). H-BTP is used instead of *n*-Pr-BTP to reduce calculation time. Analyses of the origin of the 1s electronic transitions marked with colored sticks in figure 4.11 (blue for the pyridine N (N1), green for the bonding triazine N (N3), red and purple for the N in the 1- (N4) and 4-position (N2) of the triazine, respectively, compare also figure 4.12), allow to identify the contributions of non-equivalent N atoms to the spectra. The transition sequence is the same in all calculations, whereas absolute energy positions and relative intensities are different. ADC(2) is a more accurate method than TD-DFT and thus more computationally demanding, especially for large molecules like the  $Ln/An(\text{H-BTP})_3$  complexes. Therefore, it is used here as a benchmark for the TD-DFT calculations, showing that TD-DFT can reproduce the transition order of the transitions from different N atoms.

TD-DFT calculations of  $\text{La}(\text{H-BTP})_3$  and  $\text{Ac}(\text{H-BTP})_3$  complexes show a different order of the transitions from different N atoms (figure 4.13). In contrast to the H-BTP spectra the transitions associated with the bonding N atoms shift to higher energies compared to the transition associated with the non-bonding N atoms. This shift corresponds to a lower electron density on the bonding N atoms in the complexes compared to the unbound ligand as it is expected intuitively, i.e. electrons are "pulled" towards the bonding partner. This effect can to some extent also be observed experimentally by a shift to higher energy (compare e.g. figure 4.6).

The bonding N spectra of  $\text{Ac}(\text{H-BTP})_3$  are shifted to lower energies and have higher oscillatory strength compared to the corresponding spectra of  $\text{La}(\text{H-BTP})_3$ . The energy shift might indicate higher covalency for the Ac-ligand compared to the La-ligand bonding since more electronic density is accumulated in the vicinity of the bonding N atoms for the  $\text{La}(\text{H-BTP})_3$  complex. The higher oscillatory strength is caused by less mixing of *p* ligand with *An* valence orbitals as discussed in section 4.1.2; see also the following

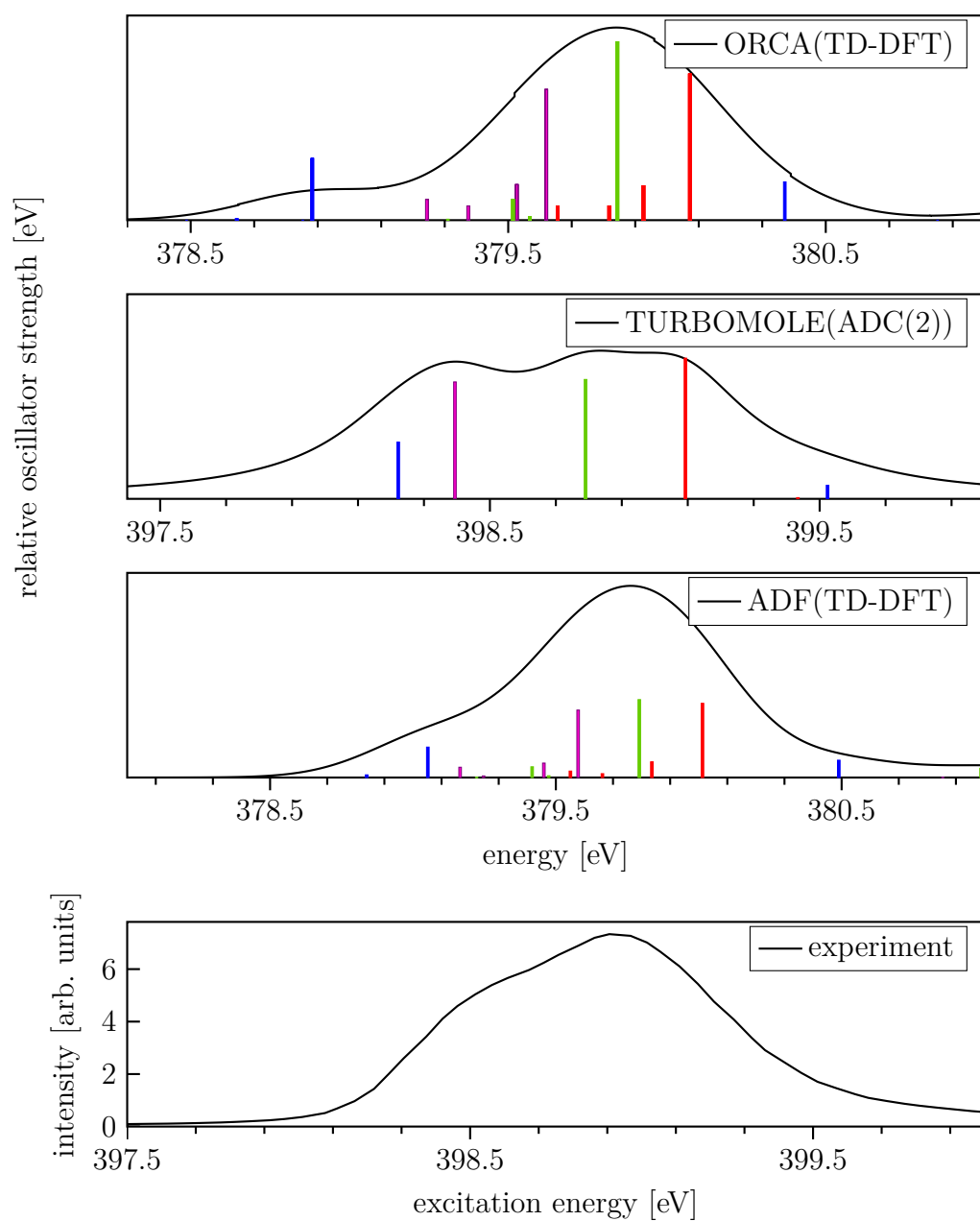


**Figure 4.11.:** Calculations of H-BTP with different methods and programs. Assignment of N according to figure 4.12.

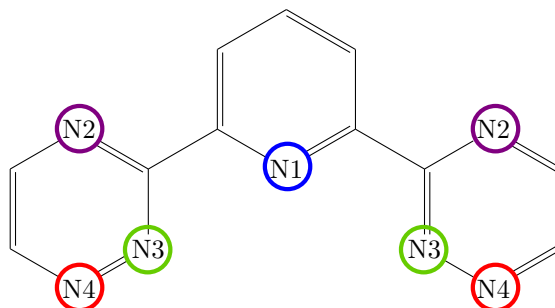


**Figure 4.12.:** Color coded assignment of excitations to different N in H-BTP.

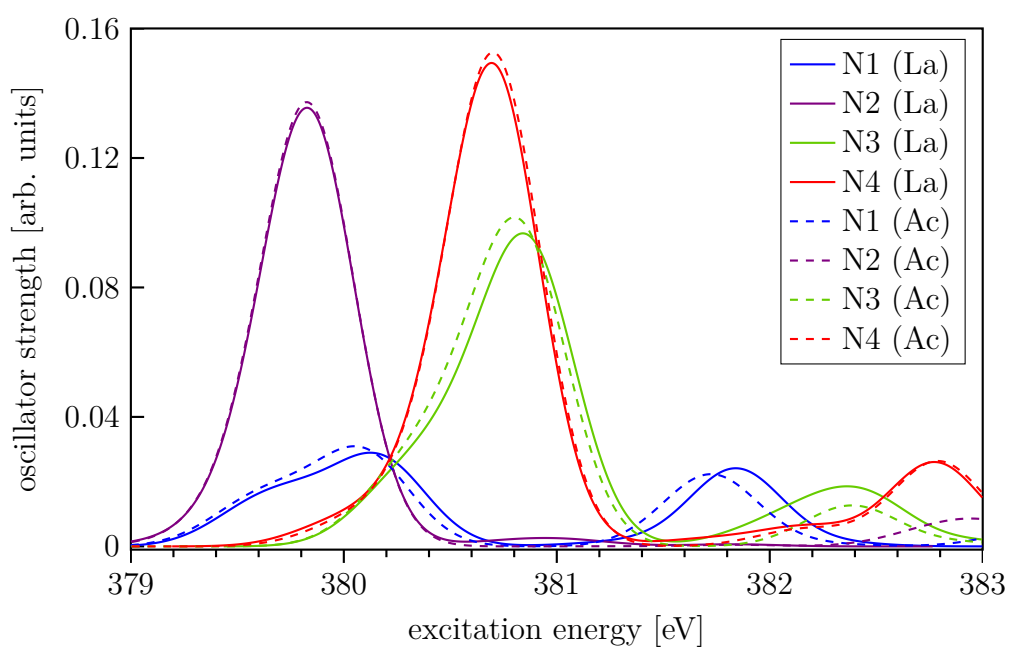


**Figure 4.13.:** Calculations of non-equivalent N in  $\text{La}(\text{H-BTP})_3$  (solid lines) and  $\text{Ac}(\text{H-BTP})_3$  (dashed lines). Assignment of N according to figure 4.12.

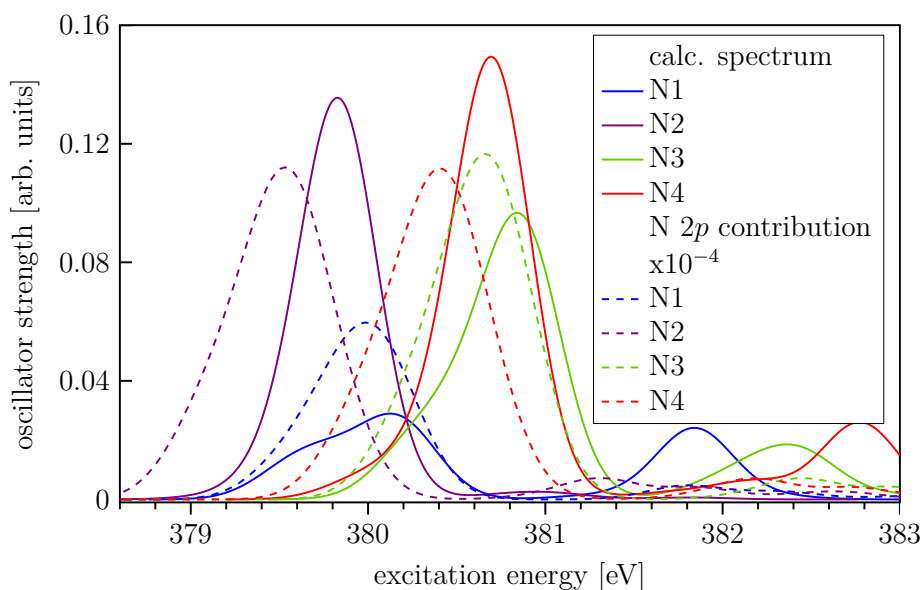


**Figure 4.14.:** N  $2p$  contributions to the spectrum of  $\text{La}(\text{H-BTP})_3$ . Assignment of N according to figure 4.12.

results and discussion. The scalar relativistic approximation used in these calculations is only appropriate for closed shell systems like La and Ac. For open shell systems, i.e. systems with partially filled  $f$  orbitals, it is necessary to take into account the spin-orbit coupling (SO coupling) to obtain reliable results. However, this was not possible for other than the closed shell  $\text{Ln}/\text{An}(\text{H-BTP})_3$  complexes with the used computational methods. Other possible approaches not used in this work include a combination of TD-DFT and linear response theory [184–186] and the combination of complete-active-space self-consistent field (CASSCF) [187] and quantum theory of atoms in molecules (QTAIM) [188] calculations that both have shown covalency effects and  $f$  orbital contribution to bonding in various  $\text{An}$  and  $\text{Ln}$  compounds (e.g. [82, 84, 85, 189–191] and references therein).

Figures 4.14 and 4.15 show for  $\text{La}(\text{H-BTP})_3$  and  $\text{Ac}(\text{H-BTP})_3$ , respectively, how much N  $2p$  character is in MOs into which N  $1s$  electrons are excited. The transition probability is not taken into account, leading to energy shifts compared to the calculated spectra for the non-equivalent N atoms. Figure 4.16 depicts the  $4f$  contributions to the  $\text{La}(\text{H-BTP})_3$  spectra. They are

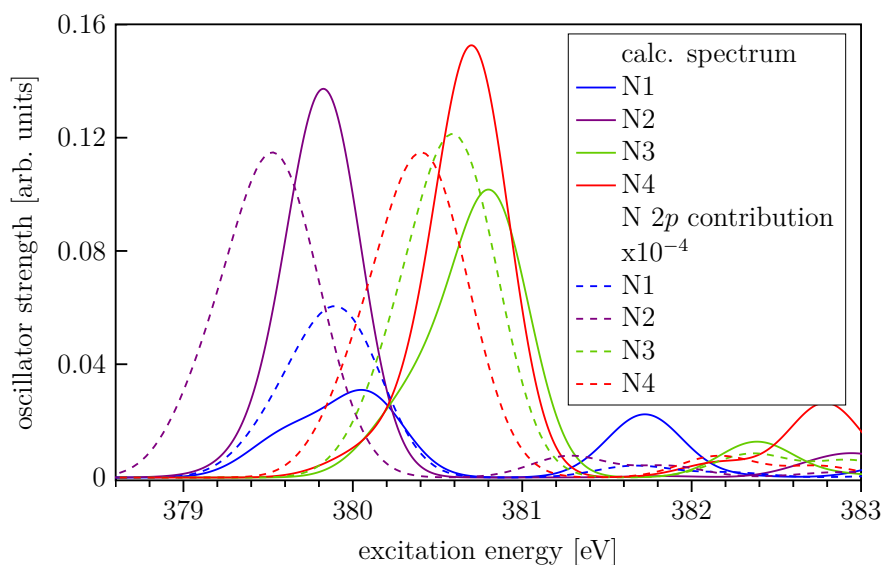


**Figure 4.15.:** N 2*p* contributions to the spectrum of Ac(H-BTP)<sub>3</sub>. Assignment of N according to figure 4.12.

more than ten times smaller than the N 2*p* contributions. The shift of the contributions compared to the spectra is smallest for the N atoms in the 2- and 4-position of triazine (N4 and N2 in figure 4.12). This might be a symmetry effect, because these atoms have a similar angle relative to the metal center. For the pyridine N atom, there are only excitations into MOs with small 4*f* contribution, while for the N atom in the triazine 1-position (N3 in figure 4.12) there are excitations into MOs with larger 4*f* contribution. Due to the unlocalized character of Ac 5*f* orbitals there are no excitations into 5*f* containing MOs in the N K edge pre-edge spectrum as it was also discussed in section 4.1.1. The experimental results discussed in section 4.1.2 agree with the results obtained by the theoretical calculations.

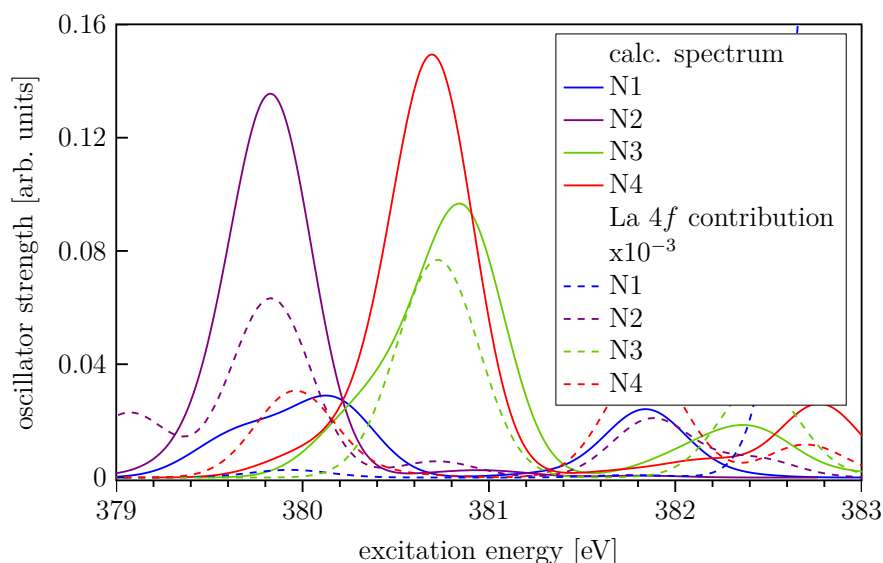


**Figure 4.16.:** La 4*f* contributions to the spectrum of La(H-BTP)<sub>3</sub>. Assignment of N according to figure 4.12.

#### 4.1.4. Comparison of N K edge spectra of ligands similar to *n*-Pr-BTP

In addition to *n*-Pr-BTP other ligands have been studied to investigate the effects of changes in ligand structure on the N K edge spectra. Figure 4.17 shows the pre-edge region of N K edge spectra of *n*-Pr-BTP, CA-BTP, CyMe<sub>4</sub>-BTBP and Et-BDP. *n*-Pr-BTP, CA-BTP and CyMe<sub>4</sub>-BTBP exhibit similar separation factors ( $SF_{Am/Eu} > 100$ ) [17, 19–21, 27] while Et-BDP performs much worse ( $SF_{Am/Eu} = 5$ ) [36, 38]. The ligands with similar structures, i.e. consisting of pyridine and triazine rings (see figure 4.18), show spectra with similar shapes and energy positions of peaks. The spectra are dominated by one peak with a shoulder on the low energy side. The pre-edges have small energy shifts ( $\sim 0.1$  eV) that could be related to a different charge distribution in the ligands. The spectrum of Et-BDP has a different peak shape due to the replacement of triazine with pyridazin. There is still a feature on the low-energy side of the main peak, but it has much lower intensity compared to the other spectra suggesting that the shoulder in the other spectra is related to the N in the 4-position (N2 in figure 4.12) of the

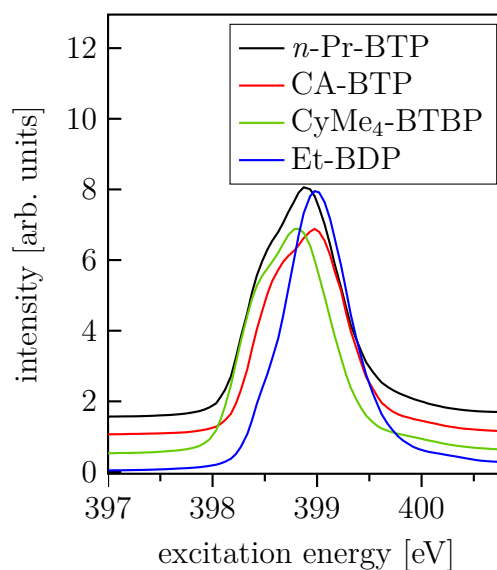


**Figure 4.17.:** N K edge spectra of *n*-Pr-BTP, CA-BTP, CyMe<sub>4</sub>-BTBP and Et-BDP. Spectra are vertically shifted for clarity.

triazine ring which agrees with the results from the calculations described in section 4.1.3. In all spectra, the excitations from the different N atoms are close in energy, so they can not be resolved experimentally.

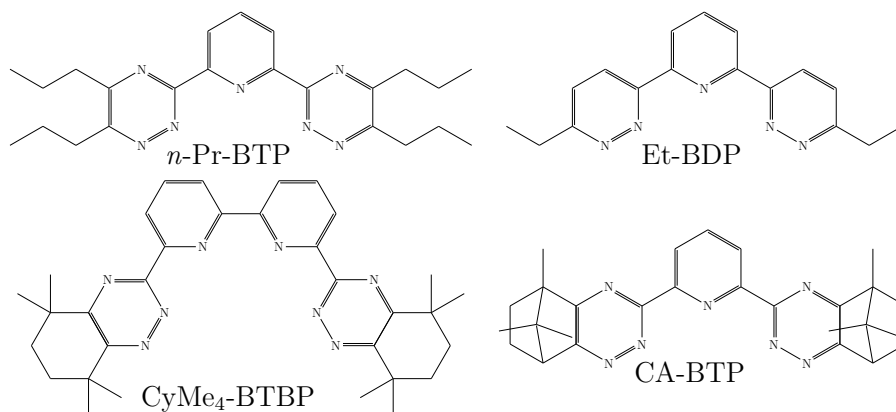


**Figure 4.18.:** Schematic structures of *n*-Pr-BTP, Et-BDP, CyMe<sub>4</sub>-BTBP and CA-BTP.

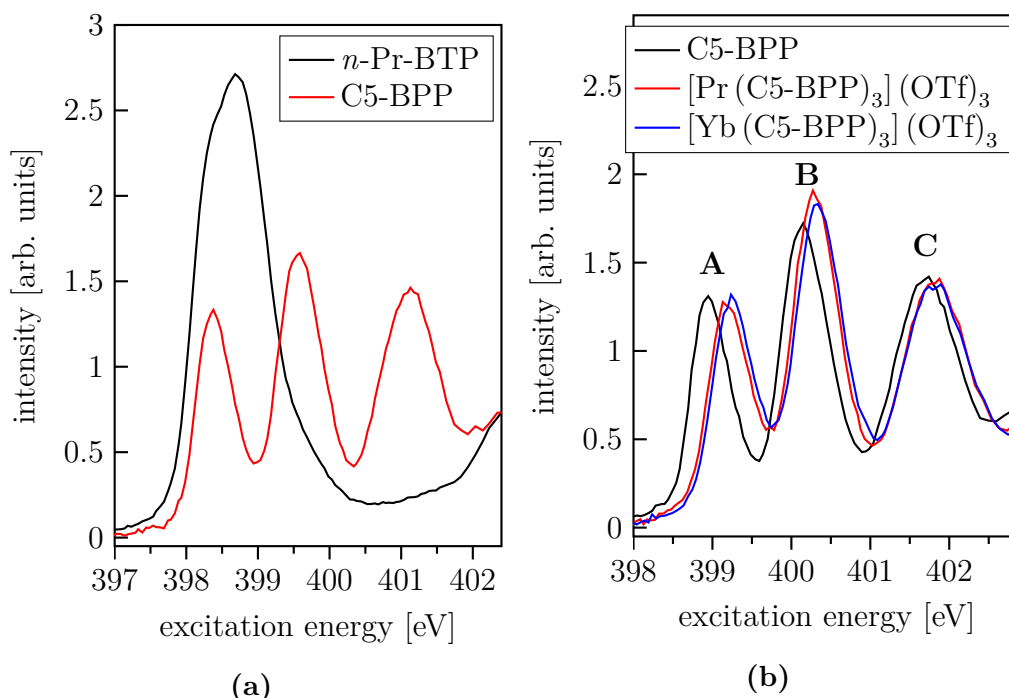


**Figure 4.19.:** N K edge spectra of  $n$ -Pr-BTP and C5-BPP (a) and different  $[Ln(C5-BPP)_3](OTf)_3$  (b).

A comparison of the pre-edge of  $n$ -Pr-BTP and C5-BPP, which has a similar extraction trend as  $n$ -Pr-BTP over a series of  $Ln$  but shifted to lower  $Z$  numbers [192], shows significant differences (figure 4.19a), due to the exchange of the 6 membered triazine with the 5 membered pyrazole (see figure 4.21). While the pre-edge of  $n$ -Pr-BTP consists of one peak with a shoulder on the low-energy side, the C5-BPP pre-edge has three clearly separated peaks. The complex spectra shown in figure 4.19b show a shift to higher energies of  $\sim 0.25$  eV for peak **A**,  $\sim 0.17$  eV for peak **B** and  $\sim 0.13$  eV for peak **C**, indicating a lower electron density on the N atoms of the complexes similar to the  $n$ -Pr-BTP compounds. Peaks **A** and **B** also exhibit a small shift  $< 0.1$  eV to higher energies of the  $[Yb(C5-BPP)_3](OTf)_3$  spectrum compared to the  $[Pr(C5-BPP)_3](OTf)_3$ . Peak **B** has a slightly increased intensity in the complex spectra compared to the ligand spectrum while the other peaks have similar intensities in all spectra. This indicates increased N  $2p$  contributions

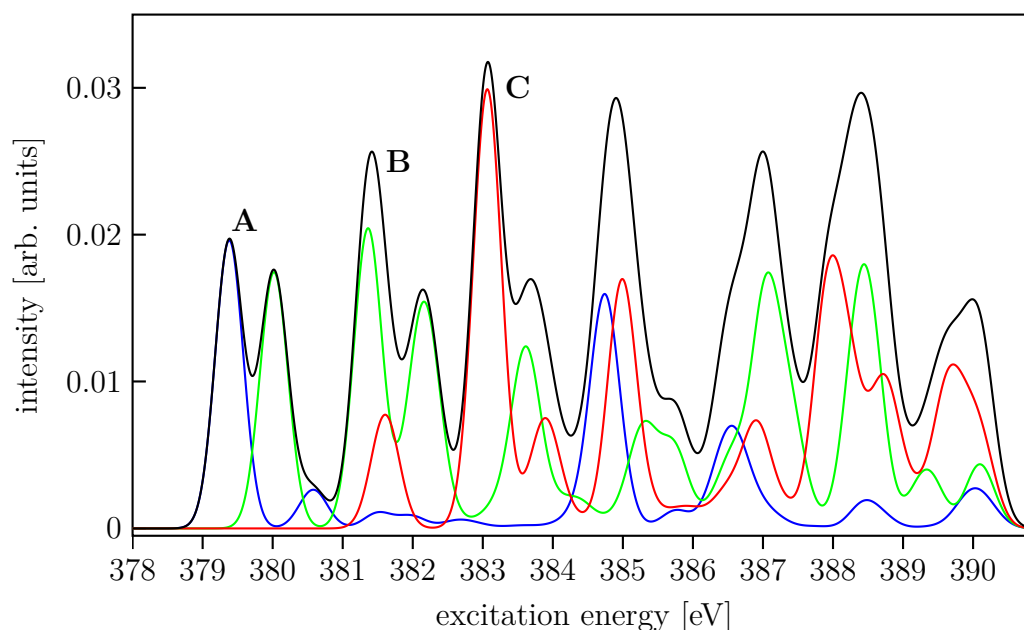


**Figure 4.20.:** TD-DFT calculations of N K edge XANES spectra for C5-BPP (black) and for different N atoms in C5-BPP. Color assignment according to figure 4.21.

to the MOs corresponding to **B** [189]. Between the complex spectra there are also small differences for the intensities of **A** and **B**, i.e. **A** has higher intensity for  $[\text{Yb}(\text{C5-BPP})_3](\text{OTf})_3$ , **B** has higher intensity for  $[\text{Pr}(\text{C5-BPP})_3](\text{OTf})_3$ . However, the differences are too small to allow a conclusive interpretation. The larger shifts of **A** and **B** and the larger intensity of **B** of the complex spectra suggest that **A** and **B** are corresponding to the bonding N atoms. TD-DFT calculations (figure 4.20) show that also for C5-BPP the pre-edge peaks (**A**, **B**, **C**) consist of overlapping contributions from several N atoms (blue for pyridine N, green for bonding pyrazole N, red for non-bonding pyrazole N, see also figure 4.21). However, the calculation correlates to the experiment as the peaks with mainly contributions from bonding N atoms (**A**, **B**) show the largest shift between bound and free ligand experimental spectra. This shows that the order of contributions from different N atoms is also reproduced for C5-BPP. This method could be used to test before the experiment if spectral difference can be expected.

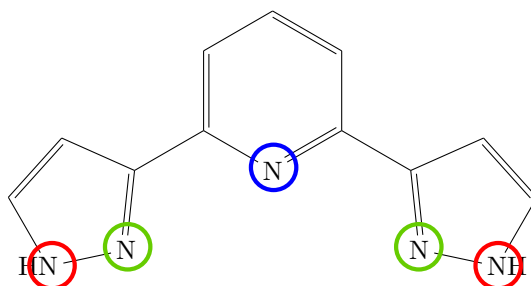


**Figure 4.21.:** Color code for the different N in the BPP ligand.

#### 4.1.5. NRIXS feasibility studies

The process of separation of  $An$  from  $Ln$  takes place in a liquid phase. However, the N K edge low photon energy ( $\sim 400$  eV) requires ultra-high vacuum investigations challenging for liquid samples. First XAS tests with a liquid, constant flow, pump-through cell equipped with 150 nm SiC window [193] at the ALS resulted in fast formation of X-ray induced radiolysis, i.e. radiation damage, coloring the  $n$ -Pr-BTP liquid sample from light orange to dark brown within 2 to 3 minutes. An alternative technique currently in development for K-edge XANES investigations of low  $Z$  elements is NRIXS. An incident beam with energies above 10 keV facilitates use of liquid sample cells and double containments necessary for investigations of radioactive materials. The high energy of the X-rays can penetrate through windows in the sample cell made from material such as Kapton, which has high chemical and X-ray stability and therefore is often used as window material. Disadvantages of the technique are: 1) the low cross section of the process ( $\sim 0.13$  cm<sup>2</sup> g<sup>-1</sup> inelastic scattering cross section compared to  $\sim 3 \times 10^4$  cm<sup>2</sup> g<sup>-1</sup> photo-absorption cross section [194]) requiring at least 3 at% concentration of N atoms in the sample for  $2 \times 10^{12}$  ph/s incident beam, 18 analyzer crystals, 2) the reduced experimental energy resolution compared to a dedicated soft X-ray beamline leading to broadening of the spectral features. Only a few NRIXS measurements of highly concentrated liquid samples are reported in the literature [195–199].

At the 20-ID beamline at the APS the feasibility studies presented here were the first measurements of liquids performed with the LERIX spectrometer therefore they contributed to the development program of the beamline to extend the range of possible samples. Figure 4.22a shows the O K edge

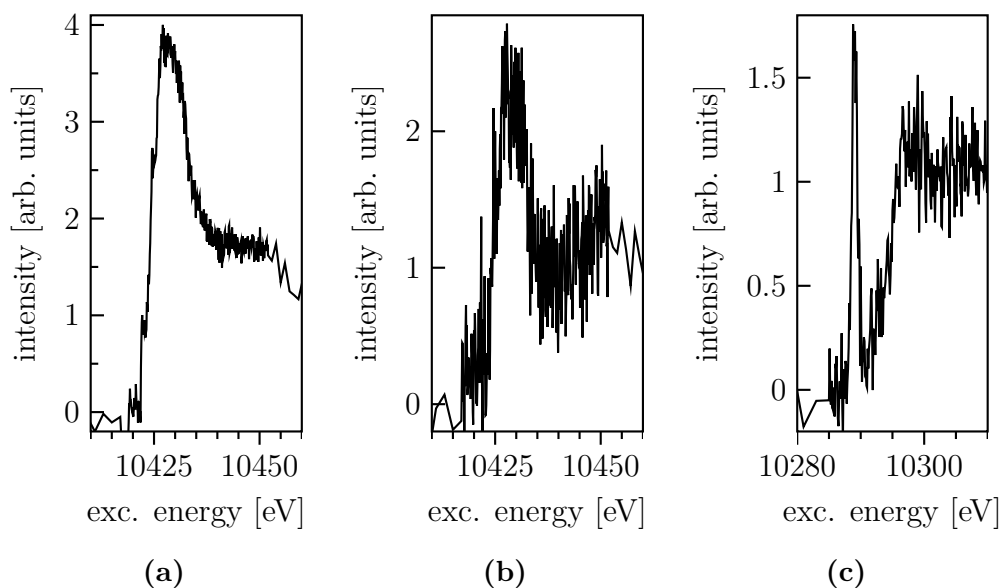


**Figure 4.22.:** O K edge spectra of isopropanol (a) and water (b). N K edge spectrum of *n*-Pr-BTP. (c)

isopropanol spectrum after averaging two scans measured 45 minutes per scan. We observed formation of gas bubbles during the measurements probably formed by radiolysis or heating of the isopropanol. The angle of the cell with respect to the incoming X-ray beam was changed from  $45^\circ$  to  $30^\circ$  to allow the bubbles to escape from the cell without disturbing the measurement. This cell arrangement reduced the number of usable analyzers from 15 to 12. The O K edge water spectrum (figure 4.22b) has a low signal-to-noise ratio due to the short accumulation time of 45 minutes. However, details for the edge region, similar to those reported for water ice in the literature [200, 201], are well distinguishable. The N K edge spectrum of crystalline *n*-Pr-BTP measured for  $\sim 30$  minutes by averaging over 18 detectors is shown in figure 4.22c. The spectrum has a lower signal-to-noise ratio than the standard XANES spectrum measured for 60 minutes by averaging over three detectors (figure 4.6). After one scan ( $\sim 30$  min) the changed surface color of the sample indicated damage by the beam. A second scan was consistently showing a lower signal. The *n*-Pr-BTP solution revealed no visible color changes after several hours

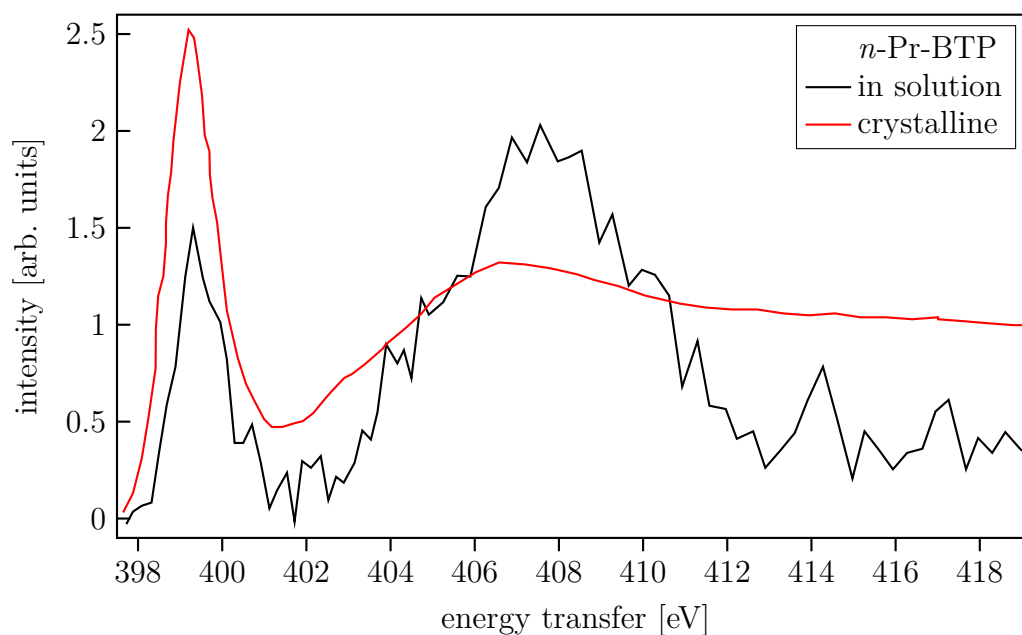


**Figure 4.23.:** N K edge spectra of *n*-Pr-BTP crystalline and in isopropanol solution.

exposure to the beam. However, due to the low concentration no discernible N signal was measured.

At the ID20 beamline at the ESRF it was possible to measure *n*-Pr-BTP solutions due the higher number of available analyzer crystals and the higher incident photon flux (ID20:  $\sim 10^{14}$  photons/s; 20-ID:  $\sim 10^{12}$  photons/s). Figure 4.23 shows the N K edge spectra of *n*-Pr-BTP crystalline and in solution. The crystalline sample has been measured with 48 crystals for 3 h in a evacuated chamber, while the solution sample was measured with 24 crystals for 10 h. The crystalline sample showed similar discoloration as the sample investigated at the 20-ID beamline. A part of the isopropanol in the solution sample evaporated during the measurements. The pre-edge and WL of the spectra have similar energy positions, but different intensities due to difficulties with the normalization. Even though the signal-to-noise ratio is much worse for the sample in solution the general structure of the spectrum can be easily recognized and it can be assumed that the structure in solved and crystalline does not differ significantly. The signal-to-noise ratio of the

spectrum of the liquid sample can be improved by utilizing more analyzer crystals and an improved cell design, e.g. using a capillary. In addition, the solution should be temperature controlled to reduce evaporation and avoid precipitation of the complex due to temperature difference between preparation lab and beamline.

#### 4.1.6. Conclusions

The investigations presented here demonstrate that it is essential to combine N K-edge XANES spectroscopy with *ab initio* quantum chemical calculations in order to obtain electronic structure information. The benchmark calculations with several methods and codes combined with comparison to the experimental *n*-Pr-BTP spectrum confirm that the DFT ADF code has reasonable accuracy and can be used for more detailed analyses.

Both experiment and calculations reveal less electronic density on the bonding N atoms for the complexes compared to the ligand. This result clearly indicates charge transfer from the ligand likely to the metal. The calculations suggest that this transfer is smaller for *An* compared to *Ln*, which is an indication for a stronger covalent bond for the *An* compared to the *Ln* bound to the H-BTP molecule. In an intuitive picture this result can be understood as an increased electronic density accumulated between the *An* and ligand atoms. The stronger covalent character for the *An*-ligand compared to the *Ln*-ligand bond is also strongly suggested by the Mulliken population analyses. They demonstrate that the *An* 5*f* compared to the *Ln* 4*f* orbitals are more strongly mixed with valence orbitals of the ligand.

The region of the spectrum sensitive to the level of mixing of valence *An* 5*f* with N 2*p* orbitals is not accessible due to broadening effects. Nevertheless, it was possible to correlate the reduced area of the pre-edge peak for *Ln* complexes compared to the Pu complex with the mixing of 4*f* with ligand 2*p* orbitals in the  $\pi^*$  anti-bonding orbitals. This is also an evidence for the good accuracy of the theoretical calculations.

The comparison of experimental spectra for ligands similar to *n*-Pr-BTP with variable extraction properties confirms the correctness of the assignments of N atoms to spectral features carried out with the help of theory. Further

comparative investigations of the  $An$  and  $Ln$  complexes for ligands with small variations in the structure but large differences in extracting properties might help to gain additional insights into the relation between electronic structure and extraction behavior of the ligands.

The benchmark NRIXS studies demonstrate the applicability of this novel technique for investigations of liquid samples of partitioning systems at the N K edge and at K absorption edges of other low Z elements. No significant differences between the N K-edge spectrum for the  $n$ -Pr-BTP molecule in solid phase or solved in isopropanol are found. This result strongly suggests that the results obtained for the solid state complexes and ligands are relevant also for their liquid forms. Based on several experiments using the state of the art spectrometers installed at the brightest synchrotrons specific practical suggestions for further improved of the experimental set-up are given.



## 4.2. *Ln/An* L<sub>3</sub> edge HR-XANES and RIXS

In this chapter the electronic and geometric structures of *An/Ln* partitioning complexes are probed from the metal 'point-of-view' using *An/Ln* L<sub>3</sub> edge HR-XANES and RIXS as well as XANES and EXAFS *ab initio* quantum chemical calculations with the *FEFF* and *FDMNES* codes. Benchmark calculations using different codes and structural models are carried out. The VB-RIXS technique is explored for the first time as a tool for electronic structure studies of partitioning systems. The main focus is on the comparison between [*Ln*(*n*-Pr-BTP)<sub>3</sub>](OTf)<sub>3</sub> and *Ln*(OTf)<sub>3</sub> L<sub>3</sub> edge HR-XANES spectra. The correlation of the different spectral features and trends with specific structural changes over a series of *Ln* are discussed.

### 4.2.1. General description of the spectrum

Figure 4.24 shows simplified a MO scheme of *An/Ln* bound to N and the excitations relevant for XAS at the *An/Ln* L<sub>3</sub> edge. At the WL (see chapter 2 and e.g. figure 2.2) electrons are excited from *An/Ln* 2*p*<sub>3/2</sub> states to unoccupied molecular orbitals with *An/Ln* 5*d*/6*d* and N 2*p* based atomic orbitals. The WL is mainly used to observe changes in the oxidation states [202], i.e. the relative energy shift of the absorption edge due to the change in valence orbital occupation and the resulting change in electron density and screening of the core-hole. The WL is also sensitive to the local structure, because the orbital occupation, and thereby the density of occupied and unoccupied states, that depend also on other factors than the oxidation state, e.g. the chemical environment, i.e. type of bonding partner [203], coordination number, local symmetry [204], changes due to induced pressure [205, 206], etc. This can lead to changes in energy position, width, shape and intensity of the WL. From a quantum chemical point of view L<sub>3</sub> edge spectra describe the angular momentum projected density of states (DOS) of unoccupied *d* like states [207], 5*d*/6*d* states in the case of *Ln/An* L<sub>3</sub> edge spectra following the dipole selection rules  $\Delta l = \pm 1$  (see also section 2.1).

After the first experimental observation of a weak pre-edge structure in Ce XANES [208], band structure calculations showed a correspondence to quadrupole transitions [92].

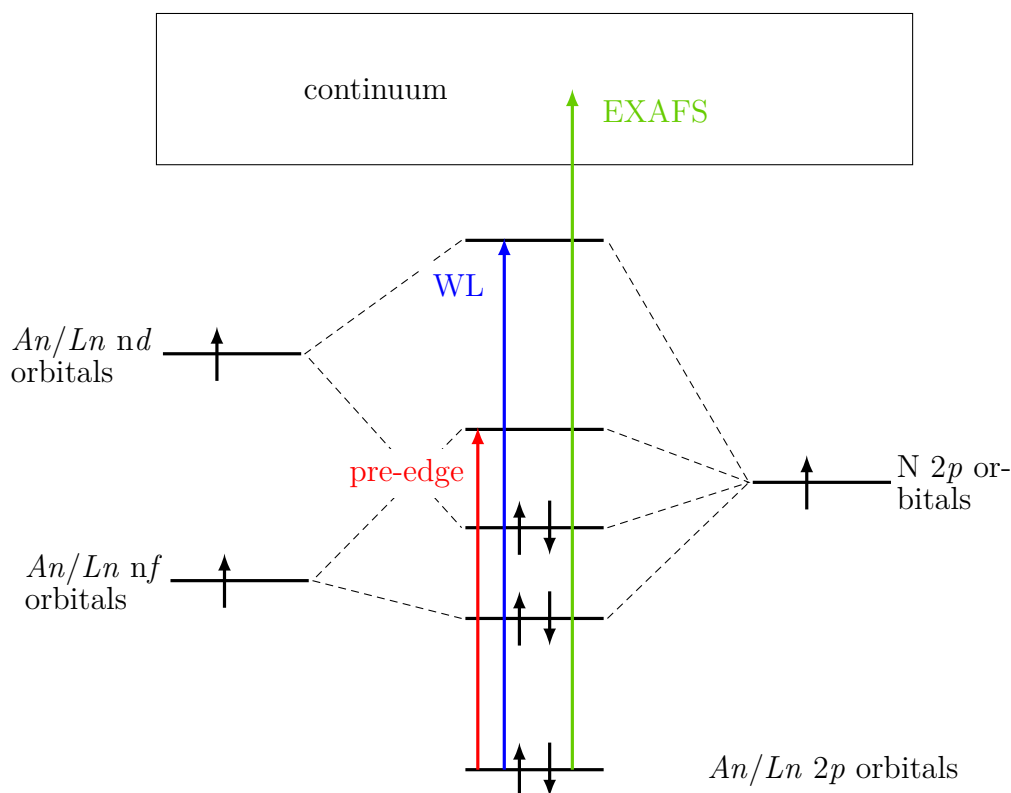


**Figure 4.24.:** Simplified MO scheme of  $An/Ln$  bound to N and the excitations causing the pre-edge (red), WL (blue) and EXAFS (green) features observed in  $An/Ln$   $L_3$  edge spectra.

Even though quadrupole transitions ( $2p_{3/2} \rightarrow 4/5f$ ) are considerably weaker than dipole transitions ( $2p_{3/2} \rightarrow 5/6d$ ), they have been observed for a variety of  $Ln$  ( $2p_{3/2} \rightarrow 4f$  transitions) and  $An$  ( $2p_{3/2} \rightarrow 5f$  transitions) materials using X-ray emission spectrometers with an instrumental energy bandwidth similar to the core-hole lifetime broadening [83, 93, 94, 133, 209–228]. Atomic multiplet calculations of the pre-edge spectral features of  $Ln$   $L_3$  HR-XANES demonstrated that they are shaped by electron-electron interactions and their shape, intensity and energy position on the excitation and emission energy scale directly depend on the number of available  $f$  electrons in the systems [94, 229, 230].

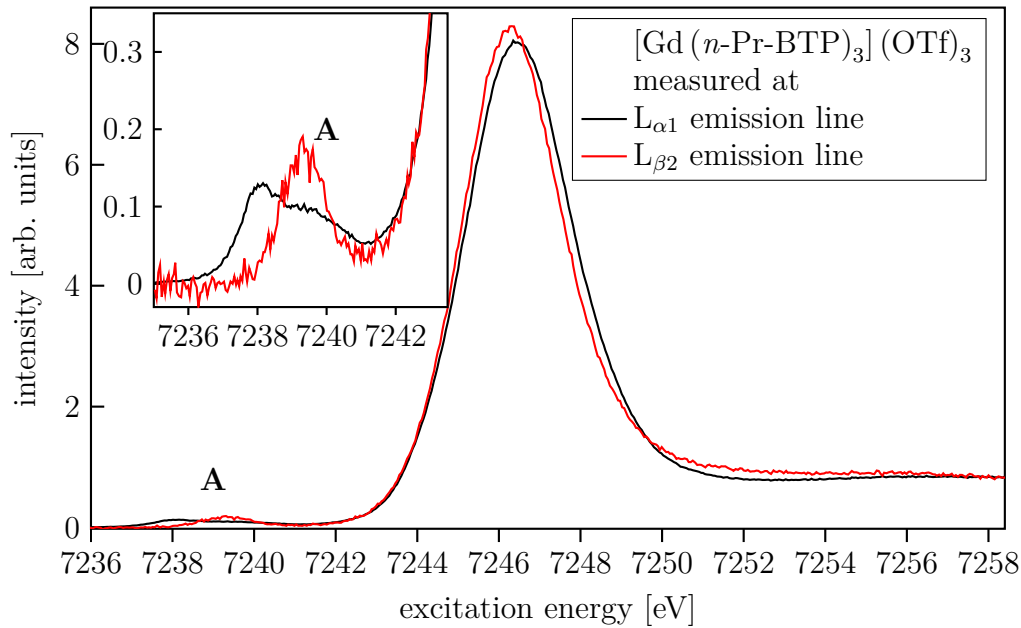


**Figure 4.25.:** Gd  $L_3$  edge HR-XANES of  $[\text{Gd}(n\text{-Pr-BTP})_3](\text{OTf})_3$  measured at the Gd  $L_{\alpha 1}$  and  $L_{\beta 2}$  emission line.

By recording HR-XANES using different emission lines, it is possible to investigate spectra of the same absorption edge with different resolutions, due to the different final state core-hole lifetime broadening (e.g. U  $L_3$  HR-XANES collected at the  $L_{\beta 5}$  emission line [231]). It can also be possible to detect additional spectral features due to different screening of core-holes at different energy levels. In the case of  $Ln$   $L_3$  edge spectra the  $L_{\beta 2}$  emission line can be used instead of the conventional high intensity  $L_{\alpha 1}$  emission line. However, the  $4d$  core-hole resulting from the  $L_{\beta 2}$  emission has a higher core-hole lifetime broadening [232] than the  $3d$  core-hole resulting from the  $L_{\alpha 1}$  emission [233] hence no increase in resolution can be achieved. In figure 4.25 the spectra of  $[\text{Gd}(n\text{-Pr-BTP})_3](\text{OTf})_3$  measured recording the emitted fluorescence by fixing the Bragg angles of the analyzer crystals at the maximum of the  $L_{\alpha 1}$  or  $L_{\beta 2}$  emission lines are compared. The WL of the spectrum measured at the  $L_{\beta 2}$  emission line is slightly narrower and the pre-edge has only one instead of two peaks. To further investigate the differences in the pre-edge region RIXS maps were recorded. Figure 4.26 shows  $2p3d$  ( $L_{\alpha 1}$ ) and  $2p4d$  ( $L_{\beta 2}$ ) RIXS

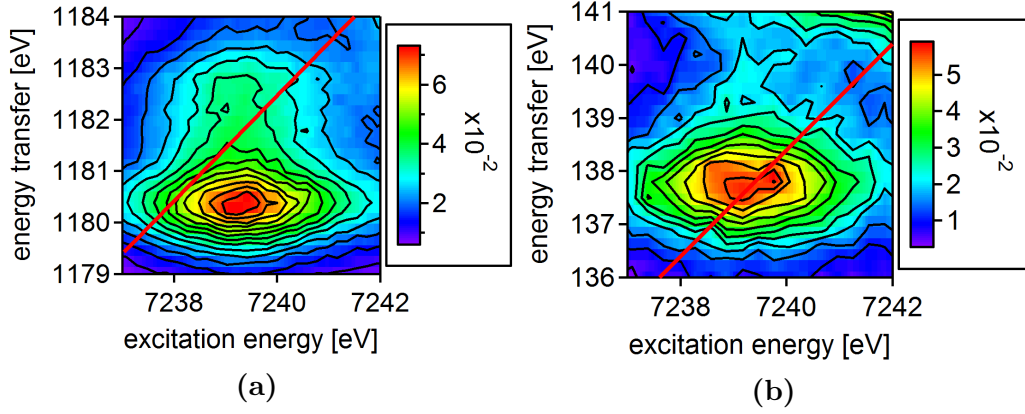


**Figure 4.26.:** Normalized  $2p3d$  (a) and  $2p4d$  (b) RIXS pre-edge maps of  $[\text{Gd}(n\text{-Pr-BTP})_3](\text{OTf})_3$  with XANES position (red line).

maps of the pre-edge of  $[\text{Gd}(n\text{-Pr-BTP})_3](\text{OTf})_3$  with a red line marking the emission energy at which the HR-XANES spectra shown in figure 4.25 were measured. The  $2p3d$  RIXS map has two features at the same excitation energy at  $\sim 1180.5$  eV and  $\sim 1182.5$  eV energy transfer. The HR-XANES spectrum cuts through both features leading to the observed double structure in the pre-edge. In contrast, the  $2p4d$  RIXS map has one feature at  $\sim 137.5$  eV energy transfer and additional intensity at  $\sim 140$  eV that could be a second feature or the overlap of pre-edge and WL tails. The HR-XANES spectrum only intersects the maximum of the first feature resulting in a single pre-edge peak. Because the differences in the RIXS maps appear along the energy transfer scale, they are related to final state effects (see also section 2.2). In this case these are different splitting of the  $2p^63d^95d^1$  and  $2p^64d^95d^1$  final states, respectively; changes in the screening of the core-hole cause an energy shift of the pre-edge resonance. Since the  $4f - 4f$  electron-electron interactions have the same influence on both spectra, the appearance of two resonances along the energy transfer scale is likely related to differences in the  $3d - 4f$  and  $4d - 4f$  electron-electron interactions. It was shown that they have the highest influence on the spectrum after the  $4f - 4f$  electron-electron interactions [94]. The double structure in the pre-edge of the spectrum measured at the  $L_{\alpha 1}$  emission line is not resolved in all measurements (e.g., figure 4.34b), because a different type of crystals positioned at different Bragg angles were used,

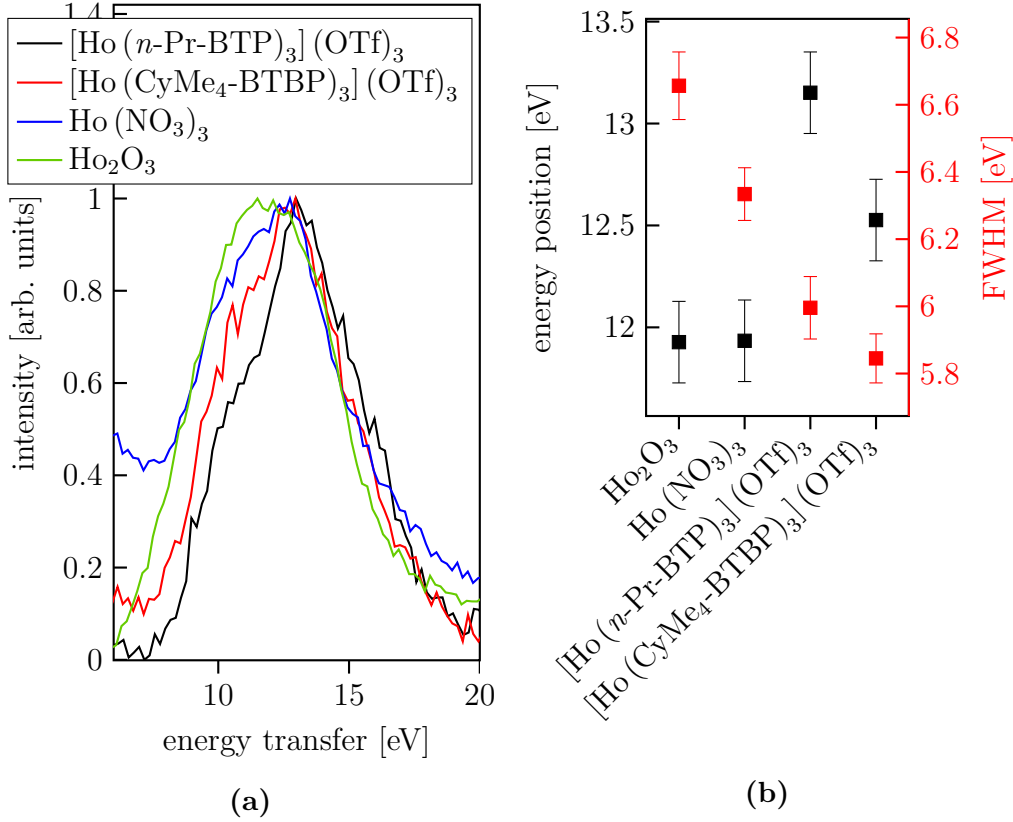


**Figure 4.27.:** normalized VB-RIXS of  $[\text{Ho}(n\text{-Pr-BTP})_3](\text{OTf})_3$ ,  $[\text{Ho}(\text{CyMe}_4\text{-BTBP})_3](\text{OTf})_3$ ,  $\text{Ho}(\text{NO}_3)_3$  and  $\text{Ho}_2\text{O}_3$  (a); fitted energy position and FWHM of the peak shown in (a) (b).

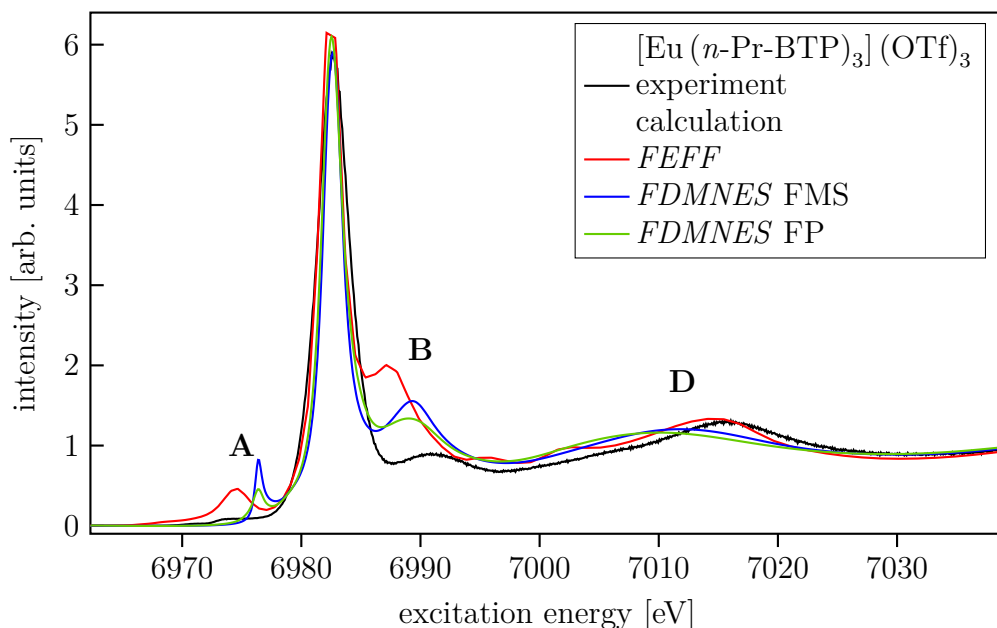
resulting in changed resolution (Si(333) at  $78.28^\circ$  for figure 4.25, Ge(333) at  $70.15^\circ$  for figures 4.34b and 4.37; see also tables 3.2 and 3.3 in section 3.3.3 and table 3.10 in section 3.3.4).

The VB-RIXS technique probes the angular momentum projected valence band of the studied element and is applied here to test its applicability for investigations of *Ln* 5*d* states in  $[\text{Ln}(n\text{-Pr-BTP})_3](\text{OTf})_3$  partitioning complexes. Due to the dipole selection rules, the method specifically probes the 5*d* unoccupied valence states by excitations of  $2p_{3/2}$  electrons. This is the main difference compared to most methods probing the valence band as those methods are not selective to specific angular momentum quantum

numbers. Figure 4.27a shows the Ho L<sub>3</sub> VB-RIXS of [Ho(*n*-Pr-BTP)<sub>3</sub>](OTf)<sub>3</sub>, [Ho(CyMe<sub>4</sub>-BTBP)<sub>3</sub>](OTf)<sub>3</sub>, Ho(NO<sub>3</sub>)<sub>3</sub> and Ho<sub>2</sub>O<sub>3</sub> on the energy transfer scale. To record the VB-RIXS spectra the excitation energy was fixed at the maximum of the WL and the emission energy was scanned close to the elastic peak. In the final state, the excited Ho atom has an electron promoted to an empty 5*d* state and a core-hole in the filled part of the VB emulating a direct excitation from the VB and describing the unoccupied 5*d* states [111, 112]. The distance between the VB-RIXS spectra to the elastic peak is shorter for Ho(NO<sub>3</sub>)<sub>3</sub> and Ho<sub>2</sub>O<sub>3</sub> than for [Ho(*n*-Pr-BTP)<sub>3</sub>](OTf)<sub>3</sub> and [Ho(CyMe<sub>4</sub>-BTBP)<sub>3</sub>](OTf)<sub>3</sub> indicating a smaller energy gap between highest occupied *d* state and lowest unoccupied valence state for Ho(NO<sub>3</sub>)<sub>3</sub> and Ho<sub>2</sub>O<sub>3</sub> [111]. The FWHM of the peaks of [Ho(*n*-Pr-BTP)<sub>3</sub>](OTf)<sub>3</sub> and [Ho(CyMe<sub>4</sub>-BTBP)<sub>3</sub>](OTf)<sub>3</sub> are smaller compared to Ho(NO<sub>3</sub>)<sub>3</sub> and Ho<sub>2</sub>O<sub>3</sub> and also exhibit a shoulder on the low energy side. The reduced FWHM indicates less *d* type of electronic density in the vicinity of the *Ln* atoms for the *n*-Pr-BTP complexes. Figure 4.27b shows the energy position and FWHM of the spectra in figure 4.27a obtained from modeling the peak with a Gaussian function. It was not possible to fit the peaks consistently with two Gaussian functions to gain more information about the shoulder in the spectra of [Ho(*n*-Pr-BTP)<sub>3</sub>](OTf)<sub>3</sub> and [Ho(CyMe<sub>4</sub>-BTBP)<sub>3</sub>](OTf)<sub>3</sub>. Both energy position and FWHM show a clear difference between [Ho(*n*-Pr-BTP)<sub>3</sub>](OTf)<sub>3</sub> and [Ho(CyMe<sub>4</sub>-BTBP)<sub>3</sub>](OTf)<sub>3</sub> compared to Ho(NO<sub>3</sub>)<sub>3</sub> and Ho<sub>2</sub>O<sub>3</sub>, but also differences between [Ho(*n*-Pr-BTP)<sub>3</sub>](OTf)<sub>3</sub> and [Ho(CyMe<sub>4</sub>-BTBP)<sub>3</sub>](OTf)<sub>3</sub> are present. To establish if the effects observed here are correlated to the extraction behavior of *n*-Pr-BTP and CyMe<sub>4</sub>-BTBP complexes additional VB-RIXS investigations of extracting and non-extracting *An/Ln* compounds are necessary. Additionally, quantum chemical calculations including population analyses of the different orbitals are needed.

#### 4.2.2. Calculations of *Ln* L<sub>3</sub> edge HR-XANES spectra of [Ln(*n*-Pr-BTP)<sub>3</sub>](OTf)<sub>3</sub>

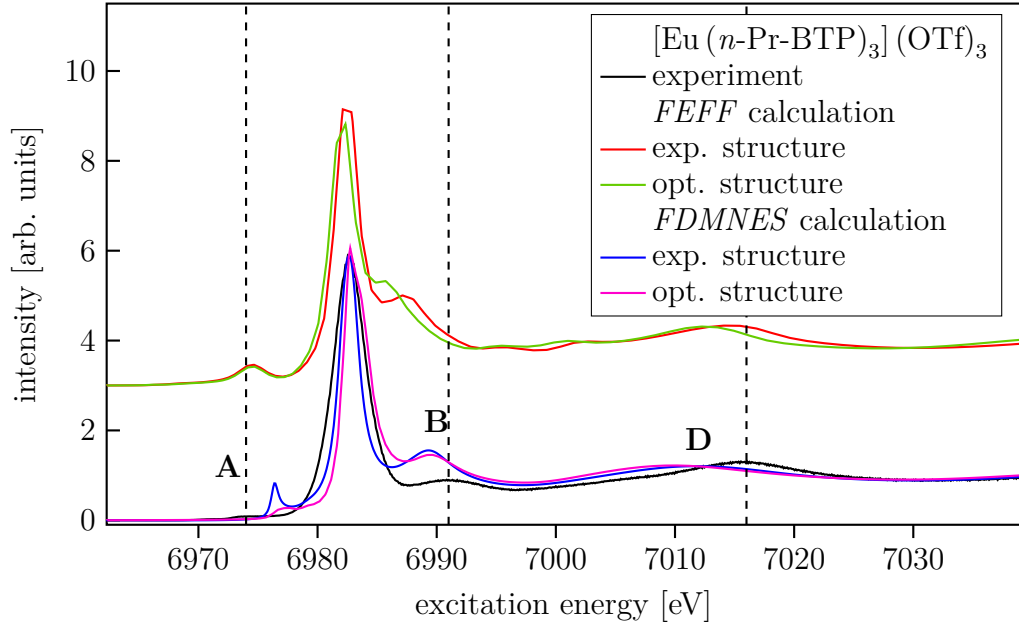
*Ln* L<sub>3</sub> edge XANES spectra of *Ln*(H-BTP)<sub>3</sub> and [Ln(*n*-Pr-BTP)<sub>3</sub>](OTf)<sub>3</sub> have been calculated with different codes and various structural models to find the best agreement between experimental and theoretical spectra. In figure 4.28 the effects of using different codes (*FEFF* and *FDMNES*) and methods (FMS



**Figure 4.28.:** Calculations of  $[\text{Eu}(n\text{-Pr-BTP})_3](\text{OTf})_3$  with  $FEFF$  (red) and  $FDMNES$  with FMS (blue) and FP (green) compared the experimental spectrum (black).

and FP) to calculate a Eu  $L_3$  edge spectrum of  $[\text{Eu}(n\text{-Pr-BTP})_3](\text{OTf})_3$  are shown and compared to experimental data. For a detailed description of the calculations see section 3.4.4.1. The calculated spectra are less broadened than the experimental spectrum to be able to see all features clearly. Therefore, the pre-edge (**A**) and the first post-edge feature (**B**) of the calculated spectra show significantly larger intensity compared to the experimental spectrum. The  $FEFF$  and  $FDMNES$  calculations reproduce well the **A**, **D** ( $FEFF$ ) and **B** ( $FDMNES$ ) features, respectively. Between the  $FDMNES$  FMS and FP calculations there are intensity differences for the **A** and **B** features and a small energy shift for the **D** peak. Since the differences are small and a FP calculation takes significantly longer than a FMS calculation (FMS:  $\sim 1$  h; FP:  $\sim 1$  week), FP calculations will not be applied for the rest of this work.

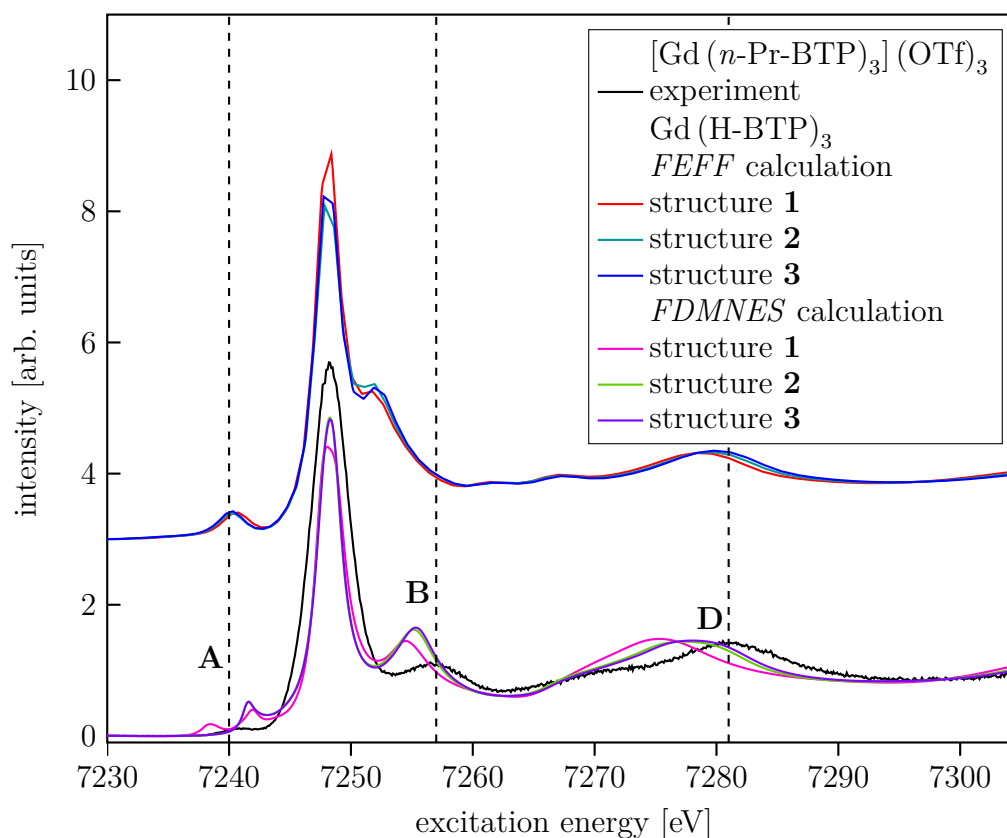
Figure 4.29 depicts the differences in the calculated spectra resulting from different structures used in the calculation. Both  $FEFF$  and  $FDMNES$  calculations were performed for a DFT optimized  $\text{Eu}(\text{H-BTP})_3$  structure. They



**Figure 4.29.:** Calculations of  $[\text{Eu}(n\text{-Pr-BTP})_3](\text{OTf})_3$  with *FEFF* (red) and *FDMNES* with experimental and DFT optimized structures compared the experimental spectrum.

are compared to the *FEFF* and *FDMNES* FMS spectra shown also in figure 4.28 calculated with the experimental crystalline  $[\text{Eu}(n\text{-Pr-BTP})_3](\text{OTf})_3$  structure and the experimental spectrum.

The **B** and **D** absorption resonances are shifted to lower energies for the spectrum calculated with *FEFF* using the DFT optimized structure compared to the spectrum using the experimental structure; the former spectrum has less agreement with the experimental spectrum. This effect is probably due to the  $\sim 5$  pm larger Eu–N bond length in the DFT optimized structure (see table 3.11). There is no effect on the pre-edge. For the *FDMNES* calculations on the other hand, the pre-edge of the spectrum using the experimental structure has larger intensity compared the spectrum using the optimized structure, perhaps due to changes in the electronic density associated with the shorter bond length. **B** and **C** exhibit only small differences, suggesting that *FDMNES* treats multiple scattering effects less accurate than *FEFF*.



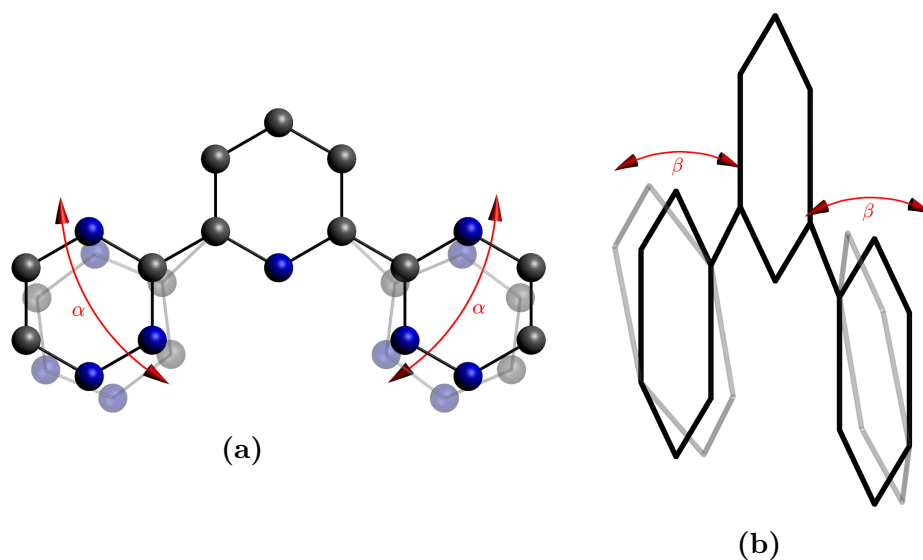
**Figure 4.30.:**  $[Gd(n\text{-Pr-BTP})_3](OTf)_3$  experimental spectrum compared to  $Gd(H\text{-BTP})_3$  spectra calculated with *FEFF* and *FDMNES* for DFT optimized structures with symmetry restrictions (structure **1**), without symmetry restrictions (structure **2**) and without symmetry restrictions and a solvation sphere (structure **3**).

Figure 4.30 shows the spectra of differently optimized  $Gd(H\text{-BTP})_3$  structures calculated with *FEFF* and *FDMNES*. Structures were optimized using DFT with symmetry restrictions (structure **1**), without symmetry restrictions (structure **2**) and without symmetry restrictions and a solvation sphere (structure **3**) (for details see section 3.4.2).  $Gd(H\text{-BTP})_3$  structures were used instead of  $Eu(H\text{-BTP})_3$  structures because a solvated  $Eu(H\text{-BTP})_3$  structure was not available. Geometric differences between the structures are summarized in table 4.1. It can be seen that the average Gd-N bond

**Table 4.1.:** Angles  $\alpha$  and  $\beta$  as shown in figure 4.31 and bond length  $R$  for differently optimized structures. Structures were optimized using DFT with symmetry restrictions (structure **1**), without symmetry restrictions (structure **2**) and without symmetry restrictions and a solvation sphere (structure **3**).

structure	ligand	$\alpha$ [°]		$\beta$ [°]		R[pm]
		left	right	left	right	
1		2.60		1.49		260.7
	1	3.32	3.33	1.73	1.43	
2	2	3.35	3.38	1.58	1.44	258.2
	3	3.33	3.32	1.42	1.48	
	1	3.94	3.99	1.90	2.20	
3	2	3.96	4.03	1.74	2.04	256.5
	3	3.94	3.99	1.98	2.03	

length changes as well as the orientation of the triazine rings with respect to the pyridine ring. In the spectra calculated with *FEFF* a shift to higher energies of **B** and **D** can be observed from structure **1** to structure **3** showing that structure **3** is closest to the real structure. The same effect is visible in the spectra for structures **2** and **3** calculated with *FDMNES*. In the spectrum of structure **1**, however, **B** and **D** are significantly shifted to lower energies and the pre-edge shows a double structure that is not visible in the other spectra. For the spectra compared here, the spectrum of structure **3** has the best agreement with the experimental spectrum indicating that structure **3** is closer to the real structure than the other two. However, it is not used for further investigations in this work because it is currently not available for all *Ln* and *An*. Further improvements can be expected using higher level quantum chemical methods, which are not always applicable for large molecules. Current studies at INE indicate that an averaged structure obtained from snapshots from Molecular Dynamics (MD) simulations can provide reliable structures as well.



**Figure 4.31.:** Angles  $\alpha$  (a) and  $\beta$  (b) describing the in-plane and out-of-plane angles of the triazine rings compared to the pyridine rings.

Figure 4.32 shows *FEFF* shell-by-shell calculations of  $\text{Gd}(\text{H-BTP})_3$  in an initial attempt to correlate the spectral features to specific groups of atoms surrounding the absorbing atom. The spectra of  $\text{Gd}(\text{H-BTP})_3$  with structure **1** were calculated with SCF and FMS radius increasing from 3 Å to 6 Å in 1 Å steps. The spectrum only including the contributions from the first shell, i.e. the bonding N atoms, is nearly featureless because only a few multiple scattering paths are available. Adding the non-bonding neighbors of the bonding N atoms to the calculation as a second shell leads to clearly resolved features **B** and **D**. When adding additional atoms to the calculation, **B** is shifted to lower energies, farther away from the experimental energy position, and **D** is shifted to higher energies, closer to the experimental energy position. These shifts are due to the interference of additional scattering signals and indicate that **B** is mainly influenced by first and second shell atoms while **D** is related to third and fourth shell atoms. The origin of the post-edge features is also discussed in section 4.2.4. The pre-edge **A** also exhibits small changes probably due to changes in the scattering potentials surrounding the Gd.

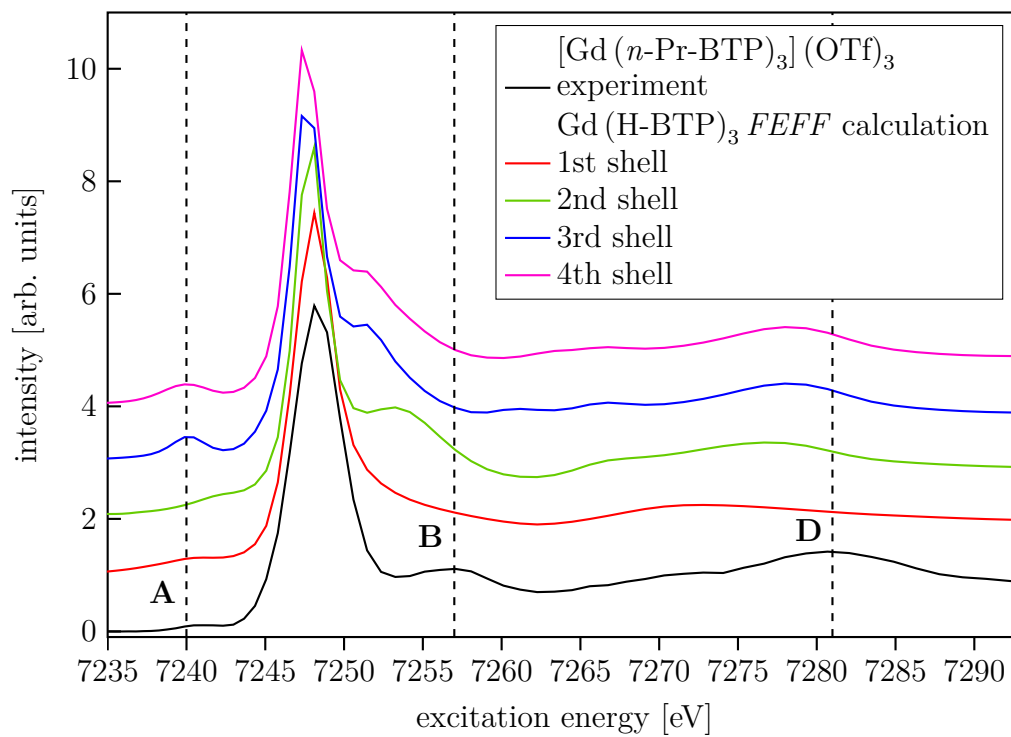


**Figure 4.32.:** *FEFF* shell-by-shell calculations of  $\text{Gd}(\text{H-BTP})_3$  compared with an experimental  $[\text{Gd}(n\text{-Pr-BTP})_3](\text{OTf})_3$  spectrum.

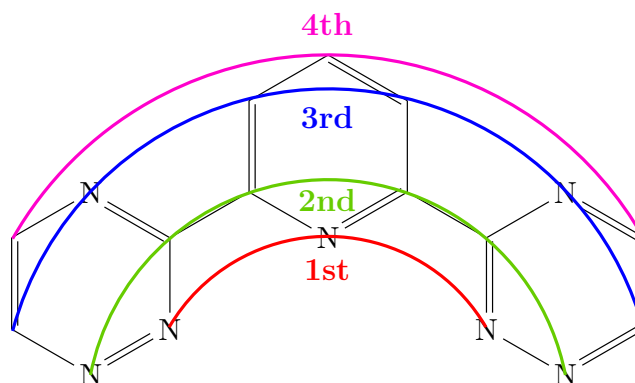


**Figure 4.33.:** The four shells used in the shell-by-shell calculations in figure 4.32.

### 4.2.3. Comparison between Gd $L_3$ edge HR-XANES of $[\text{Gd}(n\text{-Pr-BTP})_3](\text{NO}_3/\text{OTf})_3$ and $\text{Gd}(\text{NO}_3/\text{OTf})_3$

In this section the differences between  $Ln$   $L_3$  edge HR-XANES spectra of  $[\text{Ln}(n\text{-Pr-BTP})_3](\text{NO}_3/\text{OTf})_3$  and  $\text{Ln}(\text{NO}_3/\text{OTf})_3$  are described by using as an example the  $[\text{Gd}(n\text{-Pr-BTP})_3](\text{NO}_3/\text{OTf})_3$  and  $\text{Gd}(\text{NO}_3/\text{OTf})_3$  compounds. The origin of the pre-edge is explained with the help of *FEFF* and *FDMNES* quantum chemical calculations of the Gd  $L_3$  edge HR-XANES for the  $\text{Gd}(\text{H-BTP})_3$  compound.

Gd  $L_3$  edge HR-XANES spectra of  $[\text{Gd}(n\text{-Pr-BTP})_3](\text{NO}_3)_3$  and  $\text{Gd}(\text{NO}_3)_3$  are shown in figure 4.34a. The  $[\text{Gd}(n\text{-Pr-BTP})_3](\text{NO}_3)_3$  spectrum is shifted 0.4 eV to lower energies compared to the  $\text{Gd}(\text{NO}_3)_3$  spectrum indicating higher electronic density on the cation in the  $[\text{Gd}(n\text{-Pr-BTP})_3](\text{NO}_3)_3$  complex. This trend is preserved if  $\text{NO}_3^-$  is exchanged with an  $\text{OTf}^-$  anion. The

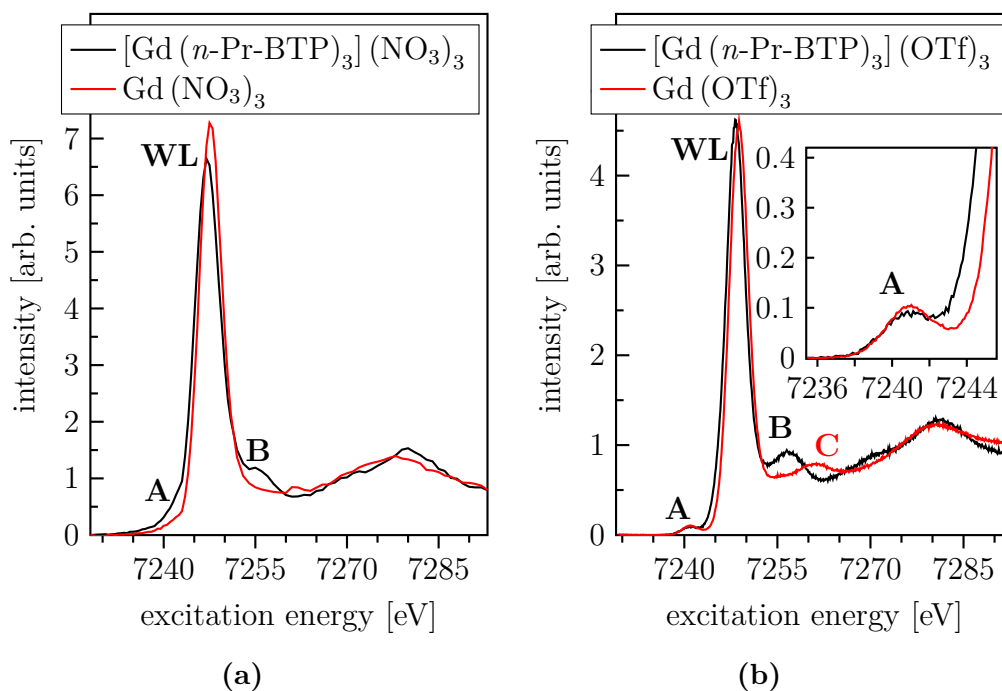


**Figure 4.34.:** Gd  $L_3$  edge HR-XANES of  $[\text{Gd}(n\text{-Pr-BTP})_3](\text{NO}_3)_3$  and  $\text{Gd}(\text{NO}_3)_3$  (a) and  $[\text{Gd}(n\text{-Pr-BTP})_3](\text{OTf})_3$  and  $\text{Gd}(\text{OTf})_3$  (b).

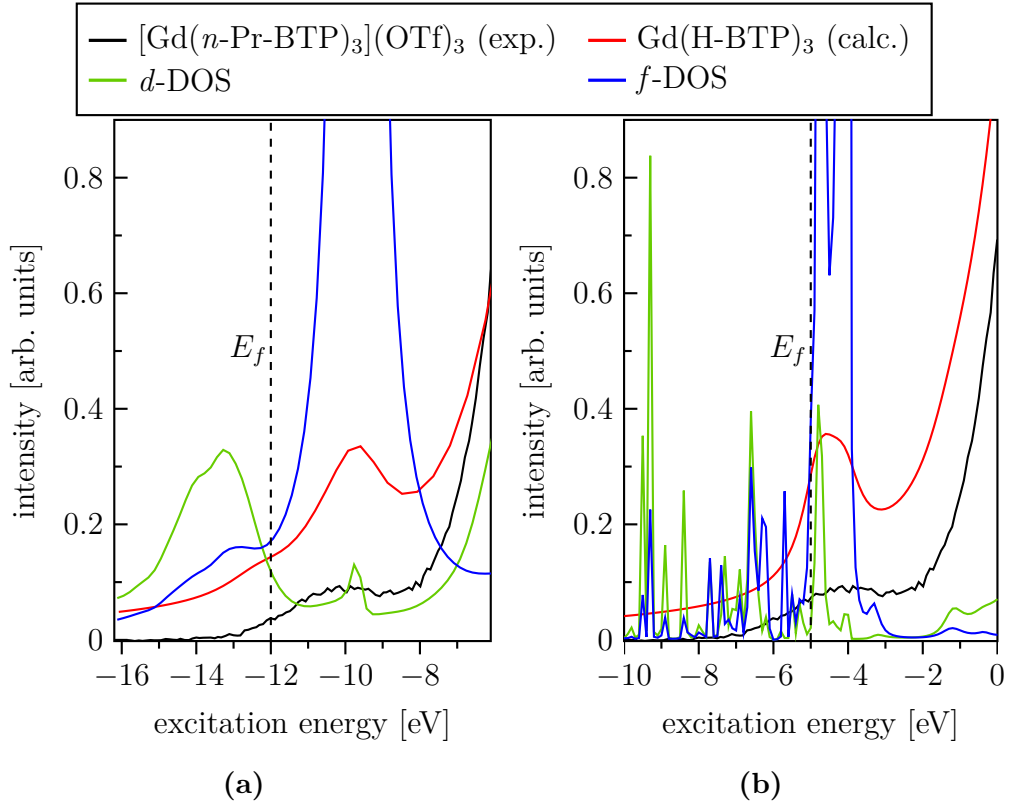


**Figure 4.35.:** Pre-edge calculated with *FEFF9.5* (a) and *FDMNES* (b) for  $\text{Gd}(\text{H-BTP})_3$ , including Gd  $f$ -,  $d$ -DOS compared to experimental spectra of  $[\text{Gd}(n\text{-Pr-BTP})_3](\text{OTf})_3$ .

$[\text{Gd}(n\text{-Pr-BTP})_3](\text{OTf})_3$  and  $\text{Gd}(\text{OTf})_3$  spectra are plotted in figure 4.34b showing a 0.5 eV energy shift of  $[\text{Gd}(n\text{-Pr-BTP})_3](\text{OTf})_3$  to lower energies. The additional pre-edge intensity at about 7241 eV (marked with **A** in figure 4.34), more noticeable for  $[\text{Gd}(n\text{-Pr-BTP})_3](\text{NO}_3)_3$  compared to  $\text{Gd}(\text{NO}_3)_3$ , can be assigned to  $2p_{3/2}$  photoelectron transitions to  $4f$  and/or  $5d$  final states. The origin of the pre-edge feature is revealed by calculations with the *FEFF9.5* and the *FDMNES* codes. The calculated  $\text{Gd}(\text{H-BTP})_3$  spectrum and the  $f$ - and  $d$ -DOS are plotted in figure 4.35. The  $f$ -DOS has high intensity at the energy position of the pre-edge feature, whereas the  $5d$  states have minor contributions. This result suggests that this feature arises from electronic transitions to orbitals with major  $4f$  and minimal  $5d$

*Ln* participations. Even though the direct bonding partners of Gd change from N in [Gd(*n*-Pr-BTP)<sub>3</sub>](OTf)<sub>3</sub> to O in Gd(OTf)<sub>3</sub>, hardly any difference between the areas of the pre-edges and WLs is detectable, indicating that the relative electronic populations of the Gd 4*f* and 5*d* states are not significantly influenced by bonding with the *n*-Pr-BTP molecule. Nevertheless, the -0.4 eV relative energy shift of the WL for [Gd(*n*-Pr-BTP)<sub>3</sub>](OTf)<sub>3</sub> over Gd(OTf)<sub>3</sub> is a clear indication for better screening of the 2*p* core-hole due to higher electron density on Gd in [Gd(*n*-Pr-BTP)<sub>3</sub>](OTf)<sub>3</sub> than in Gd(OTf)<sub>3</sub>. The post-edge feature **B** is at lower energy in [Gd(*n*-Pr-BTP)<sub>3</sub>](OTf)<sub>3</sub> than the corresponding feature **C** in Gd(OTf)<sub>3</sub>. In figure 4.34a the spectra of [Gd(*n*-Pr-BTP)<sub>3</sub>](NO<sub>3</sub>)<sub>3</sub> and Gd(NO<sub>3</sub>)<sub>3</sub> (for details of sample preparation see section 3.3.1) are compared. The same features and energy shifts are noticeable; they are less pronounced due to the different experimental setup resulting in lower energy resolution for [Gd(*n*-Pr-BTP)<sub>3</sub>](NO<sub>3</sub>)<sub>3</sub> and Gd(NO<sub>3</sub>)<sub>3</sub>. Due to the specific energy resolution of different beamlines/experimental setups and the varying intrinsic broadening of different elements it is not possible to quantitatively compare the areas of the peaks for the different compounds.

#### 4.2.4. Comparison between *Ln* L<sub>3</sub> edge HR-XANES spectra of [Ln(*n*-Pr-BTP)<sub>3</sub>](OTf)<sub>3</sub> and *Ln*(OTf)<sub>3</sub>

*n*-Pr-BTP binds preferentially to *An* over *Ln*. In addition, its bonding affinity exhibits a trend as a function of the *Ln*. In this chapter *Ln* L<sub>3</sub> edge HR-XANES spectra of [Ln(*n*-Pr-BTP)<sub>3</sub>](OTf)<sub>3</sub> and *Ln*(OTf)<sub>3</sub> are compared over a series of *Ln*. The observed experimental trends are correlated to structural differences using EXAFS (*FEFF*) and HR-XANES (*FDMNES*) *ab initio* quantum chemical calculations.

The pre-edge ranges of the [Ln(*n*-Pr-BTP)<sub>3</sub>](OTf)<sub>3</sub> and *Ln*(OTf)<sub>3</sub> HR-XANES spectra are shown in figure 4.36. The spectra are measured for selected *Ln* over the *Ln* series from La to Lu. The Lu spectra have no pre-edge due to their completely filled 4*f* orbitals. For the other *Ln* the spectra of [Ln(*n*-Pr-BTP)<sub>3</sub>](OTf)<sub>3</sub> compared to *Ln*(OTf)<sub>3</sub> exhibit a similar pre-edge structure, indicating that the 4*f* states are not much influenced by different bonding partners. The differences at the beginning of the rising absorption

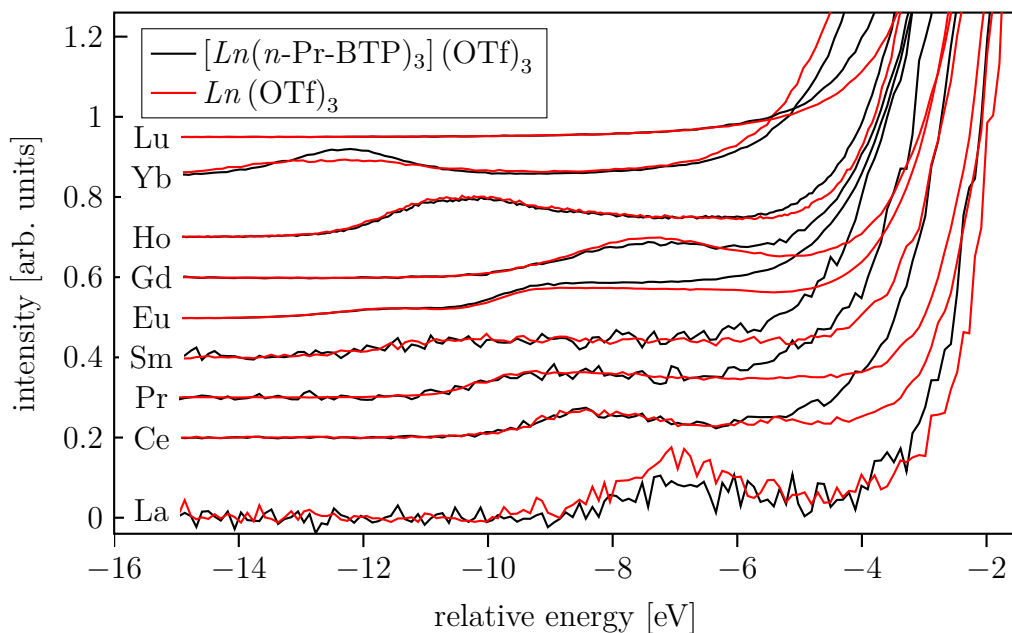


**Figure 4.36.:** Pre-edge region of different  $[Ln(n\text{-Pr-BTP})_3](\text{OTf})_3$  and  $Ln(\text{OTf})_3$  HR-XANES spectra.

edge are due to the energy shift of the WL and indicated higher electronic density on the  $Ln$  in  $[Ln(n\text{-Pr-BTP})_3](\text{OTf})_3$  compared to  $Ln(\text{OTf})_3$  (see also section 4.2.3).

In figure 4.37 trends in the post-edge regions of the  $[Ln(n\text{-Pr-BTP})_3](\text{OTf})_3$  and  $Ln(\text{OTf})_3$  spectra are marked with the help of arrows. Figure 4.38 compares the energy distances between the maxima of the **B**, **C** or **D**<sub>2</sub> absorption resonances and the WL. The energy positions of these features were determined by allocating the local maxima in the spectra using the OriginPro9.1 [234] Peak Analyzer function [235]. The low intensity of **D**<sub>1</sub> hindered consistent identification of its energy position therefore this spectral feature is not further discussed. At low  $Z$  the energy position of the **C** feature (figure 4.38a) of  $Ln(\text{OTf})_3$  follows the  $Ln$  contraction [236, 237], while at higher  $Z$  **C** deviates from this trend due to steric crowding around the smaller cations [154, 238], i.e. even though the cation radius becomes smaller, the metal-ligand bond length does not shorten as this would lead to repulsion of the ligands. The corresponding feature **B** of  $[Ln(n\text{-Pr-BTP})_3](\text{OTf})_3$  however,

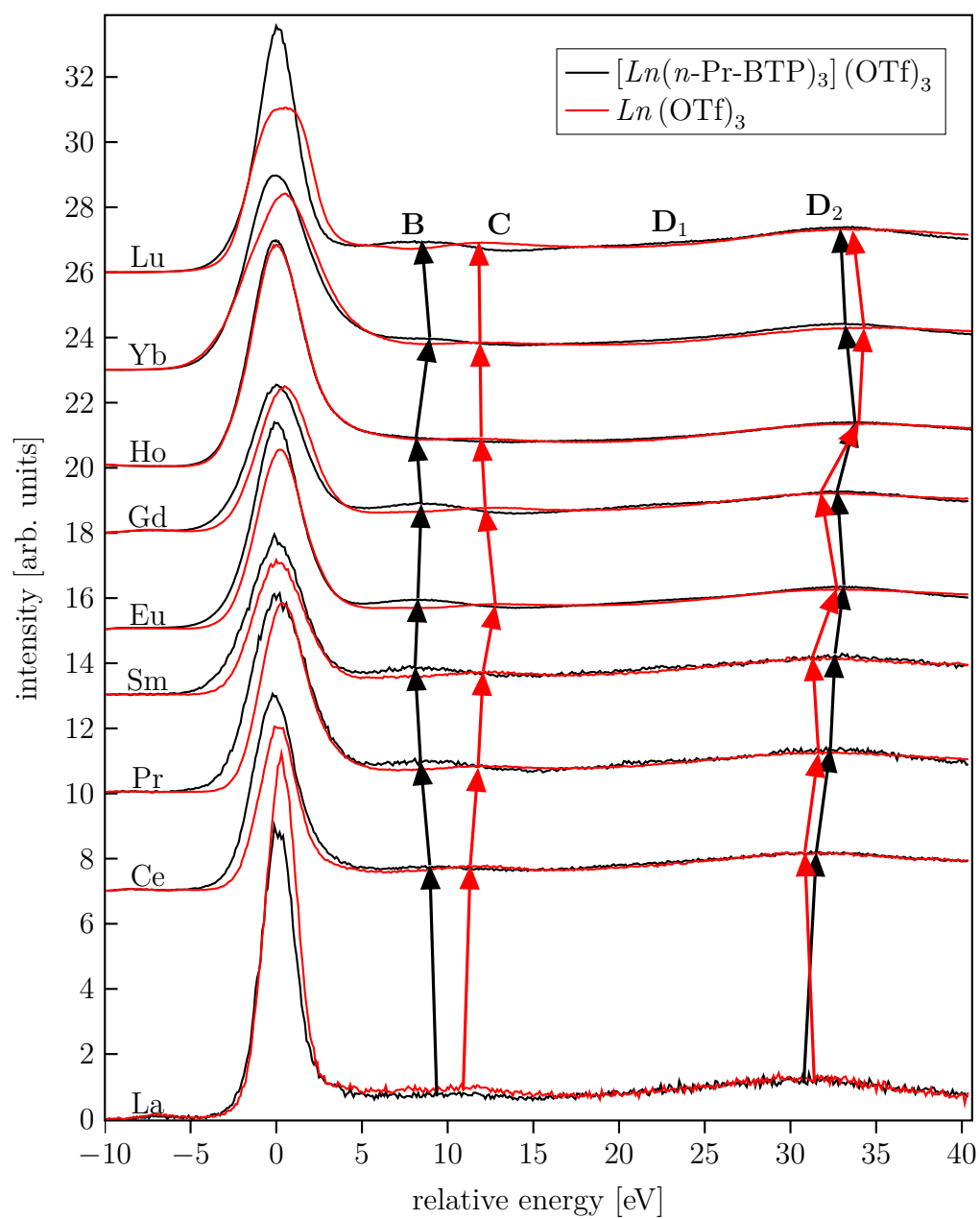


**Figure 4.37.:** Post-edge region of  $[Ln(n\text{-Pr-BTP})_3](\text{OTf})_3$  and  $Ln(\text{OTf})_3$  HR-XANES spectra.

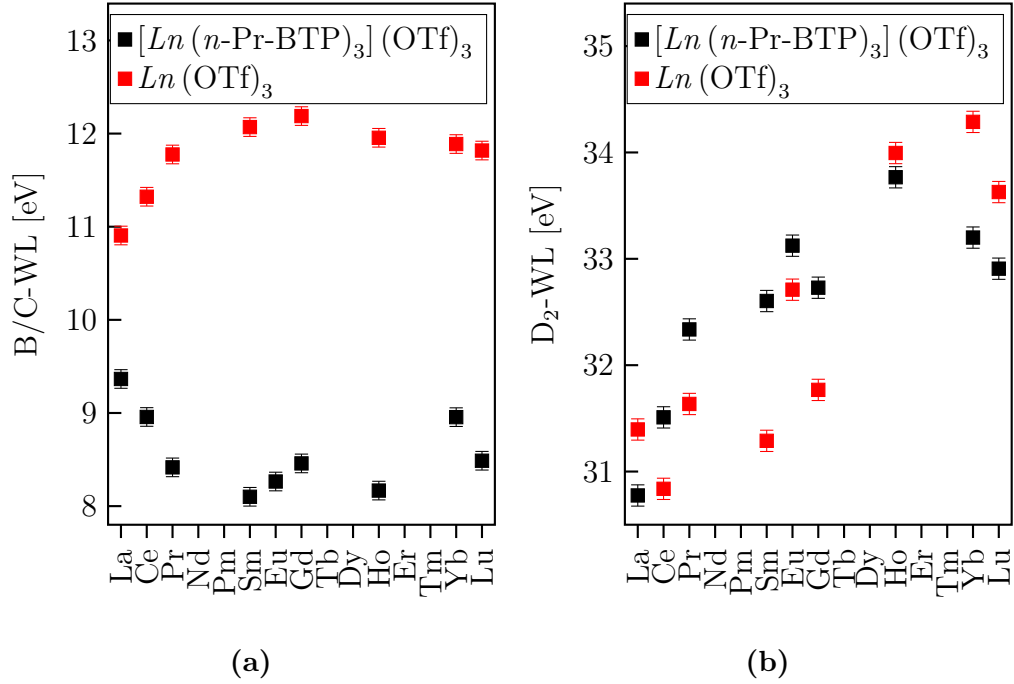


**Figure 4.38.:** Distance between **B** (**C**) and WL for  $[Ln(n\text{-Pr-BTP})_3](\text{OTf})_3$  and  $Ln(\text{OTf})_3$ , respectively (a) and distance between **D**<sub>2</sub> and WL for  $[Ln(n\text{-Pr-BTP})_3](\text{OTf})_3$  and  $Ln(\text{OTf})_3$  (b).

shows a trend in the opposite direction, i.e. the peak shifts to lower energies towards low  $Z$  numbers and slightly shifts to higher energies again with increasing  $Z$ . Feature **D**<sub>2</sub> for both  $[Ln(n\text{-Pr-BTP})_3](\text{OTf})_3$  and  $Ln(\text{OTf})_3$  (figure 4.38b) shifts to higher energies with increasing  $Z$ . **D**<sub>1</sub> is a shoulder of **D**<sub>2</sub> that is not well resolved experimentally but clearly visible in calculations.

#### 4.2.4.1. EXAFS calculations with the FEFF code

If the distance  $R$  between absorbing and scattering atom is  $R = n\lambda_e$ , where  $n$  is an integer and  $\lambda_e$  is the electron wavelength, the outgoing and scattered waves have constructive interference resulting in the appearance of an absorption resonance in the spectrum [116]. When wavelength is transformed to

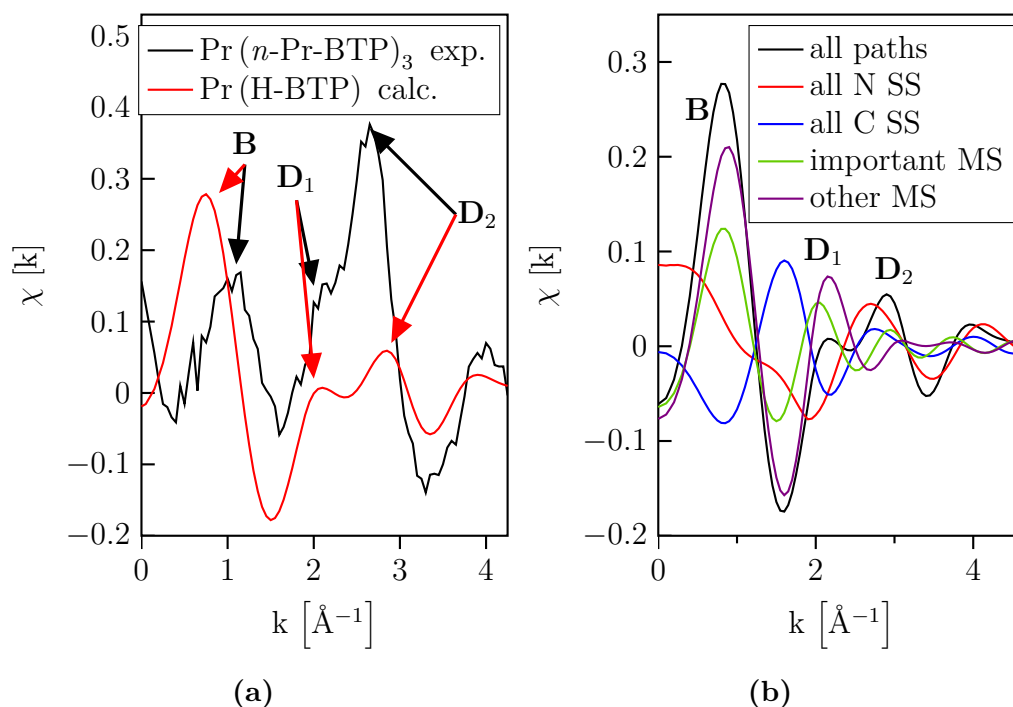


**Figure 4.39.:** Peak assignment in experimental  $[\text{Pr}(n\text{-Pr-BTP})_3](\text{OTf})_3$  and calculated  $\text{Pr}(\text{H-BTP})$  spectra (a) and the contribution of different types of single scattering (SS) and multiple scattering (MS) paths to the spectrum of  $\text{Pr}(\text{H-BTP})$ (b).

wavenumber ( $\lambda_e = 2\pi/k$  ( $e$ )) it follows that  $R = 2n\pi/k$ . According to equation (2.6),  $k \propto$  excitation energy ( $E$ ), therefore  $R \propto 1/E$ . Applied to the spectra here, the shift of **D<sub>2</sub>** to higher energies (see figure 4.38b) is correlated to a decrease in bond length, which in this case follows the lanthanide contraction [236, 237] for both compounds. EXAFS calculations with the *FEFF9.6* code (see section 3.4.4.4) using DFT-optimized structures as input (see section 3.4.2) assist in understanding the origin of features **B** and **C**. The transformation of the experimental spectra to  $\chi(k)$  functions (see section 2.1) allows to assign calculated to experimental absorption resonances as it is shown in figure 4.39a for the experimental  $[\text{Pr}(n\text{-Pr-BTP})_3](\text{OTf})_3$  and calculated  $\text{Pr}(\text{H-BTP})$  spectra. All EXAFS calculations were done for  $Ln$  bound to only one H-BTP ligand ( $Ln(\text{H-BTP})$ ) to avoid broadening due to scattering

paths with slightly different length and to simplify the investigation of the contributions of different paths to the spectrum. Differences in  $k$  positions and intensities of the peaks is due to differences between optimized and real structure, but can be also caused by the theoretical approximations made in the code. For example, the amplitudes in the theoretical spectrum are not affected by atomic disorder effects, which were not considered in the simulation. In figure 4.39b, the contributions of different types of scattering paths to the spectrum and the sum of all paths are shown. Feature **B** is best described by multiple scattering paths. The multiple scattering paths with the angle between scattering and backscattering close to  $180^\circ$  have higher amplitudes when considered individually, but their sum has less weight in the spectrum than the sum of the other multiple scattering paths, because they are not as common. The sum of all  $N$  single scattering paths has a small contribution to **B**. The single scattering paths associated with scattering from C atoms have a negative contribution that however still influences the position of the peak maximum. Detailed analysis of the paths manifests that the intensity of **B** is mainly influenced by single scattering events of the photoelectron from the bonding N atoms and multiple scattering involving the bonding N and their direct neighbors. The paths contributing to **B** are shown in appendix B.

For peak **C** of  $Ln(\text{OTf})_3$  the contributions originate mainly from single scattering paths involving the neighboring atoms in the first coordination sphere (figure 4.40a). Peak **D**<sub>1</sub> consists of multiple scattering and **D**<sub>2</sub> of single scattering paths. For  $Ln(\text{H-BTP})$  the **D**<sub>1</sub> and **D**<sub>2</sub> peaks are not well separated due to contributions from the high number of overlapping scattering paths; it is evident that there is also more multiple scattering contribution to **D**<sub>1</sub> than to **D**<sub>2</sub>.

The experimental trend for the energy positions of the spectral features of the  $[Ln(n\text{-Pr-BTP})_3](\text{OTf})_3$  spectra as a function of the Ln Z numbers is not reproduced by the EXAFS calculations (figure 4.40b). This discrepancy was investigated by varying the  $Ln$  for one structure or varying the structures for La. In figure 4.41 the trends for **B** and **D**<sub>2</sub> for EXAFS calculations with the fully optimized structures (black, system **1**), the optimized La(H-BTP) structure with La replaced by different  $Lns$  (red, system **2**) and the optimized  $Ln(\text{H-BTP})$  structures with the  $Ln$  replaced by La (blue, system **3**) are shown. For **B** (figure 4.41a) the trend for system **2** shows a parabolic shape similar

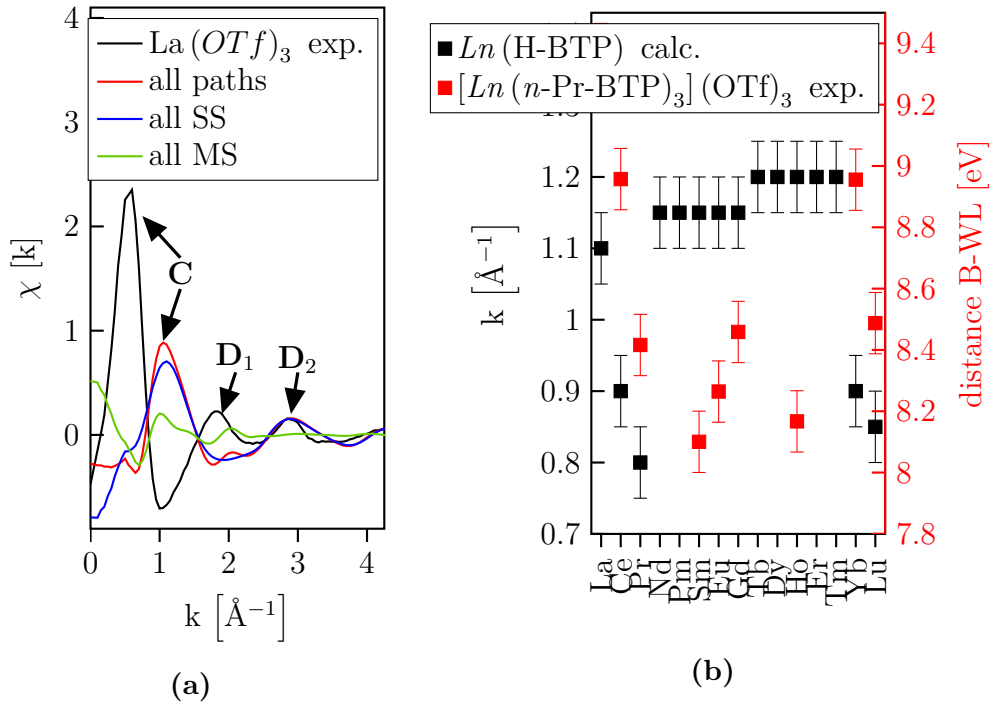


**Figure 4.40.:** The contribution of single scattering (SS) and multiple scattering (MS) paths to the spectrum of  $\text{La}(\text{OTf})_3$ (a) and position of **B** in calculated and experimental spectra (b).

to the trend for system **1**, while the trend for system **3** exhibits a linear trend to higher energies. A linear trend is also present for **D**<sub>2</sub>, which fits well the trend for system **1** and also the experimental trend. The trend for system **2** again exhibits a parabolic shape, but with the center shifted to lower  $Z$ . These results indicate that for **B** the variations of scattering properties of the  $Ln$  atoms dominate the calculation, while the energy position of **D**<sub>2</sub> is ruled by structural differences.

The change in importance from scattering properties to geometric structure can be explained by the difference between the phase-shift  $\phi(k)$  and  $2kR$ .  $k$  is the photoelectron wavenumber and  $R$  is the length of the scattering path.  $\phi(k)$  the phase shift depending on the  $Z$  number of the atoms participating in the scattering process and arises from the potential of the absorbing and scattering atoms.  $\phi(k)$  and  $2kR$  are calculated by *FEFF* for each scattering

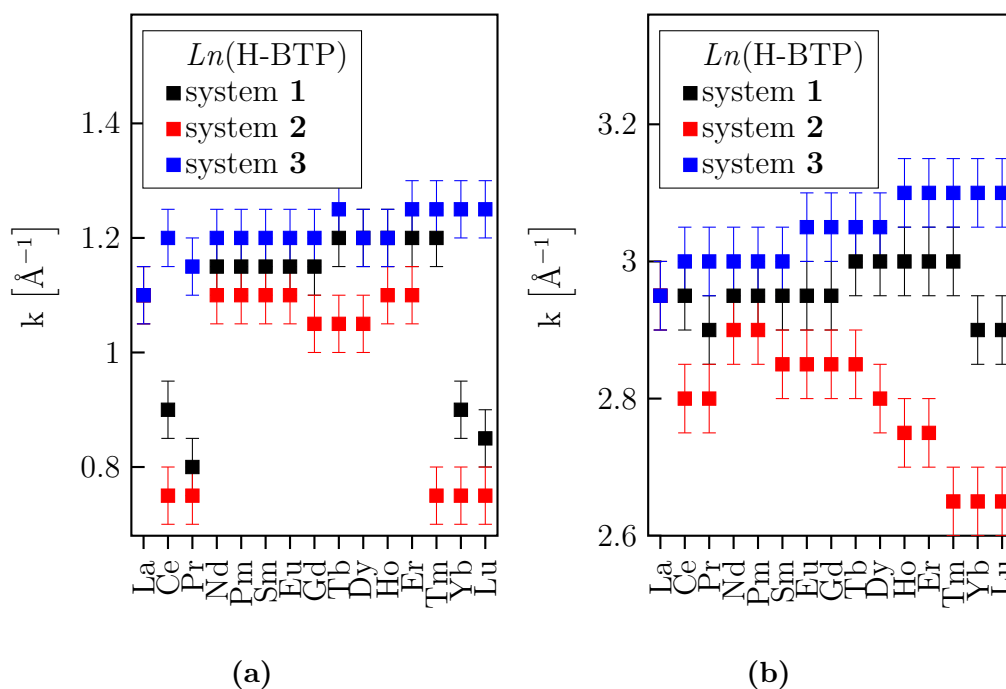


**Figure 4.41.:** FEFF calculated positions of **B** (a) and **D<sub>2</sub>** (b) in  $k$  for  $Ln(\text{H-BTP})$  with different  $Ln$ /different structures (black, system 1), different  $Ln/\text{La}(\text{H-BTP})$  structure (red, system 2) and  $\text{La}/$ different structures (blue, system 3).

path. The  $A(k)$  ( $\phi(k) - 2kR$ ) function averaged over all paths for several  $Ln(\text{H-BTP})$  compounds is shown in figure 4.42.  $\phi(k)$  and  $2kR$  have very similar values at  $k = 0$ , but the difference increases with increasing  $k$  as  $2kR$  grows faster than  $\phi(k)$ . In the EXAFS equation  $\phi(k)$  and  $R$  contribute as  $\sin(\phi(k) + 2kR)$ ; their value is responsible for the energy shift of the absorption resonances. For  $Ln(\text{OTf})_3$  all three systems exhibit a linear trend as shown in figures 4.43a and 4.43b. The energy position of feature **C** for the optimized structures (system 1) is clearly governed by structural changes, while for **D<sub>2</sub>** the three systems exhibit similar behavior as it is discussed above for  $Ln(\text{H-BTP})_3$ .

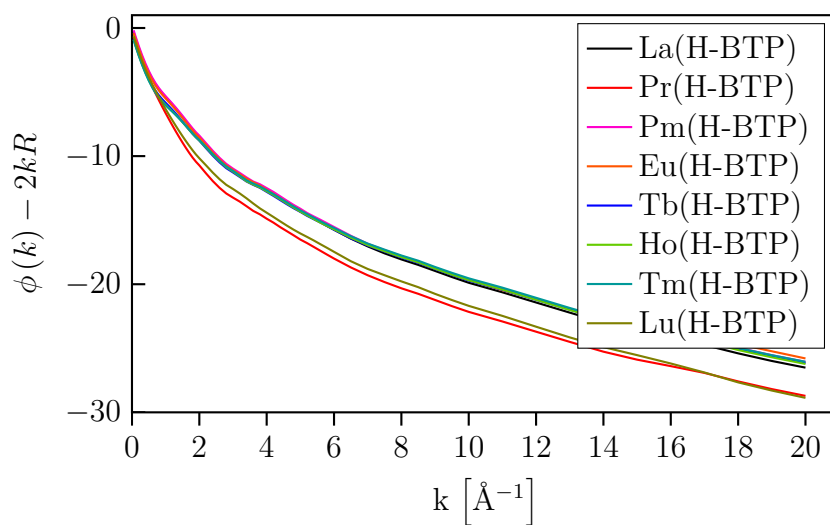


**Figure 4.42.:** Difference between the phase  $\phi(k)$  and the scattering path length  $R$  contributions to the EXAFS equation.

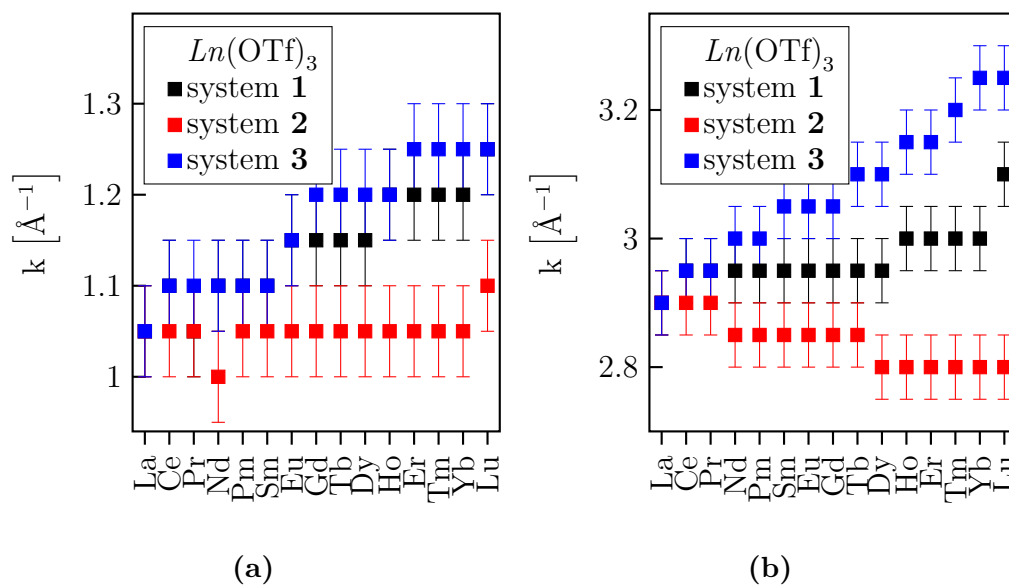


**Figure 4.43.:** Positions of **C** (a) and **D<sub>2</sub>** (b) in  $k$  for  $Ln(OTf)_3$  with different  $Ln$ /different structures (black, system 1), different  $Ln/La(OTf)_3$  structure (red, system 2) and  $La$ /different structures (blue, system 3) calculated with *FEFF*.

#### 4.2.4.2. XANES calculations with the *FDMNES* code

For the *FDMNES* XANES calculations (see section 3.4.4.5) an overall similar behavior can be observed (see section 4.2.4.2). Discontinuities in the spectral trends, which are most pronounced in the WL are due to the change from  $5d^1 4f^n$  (Dy) to  $5d^2 4f^n$  (Ho) electronic configuration implemented in the *FDMNES* code; therefore trends will only be discussed up to Dy. The trends for **B** (figure 4.45a) exhibit less variations compared to the *FEFF* EXAFS calculation. For all systems they show a parabolic shape with only small differences in slope. The trends for **D**<sub>2</sub> (figure 4.45b) are similar to the *FEFF* EXAFS calculation, but the differences between the three systems are much more pronounced. The linear trend for system **3** confirms the importance of structural differences for the **D** peaks found by the *FEFF* calculations. The *FDMNES* calculations of  $Ln(OTf)_3$  in figure 4.46 show similar but more distinct trends as the corresponding EXAFS calculations. The trend for feature **C** (figure 4.46a) for the calculations of system **1** is also governed by structural differences, but is closest of all calculations to the experimental trend (see figure 4.38), i.e. an increasing distance to the WL in the beginning of the  $Ln$  series (up to Nd) followed by decreasing distance with a much

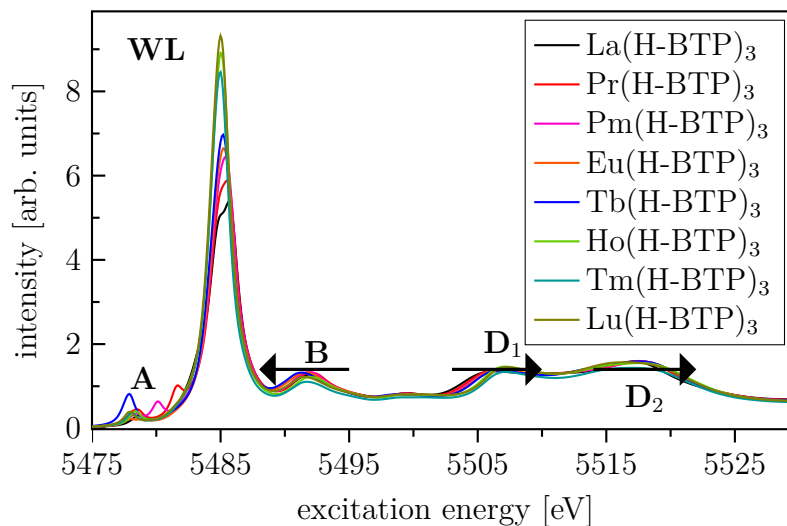


**Figure 4.44.:** *FDMNES* XANES calculations of different  $Ln(H-BTP)_3$  complexes with optimized structures.

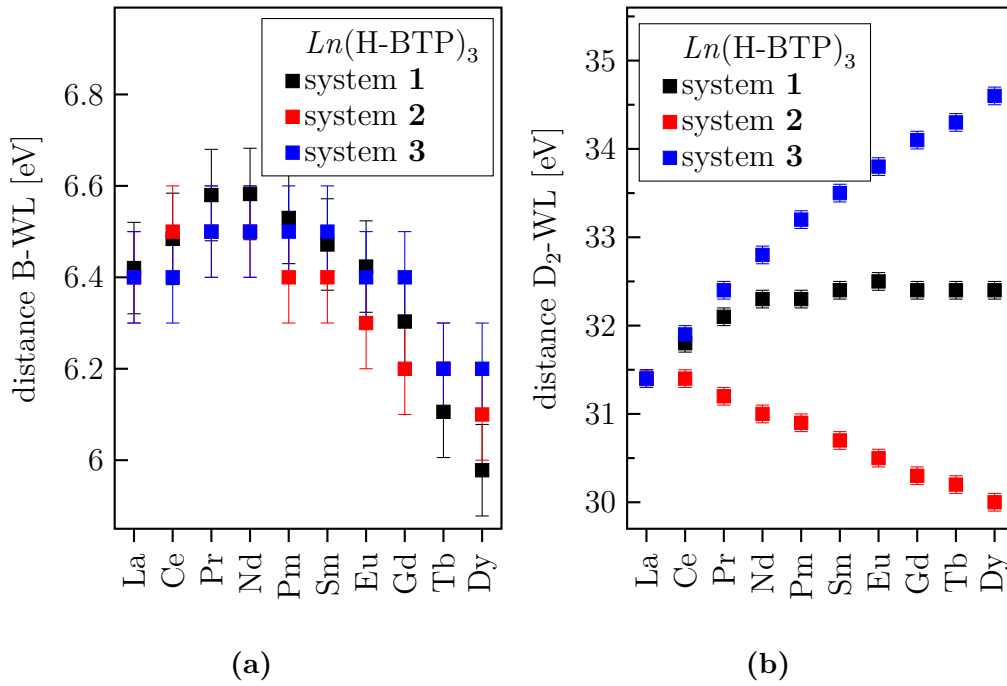


**Figure 4.45.:** *FDMNES* calculated positions of **B** (a) and **D<sub>2</sub>** (b) for  $Ln(H-BTP)_3$  with different  $Ln$ /different structures (black, system 1), different  $Ln/La(H-BTP)_3$  structure (red, system 2) and  $La$ /different structures (blue, system 3).

smaller slope. Feature **D<sub>2</sub>** (figure 4.46b) has trends similar to the *FEFF* EXAFS calculations of system 3 and is closest to the experimental data.

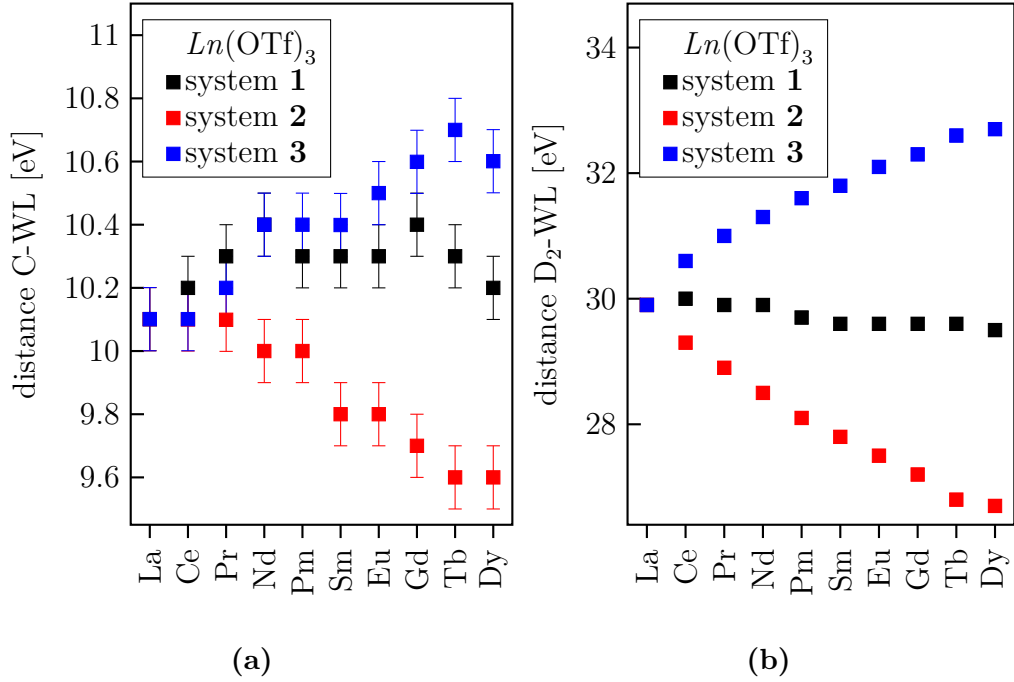


**Figure 4.46.:** Positions of **C** (a) and **D<sub>2</sub>** (b) in k for  $Ln(OTf)_3$  with different  $Ln$ /different structures (black, system 1), different  $Ln/La(OTf)_3$  structure (red, system 2) and  $La$ /different structures (blue, system 3) calculated with *FDMNES*.

#### 4.2.5. Comparison between $An$ L<sub>3</sub> edge HR-XANES of $[An(n-Pr-BTP)_3](NO_3)_3$ and $An(NO_3)_3$

$[Pu/Am(n-Pr-BTP)_3](NO_3)_3$  and  $Pu/Am(NO_3)_3$  samples have been investigated for the first time using  $Pu/Am$  L<sub>3</sub> edge HR-XANES. The measurements were performed with the MAC spectrometer that was designed and commissioned as part of this dissertation (see also section 2.4). In figure 4.47 the  $Pu$  L<sub>3</sub> edge HR-XANES spectra of  $Pu(NO_3)_3$  and  $[Pu(n-Pr-BTP)_3](NO_3)_3$  exhibit **A** and **B** features that are not resolved in conventional measurements. These spectral features are also characteristic for L<sub>3</sub> edge HR-XANES spectra of isostructural lanthanide complexes reported previously ([239], section 4.2). The **A** and **B** resonances and the WL in the  $Pu$  HR-XANES are less energy resolved due to the higher core-hole lifetime broadening contribution for  $An$

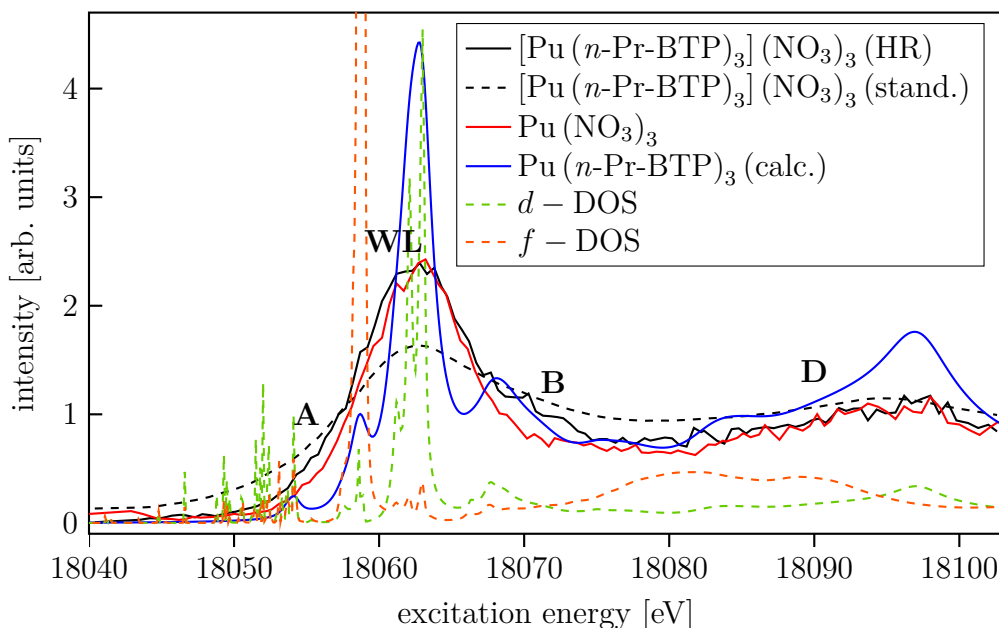


**Figure 4.47.:** Pu  $L_3$  edge HR-XANES of  $[\text{Pu}(n\text{-Pr-BTP})_3](\text{NO}_3)_3$  and  $\text{Pu}(\text{NO}_3)_3$ ; Pu  $L_3$  edge XANES of  $[\text{Pu}(n\text{-Pr-BTP})_3](\text{NO}_3)_3$ ; *FDMNES* calculations of  $\text{Pu}(\text{H-BTP})_3$  XANES and DOS.

(3.3 to 4 eV) compared to  $Ln$  (0.8 to 1.6 eV). The WL is broader in the  $[\text{Pu}(n\text{-Pr-BTP})_3](\text{NO}_3)_3$  spectrum compared to the  $\text{Pu}(\text{NO}_3)_3$  spectrum. In addition, feature **B** is visible only in the  $[\text{Pu}(n\text{-Pr-BTP})_3](\text{NO}_3)_3$  spectrum. Calculation with the *FDMNES* code [168] confirm the presence of pre-edge feature **A** arising from excitations to a mixture of  $d$  and  $f$  states. In figure 4.48, features **A** and **B** are not resolved in the Am  $L_3$  edge HR-XANES  $\text{Am}(\text{NO}_3)_3$  and  $[\text{Am}(n\text{-Pr-BTP})_3](\text{NO}_3)_3$  spectra due to the higher core-hole lifetime (Am: 3.87 eV; Pu: 3.74 eV) and experimental broadening (Am: 3.88 eV; Pu: 4.14 eV) for Am compared to Pu. The WL is broader in the  $[\text{Am}(n\text{-Pr-BTP})_3](\text{NO}_3)_3$  spectrum compared to  $\text{Am}(\text{NO}_3)_3$ . For both Pu and Am the spectra have similar feature **D**  $\sim 35$  eV above the WL and the spectra of the complexes are shifted to lower energies ( $< 0.5$  eV). This indicates a better screening of the  $2p$  core-hole due to higher charge density on the metal in  $[\text{Pu}/\text{Am}(n\text{-Pr-BTP})_3](\text{NO}_3)_3$  than in  $\text{Pu}/\text{Am}(\text{NO}_3)_3$  similar to the results for the  $Ln$  compounds. The direct comparison of experimental

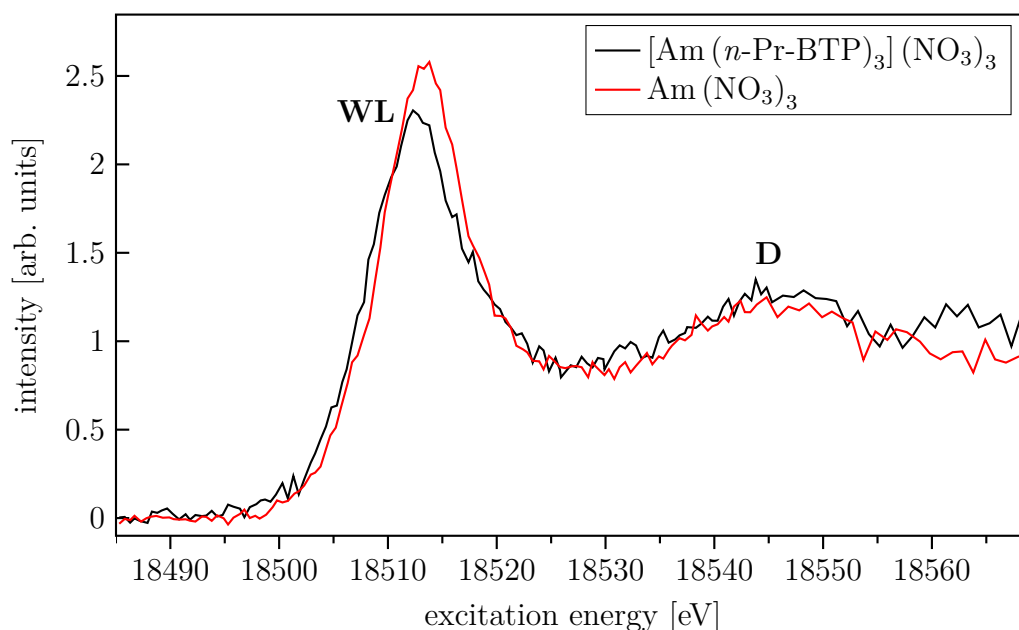


**Figure 4.48.:** Am  $L_3$  edge HR-XANES of  $[\text{Am}(n\text{-Pr-BTP})_3](\text{NO}_3)_3$  and  $\text{Am}(\text{NO}_3)_3$ .

$[\text{Pu}(n\text{-Pr-BTP})_3](\text{NO}_3)_3$  and  $[\text{Am}(n\text{-Pr-BTP})_3](\text{NO}_3)_3$  spectra (figure 4.49a) shows the slightly broader WL of  $[\text{Am}(n\text{-Pr-BTP})_3](\text{NO}_3)_3$ . Feature **D** has different intensity in both spectra due to problematic normalization. In addition, the low signal-to-noise ratio in this range prevents the detection of the expected small variations. The spectra of  $\text{Pu}(\text{H-BTP})_3$  and  $\text{Am}(\text{H-BTP})_3$  calculated with *FDMNES* (figure 4.49b) show differences in the pre-edge (**A**) due to the changing occupation of the  $5f$  orbitals ( $5f^3$  for Pu and  $5f^4$  for Am) Feature **D** in  $\text{Am}(\text{H-BTP})_3$  is shifted to higher energies due to the shorter  $An\text{-N}$  bond length in  $\text{Am}(\text{H-BTP})_3$  compared to  $\text{Pu}(\text{H-BTP})_3$ . Both these effects are not resolved experimentally.

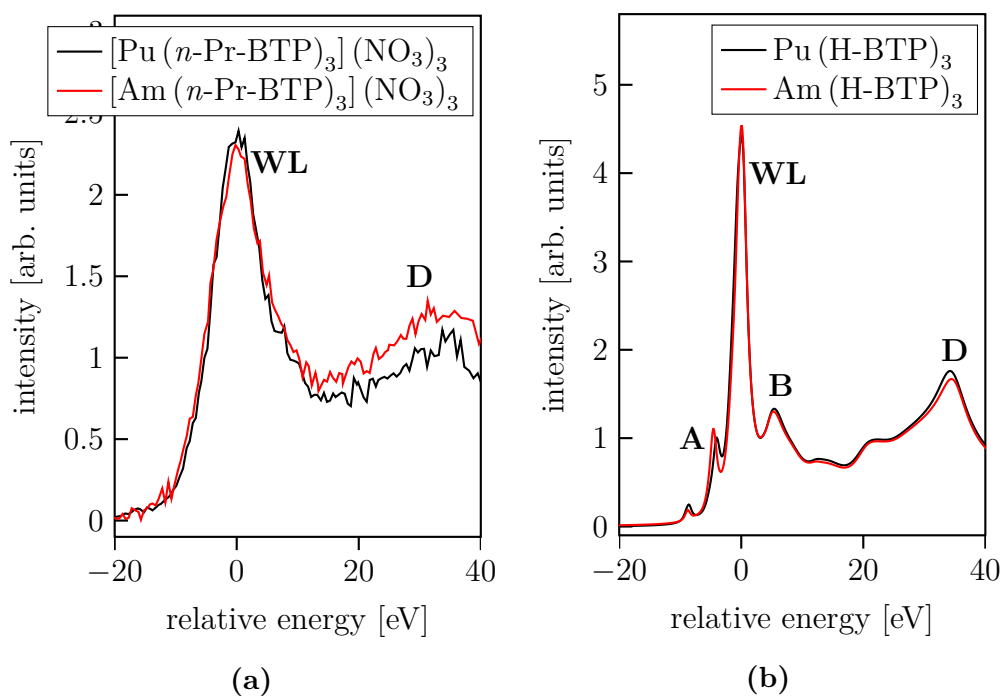


**Figure 4.49.:** Experimental spectra of  $[\text{Pu}(n\text{-Pr-BTP})_3](\text{NO}_3)_3$  and  $[\text{Am}(n\text{-Pr-BTP})_3](\text{NO}_3)_3$  (a) and spectra calculated with *FDMNES* of  $\text{Pu}(\text{H-BTP})_3$  and  $\text{Am}(\text{H-BTP})_3$  (b).

#### 4.2.6. Conclusions

The performed investigations reveal that the energy positions of feature **B** in the  $Ln$   $L_3$  edge HR-XANES spectra of the  $Ln(\text{H-BTP})_3$  compounds are more strongly influenced by the scattering properties/type of the  $Ln$  atoms compared to changes in the structure as a function of the  $Ln$   $Z$  numbers. The discrepancies between experimental and theoretical trends might be due to inaccurate calculations of the  $\phi(k)$  functions (EXAFS) at this low  $k$  value. However, the *FDMNES* code also does not provide any satisfactory agreement between theory and experiment for this feature. The **B** features are in the post-edge region of the spectra, which is traditionally well reproduced by the *FDMNES* code as it is demonstrated for the  $Ln(\text{OTf})_3$  compounds. A likely hypothesis is the existence of discrepancies between the optimized and the real structures. It is found that the energy positions of the **B** features

are influenced by changes in interatomic distances and bonding angles. It is known that DFT overestimates the metal-ligands bond lengths. Structural variations affect the calculated phases and the amplitudes of the single and multiple scattering paths as well as the density of unoccupied states, and thereby the energy positions of the **B** peaks. It is also considered that in addition to bonding distances bonding angles might be not accurately reproduced by the optimization process. This would also lead to variations in the parameters of the multiple scattering paths and thereby the energy positions of features **B**. The agreement of theoretical  $Ln(\text{H-BTP})_3$  with experimental  $[Ln(n\text{-Pr-BTP})_3](\text{OTf})_3$  spectra is improved by using structures optimized at the DFT level without symmetry restrictions, employing hybrid functionals and solvation effects described by a polarizable continuum as, e.g., with the COSMO-RS [156] approach. Structures of series of MD calculated  $Ln/An(\text{H-BTP})_3$  compounds currently under optimization will be applied in the future in following works on this topic.

The two theoretical approaches (*FEFF* EXAFS and *FDMNES* XANES) simulate with good agreement the experimentally observed trends for the energy positions of the **C** and **D** features for the  $Ln(\text{OTf})_3$  complexes. The type of  $Ln$  atoms and variations in bonding angles have less significance compared to changes in the bond lengths. The overestimation of the DFT bond lengths leads to consistent shift of the spectral features for all  $Ln$  but does not influence the trends for their energy positions. Interestingly the steric crowding, which was shown previously for this compounds [154, 238], is confirmed by the trend found in the HR-XANES spectra, which demonstrate the high potential of the technique.

The analyses carried out in this thesis are performed for the first time on  $Ln$  and  $An$   $L_3$  edge HR-XANES spectra of series of  $Ln$  and  $An$  compounds. The  $Ln/An$   $L_3$  edge HR-XANES technique can be also successfully applied to optimize theoretical codes. For example, the detailed analyses performed here strongly suggest that the influence of the type of  $Ln$  on feature **D**<sub>2</sub> is overestimated with both *FEFF* EXAFS and *FDMNES* XANES calculations.

Even though the shift of the WL between  $[An(n\text{-Pr-BTP})_3](\text{NO}_3)_3$  and  $An(\text{NO}_3)_3$  spectra is comparable to the shift between  $[Ln(n\text{-Pr-BTP})_3](\text{OTf})_3$  and  $Ln(\text{OTf})_3$  other details visible in  $Ln$   $L_3$  edge HR-XANES spectra are not resolved in the  $An$   $L_3$  edge HR-XANES spectra. The CAT-ACT Beamline

that is currently being built at ANKA will have higher incident photon flux compared to the INE-Beamline and will allow the use of  $L_{\beta 5}$  emission lines to record  $An$   $L_3$  edge HR-XANES spectra with lower broadening as it has been shown for U [231]. For better comparability with  $[Ln(n\text{-Pr-BTP})_3](\text{OTf})_3$  the  $[An(n\text{-Pr-BTP})_3](\text{NO}_3)_3$  investigations have to be extended including other  $An$ .  $M_{4,5}$  edge HR-XANES investigations, that directly probe the  $5f$  states, could provide further insight into the role of  $5f$  states in the bonding.



## 5 | Summary and Outlook

A MAC spectrometer for high-energy resolution X-ray emission spectroscopy (HRXES) and a liquid cell for NRIXS were designed, built and commissioned within this doctoral project. Both were successfully applied for investigations of sample systems with the aim to help understanding the high bonding affinity of N-donor ligands like *n*-Pr-BTP to *An* compared to *Ln*. This is the first MAC spectrometer worldwide operational in a controlled laboratory. Another focus was laid on the interpretation of the collected spectra with the help of theoretical approaches.

The obtained results demonstrate differences in relative electronic densities and mixing of metal with ligand valence orbitals for the *n*-Pr-BTP ligand, the  $[Ln(n\text{-Pr-BTP})_3](\text{OTf})_3$  and  $[An(n\text{-Pr-BTP})_3](\text{OTf})_3$  complexes using N K edge XANES spectroscopy and quantum chemical methods. TD-DFT calculations reveal a different transition order for H-BTP and  $Ln/An(\text{H-BTP})_3$ . This is correlated with the shift of the *n*-Pr-BTP spectrum to lower energies compared to the  $[Ln/An(n\text{-Pr-BTP})_3](\text{OTf})_3$  spectra and indicates less electron density on the N atoms in the complexes. The electronic charge is likely transferred to the *An* and *Ln* metals, respectively. Similar to previous reports [51–56, 81, 82, 84, 85] the calculations provide indications for stronger covalent bonding for the  $An(\text{H-BTP})_3$  complexes due to higher electronic charge density between the metal and the ligand as well as stronger mixing of *An* 5*f* compared to *Ln* 4*f* with ligand valence orbitals .

The experimental trend in the pre-edge structure is anti-correlated to the extraction behavior for a series of *Ln*, i.e. a smaller distance between the main peak and its shoulder indicates higher bonding affinity. TD-DFT also demonstrates that the N K-edge XANES pre-edge region is sensitive to the level of mixing of 4*f* *Ln* but not of 5*f* *An* with ligand valence orbitals.

Significantly more detailed electronic structure information can be obtained from the experimental spectrum if the ligand has well separated energy

positions of the  $\pi^*$  resonances for the different N atoms. For example, the change in transition order was only possible to confirm by performing quantum chemical calculations. The comparison of experimental spectra for ligands similar to *n*-Pr-BTP with variable extraction properties confirms the correctness of the assignments of N atoms to spectral features carried out with the help of theory. Further comparative investigations of the *An* and *Ln* complexes for ligands with small variations in the structure but large differences in extracting properties might help to gain additional insights into the relation between electronic structure and extraction behavior of the ligands. The obtained results allow to propose the N K-edge XANES as a direct tool for measurements of relative amounts of electronic charge transferred from the bonding N atoms to *An* and *Ln* in their respective complexes. The difference in the transferred charge might be a measure of the selectivity of the ligand. The method needs to be validated by studying series of *Ln* and *An* complexes using ligands with well separated  $\pi^*$  peaks (e.g., C5-BPP) facilitating their detailed analyses.

The benchmark NRIXS studies demonstrate the applicability of this novel technique for investigations of liquid samples of partitioning systems at the N K edge and at K absorption edges of other low *Z* elements. No significant differences between the N K-edge spectrum for the *n*-Pr-BTP molecule in solid phase or solved in isopropanol are found. This result strongly suggests that the results obtained for the solid state complexes and ligands are relevant also for their liquid forms. Specific practical suggestions for further improvement of the experimental set-up are given based on experience gained over several experiments using the state of the art spectrometers installed at the brightest synchrotrons. It is shown that N K edge NRIXS investigations of N-donor ligands in solution are in general possible at the ID20-Beamline, ESRF. However, the sample setup has to be further improved by using a capillary to allow high signal to noise ratio; temperature controlled cooling of the sample will reduce the evaporation of the solvent and possible radiation damage.

The *Ln/An*  $L_3$  edge HR-XANES technique applied here for the first time for series of lanthanide and actinide complexes reveals higher charge density on the metal *Ln/An* atoms for the  $[Ln/An(n\text{-Pr-BTP})_3](\text{OTf}/\text{NO}_3)_3$  compared to the  $Ln/An(\text{OTf}/\text{NO}_3)_3$  complexes. This is in agreement with the N K-edge results above as those found charge transfer from the ligand to the metal for the  $[Ln/An(n\text{-Pr-BTP})_3](\text{OTf})_3$  complexes. The high energy

resolution allows resolving a pre-edge feature for the  $[Ln(n\text{-Pr-BTP})_3](\text{OTf})_3$  complexes and it is shown that, as indicated in previous studies, it originates from electronic transitions to orbitals with predominant  $4f$  character. The shape and energy positions of these pre-edges do not change noticeably for the  $[Ln(n\text{-Pr-BTP})_3](\text{OTf})_3$  and  $Ln(\text{OTf})_3$  complexes. This strongly suggests that the  $4f$  states are localized on the metal atom and do not participate in bonding. The shapes of the pre-edges varies and depends on the number of  $4f$  electrons. The  $4f$  electrons induce electron-electron interactions leading to a complex structure of the  $4f$  states, i.e. multiplets. Nevertheless, it is apparent that the distance between the pre-edge and WL increases going from La to Lu reflecting the localization of the  $4f$  states as a function of the  $Ln$   $Z$  number.

Due to the large core-hole lifetime broadening effects pre-edges are not resolved for the  $[An(n\text{-Pr-BTP})_3](\text{NO}_3)_3$  complexes. The CAT-ACT beamline currently under commissioning will provide up to three orders of magnitude higher photon flux compared to the INE-Beamline and will allow to use the  $L_{\beta 5}$  emission lines for measurements of  $An$   $L_3$  edge HR-XANES spectra with reduced broadening effects. In future studies the  $5f$  states can be also directly probed by  $An$   $M_{4,5}$  edge HR-XANES and their level of participation in the chemical bond elucidated.

It is demonstrated that the HR-XANES technique allows resolving post-edge features not visible in the conventional spectra. The correlation of their energy positions to specific structural changes, i.e. interatomic distances and bonding angles are revealed with the help of *FEFF* EXAFS and *FDMNES* XANES quantum chemical calculations and simulations. Both codes are used for detailed analyses of the spectra. The trends for the energy positions of all post-edge features are well reproduced by both theoretical approaches for the  $Ln(\text{OTf})_3$  complexes. In contrary the  $Ln$   $Z$  dependent trend for the energy positions of the first post edge feature (**B**) of the  $[Ln(n\text{-Pr-BTP})_3](\text{OTf})_3$  complexes is not reproduced by the theoretical codes and simulations. This result strongly indicates that the used DFT optimized structures likely deviate from the real structures of the complexes. It is found that the larger metal–ligand bond lengths and likely differences in the bonding angles lead to the discrepancies. Optimized structures with additions of “no symmetry restrictions” and interactions with the solvation sphere improve the agreement between theory and experiment. However, the trends could not be verified

for a series of  $Ln$  and  $An$  due to lack of available  $Ln/An(\text{H-BTP})_3$  structures. MD simulations currently performed at the INE can also potentially provide more realistic structural models.

The benchmark calculations using various codes and input structures helped to select the most appropriate conditions for the simulations. The input parameters for the *FDMNES* XANES calculations were tested and defined. The HR-XANES experiments at the  $An$   $L_3$  edges were performed with the MAC spectrometer developed, tested and commissioned as part of this dissertation. Here the first measured Pu and Am HR-XANES spectra are presented and discussed.

The performed electronic and geometric structural investigations from the metal and ligand point of views suggest more covalent bonding for the  $An$ -ligand compared to the  $Ln$ -ligand bonds. As previously reported this might be related to the bonding affinity of the  $n$ -Pr-BTP ligand to  $An$  compared to  $Ln$  used in partitioning processes. A specific geometric arrangement of the ligand around the metal changing as a function of its Ln Z number is also evident. This structural detail is likely not depicted by the structures optimized on the DFT level with the BP86 functional [146, 147] employing the RI routines as implemented in TURBOMOLE [148]. Further methods like MD might help to reveal the  $Ln$  Z dependent trend. Future investigations of highly resolved studies of an extended set of  $An(n\text{-Pr-BTP})_3$  compounds will demonstrate if a similar trend is visible also for  $An$  and if it is related to the partitioning properties of the  $n$ -Pr-BTP ligand. In-situ investigations at the N K and  $Ln/An$   $L_3$  ( $M_{4,5}$ ) edges can potentially help to gain additional insights into any specific differences in the  $[Ln/An(n\text{-Pr-BTP})_3](\text{OTf})_3$  complex formation.

# Bibliography

- [1] *Implications of partitioning and transmutation in radioactive waste management*, International Atomic Energy Agency, **2004**.
- [2] *Nuclear Technology Review 2014, Report by the Director General*, International Atomic Energy Agency, **2014**.
- [3] J. Magill, V. Berthou, D. Haas, J. Galy, R. Schenkel, H.-W. Wiese, G. Heusener, J. Tommasi, G. Youinou, “Impact limits of partitioning and transmutation scenarios on the radiotoxicity of actinides in radioactive waste”, *Nuclear Energy* **2003**, *42*, 263–277.
- [4] *Status and Assessment Report on Actinide and Fission Product Partitioning and Transmutation*, OECD Nuclear Energy Agency, **1999**.
- [5] *Potential Benefits and Impacts of Advanced Nuclear Fuel Cycles with Actinide Partitioning and Transmutation*, OECD Nuclear Energy Agency, **2011**.
- [6] M. Salvatores, G. Palmiotti, “Radioactive waste partitioning and transmutation within advanced fuel cycles: Achievements and challenges”, *Prog. Part. Nucl. Phys.* **2011**, *66*, 144–166.
- [7] E.M. González-Romero, “Impact of partitioning and transmutation on the high level waste management”, *Nucl. Eng. Des.* **2011**, *241*, 3436–3444.
- [8] G.R. Choppin, J.-O. Liljenzin, J. Rydberg, *Radiochemistry and nuclear chemistry*, Butterworth-Heinemann, Woburn, MA, **2002**.
- [9] G. Modolo, A. Wilden, A. Geist, D. Magnusson, R. Malmbeck, “A review of the demonstration of innovative solvent extraction processes for the recovery of trivalent minor actinides from PUREX raffinate”, *Radiochim. Acta* **2012**, *100*, 715–725.

- [10] “Age-dependent dose to members of the public from intake of radionuclides: Part 5 compilation of ingestion and inhalation dose coefficients”, *Ann. ICRP* **1996**, *26*, 1–91.
- [11] C. Madic, B. Boullis, P. Baron, F. Testard, M.J. Hudson, J.-O. Liljezin, B. Christiansen, M. Ferrando, A. Facchini, A. Geist, G. Modolo, A.G. Espartero, J.d. Mendoza, “Futuristic back-end of the nuclear fuel cycle with the partitioning of minor actinides”, *J. Alloys Compd.* **2007**, *444-445*, 23–27.
- [12] C. Ekberg, A. Fermvik, T. Retegan, G. Skarnemark, M.R.S.J. Foreman, M.J. Hudson, S. Englund, M. Nilsson, “An overview and historical look back at the solvent extraction using nitrogen donor ligands to extract and separate An(III) from Ln(III)”, *Radiochim. Acta* **2008**, *96*, 225–233.
- [13] Z. Kolarik, “Complexation and Separation of Lanthanides(III) and Actinides(III) by Heterocyclic N-Donors in Solutions”, *Chem. Rev.* **2008**, *108*, 4208–4252.
- [14] F.W. Lewis, L.M. Harwood, M.J. Hudson, M.G.B. Drew, G. Modolo, M. Sypula, J.F. Desreux, N. Bouslimani, G. Vidick, “Interaction of 6,6''-bis(5,5,8,8-tetramethyl-5,6,7,8-tetrahydro-1,2,4-benzotriazin-3-yl)-2,2':6',2''-terpyridine (CyMe4-BTTP) with some trivalent ions such as lanthanide(III) ions and americium(III)”, *Dalton Trans.* **2010**, *39*, 5172–5182.
- [15] F.W. Lewis, M.J. Hudson, L.M. Harwood, “Development of Highly Selective Ligands for Separations of Actinides from Lanthanides in the Nuclear Fuel Cycle”, *Synlett* **2011**, *2011*, 2609–2632.
- [16] M.J. Hudson, L.M. Harwood, D.M. Laventine, F.W. Lewis, “Use of Soft Heterocyclic N-Donor Ligands To Separate Actinides and Lanthanides”, *Inorg. Chem.* **2013**, *52*, 3414–3428.
- [17] P.J. Panak, A. Geist, “Complexation and Extraction of Trivalent Actinides and Lanthanides by Triazinylpyridine N-Donor Ligands”, *Chem. Rev.* **2013**, *113*, 1199–1236.
- [18] F.H. Case, “The preparation of 2,4- and 2,6-bis-triazinyl and triazolanyl derivatives of pyridine”, *J. Heterocycl. Chem.* **1971**, *8*, 1043–1046.

- [19] Z. Kolarik, U. Müllich, F. Gassner, "Selective Extraction of Am(III) over Eu(III) by 2,6-ditriazolyl- and 2,6-ditriazinylpyridines", *Solvent Extr. Ion Exch.* **1999**, *17*, 23–32.
- [20] Z. Kolarik, U. Müllich, F. Gassner, "Extraction of Am(III) and Eu(III) nitrates by 2-6-di-(5,6-dipropyl-1,2,4-triazin-3-yl)pyridines", *Solvent Extr. Ion Exch.* **1999**, *17*, 1155–1170.
- [21] A. Geist, C. Hill, G. Modolo, M.R.S.J. Foreman, M. Weigl, K. Gompper, M.J. Hudson, "6,6'- Bis (5,5,8,8-tetramethyl-5,6,7,8-tetrahydro-benzo[1,2,4]triazin-3-yl) [2,2']bipyridine, an Effective Extracting Agent for the Separation of Americium(III) and Curium(III) from the Lanthanides", *Solvent Extr. Ion Exch.* **2006**, *24*, 463–483.
- [22] M. Steppert, C. Walther, A. Geist, T. Fanghänel, "Direct nano ESI time-of-flight mass spectrometric investigations on lanthanide BTP complexes in the extraction-relevant diluent 1-octanol", *New J. Chem.* **2009**, *33*, 2437–2442.
- [23] M. Weigl, A. Geist, U. Müllich, K. Gompper, "Kinetics of Americium(III) Extraction and Back Extraction with BTP", *Solvent Extr. Ion Exch.* **2006**, *24*, 845–860.
- [24] C. Hill, D. Guillaneux, X. Hérès, N. Boubals, L. Romain, in Proc. Internat. Conf. ATALANTE 2000 (Scientific Research on the Backend of the Nuclear Fuel Cycle for the 21st Century), **2000**.
- [25] B. Rat, X. Hérès, in Proc. Internat. Conf. ATALANTE 2000 (Scientific Research on the Back-end of the Nuclear Fuel Cycle for the 21st Century), **2000**.
- [26] M.J. Hudson, C.E. Boucher, D. Braekers, J.F. Desreux, M.G.B. Drew, M.R.S.J. Foreman, L.M. Harwood, C. Hill, C. Madic, F. Marken, T.G.A. Youngs, "New bis(triazinyl) pyridines for selective extraction of americium(III)", *New J. Chem.* **2006**, *30*, 1171.
- [27] S. Trumm, A. Geist, P.J. Panak, T. Fanghänel, "An Improved Hydrolytically-Stable Bis-Triazinyl-Pyridine (BTP) for Selective Actinide Extraction", *Solvent Extr. Ion Exch.* **2011**, *29*, 213–229.
- [28] G. Benay, R. Schurhammer, J. Desaphy, G. Wipff, "Substituent effects on BTP's basicity and complexation properties with LnIII lanthanide ions", *New J. Chem.* **2011**, *35*, 184–189.

- [29] S. Trumm, G. Wipff, A. Geist, P.J. Panak, T. Fanghänel, “Optimising BTP ligands by tuning their basicity”, *Radiochim. Acta* **2011**, *99*, 13–16.
- [30] M.J. Hudson, M.R.S.J. Foreman, C. Hill, N. Huet, C. Madic, “Studies on the Parallel Synthesis and Evaluation of New Heterocyclic Extractants for the Partitioning of Minor Actinides”, *Solvent Extr. Ion Exch.* **2003**, *21*, 637–652.
- [31] G. Benay, R. Schurhammer, G. Wipff, “BTP-based ligands and their complexes with Eu(3+) at “oil”/water interfaces. A molecular dynamics study”, *Phys. Chem. Chem. Phys.* **2010**, *12*, 11089–11102.
- [32] M.A. Halcrow, “The synthesis and coordination chemistry of 2,6-bis(pyrazolyl)pyridines and related ligands — Versatile terpyridine analogues”, *Coord. Chem. Rev.* **2005**, *249*, 2880–2908.
- [33] D. Girnt, P.W. Roesky, A. Geist, C.M. Ruff, P.J. Panak, M.A. Denecke, “6-(3,5-Dimethyl-1 H -pyrazol-1-yl)-2,2'-bipyridine as Ligand for Actinide(III)/Lanthanide(III) Separation”, *Inorg. Chem.* **2010**, *49*, 9627–9635.
- [34] A. Bremer, A. Geist, P.J. Panak, “Complexation of Cm(III) with 6-(5,6-dipentyl-1,2,4-triazin-3-yl)-2,2'-bipyridine studied by time resolved laser fluorescence spectroscopy”, *Dalton Trans.* **2012**, *41*, 7582–7589.
- [35] A. Bremer, C.M. Ruff, D. Girnt, U. Müllich, J. Rothe, P.W. Roesky, P.J. Panak, A. Karpov, T.J.J. Müller, M.A. Denecke, A. Geist, “2,6-Bis(5-(2,2-dimethylpropyl)-1H-pyrazol-3-yl)pyridine as a ligand for efficient actinide(III)/lanthanide(III) separation”, *Inorg. Chem.* **2012**, *51*, 5199–5207.
- [36] B.B. Beele, E. Rüdiger, F. Schwörer, U. Müllich, A. Geist, P.J. Panak, “A TRLFS study on the complexation of novel BTP type ligands with Cm(III)”, *Dalton Trans.* **2013**, *42*, 12139–12147.
- [37] A. Bremer, A. Geist, P.J. Panak, “Complexation of Cm(III) and Eu(III) with 2,6-bis(5-(2,2-dimethylpropyl)-1H-pyrazol-3-yl)pyridine and 2-bromohexanoic acid studied by time-resolved laser fluorescence spectroscopy”, *Radiochim. Acta* **2013**, *101*, 285–292.

- [38] B.B. Beele, U. Müllich, F. Schwörer, A. Geist, P.J. Panak, “Systematic Modifications of BTP-type Ligands and Effects on the Separation of Trivalent Lanthanides and Actinides”, *Procedia Chem.* **2012**, *7*, 146–151.
- [39] M.G.B. Drew, D. Guillaneux, M.J. Hudson, P.B. Iveson, C. Madic, “Unusual complexes formed by the early lanthanides with 2,6-bis(5,6-dialkyl-1,2,4-triazin-3-yl)-pyridines”, *Inorg. Chem. Commun.* **2001**, *4*, 462–466.
- [40] M.G.B. Drew, D. Guillaneux, M.J. Hudson, P.B. Iveson, M.L. Russell, C. Madic, “Lanthanide(III) complexes of a highly efficient actinide(III) extracting agent – 2,6-bis(5,6-dipropyl-1,2,4-triazin-3-yl)pyridine”, *Inorg. Chem. Commun.* **2001**, *4*, 12–15.
- [41] P.B. Iveson, C. Rivière, D. Guillaneux, M. Nierlich, P. Thuéry, M. Ephritikhine, C. Madic, “Selective complexation of uranium(III) over cerium(III) by 2,6-bis(5,6-dialkyl-1,2,4-triazin-3-yl)pyridines: <sup>1</sup>H NMR and X-ray crystallography studies”, *Chem. Commun.* **2001**, 1512–1513.
- [42] J.-C. Berthet, Y. Miquel, P.B. Iveson, M. Nierlich, P. Thuéry, C. Madic, M. Ephritikhine, “The affinity and selectivity of terdentate nitrogen ligands towards trivalent lanthanide and uranium ions viewed from the crystal structures of the 1:3 complexes”, *Dalton Trans.* **2002**, 3265–3272.
- [43] S. Colette, B. Amekraz, C. Madic, L. Berthon, G. Cote, C. Moulin, “Europium(III) interaction with a polyaza-aromatic extractant studied by time-resolved laser-induced luminescence: a thermodynamical approach”, *Inorg. Chem.* **2004**, *43*, 6745–6751.
- [44] M.A. Denecke, A. Rossberg, P.J. Panak, M. Weigl, B. Schimmelpfennig, A. Geist, “Characterization and comparison of Cm(III) and Eu(III) complexed with 2,6-di(5,6-dipropyl-1,2,4-triazin-3-yl)pyridine using EXAFS, TRFLS, and quantum-chemical methods”, *Inorg. Chem.* **2005**, *44*, 8418–8425.
- [45] M.A. Denecke, P.J. Panak, F. Burdet, M. Weigl, A. Geist, R. Klenze, M. Mazzanti, K. Gompper, “A comparative spectroscopic study of U(III)/Am(III) and Ln(III) complexed with N-donor ligands”, *C. R. Chimie* **2007**, *10*, 872–882.

- [46] S. Trumm, P.J. Panak, A. Geist, T. Fanghänel, “A TRLFS Study on the Complexation of CmIII and EuIII with 2,6-Bis(5,6-dipropyl-1,2,4-triazin-3-yl)pyridine in Water/Methanol Mixture”, *Eur. J. Inorg. Chem.* **2010**, *2010*, 3022–3028.
- [47] S. Trumm, G. Lieser, M.R.S.J. Foreman, P.J. Panak, A. Geist, T. Fanghänel, “A TRLFS study on the complexation of Cm(III) and Eu(III) with 4-t-butyl-6,6'-bis-(5,6-diethyl-1,2,4-triazin-3-yl)-2,2'-bipyridine in a water/2-propanol mixture”, *Dalton Trans.* **2010**, *39*, 923–929.
- [48] N. Rawat, A. Bhattacharyya, S.K. Ghosh, T. Gadly, B.S. Tomar, “Thermodynamics of complexation of lanthanides with 2,6-bis(5,6-diethyl-1,2,4-triazin-3-yl) pyridine”, *Radiochim. Acta* **2011**, *99*, 705–712.
- [49] N.L. Banik, M.A. Denecke, A. Geist, G. Modolo, P.J. Panak, J. Rothe, “2,6-Bis(5,6-dipropyl-1,2,4-triazin-3-yl)-pyridine: Structures of An(III) and Ln(III) 1:3 complexes and selectivity”, *Inorg. Chem. Commun.* **2013**, *29*, 172–174.
- [50] N.L. Banik, B. Schimmelpfennig, C.M. Marquardt, B. Brendebach, A. Geist, M.A. Denecke, “Characterization of redox sensitive plutonium(iii) complexed with alkylated 2,6-ditriazinylpyridine (BTP) in organic solution”, *Dalton Trans.* **2010**, *39*, 5117–5122.
- [51] G.R. Choppin, “Covalency in f-element bonds”, *J. Alloys Compd.* **2002**, *344*, 55–59.
- [52] K.I.M. Ingram, M.J. Tassell, A.J. Gaunt, N. Kaltsoyannis, “Covalency in the f Element-Chalcogen Bond. Computational Studies of  $M[N(EPR_2)_2]_3$  ( $M = La, Ce, Pr, Pm, Eu, U, Np, Pu, Am, Cm$ ;  $E = O, S, Se, Te$ ;  $R = H, ^iPr, Ph$ )”, *Inorg. Chem.* **2008**, *47*, 7824–7833.
- [53] N. Kaltsoyannis, “Does covalency increase or decrease across the actinide series? Implications for minor actinide partitioning”, *Inorg. Chem.* **2013**, *52*, 3407–3413.
- [54] M.L. Neidig, D.L. Clark, R.L. Martin, “Covalency in f-element complexes”, *Coord. Chem. Rev.* **2013**, *257*, 394–406.

- [55] C. Adam, P. Kaden, B.B. Beele, U. Müllich, S. Trumm, A. Geist, P.J. Panak, M.A. Denecke, "Evidence for covalence in a N-donor complex of americium(III)", *Dalton Trans.* **2013**, *42*, 14068–14074.
- [56] C. Adam, B.B. Beele, A. Geist, U. Müllich, P. Kaden, P.J. Panak, "NMR and TRIFS studies of Ln(III) and An(III) C5-BPP complexes", *Chem. Sci.* **2015**, *6*, 1548–1561.
- [57] W.B. Lewis, J.A. Jackson, J.F. Lemons, H. Taube, "Oxygen<sup>17</sup> NMR Shifts in Aqueous Solutions of Rare-Earth Ions", *J. Chem. Phys.* **1962**, *36*, 694–701.
- [58] M.I. da Costa, E.F.R. Fraga, T. Sonnino, "Rare-Earth Tri-iodides – Mössbauer Effect Using <sup>129</sup>I", *J. Chem. Phys.* **1970**, *52*, 1611–1612.
- [59] C.K. Jørgensen, "The Persistence of p, d, f and g Orbitals in Compounds", *Isr. J. Chem.* **1980**, *19*, 174–192.
- [60] H.G. Friedman, G.R. Choppin, D.G. Feuerbacher, "The shapes of the f orbitals", *Journal of Chemical Education* **1964**, *41*, 354.
- [61] M.J. Tassell, N. Kaltsoyannis, "Covalency in AnCp<sub>4</sub> (An = Th-Cm): a comparison of molecular orbital, natural population and atoms-in-molecules analyses", *Dalton Trans.* **2010**, *39*, 6719–6725.
- [62] K. Tatsumi, R. Hoffmann, "Bent cis d<sup>0</sup> MoO<sub>2</sub><sup>2+</sup> vs. linear trans d<sup>0</sup>f<sup>0</sup> UO<sub>2</sub><sup>2+</sup> : a significant role for nonvalence 6p orbitals in uranyl", *Inorg. Chem.* **1980**, *19*, 2656–2658.
- [63] R.G. Denning, "Electronic structure and bonding in actinyl ions", in *Complexes, Clusters and Crystal Chemistry, Vol. 79*, Structure and Bonding, Springer Berlin Heidelberg, **1992**, pp. 215–276.
- [64] R.G. Denning, J.C. Green, T.E. Hutchings, C. Dallera, A. Tagliaferri, K. Giarda, N.B. Brookes, L. Braicovich, "Covalency in the uranyl ion: A polarized x-ray spectroscopic study", **2002**, *117*, 8008–8020.
- [65] R.G. Denning, "Electronic structure and bonding in actinyl ions and their analogs", *J. Phys. Chem. A* **2007**, *111*, 4125–4143.
- [66] A. Zalkin, K.N. Raymond, "Structure of Di- $\pi$ -cyclooctatetraeneuranium (uranocene)", *J. Am. Chem. Soc.* **1969**, *91*, 5667–5668.

- [67] A. Avdeef, K.N. Raymond, K.O. Hodgson, A. Zalkin, "Two isostructural actinide  $\pi$  complexes. The crystal and molecular structure of bis(cyclo-octa-tetraenyl)uranium(IV),  $U(C_8H_8)_2$ , and bis(cyclo-octa-tetraenyl)thorium(IV),  $Th(C_8H_8)_2$ ", *Inorg. Chem.* **1972**, *11*, 1083–1088.
- [68] J.P. Clark, J.C. Green, "The He-I photoelectron spectra of uranocene and thorocene", *J. Organomet. Chem.* **1976**, *112*, C14–C16.
- [69] J.C. Green, "Gas phase photoelectron spectra of d- and f-block organometallic compounds", in *Bonding Problems, Vol. 43*, Structure and Bonding, Springer Berlin Heidelberg, **1981**, pp. 37–112.
- [70] J.G. Brennan, J.C. Green, C.M. Redfern, "Covalency in bis([8]annulene)-uranium from photoelectron spectroscopy with variable photon energy", *J. Am. Chem. Soc.* **1989**, *111*, 2373–2377.
- [71] M. Pepper, B.E. Bursten, "The electronic structure of actinide-containing molecules: A challenge to applied quantum chemistry", *Chem. Rev.* **1991**, *91*, 719–741.
- [72] W. Liu, M. Dolg, P. Fulde, "Low-lying electronic states of lanthanocenes and actinocenes  $M(C_8H_8)_2$  ( $M=Nd, Tb, Yb, U$ )", *J. Chem. Phys.* **1997**, *107*, 3584–3591.
- [73] D. Seyferth, "Uranocene. The First Member of a New Class of Organometallic Derivatives of the f Elements", *Organometallics* **2004**, *23*, 3562–3583.
- [74] A. Kerridge, N. Kaltsoyannis, "Are the Ground States of the Later Actinocenes Multiconfigurational? All-Electron Spin-Orbit Coupled CASPT2 Calculations on  $An(\eta^8-C_8H_8)_2$  ( $An = Th, U, Pu, Cm$ )", *J. Phys. Chem. A* **2009**, *113*, 8737–8745.
- [75] M. Mazzanti, R. Wietzke, J. Pécaut, J.-M. Latour, P. Maldivi, M. Remy, "Structural and Density Functional Studies of Uranium(III) and Lanthanum(III) Complexes with a Neutral Tripodal N-Donor Ligand Suggesting the Presence of a U-N Back-Bonding Interaction", *Inorg. Chem.* **2002**, *41*, 2389–2399.

- [76] T. Mehdoui, J.-C. Berthet, P. Thuéry, M. Ephritikhine, “Lanthanide(III)/actinide(III) differentiation in coordination of azine molecules to tris-(cyclopentadienyl) complexes of cerium and uranium”, *Dalton Trans.* **2004**, 579–590.
- [77] A.J. Gaunt, B.L. Scott, M.P. Neu, “Homoleptic uranium(III) imido-diphosphinochalcogenides including the first structurally characterised molecular trivalent actinide-Se bond”, *Chem. Commun.* **2005**, 3215–3217.
- [78] G.R. Choppin, M.P. Jensen, “The Chemistry of the Actinide and Transactinide Elements”, in *The Chemistry of the Actinide and Transactinide Elements*, Springer: Berlin, **2006**, p. 2562.
- [79] A.J. Gaunt, B.L. Scott, M.P. Neu, “A molecular actinide-tellurium bond and comparison of bonding in”, *Angew. Chem.* **2006**, *45*, 1638–1641.
- [80] A.J. Gaunt, S.D. Reilly, A.E. Enriquez, B.L. Scott, J.A. Ibers, P. Sekar, K.I.M. Ingram, N. Kaltsoyannis, M.P. Neu, “Experimental and theoretical comparison of actinide and lanthanide”, *Inorg. Chem.* **2008**, *47*, 29–41.
- [81] S.R. Daly, J.M. Keith, E.R. Batista, K.S. Boland, D.L. Clark, S.A. Kozimor, R.L. Martin, “Sulfur K-edge X-ray Absorption Spectroscopy and Time-Dependent Density Functional Theory of Dithiophosphate Extractants: Minor Actinide Selectivity and Electronic Structure Correlations”, *J. Am. Chem. Soc.* **2012**, *134*, 14408–14422.
- [82] S.A. Kozimor, P. Yang, E.R. Batista, K.S. Boland, C.J. Burns, D.L. Clark, S.D. Conradson, R.L. Martin, M.P. Wilkerson, L.E. Wolfsberg, “Trends in Covalency for d- and f-Element Metallocene Dichlorides Identified Using Chlorine K-Edge X-ray Absorption Spectroscopy and Time-Dependent Density Functional Theory”, *J. Am. Chem. Soc.* **2009**, *131*, 12125–12136.
- [83] T. Vitova, K.O. Kvashnina, G. Nocton, G. Sukharina, M.A. Denecke, S.M. Butorin, M. Mazzanti, R. Caciuffo, A. Soldatov, T. Behrends, H. Geckeis, “High energy resolution x-ray absorption spectroscopy study of uranium in varying valence states”, *Phys. Rev. B* **2010**, *82*, 235118.

- [84] S.G. Minasian, J.M. Keith, E.R. Batista, K.S. Boland, D.L. Clark, S.D. Conradson, S.A. Kozimor, R.L. Martin, D.E. Schwarz, D.K. Shuh, G.L. Wagner, M.P. Wilkerson, L.E. Wolfsberg, P. Yang, “Determining Relative f and d Orbital Contributions to M-Cl Covalency”, *J. Am. Chem. Soc.* **2012**, *134*, 5586–5597.
- [85] S.G. Minasian, J.M. Keith, E.R. Batista, K.S. Boland, D.L. Clark, S.A. Kozimor, R.L. Martin, D.K. Shuh, T. Tyliczszak, “New evidence for 5f covalency in actinocenes determined from carbon K-edge XAS and electronic structure theory”, *Chem. Sci.* **2014**, *5*, 351–359.
- [86] J.J. Rehr, R.C. Albers, “Theoretical approaches to x-ray absorption fine structure”, *Rev. Mod. Phys.* **2000**, *72*, 621–654.
- [87] A.L. Ankudinov, B. Ravel, J.J. Rehr, S.D. Conradson, “Real-space multiple-scattering calculation and interpretation of x-ray-absorption near-edge structure”, *Phys. Rev. B* **1998**, *58*, 7565–7576.
- [88] B. Ravel, “A practical introduction to multiple scattering theory”, *J. Alloys Compd.* **2005**, *401*, 118–126.
- [89] M. Newville, *Fundamentals of XAFS*, Consortium for Advanced Radiation Sources, University of Chicago, **2004**.
- [90] A.H. Compton, “A precision X-ray spectrometer and the wave length of Mo  $K_{\alpha 1}$ ”, *Rev. Sci. Instrum.* **1931**, *2*, 365.
- [91] M. Lemonnier, O. Collet, C. Depautex, J.-M. Esteve, D. Raoux, “High vacuum two crystal soft X-ray monochromator”, *Nucl. Instrum. Methods* **1978**, *152*, 109–111.
- [92] L.D. Finkelstein, A.V. Postnikov, N.N. Efremova, E.Z. Kurmaev, “X-ray Ce  $L_{III}$  absorption in  $CeO_2$  and  $BaCeO_3$ : experiment and interpretation on the basis of LMTO band structure calculations”, *Mater. Lett.* **1992**, *14*, 115–118.
- [93] M.H. Krisch, C.C. Kao, F. Sette, W.A. Caliebe, K. Hämäläinen, J.B. Hastings, “Evidence for a Quadrupolar Excitation Channel at the  $L_{III}$  Edge of Gadolinium by Resonant Inelastic X-Ray Scattering”, *Phys. Rev. Lett.* **1995**, *74*, 4931–4934.
- [94] K.O. Kvashnina, S.M. Butorin, P. Glatzel, “Direct study of the f-electron configuration in lanthanide systems”, *J. Anal. At. Spectrom.* **2011**, *26*, 1265.

- [95] J.C. Slater, “Wave Functions in a Periodic Potential”, *Phys. Rev.* **1937**, *51*, 846–851.
- [96] P.A. Lee, J.B. Pendry, “Theory of the extended x-ray absorption fine structure”, *Phys. Rev. B* **1975**, *11*, 2795–2811.
- [97] M.P. Seah, W.A. Dench, “Quantitative electron spectroscopy of surfaces: A standard data base for electron inelastic mean free paths in solids”, *Surf. Interface Anal.* **1979**, *1*, 2–11.
- [98] D.E. Sayers, E.A. Stern, F.W. Lytle, “New Technique for Investigating Noncrystalline Structures: Fourier Analysis of the Extended X-Ray-Absorption Fine Structure”, *Phys. Rev. Lett.* **1971**, *27*, 1204–1207.
- [99] E.A. Stern, “Theory of the extended x-ray-absorption fine structure”, *Phys. Rev. B* **1974**, *10*, 3027–3037.
- [100] F.W. Lytle, D.E. Sayers, E.A. Stern, “Extended x-ray-absorption fine-structure technique. II. Experimental practice and selected results”, *Phys. Rev. B* **1975**, *11*, 4825–4835.
- [101] E.A. Stern, D.E. Sayers, F.W. Lytle, “Extended x-ray-absorption fine-structure technique. III. Determination of physical parameters”, *Phys. Rev. B* **1975**, *11*, 4836–4846.
- [102] C.A. Ashley, S. Doniach, “Theory of extended x-ray absorption edge fine structure (EXAFS) in crystalline solids”, *Phys. Rev. B* **1975**, *11*, 1279–1288.
- [103] P. Glatzel, A. Juhin, “X-ray Absorption and Emission Spectroscopy”, in *Local Structural Characterisation*, (Eds.: D.W. Bruce, D. O’Hare, R.I. Walton), John Wiley & Sons, Ltd, **2013**, pp. 89–171.
- [104] A. Kotani, S. Shin, “Resonant inelastic x-ray scattering spectra for electrons in solids”, *Rev. Mod. Phys.* **2001**, *73*, 203–246.
- [105] W. Schülke, *Electron dynamics by inelastic X-ray scattering, Vol. 7*, Oxford series on synchrotron radiation, Oxford Univ. Press, **2007**.
- [106] J.-E. Rubensson, D. Mueller, R. Shuker, D.L. Ederer, C.H. Zhang, J. Jia, T.A. Callcott, “Excitation-energy dependence in the  $L_{2,3}$  fluorescence spectrum of Si”, *Phys. Rev. Lett.* **1990**, *64*, 1047–1050.
- [107] P. Salek, A. Baev, F. Gel’mukhanov, H. Agren, “Dynamical properties of X-ray Raman scattering”, *Phys. Chem. Chem. Phys.* **2003**, *5*, 1–11.

- [108] P. Glatzel, U. Bergmann, “High resolution 1s core hole X-ray spectroscopy in 3d transition metal complexes - electronic and structural information”, *Coord. Chem. Rev.* **2005**, *249*, 65–95.
- [109] F.M.F. de Groot, A. Kotani, *Core level spectroscopy of solids, Vol. v. 6*, Advances in condensed matter science, CRC Press, **2008**.
- [110] L.J.P. Ament, M. van Veenendaal, T.P. Devereaux, J.P. Hill, J. van den Brink, “Resonant inelastic x-ray scattering studies of elementary excitations”, *Rev. Mod. Phys.* **2011**, *83*, 705–767.
- [111] P. Glatzel, J. Singh, K.O. Kvashnina, J.A. van Bokhoven, “In Situ Characterization of the 5d Density of States of Pt Nanoparticles upon Adsorption of CO”, *J. Am. Chem. Soc.* **2010**, *132*, 2555–2557.
- [112] T. Vitova, M.A. Denecke, J. Göttlicher, K. Jorissen, J.J. Kas, K.O. Kvashnina, T. Prüßmann, J.J. Rehr, J. Rothe, “Actinide and lanthanide speciation with high-energy resolution X-ray techniques”, *J. Phys.: Conf. Ser.* **2013**, *430*, 12117.
- [113] P. Glatzel, J. Yano, U. Bergmann, H. Visser, J.H. Robblee, W. Gu, F.M.F. de Groot, S.P. Cramer, V.K. Yachandra, “Resonant inelastic X-ray scattering (RIXS) spectroscopy at the Mn K absorption pre-edge - a direct probe of the 3d orbitals”, *J. Phys. Chem. Solids* **2005**, *66*, 2163–2167.
- [114] P. Glatzel, M. Sikora, M. Fernández-García, “Resonant X-ray spectroscopy to study K absorption pre-edges in 3d transition metal compounds”, *Eur. Phys. J. Special Topics* **2009**, *169*, 207–214.
- [115] M.O. Krause, J.H. Oliver, “Natural widths of atomic K and L levels,  $K_{\alpha}$  X-ray lines and several KLL Auger lines”, *J. Phys. Chem. Ref. Data* **1979**, *8*, 329–338.
- [116] G. Bunker, *Introduction to XAFS: A practical guide to X-ray absorption fine structure spectroscopy*, Cambridge Univ. Press, **2010**.
- [117] H.A. Kramers, W. Heisenberg, “Über die Streuung von Strahlung durch Atome”, *Zeitschrift für Physik* **1925**, *31*, 681–708.
- [118] F.M.F. de Groot, M.H. Krisch, J. Vogel, “Spectral sharpening of the Pt L edges by high-resolution x-ray emission”, *Phys. Rev. B* **2002**, *66*, 195112.

- [119] R. Alonso-Mori, P. Glatzel, *RT4XES*, <https://sites.google.com/site/rt4xes/> (visited on 05/27/2014).
- [120] M. Sanchez del Rio, C. Ferrero, V. Mocella, “Computer simulation of bent perfect crystal diffraction profiles”, in *Optical Science, Engineering and Instrumentation '97*, (Eds.: A.T. Macrander, A.M. Khounsary), SPIE Proceedings, SPIE, **1997**, pp. 312–323.
- [121] M. Sanchez del Rio, R.J. Dejus, “XOP: a multiplatform graphical user interface for synchrotron radiation spectral and optics calculations”, in *Optical Science, Engineering and Instrumentation '97*, (Eds.: P.Z. Takacs, T.W. Tonnessen), SPIE Proceedings, SPIE, **1997**, pp. 148–157.
- [122] H.H. Johann, “Die Erzeugung lichtstarker Röntgenspektren mit Hilfe von Konkavkristallen”, *Zeitschrift für Physik* **1931**, *69*, 185–206.
- [123] U. Bergmann, S.P. Cramer, “High-resolution large-acceptance analyzer for x-ray fluorescence and Raman spectroscopy”, in *SPIE’s International Symposium on Optical Science, Engineering, and Instrumentation*, (Eds.: A.T. Macrander, A.K. Freund, T. Ishikawa, D.M. Mills), SPIE Proceedings, SPIE, **1998**, pp. 198–209.
- [124] E. Collart, A. Shukla, F. Gélébart, M. Morand, C. Malgrange, N. Bardou, A. Madouri, J.-L. Pelouard, “Spherically bent analyzers for resonant inelastic X-ray scattering with intrinsic resolution below 200 meV”, *J. Synchrotron Radiat.* **2005**, *12*, 473–478.
- [125] E. Klymenov, J.A. van Bokhoven, C. David, P. Glatzel, M. Janousch, R. Alonso-Mori, M. Studer, M. Willmann, A. Bergamaschi, B. Henrich, M. Nachtegaal, “Five-element Johann-type x-ray emission spectrometer with a single-photon-counting pixel detector”, *Rev. Sci. Instrum.* **2011**, *82*, 65107.
- [126] J.J. Olivero, R.L. Longbothum, “Empirical fits to the Voigt line width: A brief review”, *J. Quant. Spectrosc. Radiat. Transfer* **1977**, *17*, 233–236.
- [127] J.C. Swarbrick, U. Skyllberg, T. Karlsson, P. Glatzel, “High Energy Resolution X-ray Absorption Spectroscopy of Environmentally Relevant Lead(II) Compounds”, *Inorg. Chem.* **2009**, *48*, 10748–10756.

- [128] P. Glatzel, T.-C. Weng, K.O. Kvashnina, J.C. Swarbrick, M. Sikora, E. Gallo, N. Smolentsev, R.A. Mori, “Reflections on hard X-ray photon-in/photon-out spectroscopy for electronic structure studies”, *J. Electron. Spectrosc. Relat. Phenom.* **2013**, *188*, 17–25.
- [129] Wikipedia, *Synchrotron light source*, [http://en.wikipedia.org/wiki/Synchrotron\\_light\\_source](http://en.wikipedia.org/wiki/Synchrotron_light_source) (visited on 02/22/2015).
- [130] P.R. Willmott, *An introduction to synchrotron radiation: Techniques and applications*, Wiley, Chichester, West Sussex, U.K, **2011**.
- [131] DESY, *Synchrotron Radiation*, [http://photon-science.desy.de/research/studentsteaching/primers/synchrotron\\_radiation/](http://photon-science.desy.de/research/studentsteaching/primers/synchrotron_radiation/) (visited on 02/24/2015).
- [132] J. Rothe, S.M. Butorin, K. Dardenne, M.A. Denecke, B. Kienzler, M.W. Löble, V. Metz, A. Seibert, M. Steppert, T. Vitova, C. Walther, H. Geckeis, “The INE-Beamline for actinide science at ANKA”, *Rev. Sci. Instrum.* **2012**, *83*, 43105.
- [133] K. Hämäläinen, D.P. Siddons, J.B. Hastings, L.E. Berman, “Elimination of the inner-shell lifetime broadening in x-ray-absorption spectroscopy”, *Phys. Rev. Lett.* **1991**, *67*, 2850–2853.
- [134] X. Llopart, M. Campbell, R. Dinapoli, D. San Segundo, E. Pernigotti, “Medipix2: A 64-k pixel readout chip with 55- $\mu\text{m}$  square elements working in single photon counting mode”, *IEEE Trans. Nucl. Sci.* **2002**, *49*, 2279–2283.
- [135] J.S. Iwanczyk, B.E. Patt, S. Barkan, L. Feng, C.R. Tull, “High throughput high resolution Vortex<sup>TM</sup> detector for X-ray diffraction”, *IEEE Trans. Nucl. Sci.* **2003**, *50*, 2470–2473.
- [136] C. Hill, F. Arnaud-Neu, A.G. Espartero, J.F. Desreux, G. Modolo, S. Bourg, R. Malmbeck, C. Caravaca, M. Harrison, G.d. Angelis, et al., “EUROPART–Final Activity Report”, **2007**, *Contract Number: F16W-CT-2003-508 854*.
- [137] C.E. Boucher, M.G.B. Drew, P. Giddings, L.M. Harwood, M.J. Hudson, P.B. Iveson, C. Madic, “12-coordinate complexes formed by the early lanthanide metals with 2,6-bis(-1,2,4-triazin-3-yl)-pyridine”, *Inorg. Chem. Commun.* **2002**, *5*, 596–599.

- [138] T.T. Fister, G.T. Seidler, L. Wharton, A.R. Battle, T.B. Ellis, J.O. Cross, A.T. Macrander, W.T. Elam, T.A. Tyson, Q. Qian, “Multi-element spectrometer for efficient measurement of the momentum transfer dependence of inelastic x-ray scattering”, *Rev. Sci. Instrum.* **2006**, *77*, 63901.
- [139] A.P. Hitchcock, *axis2000*, <http://unicorn.mcmaster.ca/aXis2000.html> (visited on 11/11/2013).
- [140] C. Jacobsen, S. Wirick, G. Flynn, C. Zimba, “Soft X-ray spectroscopy from image sequences with sub-100 nm spatial resolution”, *J. Microsc.* **2000**, *197*, 173–184.
- [141] E. Welter, P. Machek, G. Dräger, U. Brüggmann, M. Fröba, “A new X-ray spectrometer with large focusing crystal analyzer”, *J. Synchrotron Radiat.* **2005**, *12*, 448–454.
- [142] P. Glatzel, M. Sikora, G. Smolentsev, M. Fernández-García, “Hard X-ray photon-in photon-out spectroscopy”, *Catal. Today* **2009**, *145*, 294–299.
- [143] J.J. Rehr, J.J. Kas, M.P. Prange, A.P. Sorini, Y. Takimoto, F.D. Vila, “Ab initio theory and calculations of X-ray spectra”, *C.R. Phys.* **2009**, *10*, 548–559.
- [144] J.J. Rehr, J.J. Kas, F.D. Vila, M.P. Prange, K. Jorissen, “Parameter-free calculations of X-ray spectra with FEFF9”, *Phys. Chem. Chem. Phys.* **2010**, *12*, 5503–5513.
- [145] M. Wojdyr, “Fityk: a general-purpose peak fitting program”, *J. Appl. Cryst.* **2010**, *43*, 1126–1128.
- [146] A.D. Becke, “Density-functional exchange-energy approximation with correct asymptotic behavior”, *Phys. Rev. A* **1988**, *38*, 3098–3100.
- [147] J.P. Perdew, “Density-functional approximation for the correlation energy of the inhomogeneous electron gas”, *Phys. Rev. B* **1986**, *33*, 8822–8824.
- [148] TURBOMOLE V6.4 2012, a development of University of Karlsruhe and Forschungszentrum Karlsruhe GmbH 1989-2007, TURBOMOLE GmbH, since 2007; available from <http://www.turbomole.com>.

- [149] F. Weigend, M. Häser, H. Patzelt, R. Ahlrichs, “RI-MP2: Optimized auxiliary basis sets and demonstration of efficiency”, *Chem. Phys. Lett.* **1998**, *294*, 143–152.
- [150] K. Eichkorn, F. Weigend, O. Treutler, R. Ahlrichs, “Auxiliary basis sets for main row atoms and transition metals and their use to approximate Coulomb potentials”, *Theor. Chem. Acc.* **1997**, *97*, 119–124.
- [151] L. Petit, C. Adamo, P. Maldivi, “Toward a clear-cut vision on the origin of 2,6-di(1,2,4-triazin-3-yl)pyridine selectivity for trivalent actinides: insights from theory”, *Inorg. Chem.* **2006**, *45*, 8517–8522.
- [152] M. Dolg, H. Stoll, A. Savin, H. Preuss, “Energy-adjusted pseudopotentials for the rare earth elements”, *Theor. Chim. Acta* **1989**, *75*, 173–194.
- [153] M. Dolg, H. Stoll, H. Preuss, “A combination of quasirelativistic pseudopotential and ligand field calculations for lanthanoid compounds”, *Theor. Chim. Acta* **1993**, *85*, 441–450.
- [154] C. Apostolidis, B. Schimmelpfennig, N. Magnani, P. Lindqvist-Reis, O. Walter, R. Sykora, A. Morgenstern, E. Colineau, R. Caciuffo, R. Klenze, R.G. Haire, J. Rebizant, F. Bruchertseifer, T. Fanghänel, “[An(H<sub>2</sub>O)<sub>9</sub>](CF<sub>3</sub>SO<sub>3</sub>)<sub>3</sub> (An=U-Cm, Cf): exploring their stability, structural chemistry, and magnetic behavior by experiment and theory”, *Angew. Chem.* **2010**, *49*, 6343–6347.
- [155] A.D. Becke, “A new mixing of Hartree–Fock and local density-functional theories”, *J. Chem. Phys.* **1993**, *98*, 1372.
- [156] A. Klamt, “Conductor-like Screening Model for Real Solvents: A New Approach to the Quantitative Calculation of Solvation Phenomena”, *J. Phys. Chem.* **1995**, *99*, 2224–2235.
- [157] U. Becker, D. Ganyushin, A. Hansen, D. Liakos, C. Kollmar, S. Kossmann, T. Petrenko, C. Reimann, C. Riplinger, K. Sivalingam, B. Wezislá, F. Wennmohs, *ORCA - An Ab Initio, DFT and Semiempirical electronic structure package*, **2010**.
- [158] T.H. Dunning, “Gaussian basis sets for use in correlated molecular calculations. I. The atoms boron through neon and hydrogen”, *J. Chem. Phys.* **1989**, *90*, 1007.

- [159] J. Schirmer, “Beyond the random-phase approximation: A new approximation scheme for the polarization propagator”, *Phys. Rev. A* **1982**, *26*, 2395–2416.
- [160] A.B. Trofimov, J. Schirmer, “An efficient polarization propagator approach to valence electron excitation spectra”, *J. Phys. B: At. Mol. Opt. Phys.* **1995**, *28*, 2299–2324.
- [161] G. te Velde, F.M. Bickelhaupt, E.-J. Baerends, C. Fonseca Guerra, S.J.A. van Gisbergen, J.G. Snijders, T. Ziegler, “Chemistry with ADF”, *J. Comput. Chem.* **2001**, *22*, 931–967.
- [162] C. Fonseca Guerra, J.G. Snijders, G. te Velde, E.-J. Baerends, “Towards an order-N DFT method”, *Theor. Chem. Acc.* **1998**, *99*, 391–403.
- [163] SCM, Theoretical Chemistry, Vrije Universiteit, Amsterdam, The Netherlands, Ed., *ADF2013*, <http://www.scm.com>.
- [164] C. Chang, M. Pelissier, P. Durand, “Regular Two-Component Pauli-Like Effective Hamiltonians in Dirac Theory”, *Phys. Scr.* **1986**, *34*, 394–404.
- [165] E. van Lenthe, J.G. Snijders, E.-J. Baerends, “The zero-order regular approximation for relativistic effects: The effect of spin-orbit coupling in closed shell molecules”, *J. Chem. Phys.* **1996**, *105*, 6505.
- [166] E. van Lenthe, R. van Leeuwen, E.-J. Baerends, J.G. Snijders, “Relativistic regular two-component Hamiltonians”, *Int. J. Quantum Chem.* **1996**, *57*, 281–293.
- [167] E. van Lenthe, A. Ehlers, E.-J. Baerends, “Geometry optimizations in the zero order regular approximation for relativistic effects”, *J. Chem. Phys.* **1999**, *110*, 8943–8953.
- [168] O. Bunău, Y. Joly, “Self-consistent aspects of x-ray absorption calculations”, *J. Phys. Condens. Matter.* **2009**, *21*, 345501.
- [169] Y. Jugnet, F.J. Himpsel, P. Avouris, E.E. Koch, “High-Resolution C 1s and O 1s Core-Excitation Spectroscopy of Chemisorbed, Physisorbed, and Free CO”, *Phys. Rev. Lett.* **1984**, *53*, 198–201.

- [170] R. McLaren, S.A.C. Clark, I. Ishii, A.P. Hitchcock, "Absolute oscillator strengths from K -shell electron-energy-loss spectra of the fluoroethenes and 1,3-perfluorobutadiene", *Phys. Rev. A* **1987**, *36*, 1683–1701.
- [171] M.B. Robin, I. Ishii, R. McLaren, A.P. Hitchcock, "Fluorination effects on the inner-shell spectra of unsaturated molecules", *J. Electron. Spectrosc. Relat. Phenom.* **1988**, *47*, 53–92.
- [172] E.I. Solomon, B. Hedman, K.O. Hodgson, A. Dey, R.K. Szilagy, "Ligand K-edge X-ray absorption spectroscopy: Covalency of ligand–metal bonds", *Coord. Chem. Rev.* **2005**, *249*, 97–129.
- [173] W.E.S. Unger, T. Gross, O. Bose, A. Lippitz, T. Fritz, U. Gelius, "VAMAS TWA2 Project A2: evaluation of static charge stabilization and determination methods in XPS on non-conducting samples. Report on an inter-laboratory comparison", **2000**, *29*, 535–543.
- [174] G.R. Wight, C.E. Brion, M.J. van der Wiel, "K-shell energy loss spectra of 2.5 keV electrons in N<sub>2</sub> and CO", *J. Electron. Spectrosc. Relat. Phenom.* **1972**, *1*, 457–469.
- [175] A.P. Hitchcock, C.E. Brion, "K-shell excitation spectra of CO, N<sub>2</sub> and O<sub>2</sub>", *J. Electron. Spectrosc. Relat. Phenom.* **1980**, *18*, 1–21.
- [176] C.T. Chen, Y. Ma, F. Sette, "K -shell photoabsorption of the N<sub>2</sub> molecule", *Phys. Rev. A* **1989**, *40*, 6737–6740.
- [177] J. Stöhr, *NEXAFS Spectroscopy*, Vol. 25, Springer series in surface sciences, Springer, Berlin, Heidelberg, **1992**.
- [178] C.R. Natoli, in *EXAFS and Near Edge Structure*, (Eds.: A. Bianconi, L. Incoccia, S. Stipcich), Vol. 27, Springer Ser. Chem. Phys, Springer, **1983**.
- [179] A.P. Hitchcock, S. Beaulieu, T. Steel, J. Stöhr, F. Sette, "Carbon K-shell electron energy loss spectra of 1- and 2-butenes, trans-1,3-butadiene, and perfluoro-2-butene. Carbon-carbon bond lengths from continuum shape resonances", *J. Chem. Phys.* **1984**, *80*, 3927–3935.
- [180] F. Sette, J. Stöhr, A.P. Hitchcock, "Determination of intramolecular bond lengths in gas phase molecules from K shell shape resonances", *J. Chem. Phys.* **1984**, *81*, 4906–4914.

- [181] A.P. Hitchcock, J. Stöhr, “K-shell shape resonances and intramolecular bond lengths. Comments on “The relationship between shape resonances and bond lengths””, *J. Chem. Phys.* **1987**, *87*, 3253.
- [182] J.A. Sheehy, T.J. Gil, C.L. Winstead, R.E. Farren, P.W. Langhoff, “Correlation of molecular valence- and K-shell photoionization resonances with bond lengths”, *J. Chem. Phys.* **1989**, *91*, 1796–1812.
- [183] J.L. Dehmer, D. Dill, S. Wallace, “Shape-Resonance-Enhanced Nuclear-Motion Effects in Molecular Photoionization”, *Phys. Rev. Lett.* **1979**, *43*, 1005–1008.
- [184] R. Bauernschmitt, R. Ahlrichs, “Treatment of electronic excitations within the adiabatic approximation of time dependent density functional theory”, *Chem. Phys. Lett.* **1996**, *256*, 454–464.
- [185] M.E. Casida, C. Jamorski, K.C. Casida, D.R. Salahub, “Molecular excitation energies to high-lying bound states from time-dependent density-functional response theory: Characterization and correction of the time-dependent local density approximation ionization threshold”, *J. Chem. Phys.* **1998**, *108*, 4439–4449.
- [186] R.E. Stratmann, G.E. Scuseria, M.J. Frisch, “An efficient implementation of time-dependent density-functional theory for the calculation of excitation energies of large molecules”, *J. Chem. Phys.* **1998**, *109*, 8218–8224.
- [187] B.O. Roos, P.R. Taylor, P.E. Siegbahn, “A complete active space SCF method (CASSCF) using a density matrix formulated super-CI approach”, *Chem. Phys.* **1980**, *48*, 157–173.
- [188] R.F.W. Bader, *Atoms in molecules: A quantum theory*, Vol. 22, The international series of monographs on chemistry, Clarendon Press, Oxford, **2003**.
- [189] M.W. Löble, J.M. Keith, A.B. Altman, S.C.E. Stieber, E.R. Batista, K.S. Boland, S.D. Conradson, D.L. Clark, L.P. Juan, S.A. Kozimor, R.L. Martin, S.G. Minasian, A.C. Olson, B.L. Scott, D.K. Shuh, T. Tylliszczak, M.P. Wilkerson, R.A. Zehnder, “Covalency in Lanthanides. An X-ray Absorption Spectroscopy and Density”, *J. Am. Chem. Soc.* **2015**, *137*, 2506–2523.

- [190] A. Kerridge, “f-Orbital covalency in the actinocenes (An = Th–Cm): Multiconfigurational studies and topological analysis”, *RSC Adv.* **2014**, *4*, 12078–12086.
- [191] Q.-R. Huang, J.R. Kingham, N. Kaltsoyannis, “The strength of actinide-element bonds from the quantum theory of atoms-in-molecules”, *Dalton Trans.* **2015**, *44*, 2554–2566.
- [192] A. Wilden, G. Modolo, P. Kaufholz, F. Sadowski, S. Lange, D. Munzel, A. Geist, “Process Development and Laboratory-Scale Demonstration of a Regular-SANEX Process Using C5-BPP (2,6-Bis(5-(2,2-dimethylpropyl)-1H-pyrazol-3-yl)pyridine)”, *Sep. Sci. Technol.* **2015**, *50*, 2467–2475.
- [193] M. Blum, L. Weinhardt, O. Fuchs, M. Bär, Y. Zhang, M. Weigand, S. Krause, S. Pookpanratana, T. Hofmann, W. Yang, J.D. Denlinger, E. Umbach, C. Heske, “Solid and liquid spectroscopic analysis (SALSA)—a soft x-ray spectroscopy endstation with a novel flow-through liquid cell”, *Rev. Sci. Instrum.* **2009**, *80*, 123102.
- [194] B.L. Henke, E.M. Gullikson, J.C. Davis, “X-Ray Interactions: Photoabsorption, Scattering, Transmission, and Reflection at  $E = 50\text{--}30,000$  eV,  $Z = 1\text{--}92$ ”, *At. Data Nucl. Data Tables* **1993**, *54*, 181–342.
- [195] D.T. Bowron, M.H. Krisch, A.C. Barnes, J.L. Finney, A. Kaprolat, M. Lorenzen, “X-ray-Raman scattering from the oxygen K edge in liquid and solid  $\text{H}_2\text{O}$ ”, *Phys. Rev. B* **2000**, *62*, R9223–R9227.
- [196] U. Bergmann, P. Wernet, P. Glatzel, M. Cavalleri, L.G.M. Pettersson, A. Nilsson, S.P. Cramer, “X-ray Raman spectroscopy at the oxygen K edge of water and ice: Implications on local structure models”, *Phys. Rev. B* **2002**, *66*, 92107.
- [197] L.-A. Näslund, J. Luning, Y. Ufuktepe, H. Ogasawara, P. Wernet, U. Bergmann, L.G.M. Pettersson, A. Nilsson, “X-ray absorption spectroscopy measurements of liquid water”, *J. Phys. Chem. B* **2005**, *109*, 13835–13839.
- [198] U. Bergmann, A. Di Cicco, P. Wernet, E. Principi, P. Glatzel, A. Nilsson, “Nearest-neighbor oxygen distances in liquid water and ice observed by x-ray Raman based extended x-ray absorption fine structure”, *J. Chem. Phys.* **2007**, *127*, 174504.

- [199] I. Juurinen, T. Pylkkänen, C.J. Sahle, L. Simonelli, K. Hämäläinen, S. Huotari, M. Hakala, “Effect of the Hydrophobic Alcohol Chain Length on the Hydrogen-Bond Network of Water”, *J. Phys. Chem. B* **2014**, *118*, 8750–8755.
- [200] T.T. Fister, K.P. Nagle, F.D. Vila, G.T. Seidler, C. Hamner, J.O. Cross, J.J. Rehr, “Intermediate-range order in water ices: Nonresonant inelastic x-ray scattering measurements and real-space full multiple scattering calculations”, *Phys. Rev. B* **2009**, *79*, 174117.
- [201] Y. Zubavichus, M. Zharnikov, Y.-J. Yang, O. Fuchs, E. Umbach, C. Heske, M. Grunze, “Oxygen K-edge X-ray absorption fine structure studies of vacuum-deposited ice films”, *Langmuir* **2006**, *22*, 7241–7247.
- [202] M.A. Centeno, P. Malet, I. Carrizosa, J.A. Odriozola, “Lanthanide Doped V<sub>2</sub>O<sub>5</sub>/Al<sub>2</sub>O<sub>3</sub> Catalysts: Structure-Activity Relationship in the SCR of NO<sub>x</sub>”, *J. Phys. Chem. B* **2000**, *104*, 3310–3319.
- [203] H. Asakura, T. Shishido, S. Fuchi, K. Teramura, T. Tanaka, “Local Structure of Pr, Nd, and Sm Complex Oxides and Their X-ray Absorption Near Edge Structure Spectra”, *J. Phys. Chem. C* **2014**, *118*, 20881–20888.
- [204] H. Asakura, T. Shishido, K. Teramura, T. Tanaka, “Local Structure and L<sub>1</sub>- and L<sub>3</sub>-Edge X-ray Absorption Near Edge Structure of Late Lanthanide Elements (Ho, Er, Yb) in Their Complex Oxides”, *J. Phys. Chem. C* **2015**, *119*, 8070–8077.
- [205] J.-P. Rueff, “High pressure electronic properties in the light of inelastic X-ray scattering”, *Eur. Phys. J. Special Topics* **2009**, *169*, 215–220.
- [206] S. Heathman, J.-P. Rueff, L. Simonelli, M.A. Denecke, J.-C. Griveau, R. Caciuffo, G.H. Lander, “Resonant x-ray emission spectroscopy at the L<sub>3</sub> edge of americium up to 23 GPa”, *Phys. Rev. B* **2010**, *82*, 201103.
- [207] N.F. Mott, “The Basis of the Electron Theory of Metals, with Special Reference to the Transition Metals”, *Proc. Phys. Soc. A* **1949**, *62*, 416–422.

- [208] A. Bianconi, A. Marcelli, H. Dexpert, R. Karnatak, A. Kotani, T. Jo, J. Petiau, “Specific intermediate-valence state of insulating 4 f compounds detected by  $L_3$  x-ray absorption”, *Phys. Rev. B* **1987**, *35*, 806–812.
- [209] P. Carra, M. Altarelli, “Dichroism in the x-ray absorption spectra of magnetically ordered systems”, *Phys. Rev. Lett.* **1990**, *64*, 1286–1288.
- [210] S. Tanaka, K. Okada, A. Kotani, “Resonant X-Ray Emission Spectroscopy in Dy Compounds”, *J. Phys. Soc. Jpn.* **1994**, *63*, 2780–2787.
- [211] P. Carra, M. Fabrizio, B. Thole, “High Resolution X-Ray Resonant Raman Scattering”, *Phys. Rev. Lett.* **1995**, *74*, 3700–3703.
- [212] F. Bartolomé, J.-M. Tonnerre, L. Sève, D. Raoux, J. Chaboy, L.M. García, M.H. Krisch, C.C. Kao, “Identification of Quadrupolar Excitation Channels at the  $L_3$  Edge of Rare-Earth Compounds”, *Phys. Rev. Lett.* **1997**, *79*, 3775–3778.
- [213] F. Bartolomé, M.H. Krisch, D. Raoux, J.-M. Tonnerre, “Quadrupolar excitation channels at the  $L_3$  edge of rare-earth ions probed by resonant inelastic x-ray scattering”, *Phys. Rev. B* **1999**, *60*, 13497–13506.
- [214] J.-J. Gallet, J.-M. Mariot, L. Journal, C.F. Hague, A. Rogalev, H. Ogasawara, A. Kotani, M. Sacchi, “Resonant inelastic x-ray scattering at the  $L_3$  edge of samarium”, *Phys. Rev. B* **1999**, *60*, 14128–14131.
- [215] C. Dallera, M.H. Krisch, A. Rogalev, C. Gauthier, J. Goulon, F. Sette, A. Sole, “Resonant inelastic x-ray scattering at the  $L_2$  and  $L_3$  edge of terbium in  $TbCo_2$  and  $TbF_3$ ”, *Phys. Rev. B* **2000**, *62*, 7093–7097.
- [216] C. Dallera, M. Grioni, A. Shukla, G. Vankó, J. Sarrao, J.-P. Rueff, D. Cox, “New Spectroscopy Solves an Old Puzzle: The Kondo Scale in Heavy Fermions”, *Phys. Rev. Lett.* **2002**, *88*, 196403.
- [217] L. Journal, J.-M. Mariot, J.-P. Rueff, C.F. Hague, G. Krill, M. Nakazawa, A. Kotani, A. Rogalev, F. Wilhelm, J.-P. Kappler, G. Schmerber, “Resonant inelastic x-ray scattering at the lanthanum  $L_3$  edge”, *Phys. Rev. B* **2002**, *66*, 45106.
- [218] M. Nakazawa, K. Fukui, H. Ogasawara, A. Kotani, C. Hague, “X-ray absorption and resonant x-ray emission spectra by electric quadrupole excitation in light rare-earth systems”, *Phys. Rev. B* **2002**, *66*, 113104.

- [219] C. Dallera, E. Annese, J.-P. Rueff, A. Palenzona, G. Vankó, L. Braicovich, A. Shukla, M. Grioni, “Determination of pressure-induced valence changes in  $\text{YbAl}_2$  by resonant inelastic x-ray emission”, *Phys. Rev. B* **2003**, *68*, 245114.
- [220] C. Dallera, M. Grioni, A. Palenzona, M. Taguchi, E. Annese, G. Ghiringhelli, A. Tagliaferri, N. Brookes, T. Neisius, L. Braicovich, “ $\alpha$ - $\gamma$  transition in metallic Ce studied by resonant x-ray spectroscopies”, *Phys. Rev. B* **2004**, *70*, 85112.
- [221] J.-P. Rueff, C. Hague, J.-M. Mariot, L. Journel, R. Delaunay, J.-P. Kappler, G. Schmerber, A. Derory, N. Jaouen, G. Krill, “f-State Occupancy at the  $\gamma$ - $\alpha$  Phase Transition of Ce-Th and Ce-Sc Alloys”, *Phys. Rev. Lett.* **2004**, *93*, 67402.
- [222] P. Glatzel, F.M.F. de Groot, O. Manoilova, D. Grandjean, B. Weckhuysen, U. Bergmann, R. Barrea, “Range-extended EXAFS at the L edge of rare earths using high-energy-resolution fluorescence detection: A study of La in  $\text{LaOCl}$ ”, *Phys. Rev. B* **2005**, *72*, 14117.
- [223] T. Sham, R. Gordon, S. Heald, “Resonant inelastic x-ray scattering at the Ce  $L_3$  edge of  $\text{CePO}_4$  and  $\text{CeO}_2$ : Implications for the valence of  $\text{CeO}_2$  and related phenomena”, *Phys. Rev. B* **2005**, *72*, 35113.
- [224] C. Dallera, O. Wessely, M. Colarieti-Tosti, O. Eriksson, R. Ahuja, B. Johansson, M. Katsnelson, E. Annese, J.-P. Rueff, G. Vankó, L. Braicovich, M. Grioni, “Understanding mixed valent materials: Effects of dynamical core-hole screening in high-pressure x-ray spectroscopy”, *Phys. Rev. B* **2006**, *74*, 81101.
- [225] J.-P. Rueff, J.-P. Itié, M. Taguchi, C. Hague, J.-M. Mariot, R. Delaunay, J.-P. Kappler, N. Jaouen, “Probing the  $\gamma$ - $\alpha$  Transition in Bulk Ce under Pressure: A Direct Investigation by Resonant Inelastic X-Ray Scattering”, *Phys. Rev. Lett.* **2006**, *96*, 237403.
- [226] H. Yamaoka, M. Taguchi, A. M. Vlaicu, H. Oohashi, K. Yokoi, D. Horiguchi, T. Tochio, Y. Ito, K. Kawatsura, K. Yamamoto, A. Chainani, S. Shin, M. Shiga, H. Wada, “Resonant Inelastic X-ray Scattering of  $\text{EuNi}_2(\text{Si}_{1-x}\text{Ge}_x)_2$  and  $\text{Eu}_2\text{O}_3$  at Eu  $L_3$  Absorption Edge”, *J. Phys. Soc. Jpn.* **2006**, *75*, 34702.

- [227] C. Brouder, A. Juhin, A. Bordage, M.-A. Arrio, “Site symmetry and crystal symmetry: a spherical tensor analysis”, *J. Phys. Condens. Matter.* **2008**, *20*, 455205.
- [228] A. Kotani, “Unified theory of x-ray magnetic circular dichroism at  $L_{2,3}$  absorption edges for a series of Ce compounds”, *Phys. Rev. B* **2008**, *78*, 195115.
- [229] A. Severing, E. Holland-Moritz, B. Rainford, S. Culverhouse, B. Frick, “Crystal-field excitations in  $CeX_2Si_2$  ( $X=Au, Ag, Pd, \text{ and } Ru$ )”, *Phys. Rev. B* **1989**, *39*, 2557–2561.
- [230] P. Hansmann, A. Severing, Z. Hu, M. Haverkort, C. Chang, S. Klein, A. Tanaka, H. Hsieh, H.-J. Lin, C. Chen, B. Fåk, P. Lejay, L. Tjeng, “Determining the Crystal-Field Ground State in Rare Earth Heavy Fermion Materials Using Soft-X-Ray Absorption Spectroscopy”, *Phys. Rev. Lett.* **2008**, *100*, 66405.
- [231] K.O. Kvashnina, Y.O. Kvashnin, S.M. Butorin, “Role of resonant inelastic X-ray scattering in high-resolution core-level spectroscopy of actinide materials”, *J. Electron. Spectrosc. Relat. Phenom.* **2014**, *194*, 27–36.
- [232] E.J. McGuire, “Atomic M-Shell Coster-Kronig, Auger, and Radiative Rates, and Fluorescence Yields for Ca-Th”, *Phys. Rev. A* **1972**, *5*, 1043–1047.
- [233] E.J. McGuire, “Atomic N-shell Coster - Kronig, Auger, and radiative rates and fluorescence yields for  $38 < Z < 103$ ”, *Phys. Rev. A* **1974**, *9*, 1840–1851.
- [234] E. Seifert, “OriginPro 9.1: scientific data analysis and graphing software-software review”, *J. Chem. Inf. Model.* **2014**, *54*, 1552.
- [235] *Origin PeakAnalyzer*, <http://www.originlab.com/doc/Origin-Help/FindPeak-PA> (visited on 05/26/2015).
- [236] R.D. Shannon, “Revised effective ionic radii and systematic studies of interatomic distances in halides and chalcogenides”, *Acta. Cryst. A* **1976**, *32*, 751–767.
- [237] F. David, “Thermodynamic properties of lanthanide and actinide ions in aqueous solution”, *Journal of the Less Common Metals* **1986**, *121*, 27–42.

- [238] A. Abbasi, P. Lindqvist-Reis, L. Eriksson, D. Sandström, S. Lidin, I. Persson, M. Sandström, “Highly hydrated cations: deficiency, mobility, and coordination of water in crystalline nonahydrated scandium(III), yttrium(III), and lanthanoid(III) trifluoromethanesulfonates”, *Chem. Eur. J.* **2005**, *11*, 4065–4077.
- [239] T. Prüßmann, M.A. Denecke, A. Geist, J. Rothe, P. Lindqvist-Reis, M.W. Löble, F. Breher, D.R. Batchelor, C. Apostolidis, O. Walter, W.A. Caliebe, K.O. Kvashnina, K. Jorissen, J.J. Kas, J.J. Rehr, T. Vitova, “Comparative investigation of N donor ligand-lanthanide complexes from the metal and ligand point of view”, *J. Phys.: Conf. Ser.* **2013**, *430*, 12115.



# List of Figures

1.1.	Ingestion radiotoxicity of one ton used nuclear fuel based on ICRP72 effective dose coefficients. . . . .	2
2.1.	The photoelectric effect where an X-ray photon is absorbed by a core-shell electron that is ejected, i.e. excited into the continuum. This is followed by the relaxation of the atom via X-ray fluorescence ( $K_\alpha$ or $K_\beta$ ) or the Auger effect. . . . .	8
2.2.	Schematic example spectrum showing pre-edge, WL, XANES and EXAFS region. . . . .	9
2.3.	Schematic diagram of different RIXS processes. . . . .	12
2.4.	RIXS map of $\text{Ho}(\text{OTf})_3$ with intermediate ( $\Gamma_{INT}$ ) and final state ( $\Gamma_{FIN}$ ) broadenings (solid lines) and HR-XANES (dashed line). . . . .	13
2.5.	Standard and HR-XANES of $[\text{Eu}(n\text{-Pr-BTP})_3](\text{OTf})_3$ . . . . .	16
2.6.	Scheme of a typical synchrotron radiation facility with (1) an electron gun, (2) a linear accelerator, (3) a booster ring, (4) a storage ring and (5) several beamlines. . . . .	17
2.7.	Scheme of the (exaggerated) electron paths and emitted radiation in wiggler and undulator (a) and the spectral brilliance of wiggler and undulator compared to a standard bending magnet (b). . . . .	19
2.8.	Schematic view of a typical XAS beamline (angles and distances are not to scale). . . . .	19
2.9.	3D CAD model with part of the He environment (left) and photo of the MAC-Spectrometer during initial mechanical performance tests (right). . . . .	21
2.10.	Scheme of the Johann geometry. . . . .	22
2.11.	Crystal positioning stages with four degrees of freedom. . . . .	23

2.12. Example of the Cu $K\alpha_1$ fluorescence focused on the Medipix detector with one crystal. . . . .	25
2.13. Experimental setup for U $L_3$ edge HR-XANES measurements with the Vortex detector. . . . .	25
2.14. U $L_3$ edge HR-XANES 30 min (black) and 3 h measurement time (red) and standard transmission mode (green) spectra of Metastudtite. . . . .	26
2.15. Emission energies and the corresponding analyzer crystals and Bragg angles for An $L\alpha_1$ (a) and An $M\alpha/M\beta$ (b) emission lines. Ge(311) and Ge(220) are marked with dash lines, as they are currently not available. . . . .	27
2.16. He environment for the HR-XANES spectrometer at the INE-Beamline (a). Transfer lock for the He environment (b). . . . .	28
2.17. $3d4f$ RIXS map of $\text{Pu}^{6+}$ in aqueous solution. . . . .	28
3.1. $n$ -Pr-BTP . . . . .	31
3.2. CA-BTP . . . . .	32
3.3. $\text{CyMe}_4$ -BTBP . . . . .	32
3.4. Et-BDP . . . . .	32
3.5. C5-BPP . . . . .	33
3.6. $An/Ln(\text{H-BTP})_3$ . . . . .	33
3.7. N K edge spectra of $[\text{Ho}(n\text{-Pr-BTP})_3](\text{NO}_3)_3$ measured in different detection modes. . . . .	36
3.8. N K edge spectra of $n$ -Pr-BTP measured at the UE52-PGM beamline at BESSY and at the WERA-Beamline at ANKA. . . . .	37
3.9. The effects of radiation damage in $[\text{Ho}(n\text{-Pr-BTP})_3](\text{ClO}_4)_3$ N K edge spectra after irradiation of the samples. . . . .	38
3.10. The contribution of $\text{NO}_3^-$ to $[\text{Ln}(n\text{-Pr-BTP})_3](\text{NO}_3)_3$ N K edge spectra. . . . .	38
3.11. LERIX spectrometer at the 20-ID beamline at the APS. . . . .	39
3.12. Constant-liquid-flow cell for NRIXS measurements. . . . .	40
3.13. NRIXS spectrometer at the ID20 beamline at the ESRF. . . . .	41
3.14. Optical microscopy image and STXM image (inset) of $[\text{Am}(n\text{-Pr-BTP})_3](\text{OTf})_3$ . . . . .	42
3.15. Comparison of $L_3$ edge HR-XANES spectra of $[\text{Pr}(n\text{-Pr-BTP})_3](\text{OTf})_3$ in crystalline form and in solution. . . . .	46

---

3.16. $k^2$ weighted $L_3$ edge EXAFS (left) of $[\text{Eu}(n\text{-Pr-BTP})_3](\text{OTf})_3$ in solution (top) and crystalline (bottom) and their corresponding Fourier transform data (right). . . . .	47
3.17. $k^2$ weighted $L_3$ edge EXAFS (left) of $[\text{Ho}(n\text{-Pr-BTP})_3](\text{OTf})_3$ in solution (top) and crystalline (bottom) and their corresponding Fourier transform data (right). . . . .	49
3.18. $k^2$ weighted $L_3$ edge EXAFS (left) of $[\text{Pu}(n\text{-Pr-BTP})_3](\text{OTf})_3$ in solution (top) and crystalline (bottom) and their corresponding Fourier transform data (right). . . . .	50
4.1. Simplified MO scheme of $An/Ln$ bound to N and the excitations generating the pre-edge (red), WL (blue) and EXAFS (green) features observed in N K edge spectra. . . . .	60
4.2. Pre-edge <b>A</b> and WL <b>B</b> of the N K edge XANES of $n\text{-Pr-BTP}$ . The energy position of the ionization potential is marked by a line. . . . .	61
4.3. Unoccupied MOs of $\text{La}(\text{H-BTP})_3$ with N $2p$ , C $2p$ , La $6s$ , La $7s$ , La $5d$ and La $4f$ contributions. . . . .	64
4.4. Unoccupied MOs of $\text{Ac}(\text{H-BTP})_3$ with N $2p$ , C $2p$ , Ac $7s$ , Ac $6d$ and Ac $5f$ contributions. . . . .	64
4.5. Distribution ratios for lanthanide extraction to the organic phase with a BTP ligand. . . . .	65
4.6. Comparison of the pre-edge features of different $[An/Ln(n\text{-Pr-BTP})_3](\text{OTf})_3$ compounds. . . . .	66
4.7. An example of the pre-edge of N K edge XANES pre-peak modeled with PV functions. . . . .	67
4.8. Peak positions of $n\text{-Pr-BTP}$ and $An/Ln(n\text{-Pr-BTP})_3$ complexes with different counter-ions. The colors of the $n\text{-Pr-BTP}$ peak positions mark the beamline at which they were measured. . . . .	67
4.9. Energy difference between peaks <b>1</b> and <b>2</b> as shown in figure 4.7 for different $[Ln/An(n\text{-Pr-BTP})_3](\text{OTf})_3$ complexes and $n\text{-Pr-BTP}$ (a) and areas of peaks <b>1</b> and <b>2</b> for $n\text{-Pr-BTP}$ and $[Ln/\text{Pu}(n\text{-Pr-BTP})_3](\text{OTf})_3$ (b). . . . .	68
4.10. $[\text{Pr}(n\text{-Pr-BTP})_3](\text{OTf})_3$ N K edge spectra from different measurement campaigns. . . . .	69
4.11. Calculations of H-BTP with different methods and programs. Assignment of N according to figure 4.12. . . . .	71

4.12. Color coded assignment of excitations to different N in H-BTP.	72
4.13. Calculations of non-equivalent N in La(H-BTP) <sub>3</sub> (solid lines) and Ac(H-BTP) <sub>3</sub> (dashed lines). Assignment of N according to figure 4.12. . . . .	72
4.14. N 2 <i>p</i> contributions to the spectrum of La(H-BTP) <sub>3</sub> . Assignment of N according to figure 4.12. . . . .	73
4.15. N 2 <i>p</i> contributions to the spectrum of Ac(H-BTP) <sub>3</sub> . Assignment of N according to figure 4.12. . . . .	74
4.16. La 4 <i>f</i> contributions to the spectrum of La(H-BTP) <sub>3</sub> . Assignment of N according to figure 4.12. . . . .	75
4.17. N K edge spectra of <i>n</i> -Pr-BTP, CA-BTP, CyMe <sub>4</sub> -BTBP and Et-BDP. Spectra are vertically shifted for clarity. . . . .	76
4.18. Schematic structures of <i>n</i> -Pr-BTP, Et-BDP, CyMe <sub>4</sub> -BTBP and CA-BTP. . . . .	76
4.19. N K edge spectra of <i>n</i> -Pr-BTP and C5-BPP (a) and different [Ln(C5-BPP) <sub>3</sub> ](OTf) <sub>3</sub> (b). . . . .	77
4.20. TD-DFT calculations of N K edge XANES spectra for C5-BPP (black) and for different N atoms in C5-BPP. Color assignment according to figure 4.21. . . . .	78
4.21. Color code for the different N in the BPP ligand. . . . .	79
4.22. O K edge spectra of isopropanol (a) and water (b). N K edge spectrum of <i>n</i> -Pr-BTP. (c) . . . . .	80
4.23. N K edge spectra of <i>n</i> -Pr-BTP crystalline and in isopropanol solution. . . . .	81
4.24. Simplified MO scheme of <i>An/Ln</i> bound to N and the excitations causing the pre-edge (red), WL (blue) and EXAFS (green) features observed in <i>An/Ln</i> L <sub>3</sub> edge spectra. . . . .	86
4.25. Gd L <sub>3</sub> edge HR-XANES of [Gd( <i>n</i> -Pr-BTP) <sub>3</sub> ](OTf) <sub>3</sub> measured at the Gd Lα <sub>1</sub> and Lβ <sub>2</sub> emission line. . . . .	87
4.26. Normalized 2 <i>p</i> 3 <i>d</i> (a) and 2 <i>p</i> 4 <i>d</i> (b) RIXS pre-edge maps of [Gd( <i>n</i> -Pr-BTP) <sub>3</sub> ](OTf) <sub>3</sub> with XANES position (red line). . . . .	88
4.27. Normalized VB-RIXS of [Ho( <i>n</i> -Pr-BTP) <sub>3</sub> ](OTf) <sub>3</sub> , [Ho(CyMe <sub>4</sub> -BTBP) <sub>3</sub> ](OTf) <sub>3</sub> , Ho(NO <sub>3</sub> ) <sub>3</sub> and Ho <sub>2</sub> O <sub>3</sub> (a); fitted energy position and FWHM of the peak shown in (a) (b). . . . .	89
4.28. Calculations of [Eu( <i>n</i> -Pr-BTP) <sub>3</sub> ](OTf) <sub>3</sub> with <i>FEFF</i> (red) and <i>FDMNES</i> with FMS (blue) and FP (green) compared the experimental spectrum (black). . . . .	91

---

4.29. Calculations of $[\text{Eu}(n\text{-Pr-BTP})_3](\text{OTf})_3$ with <i>FEFF</i> (red) and <i>FDMNES</i> with experimental and DFT optimized structures compared the experimental spectrum. . . . .	92
4.30. $[\text{Gd}(n\text{-Pr-BTP})_3](\text{OTf})_3$ experimental spectrum compared to $\text{Gd}(\text{H-BTP})_3$ spectra calculated with <i>FEFF</i> and <i>FDMNES</i> for DFT optimized structures with symmetry restrictions (structure <b>1</b> ), without symmetry restrictions (structure <b>2</b> ) and without symmetry restrictions and a solvation sphere (structure <b>3</b> ). . . . .	93
4.31. Angles $\alpha$ (a) and $\beta$ (b) describing the in-plane and out-of-plane angles of the triazine rings compared to the pyridine rings. . .	95
4.32. <i>FEFF</i> shell-by-shell calculations of $\text{Gd}(\text{H-BTP})_3$ compared with an experimental $[\text{Gd}(n\text{-Pr-BTP})_3](\text{OTf})_3$ spectrum. . . .	96
4.33. The four shells used in the shell-by-shell calculations in figure 4.32. . . . .	96
4.34. $\text{Gd L}_3$ edge HR-XANES of $[\text{Gd}(n\text{-Pr-BTP})_3](\text{NO}_3)_3$ and $\text{Gd}(\text{NO}_3)_3$ (a) and $[\text{Gd}(n\text{-Pr-BTP})_3](\text{OTf})_3$ and $\text{Gd}(\text{OTf})_3$ (b). . . . .	97
4.35. Pre-edge calculated with <i>FEFF9.5</i> (a) and <i>FDMNES</i> (b) for $\text{Gd}(\text{H-BTP})_3$ , including $\text{Gd } f\text{-}, d\text{-DOS}$ compared to experimental spectra of $[\text{Gd}(n\text{-Pr-BTP})_3](\text{OTf})_3$ . . . . .	98
4.36. Pre-edge region of different $[\text{Ln}(n\text{-Pr-BTP})_3](\text{OTf})_3$ and $\text{Ln}(\text{OTf})_3$ HR-XANES spectra. . . . .	100
4.37. Post-edge region of $[\text{Ln}(n\text{-Pr-BTP})_3](\text{OTf})_3$ and $\text{Ln}(\text{OTf})_3$ HR-XANES spectra. . . . .	101
4.38. Distance between <b>B</b> ( <b>C</b> ) and WL for $[\text{Ln}(n\text{-Pr-BTP})_3](\text{OTf})_3$ and $\text{Ln}(\text{OTf})_3$ , respectively (a) and distance between <b>D</b> <sub>2</sub> and WL for $[\text{Ln}(n\text{-Pr-BTP})_3](\text{OTf})_3$ and $\text{Ln}(\text{OTf})_3$ (b). . . . .	102
4.39. Peak assignment in experimental $[\text{Pr}(n\text{-Pr-BTP})_3](\text{OTf})_3$ and calculated $\text{Pr}(\text{H-BTP})$ spectra (a) and the contribution of different types of single scattering (SS) and multiple scattering (MS) paths to the spectrum of $\text{Pr}(\text{H-BTP})$ (b). . . . .	103
4.40. The contribution of single scattering (SS) and multiple scattering (MS) paths to the spectrum of $\text{La}(\text{OTf})_3$ (a) and position of <b>B</b> in calculated and experimental spectra (b). . . . .	105

4.41. <i>FEFF</i> calculated positions of <b>B</b> (a) and <b>D</b> <sub>2</sub> (b) in <i>k</i> for <i>Ln</i> (H-BTP) with different <i>Ln</i> /different structures (black, system <b>1</b> ), different <i>Ln</i> /La(H-BTP) structure (red, system <b>2</b> ) and La/different structures (blue, system <b>3</b> ). . . . .	106
4.42. Difference between the phase $\phi(k)$ and the scattering path length <i>R</i> contributions to the EXAFS equation. . . . .	107
4.43. Positions of <b>C</b> (a) and <b>D</b> <sub>2</sub> (b) in <i>k</i> for <i>Ln</i> (OTf) <sub>3</sub> with different <i>Ln</i> /different structures (black, system <b>1</b> ), different <i>Ln</i> /La(OTf) <sub>3</sub> structure (red, system <b>2</b> ) and La/different structures (blue, system <b>3</b> ) calculated with <i>FEFF</i> . . . . .	107
4.44. <i>FDMNES</i> XANES calculations of different <i>Ln</i> (H-BTP) <sub>3</sub> complexes with optimized structures. . . . .	108
4.45. <i>FDMNES</i> calculated positions of <b>B</b> (a) and <b>D</b> <sub>2</sub> (b) for <i>Ln</i> (H-BTP) <sub>3</sub> with different <i>Ln</i> /different structures (black, system <b>1</b> ), different <i>Ln</i> /La(H-BTP) <sub>3</sub> structure (red, system <b>2</b> ) and La/different structures (blue, system <b>3</b> ). . . . .	109
4.46. Positions of <b>C</b> (a) and <b>D</b> <sub>2</sub> (b) in <i>k</i> for <i>Ln</i> (OTf) <sub>3</sub> with different <i>Ln</i> /different structures (black, system <b>1</b> ), different <i>Ln</i> /La(OTf) <sub>3</sub> structure (red, system <b>2</b> ) and La/different structures (blue, system <b>3</b> ) calculated with <i>FDMNES</i> . . . . .	110
4.47. Pu L <sub>3</sub> edge HR-XANES of [Pu( <i>n</i> -Pr-BTP) <sub>3</sub> ](NO <sub>3</sub> ) <sub>3</sub> and Pu(NO <sub>3</sub> ) <sub>3</sub> ; Pu L <sub>3</sub> edge XANES of [Pu( <i>n</i> -Pr-BTP) <sub>3</sub> ](NO <sub>3</sub> ) <sub>3</sub> ; <i>FDMNES</i> calculations of Pu(H-BTP) <sub>3</sub> XANES and DOS. . . . .	111
4.48. Am L <sub>3</sub> edge HR-XANES of [Am( <i>n</i> -Pr-BTP) <sub>3</sub> ](NO <sub>3</sub> ) <sub>3</sub> and Am(NO <sub>3</sub> ) <sub>3</sub> . . . . .	112
4.49. Experimental spectra of [Pu( <i>n</i> -Pr-BTP) <sub>3</sub> ](NO <sub>3</sub> ) <sub>3</sub> and [Am( <i>n</i> -Pr-BTP) <sub>3</sub> ](NO <sub>3</sub> ) <sub>3</sub> (a) and spectra calculated with <i>FDMNES</i> of Pu(H-BTP) <sub>3</sub> and Am(H-BTP) <sub>3</sub> (b). . . . .	113

# List of Tables

3.1.	Sample composition for $An$ HR-XANES measurements. . . . .	44
3.2.	The crystals and Bragg angles $\theta$ used for $Ln$ $L_3$ edge HR-XANES.	44
3.3.	The crystals and Bragg angles $\theta$ used for $Ln$ $L_3$ edge HR-XANES in solution. . . . .	45
3.4.	Parameters of EXAFS fit of $[Eu(n-Pr-BTP)_3](OTf)_3$ in solution.	48
3.5.	Parameters of EXAFS fit of crystalline $[Eu(n-Pr-BTP)_3](OTf)_3$ .	48
3.6.	Parameters of EXAFS fit of $[Ho(n-Pr-BTP)_3](OTf)_3$ in solution.	48
3.7.	Parameters of EXAFS fit of crystalline $[Ho(n-Pr-BTP)_3](OTf)_3$ .	48
3.8.	Parameters of EXAFS fit of $[Pu(n-Pr-BTP)_3](OTf)_3$ in solution.	51
3.9.	Parameters of EXAFS fit of crystalline $[Pu(n-Pr-BTP)_3](OTf)_3$ .	51
3.10.	The emission line, emission energy, crystal and angle $\theta$ at which the HR-XANES spectra were measured. $\Gamma_{INT}$ and $\Gamma_{FIN}$ are the intermediate and final state core-hole lifetime broadening (taken from <i>FEFF9.6</i> ) and $\Gamma_{APP}$ is the resulting spectral broadening. $E_{INC}$ and $E_{EM}$ are the beamline and spectrometer broadening and $E_{TOT}$ is the total theoretical experimental broadening. $\Gamma_{TOT}$ is the combined spectral and experimental broadening. $E_{INC}$ for $Ln$ is calculated with $\Delta E/E = 3 * 10^{-5}$ and for $An$ with $\Delta E/E = 2 * 10^{-4}$ . . . . .	52
3.11.	$Ln/An$ -ligand bond length $R$ . Calculated values are for $Ln/An(H-BTP)_3$ , EXAFS bond length as found in literature for $Ln/An(n-Pr-BTP)_3$ with estimated uncertainties. . . . .	54
4.1.	Angles $\alpha$ and $\beta$ as shown in figure 4.31 and bond length $R$ for differently optimized structures. Structures were optimized using DFT with symmetry restrictions (structure <b>1</b> ), without symmetry restrictions (structure <b>2</b> ) and without symmetry restrictions and a solvation sphere (structure <b>3</b> ). . . . .	94



# List of Abbreviations

**ADC(2)** second order Algebraic Diagrammatic Construction

**ADF** Amsterdam Density Functional

**ALS** Advanced Light Source

**An** actinide

**ANKA** Angströmquelle Karlsruhe

**APD** avalanche photodiode

**APS** Advanced Photon Source

**C5-BPP** 2,6-Bis(5-(2,2-dimethylpropyl)-1H-pyrazol-3-yl)-pyridine

***n*-Pr-BTP** 2,6-bis(5,6-dipropyl-1,2,4-triazin-3-yl)-pyridine

**CA-BTP** bis-2,6-(5,6,7,8-tetra-hydro-5,9,9-tri-methyl-5,8-methano-1,2,4-ben-zo-triazin-3-yl)-pyridine

**CASSCF** complete-active-space self-consistent field

**CyMe<sub>4</sub>-BTBP** 6,6'-bis(5,5,8,8- tetramethyl-5,6,7,8-tetrahydrobenzo-1,2,4-tri-azin-3-yl)-2,2'-bipyridine

**CyMe<sub>4</sub>-BTP** 6,6'-bis(5,5,8,8- tetramethyl-5,6,7,8-tetrahydrobenzo-1,2,4-tri-azin-3-yl)-pyridine

**DCM** double crystal monochromator

**DFT** density functional theory

**DOS** density of states

**ESRF** European Synchrotron Radiation Facility

- Et-BDP** 6-bis(4-ethyl-pyridazin-1-yl)-pyridine
- EXAFS** extended X-ray absorption fine structure
- FMS** full multiple scattering
- FP** full potential
- FWHM** full width at half maximum
- HASYLAB** Hamburger Synchrotronlabor
- H-BTP** 2, 6-bis-(1,2,4-triazin-3-yl)-pyridine
- HLW** high-level waste
- HR-XANES** high-energy resolution XANES
- HRXES** high-energy resolution X-ray emission spectroscopy
- INE** Institute for Nuclear Waste Disposal
- ITU** Institute for Transuranium Elements
- IXS** inelastic X-ray scattering
- LERIX** Lower Energy Resolution Inelastic X-ray scattering
- Ln*** lanthanide
- LUMO** lowest unoccupied molecular orbital
- LWR** light water reactor
- MAC** multi analyzer crystal
- MD** Molecular Dynamics
- MO** molecular orbital
- MS** multiple scattering
- NEXAFS** near edge X-ray absorption fine structure
- NMR** nuclear magnetic resonance
- NRIXS** non-resonant inelastic X-ray scattering
- OTf**  $\text{CF}_3\text{SO}_3^-$

- 
- PEY** partial electron yield
- PGM** plane grating monochromator
- P&T** Partitioning and Transmutation
- PV** pseudo-Voigt
- QTAIM** quantum theory of atoms in molecules
- RF** radio frequency
- RI** resolution-of-the-identity
- RIXS** resonant inelastic X-ray scattering
- SCF** self-consistent field
- SO coupling** spin-orbit coupling
- STXM** scanning transmission X-ray microscopy
- TD-DFT** time dependent density functional theory
- TEY** total electron yield
- TRLFS** time-resolved laser fluorescence spectroscopy
- VB** valence band
- VB-RIXS** valence band RIXS
- WL** white line
- XANES** X-ray absorption near edge structure
- XAS** X-ray absorption spectroscopy
- XES** X-ray emission spectroscopy
- XPS** X-ray photoelectron spectroscopy
- XRD** X-ray diffraction



# Acknowledgments

I would like to thank:

Dr. T. Vitova and Prof. Dr. H. Geckeis for the opportunity to work at the Institute for Nuclear Waste Disposal.

Dr. T. Vitova for the support and discussions over all the years, for teaching me how X-ray absorption experiments work and traveling around the world with me for beamtimes.

Prof. Dr. P. Panak for agreeing to be co-examiner.

Dr. J. Rothe and Dr. K. Dardenne for allowing the spectrometer to be built at the INE-Beamline, for support during the experiments at the INE-Beamline and for always being ready to help with anything.

Dr. A. Geist for introducing me to P&T and for synthesizing  $[\text{Am}(n\text{-Pr-BTP})_3](\text{OTf})_3$ .

Dr. P. Lindqvist-Reis for sharing his knowledge about lanthanides.

U. Müllich, Dr. A. Bremer and Dr. B. Beele for supplying all necessary ligands.

Dr. C. Apostolidis for synthesizing  $[\text{Pu}(n\text{-Pr-BTP})_3](\text{OTf})_3$ .

Dr. W. Caliebe for the support at the W1 beamline at HASYLAB.

Dr. D. Batchelor for the support at the UE52-PGM beamline at BESSY II.

Dr. K. Kvashnina and Dr. J.-D. Cafun for the support at the ID26-Beamline at ESRF.

Dr. K. Kvashnina also for discussions about HR-XANES and RIXS.

Dr. S. Schuppler and Dr. P. Nagel for the support at the WERA beamline at ANKA.

Dr. R. Gordon for the support at the 20-ID beamline at APS.

Dr. L. Simonelli and Dr. A. Al Zein for the support at the ID20 beamline at ESRF.

Dr. D. Shuh and Dr. S. Minasian for the provided beamtime and support at beamline 11.0.2 at the ALS.

Dr. B. Schimmelpfenning for structure optimization and TD-DFT calculations.

I. Fryer-Kanssen for additional structure optimizations.

Prof. Dr. J. Rehr, Dr. J. Kas and Dr. K. Jorissen for revealing the secrets of *FEFF*.

A. Neumann, A. Ernst, V. Traunfelder, A. Gensch and the INE workshop for bringing all the crazy ideas to life.

# A | Calculations

## A.1. Comparison of methods

### A.1.1. FEFF

\*Eu L3 edge in EuBTP3OTf3

EDGE L3

S02 1.0

*	pot	xsph	fms	paths	genfmt	ff2chi
CONTROL	1	1	1	1	1	1
PRINT	1	0	0	0	0	0

EXCHANGE 0 15 -1.5

SCF 4.0

XANES 5.0

FMS 5

MULTIPOLE 2

EGRID

e\_grid -20 0 0.2

k\_grid last 5 0.05

POTENTIALS

*	ipot	Z	element	l_scm	l_fms	stoichiometry
	0	63	Eu	-1	-1	1
	1	16	S	-1	-1	4
	2	9	F	-1	-1	16
	3	8	O	-1	-1	17
	4	7	N	-1	-1	21

---

	5	6	C	-1	-1	91
ATOMS						
*x			y		z	ipot
0			0		0	0
-0.62329			-1.81917		-1.65159	4
0.70697			0.06468		2.43770	4
-1.57400			1.66066		1.12255	4
-0.44382			1.71040		-1.84110	4
-2.47377			-0.15358		-0.64871	4
2.03844			-1.54171		0.19277	4
1.70133			0.08736		-1.91728	4
1.72800			1.79497		0.61515	4
-1.08652			-1.75416		1.54770	4
0.33711			-2.64943		-2.11171	4
-1.07076			2.57031		1.99411	4
2.13545			1.92047		1.86820	5
-1.87595			-2.02233		-2.04284	5
-1.52549			2.51384		-1.77335	4
-2.85333			1.73898		0.79264	5
1.61159			0.96725		2.87559	5
2.14636			-2.37072		1.26361	4
2.90790			-1.65698		-0.79523	5
-0.74092			-1.82747		2.82078	5
0.21827			-0.80395		3.33983	5
0.35894			1.83303		-2.89428	5
-2.89941			-1.07279		-1.53361	5
-3.37234			0.73230		-0.16413	5
1.53520			0.94453		-2.95325	5
2.76966			-0.74692		-1.94519	5
2.21791			2.64543		-0.32129	4
-1.96689			-2.67396		1.05952	4
0.00243			-3.62990		-2.93199	5
-1.87958			3.48830		2.48078	5
-0.89371			-0.53426		-4.56279	3
-1.77166			3.34962		-2.75877	5
3.12132			-3.25715		1.27897	5

---

-2.81695	0.41663	3.73367	3
3.06190	3.58805	0.05520	5
-2.40465	-3.62104	1.86832	5
-2.29188	-2.99838	-2.85415	4
0.18068	2.67317	-3.91950	4
-3.73006	2.67413	1.22751	4
3.00248	2.86409	2.31508	4
-1.12775	-2.77597	3.68807	4
3.93136	-2.53908	-0.83596	4
2.06148	1.01151	4.19177	5
0.60268	-0.81117	4.67430	5
-4.70502	0.70825	-0.54147	5
-4.22239	-1.16491	-1.95253	5
3.70096	-0.71478	-2.97939	5
2.41678	1.01762	-4.04099	5
-1.35936	-3.81773	-3.31807	5
-3.24622	3.55989	2.07492	5
-0.91675	3.41419	-3.88724	5
4.06596	-3.32989	0.22326	5
3.45116	3.71462	1.41729	5
-1.92566	-3.70277	3.21680	5
1.54490	0.10396	5.10057	5
-5.12823	-0.25557	-1.44264	5
3.51664	0.17837	-4.04242	5
-1.08167	5.30538	0.02587	2
1.32420	-5.44197	-0.16242	3
-2.56593	1.10689	-4.98713	3
1.16292	-4.45091	-3.42690	5
2.18759	-3.96156	3.55176	5
-3.03765	4.14426	-2.60766	5
-1.65403	0.16794	-5.52464	1
0.11641	4.25455	3.89814	5
0.32620	5.59593	-1.49141	2
-2.82786	1.20760	4.93240	1
-1.32056	4.48245	3.47247	5
3.24258	-4.15298	2.48534	5
5.71151	1.14284	-0.26731	5

---

-1.54005	1.58796	5.43040	3
3.61971	4.51295	-0.98125	5
-3.76644	-4.50901	-0.10124	5
3.36506	4.18222	-2.40435	5
-3.34081	-4.66488	1.32806	5
-0.26799	-5.87706	1.59003	3
-0.35651	6.10810	-0.48527	5
-5.51021	-1.48984	2.30254	5
5.60965	-1.58829	2.12836	3
0.63178	-6.26561	0.62095	1
1.73164	-3.87247	-4.69628	5
5.40835	-0.76758	3.27580	5
-4.23209	3.45860	-3.27719	5
1.51701	6.12313	1.18649	3
-3.64397	-1.54715	-5.25266	2
-3.79070	2.26630	4.95077	3
6.57733	0.04806	-0.90372	5
-1.13503	-6.49945	-1.24386	2
-0.93130	0.59526	-6.64504	3
-1.78379	-4.92609	-4.24774	5
-4.15206	4.63321	2.60574	5
-1.24416	4.26120	-5.08877	5
5.21675	-4.29115	0.24105	5
4.37882	4.80815	1.88369	5
-2.29430	-4.86020	4.16611	5
-2.77087	-1.11749	-6.16301	5
-2.67628	-1.01745	6.29117	2
-1.13503	6.88345	-1.24386	2
-3.42569	0.06624	6.20351	5
-6.71799	-0.52179	2.21463	5
5.28102	-1.51269	4.53903	5
0.63178	7.11729	0.62095	1
2.43982	-4.84779	4.75558	5
-2.09179	-2.18954	-6.57676	2
0.52628	5.27229	4.95693	5
-0.35651	-7.27480	-0.48527	5
-4.65409	-5.68805	-0.55365	5

---

3.98108	5.23637	-3.32647	5
3.05826	-4.50817	-5.08175	5
5.40835	-5.12814	-0.68684	5
-3.24865	-5.05221	-4.47044	5
4.48432	4.96606	3.36341	5
-5.54295	4.13854	-2.91905	5
1.51701	-7.25977	1.18649	3
-5.54902	4.65441	1.99775	5
-0.11399	4.46119	-6.07634	5
-3.54089	-4.54751	4.87006	5
-4.66258	-0.32943	5.95768	2
-6.90959	0.31520	3.14252	5
-0.26799	7.50584	1.59003	3
2.35009	-0.97180	-7.36213	5
0.93737	5.39468	-5.57411	5
0.32620	-7.78697	-1.49141	2
7.97428	0.02686	-0.29573	5
-3.48390	-0.69539	-7.18591	2
3.16740	2.89414	-6.79343	3
-6.19777	0.79274	-5.06300	5
1.32420	7.94093	-0.16242	3
5.67513	2.07684	5.32677	2
0.69120	2.59263	7.63426	5
-1.08167	-8.07752	0.02587	2
-3.43903	0.61975	7.40806	2
1.29873	-1.90528	-7.86436	5
3.77614	1.10863	7.30443	3
1.70981	-2.57570	7.77790	5
-6.40635	-4.59176	-3.35109	2
-8.19498	2.06727	2.06551	4
0.17462	1.68508	8.54306	5
-8.06038	1.27647	3.12473	5
-6.51670	3.01806	5.02983	3
8.39628	-1.93222	-1.67396	4
7.47225	3.08850	-3.45512	5
6.58339	-0.46781	-5.82052	5
-8.14527	-3.54018	-0.42500	5

8.33565	-2.34005	2.04930	3
4.91238	3.71404	6.44366	2
1.63342	3.50777	8.06053	5
-3.69247	-6.07989	-5.47400	5
8.88012	-1.04646	-0.82655	5
5.46656	6.04808	3.77749	5
-6.24628	-3.74000	-5.28434	2
-6.64160	-0.23495	-6.06655	5

END

### A.1.2. FDMNES – FMS

! Eu L3-edge in EuBTP3OTf3

Filout

Eubtp

Range

-18 .1 69

energpho

Edge

L3

Green

Radius

4

quadrupole

molecule

1 1 1 90 90 90

63 0 0 0

7 -0.62329 -1.81917 -1.65159

7 0.70697 0.06468 2.4377

7 -1.574 1.66066 1.12255

7 -0.44382 1.7104 -1.8411

7 -2.47377 -0.15358 -0.64871

⋮

8 -1.54005 1.58796 5.4304

6 3.61971 4.51295 -0.98125

6	-3.76644	-4.50901	-0.10124
6	3.36506	4.18222	-2.40435
6	-3.34081	-4.66488	1.32806

```
convolution
gamma_max
  1
gamma_hole
  1
End
```

### A.1.3. FDMNES – FP

```
! Eu L3-edge in EuBTP3OTf3
Filout
  Eubtp
Range
  -18 .1 69
energpho
Edge
  L3
!Green
Radius
  4
quadrupole
molecule
  1 1 1 90 90 90
  63 0 0 0
  7 -0.62329 -1.81917 -1.65159
  7 0.70697 0.06468 2.4377
  7 -1.574 1.66066 1.12255
  7 -0.44382 1.7104 -1.8411
  7 -2.47377 -0.15358 -0.64871
  :
  8 -1.54005 1.58796 5.4304
  6 3.61971 4.51295 -0.98125
```

6	-3.76644	-4.50901	-0.10124
6	3.36506	4.18222	-2.40435
6	-3.34081	-4.66488	1.32806

```
convolution
gamma_max
  1
gamma_hole
  1
End
```

## A.2. FEFF – XANES pre-edge

```
*Gd L3 edge in GdBTP3OTf3 pre-edge calculation
EDGE L3
S02 1.0
*      pot      xsph   fms    paths  genfmt  ff2chi
CONTROL  1      1      1      1      1      1
PRINT   1      0      0      0      0      0

EXCHANGE 0 3 -1 2
SCF 10 1 100 0.01 10
XANES 6 0.02 0.3
FMS 10 1

COREHOLE RPA
SCREEN rfms 6.0

MULTIPOLE 2
UNFREEZEF

EGRID
e_grid -30 0 0.2
k_grid last 5 0.05

LDOS -30 20 0.1
```

## POTENTIALS

*	ipot	Z	element	l_scmt	l_fms	stoichiometry
	0	64	Gd	-1	-1	1
	1	16	S	-1	-1	4
	2	9	F	-1	-1	16
	3	8	O	-1	-1	17
	4	7	N	-1	-1	21
	5	6	C	-1	-1	91

## ATOMS

*x	y	z	ipot
0	0	0	0
-0.62329	-1.81917	-1.65159	4
0.70697	0.06468	2.43770	4
-1.57400	1.66066	1.12255	4
-0.44382	1.71040	-1.84110	4
-2.47377	-0.15358	-0.64871	4
:			
5.46656	6.04808	3.77749	5
-6.24628	-3.74000	-5.28434	2
-6.64160	-0.23495	-6.06655	5

END

## A.3. FEFF – EXAFS

\*La L3-edge in optimized La(H-BTP) structure

EDGE	L3					
S02	1.0					
*	pot	xsph	fms	paths	genfmt	ff2chi
CONTROL	1	1	1	1	1	1
PRINT	1	0	0	0	0	3
EXCHANGE	0	0	0			
SCF	6.0	1				

```

RPATH      5
EXAFS     20

```

## POTENTIALS

*	ipot	Z	element	l_scm	l_fms	stoichiometry
	0	57	La	3	3	1
	1	7	N	3	3	7
	2	6	C	1	1	11

## ATOMS

*x	y	z	ipot
0	0	0	0
-0.6572603	-1.9064901	1.8031183	1
1.979699	-0.384041	-1.8031183	1
1.3671623	-2.3679946	0	1
-1.6308511	-1.6392186	2.681959	1
2.2350306	0.5927492	-2.681959	1
0.005857	-3.0776216	1.8841087	2
2.66237	-1.5438831	-1.8841087	2
1.085375	-3.3379757	0.8981796	2
2.3480843	-2.6089502	-0.8981796	2
-1.9123757	-2.5524971	3.6094474	2
3.1667152	0.3799174	-3.6094474	2
-0.2485879	-4.0340645	2.7945099	1
3.6178963	-1.8017488	-2.7945099	1
3.0721528	-3.8090646	-0.9293109	2
1.7626703	-4.565094701	0.9293109	2
-1.2143745	-3.7730839	3.6648767	2
3.8747738	-0.8348628	-3.6648767	2
2.771831	-4.800952101	0	2

END

## A.4. FDMNES

! La L3-edge in optimized La(H-BTP)\_3 structure

```
Filout
  Labtp
Range
  -35 .1 80 .5 100 1 200
Edge
  L3
Green
SCF
Spinorbite
quadrupole
Eimag
  0.1
Density
Radius
  8
molecule
  1 1 1 90 90 90
  57 0 0 0
  7 -1.3224387 -1.5224491 -1.8031183
  7 -1.3224387 1.5224491 1.8031183
  :
  1 -6.6325216 0 0
  1 3.3162608 -5.7439322 0
  1 3.3162608 5.7439322 0

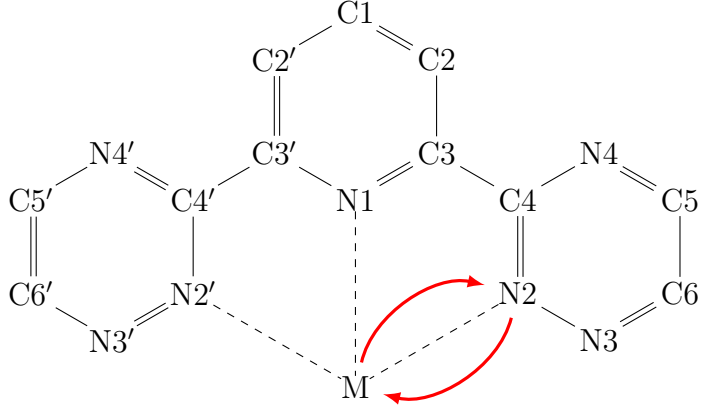
convolution
gamma_max
  1
gamma_hole
  1
End
```

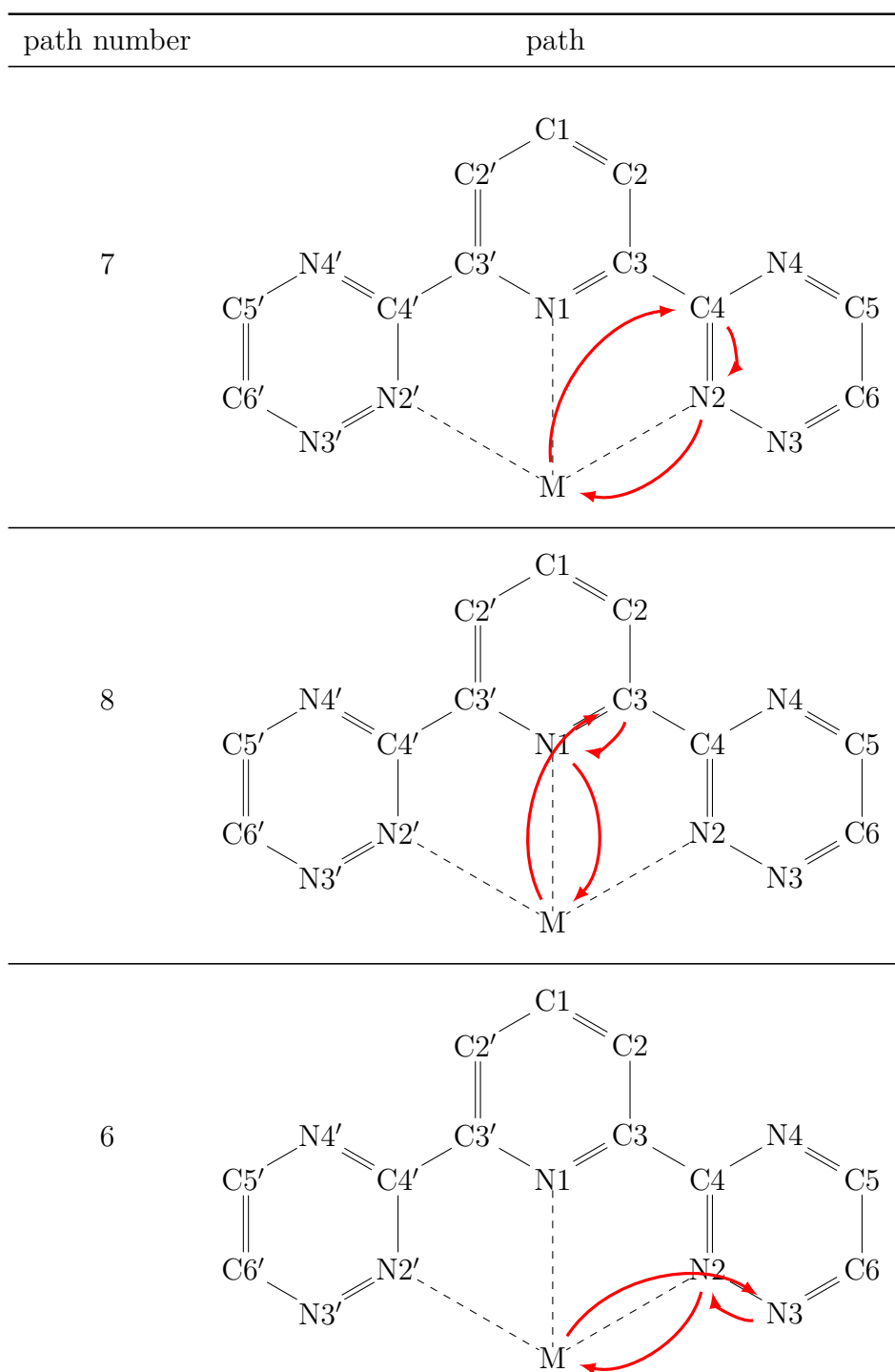


## B | EXAFS paths

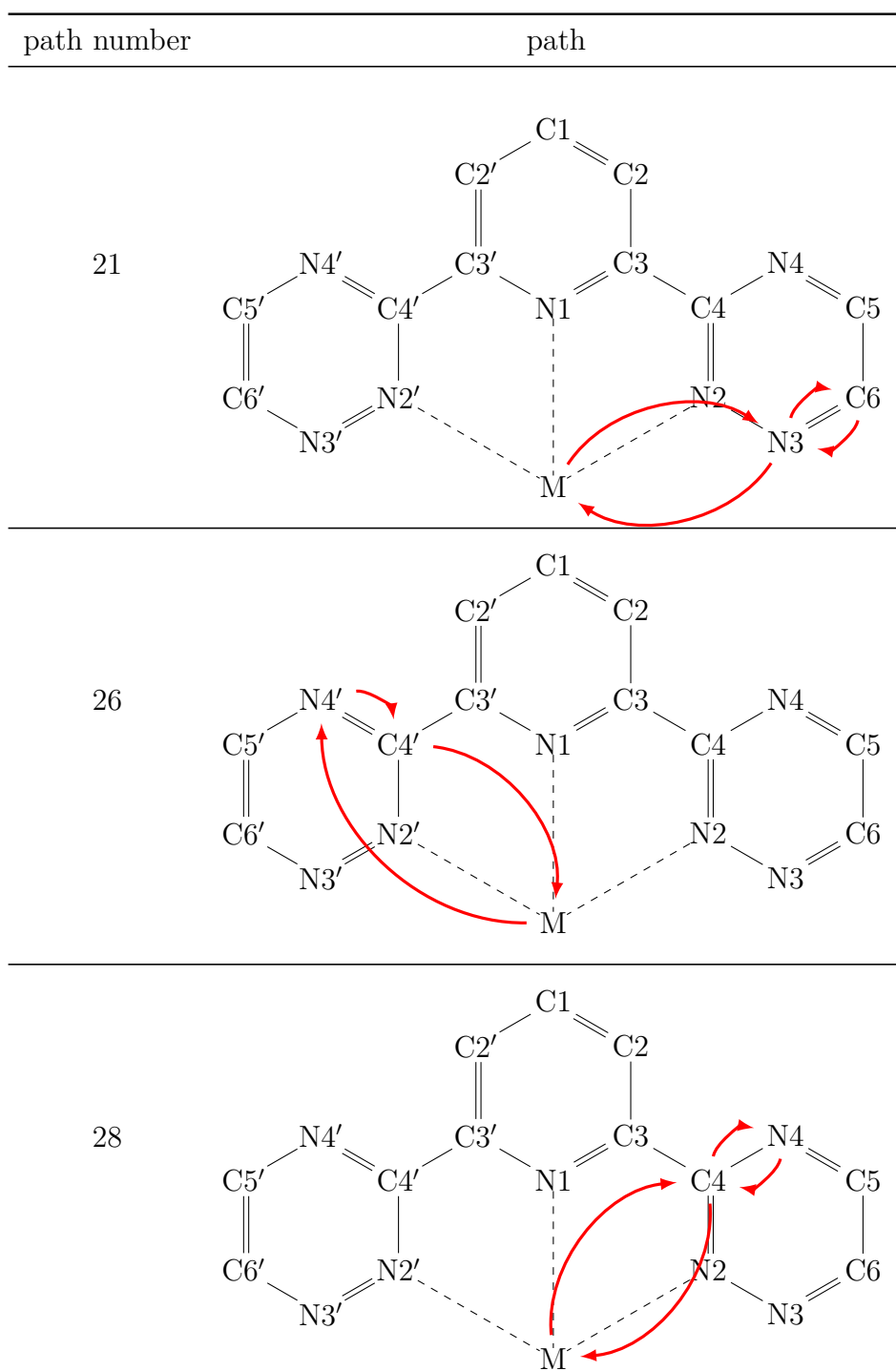
### B.1. $L_n(\text{H-BTP})$

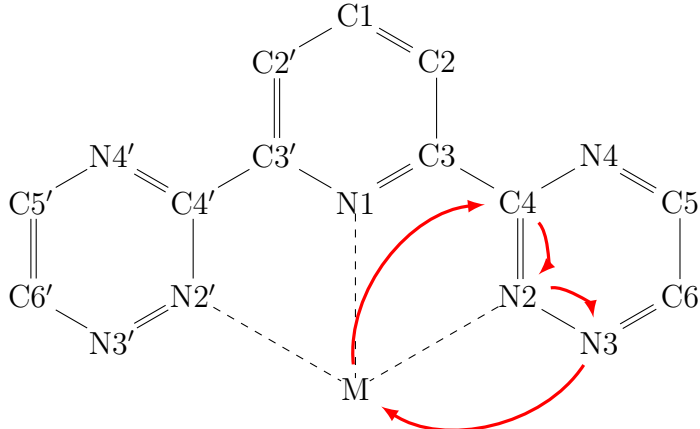
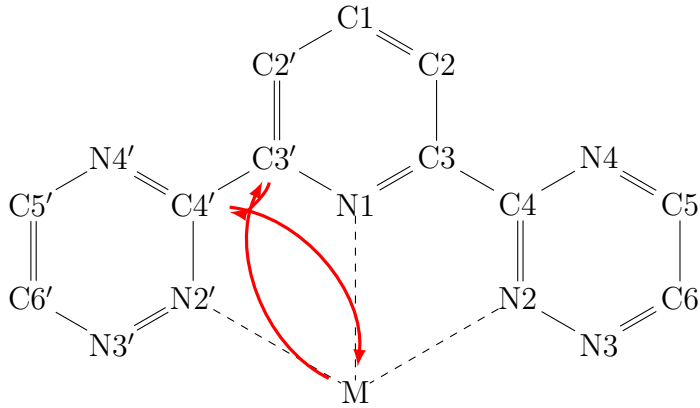
**Table B.1.:** Scattering paths in  $L_n(\text{H-BTP})$  sorted by contribution to the first post-edge peak.

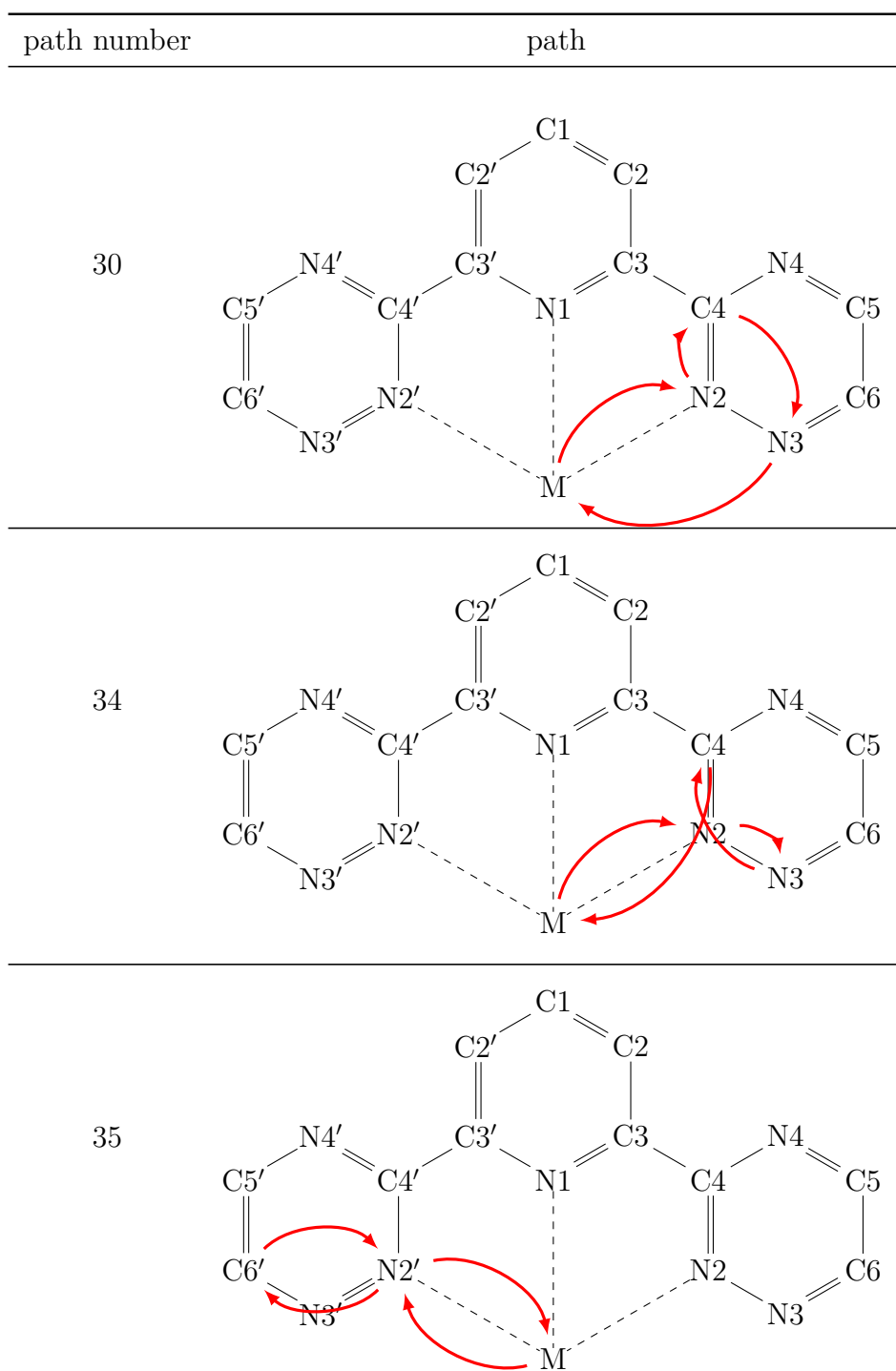
path number	path
1	

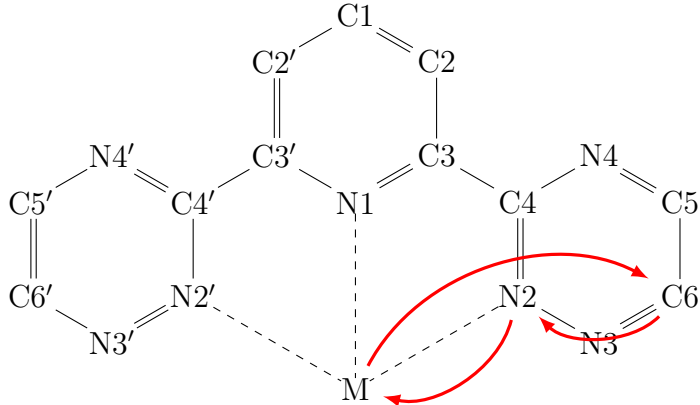
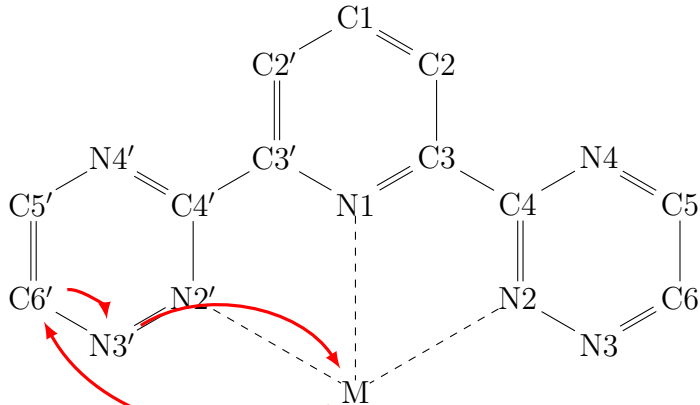






path number	path
25	
13	



path number	path
23	 <p>Chemical structure diagram for path 23. The structure shows a central metal atom M coordinated to a porphyrin ring. The atoms are labeled C1, C2, C3, C4, C5, C6, N1, N2, N3, N4, C2', C3', C4', C5', C6', N3', N4'. The metal M is coordinated to N1, N2, and N3. Red arrows indicate the path: M → N2 → C4 → N3 → C6 → N2 → M.</p>
20	 <p>Chemical structure diagram for path 20. The structure shows a central metal atom M coordinated to a porphyrin ring. The atoms are labeled C1, C2, C3, C4, C5, C6, N1, N2, N3, N4, C2', C3', C4', C5', C6', N3', N4'. The metal M is coordinated to N1, N2, and N3. Red arrows indicate the path: M → N2 → C6 → N3 → N2 → M.</p>

path number	path
32	<p>Diagram illustrating the path 32. The structure shows a central metal atom (M) coordinated to four nitrogen atoms (N1, N2, N3, N4) in a porphyrin ring. The path is highlighted in red, starting from M, going to N1, then to C3, C2, C1, C2', C3', and back to M.</p>
12	<p>Diagram illustrating the path 12. The structure shows a central metal atom (M) coordinated to four nitrogen atoms (N1, N2, N3, N4) in a porphyrin ring. The path is highlighted in red, starting from M, going to N1, then to C3, C2, C1, C2', N2', N3', and back to M.</p>
14	<p>Diagram illustrating the path 14. The structure shows a central metal atom (M) coordinated to four nitrogen atoms (N1, N2, N3, N4) in a porphyrin ring. The path is highlighted in red, starting from M, going to N1, then to C3, C4, N2, and back to M.</p>

# C | List of Publications

## C.1. Articles (peer-reviewed)

S. Ibrahimkuty, A. Seiler, T. Prüßmann, T. Vitova, R. Pradip, O. Bauder, P. Wochner, A. Plech, T. Baumbach, S. Stankov, “A portable ultrahigh-vacuum system for advanced synchrotron radiation studies of thin films and nanostructures: EuSi<sub>2</sub> nano-islands”, *J. Synchrotron Radiat.* **2015**, *22*, 91–98.

R. Böhler, M. Welland, D. Prieur, P. Cakir, T. Vitova, T. Pruessmann, I. Pidchenko, C. Hennig, C. Guéneau, R. Konings, D. Manara, “Recent advances in the study of the UO<sub>2</sub>-PuO<sub>2</sub> phase diagram at high temperatures”, *J. Nucl. Mater.* **2014**, *448*, 330–339.

D. Hudry, C. Apostolidis, O. Walter, A. Janßen, D. Manara, J.-C. Griveau, E. Colineau, T. Vitova, T. Prüßmann, D. Wang, C. Kübel, D. Meyer, “Ultra-small plutonium oxide nanocrystals: An innovative material in plutonium science”, *Chem. Eur. J.* **2014**, *20*, 10431–10438.

A. Seiler, O. Bauder, S. Ibrahimkuty, R. Pradip, T. Prüßmann, T. Vitova, M. Fiederle, T. Baumbach, S. Stankov, “Growth and structure characterization of EuSi<sub>2</sub> films and nanoislands on vicinal Si(001) surface”, *J. Cryst. Growth* **2014**, *407*, 74–77.

A. Walshe, T. Prüßmann, T. Vitova, R. Baker, “An EXAFS and HR-XANES study of the uranyl peroxides [UO<sub>2</sub>(η<sup>2</sup>-O<sub>2</sub>)(H<sub>2</sub>O)<sub>2</sub>] $\cdot$ nH<sub>2</sub>O (n = 0, 2) and uranyl (oxy)hydroxide [(UO<sub>2</sub>)<sub>4</sub>O(OH)<sub>6</sub>] $\cdot$ 6H<sub>2</sub>O”, *Dalton Trans.* **2014**, *43*, 4400–4407.

M. Denecke, T. Petersmann, R. Marsac, K. Dardenne, T. Vitova, T. Prüßmann, M. Borchert, U. Bösenberg, G. Falkenberg, G. Wellenreuther, “XANES characterization of UO<sub>2</sub>/Mo(Pd) thin films as models for  $\epsilon$ -particles in spent nuclear fuel”, *J. Phys. Conf. Ser.* **2013**, *430*, 012113.

B. Mihailova, N. Waesermann, B. Maier, R. Angel, T. Prüßmann, C. Paulmann, M. Gospodinov, U. Bismayer, “Chemically induced renormalization phenomena in Pb-based relaxor ferroelectrics under high pressure”, *J. Phys.: Condens. Matter* **2013**, *25*, 115403.

T. Prüßmann, M. Denecke, A. Geist, J. Rothe, P. Lindqvist-Reis, M. Löble, F. Breher, D. Batchelor, C. Apostolidis, O. Walter, W. Caliebe, K. Kvashnina, K. Jorissen, J. Kas, J. Rehr, T. Vitova, “Comparative investigation of N donor ligand-lanthanide complexes from the metal and ligand point of view”, *J. Phys. Conf. Ser.* **2013**, *430*, 012115.

J. Rothe, B. Brendebach, C. Bube, K. Dardenne, M. Denecke, B. Kienzler, V. Metz, T. Prüßmann, K. Rickers-Appel, D. Schild, E. Soballa, T. Vitova, “Characterization of U(VI)-phases in corroded cement products by micro( $\mu$ )-spectroscopic methods”, *J. Phys. Conf. Ser.* **2013**, *430*, 012114.

T. Vitova, M. Denecke, J. Göttlicher, K. Jorissen, J. Kas, K. Kvashnina, T. Prüßmann, J. Rehr, J. Rothe, “Actinide and lanthanide speciation with high-energy resolution X-ray techniques”, *J. Phys. Conf. Ser.* **2013**, *430*, 012117.

M. Denecke, M. Borchert, R. Denning, W. De Nolf, G. Falkenberg, S. Hönig, M. Klinkenberg, K. Kvashnina, S. Neumeier, J. Patommel, T. Petersmann, T. Pruessmann, S. Ritter, C. Schroer, S. Stephan, J. Villanova, T. Vitova, G. Wellenreuther, “Highly resolved synchrotron-based investigations related to nuclear waste disposal”, *Mater. Res. Soc. Symp. Proc.* **2012**, *1444*, 269–280.

## C.2. Articles (unpublished)

Y. Podkovyrina, I. Pidchenko, T. Prüßmann, S. Bahl, A. Soldatov, T. Vitova, “Probing Covalency in the  $\text{UO}_3$  Polymorphs by U  $M_4$  edge HR-XANES”, *J. Phys. Conf. Ser.* **2015**, (accepted).

A. Zimina, K. Dardenne, M.A. Denecke, J.D. Grundwaldt, E. Huttel, H. Lichtenberg, S. Mangold, T. Prüßmann, J. Rothe, R. Steininger, T. Vitova, “The CAT-ACT Beamline at ANKA: A new high energy X-ray spectroscopy facility for CATalysis and ACTinide research”, *J. Phys. Conf. Ser.* **2015**, (accepted).

S. Bahl, et al., “The impact of Mo on the vitrification properties of borosilicate glass”, (in preparation).

I. Pidchenko, E. Bohnert, T. Vitova, T. Prüßmann, R.J. Baker, “Neptunium Carbonate Incorporation into Uranyl Carbonate Minerals: An EXAFS and HR-XANES study of the reactivity of Np(V) with Grimselite,  $K_3Na[UO_2(CO_3)_3] \cdot H_2O$ ”, (in preparation).

T. Prüßmann, et al., “Electronic structure study of partitioning ligands, lanthanide and actinide complexes”, (in preparation).

T. Prüßmann, et al., “High energy resolution XANES studies of lanthanide partitioning complexes”, (in preparation).

T. Prüßmann, et al., “High energy resolution X-ray emission set-up for M and L edge studies of uranium and transuranium materials”, (in preparation).

### C.3. Contributions to conferences (Poster)

T. Prüßmann, A. Geist, J. Rothe, P. Lindqvist-Reis, B. Schimmelpfennig, K. Kvashnina, A. Kerridge, I. Fryer-Kanssen, T. Vitova, “High energy resolution XANES studies of lanthanide partitioning complexes”, in XAFS16, Karlsruhe, Germany, **23. - 28. August 2015**.

T. Prüßmann, M. Denecke, A. Geist, J. Rothe, P. Lindqvist-Reis, N. Banik, B. Schimmelpfennig, D. Fellhauer, C. Apostolidis, O. Walter, D. Batchelor, P. Nagel, S. Schuppler, K. Kvashnina, T. Vitova, “Comparative investigation of N donor ligand and lanthanide/actinide partitioning complexes from the metal and ligand point of view”, in Actinide XAS 2014, Schloss Böttstein, Switzerland, **20. - 22. May 2014**.

T. Prüßmann, M. Denecke, A. Geist, J. Rothe, P. Lindqvist-Reis, N. Banik, B. Schimmelpfennig, D. Fellhauer, C. Apostolidis, O. Walter, D. Batchelor, P. Nagel, S. Schuppler, K. Kvashnina, K. Jorissen, J. Kas, J. Rehr, T. Vitova, “Structural investigation of N donor ligand – Ln/An complexes from the metal and ligand point of view”, in GDCh Wissenschaftsforum 2013, Darmstadt, Germany, **1. - 4. September 2013**.

T. Prüßmann, M. Denecke, A. Geist, J. Rothe, M. Löble, W. Caliebe, D. Batchelor, T. Vitova, “Comparative investigation of N donor ligand – lanthanide complexes from the metal and ligand point of view”, in XAFS15, Beijing, China, **22. - 28. July 2012.**

T. Prüßmann, D. Batchelor, M. Denecke, A. Geist, M. Löble, H. Morin, J. Rothe, T. Vitova, “X-ray absorption spectroscopy investigations of partitioning lanthanide complexes from the metal and ligand point of view”, in Terrae Rarae 2011, Karlsruhe, Germany, **12. - 14. October 2011.**

T. Prüßmann, B. Maier, B. Mihailova, C. Paulmann, M. Gospodinov, B. U., “Temperature dependence of X-ray diffuse scattering near  $T^*$  for  $\text{Pb}_{0.78}\text{Ba}_{0.22}\text{Sc}_{0.5}\text{Ta}_{0.5}\text{O}_3$  relaxor”, in Frühjahrstagung der Deutschen Physikalischen Gesellschaft, Dresden, Germany, **13. - 18. March 2011.**